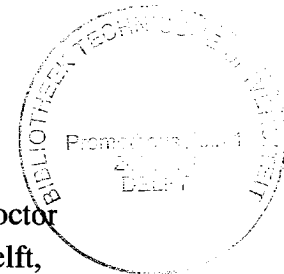


IMPROVING PREDRILLING VIEWS BY PSEUDO SEISMIC BOREHOLE DATA

PROEFSCHRIFT

Ter verkrijging van de graad van doctor
aan de Technische Universiteit Delft,
op gezag van de Rector Magnificus,
Prof. dr. ir. J. Blaauwendraad
in het openbaar te verdedigen
ten overstaan van een commissie,
door het College van Dekanen aangewezen,
op donderdag 25 september 1997 te 10.30 uur
door



RIAZ ALÁ'I

elektrotechnisch ingenieur
geboren te Teheran (Iran)

Dit proefschrift is goedgekeurd door de promotor :

Prof. dr. ir. A.J. Berkhout

Toegeweegd promotor :

Dr. ir. C.P.A. Wapenaar

Promotiecommissie :

Rector Magnificus, voorzitter

Prof. dr. ir. A.J. Berkhout (*Technische Universiteit Delft, Technische Natuurkunde*)

Dr. ir. C.P.A. Wapenaar (*Technische Universiteit Delft, Technische Natuurkunde*)

Prof. dr. ir. H. Blok (*Technische Universiteit Delft, Elektrotechniek*)

Prof. dr. ir. J.T. Fokkema (*Technische Universiteit Delft, Technische Aardwetenschappen*)

Prof. dr. J.C. Mondt (*Universiteit Utrecht, Aardwetenschappen*)

Dr. J.O.A. Robertsson (*Schlumberger Cambridge Research, Cambridge, United Kingdom*)

Dr. ir. D.J. Verschuur (*Technische Universiteit Delft, Technische Natuurkunde*)

Prof. dr. ir. P.M. van den Berg (*Technische Universiteit Delft, Elektrotechniek*)

Copyright ©1997, by Riaz Alá'i, Delft University of Technology, Delft, The Netherlands

All rights reserved. No part of this publication may be reproduced, stored in a retrieval system or transmitted in any form or by any means, electronic, mechanical, photocopying, recording or otherwise, without the prior written permission of the author, R. Alá'i, Delft University of Technology, Faculty of Applied Physics, P.O. Box 5046, 2600 GA, Delft, The Netherlands.

ISBN 90-9010768-1

SUPPORT

The research for this thesis has been financially supported by the DELPHI consortium, Delft fund for the advancement of research, and THERMIE (contract number OG/110/95-FR/NL/IT).

Typesetting system : FrameMaker®

Printed in The Netherlands by : Beeld en Grafisch Centrum Technische Universiteit Delft.

IMPROVING PREDRILLING VIEWS BY PSEUDO SEISMIC BOREHOLE DATA

DISSERTATION

In fulfilment of the requirements for the degree of
Doctor of Technical Science at the Delft University of Technology,
under the authority of the Rector Magnificus,

Prof. dr. ir. J. Blaauwendraad
and to be defended in public
before a committee,
appointed by the Board of Deans,
on Thursday September 25, 1997 at 10.30
by

RIAZ ALÁ'I

Master of Science in Electrical Engineering

Born in Teheran (Iran)

IMPROVING PREDRILLING VIEWS BY PSEUDO SEISMIC BOREHOLE DATA

پایان نامه

جهت تکمیل مقررات اخذ درجه دکترا
از دانشگاه فنی دلفت،
و تحت نظر رئیس محترم دانشگاه،
Prof. dr. ir. J. Blaauwendraad
تیپه شده و در حضور کمیته،
منصوب از طرف هیئت رئیسی دانشکده،
در جمع از آن دفاع خواهد شد،
 ساعت ۱۰:۳۰ صبح روز پنجم شنبه ۲۵ سپتامبر ۱۹۹۷
توسط

ریاض علائی

مهندس برق
متولد تهران (ایران)

*Dedicated with respectful remembrance
to my beloved and unforgettable father*

Djalaleddin Alá'i

*Who would be the proudest father to attend this graduation,
my most illustrious example,
I am the proudest son to have had such a father*



Preface

The research reported in this dissertation has been carried out at the Laboratory of Seismics and Acoustics, Department of Applied Physics, Centre for Technical Geoscience, Delft University of Technology in the Netherlands.

This research started in 1992 and was carried out within the framework of the Internationally sponsored DELPHI (DELfT PHilosophy on Inversion) Consortium. I would like to thank the following companies who sponsored the Consortium during the period of my stay:

Advance Geophysical, AGIP, Amerada Hess, Amoco, Applied Geophysical Software, Atlantic Richfield Company (ARCO), BHP Petroleum, British Gas, Chevron, CogniSeis, Compagnie Générale de Géophysique, Ensign, Exxon, Hewlett Packard / Convex, Japan National Oil Corporation, Jason Geosystems, Marathon International Oil Company, Mobil, National Iranian Oil Company, Norsk Hydro, PGS Seres, SAGA Petroleum, Saudi ARAMCO, Schlumberger GECO-Prakla, Shell, Silicon Graphics / Cray Research, Société Nationale Elf Aquitaine, Statoil, Texaco, TNO NITG, Total Compagnie Française des Pétroles, Unocal, Western Geophysical.

It is of great privilege and honour to be able to be involved in of the world leading research groups in Seismic Data Processing. Therefore I am grateful and wish to express my deep gratitude to Professor Berkhou, for providing me with this opportunity to do research under his supervision and guidance and to take part in meetings all over the world. I very much appreciate his continued enthusiasm, stimulating force and strong leadership which I will never forget.

I am greatly indebted to my co-promoter Mr. Kees Wapenaar, for his kind support especially on the theoretical aspects of this research. His availability at any time during the day for questions and discussions were of great help. I would also like to thank him for the many ideas and suggestions and careful proofreading. I would like to thank Mr. Eric Verschuur for all his kind support and availability throughout all these years. My warm thanks and respect are expressed towards Professor Jacob Fokkema for his care, support and many advices.

My sincere gratitude and thanks go to my colleagues, Mr. Jan Thorbecke, Mr. Alexander Koek, Mr. Frédéric Verhelst, Mr. Nurul Kabir, Mr. Walter Rietveld and Mr. Aart-Jan van Wijngaarden for their numerous support, cooperations, proof reading, discussions and friendship. Many things would not have been possible without the kind help, support and friendship of Mr. Jan Thorbecke.

I am also thankful to my former and present colleagues : Mr. Jan-Willem de Bruijn, Mr. Greg Haimé, Mr. Cees de Bruin, Mr. Erwin Giling, Mr. Felix Herrmann, Mr. Frank Dessing, Miss Karin Schalkwijk, Mr. Jeroen Goudswaard, Mr. Ewoud van Dedem, Mr. Maurits van der Heiden, Mr. Wim van Geloven and Mr. John Bolte.

The watertank data would not have been recorded without the help of Mr. Alexander Koek, Mr. Gerrit van Dijk, Mr. Gerard Faber and Mr. Gerrit Blacquière. Their help is gratefully acknowledged.

Thanks are also due to Mr. Edo Bergsma, Mr. Leen Buitelaar and Mr. Henry den Bok for keeping the computers running. Special thanks to Mr. Leen Buitelaar for the many extra gigabytes of disk space.

I thank my former student Mr. Frank Weissbach for his cooperation. Thanks also due to Mr. Ruud Prein, Mr. Arno Baels, Mr. Benno Rummel, Mr. Mathieu Ter Morshuizen, Mr. Peter Frinking, Mr. David 't Hart, Mr. Huibert Baud, Mr. Ivo van Barneveld and Mr. Edo Hoekstra.

I would like to thank the secretary of our Laboratory, Mrs. Hanneke Berkhouwt, for her kind and friendly support throughout the years.

Many people from different International Companies provided me with numerical and field datasets used in this dissertation. The cooperation of the following people is gratefully acknowledged : Mr. Takeshi Kozawa and Mr. Tetsuro Tsuru (JNOC), Mr. David Campbell and Mr. Bruce VerWest (ARCO), Mr. Johan Robertsson (Schlumberger Cambridge Research), Mr. Jean Brac and Mrs. Laurence Nicoletis (IFP), Mr. Bob Keys and Mr. Doug Foster (Mobil) and Mr. Mundy Brink (SAGA).

I would like to thank the following people for the many fruitful discussions and acts of kindness : Mr. Rick Chimblo and Mr. Panos Kelamis (Saudi ARAMCO), Mr. Colin MacBeth (BGS), Mr. Michael Oristaglio (Schlumberger-Doll Research), Mr. Lorenzo Barzaghi (AGIP), Mr. Peter Dillon (CGG), Mr. Salah Al-Tweel (QGPC), Mr. Moujahed Al-Husseini (Gulf Petrolink), Mr. Benoit Barbier and Mr. Azhar Akhtar (Schlumberger Middle East), Mr. Dick Ireson (Schlumberger Geco-Prakla), Mr. Guildas Omnes (CGG), Mr. Ted Ter Burg (Schlumberger Wireline and Testing), Mr. Jim O'Connell, Mr. Cathal Daly and Mr. Arthur Weglein (ARCO) and Mr. Mohamed Hadidi (Mobil).

I would like to thank all the people who gave me the opportunity to visit : Amoco, ARCO, Exxon, Saudi ARAMCO, Schlumberger, PGS, Texaco, Advance, Cogniseis, Mobil, AGIP and CGG.

Special thanks to Mr. Hamed Alá'i for the idea of the cover, and Mr. Alexander Koek, Mr. Frédéric Verhelst and Mr. John Snabel for their support in its realization.

Furthermore I wish to thank Mr. Taraz Jaber and Mrs. Bahereh Jaber who made my stays in Bahrain unforgettable. I wish to thank Mrs. Mina Farees for correcting the Farsi text. Thanks to Mrs. Attieh Haghghi for the many advices.

Most of all I want to express my sincere and deepest gratitude to my parents and my brother for their full guidance, encouragement and kind and resolute support throughout the years. Without their support I would never have achieved this goal.

Words are lacking to express my thankfulness for the everlasting support and guidance of my father Mr. Djalaleddin Alá'i and my mother Mrs. Mehrnoush Alá'i. They played a very important role in my life and education.

I end up with saying that I will always remember the unforgettable times I had during my Ph.D. research with gratitude, honour and affection.

Contents

Preface	ix
----------------	----

Symbols and Definitions	xv
--------------------------------	----

1	Introduction	19
----------	---------------------	-----------

1.1	The seismic method.....	19
1.2	Seismic borehole data.....	23
1.2.1	Vertical Seismic Profiling.....	23
1.2.2	Crosswell Seismic Profiling	24
1.3	Motivation and aim of research.....	25
1.4	Importance of data reorganization and wave propagation	25
1.5	Outline of this thesis	30

2	Formulation of propagation and reflection	33
----------	--	-----------

2.1	Introduction	33
2.2	Review of the two-way and one-way wave equations	34
2.3	Two-way versus one-way wave field extrapolation.....	40
2.4	Review of the one-way forward model ('WRW' model).....	45

3 From surface to pseudo VSP data 51

3.1	Introduction	51
3.2	Algorithm for the generation of pseudo VSP depth records	52
3.3	One-way and two-way formulation.....	54
3.4	Data integration	62
3.5	Boundary conditions.....	69
3.6	Illustrations on synthetic data.....	77
3.6.1	The Marmousi model and dataset.....	77
3.6.2	Aliasing issues	84
3.6.3	Laterally invariant subsurface model.....	85
3.6.4	Accuracy aspects	88
3.6.5	Numerical example on internal multiples.....	89

4 Pseudo VSP data and Common Focus Point Technology 93

4.1	Introduction	93
4.2	Common Focus Point technology	94
4.2.1	Designing areal sources	95
4.2.2	Controlled illumination.....	97
4.2.3	Focusing in emission	98
4.2.4	Focusing in detection.....	100
4.3	Pseudo VSP generation in relation with Common Focus Point Technology.	104
4.4	Pseudo VSP data in one-way time : (t, t') display.....	115
4.5	Real VSP data in one-way time : (t, t') display.....	118
4.5.1	Marine data example.....	118
4.5.2	Land data example (I).....	120
4.5.3	Land data example (II).....	123

5 Imaging with multi-offset, common-well pseudo VSP data 125

5.1	Introduction	125
5.2	From surface to pseudo VSP depth and one-way time records.....	126
5.3	Construction of <i>depth</i> and <i>one-way time</i> image gathers.....	128
5.3.1	From pseudo VSP depth records to <i>depth</i> image gathers	129
5.3.2	From pseudo VSP one-way time records to <i>one-way time</i> image gathers	130
5.4	Picrocol model and dataset.....	140

6 Imaging with multi-well, common-offset pseudo VSP data 149

6.1	Introduction	149
6.2	From image gathers to common-offset sections.....	150
6.2.1	Construction of <i>two-way</i> and <i>one-way</i> common-offset sections	151
6.3	Synthetic data examples	152
6.3.1	Syncline model and dataset	152
6.3.2	Picocol model and dataset	154
6.3.3	SEG/EAGE Salt model and dataset.....	158
6.4	Field data examples	168
6.4.1	ELF model and dataset	168
6.4.2	NAM model and dataset	174

7 2-D case studies 177

7.1	Introduction	177
7.2	Marine dataset (I)	178
7.2.1	Integration of pseudo VSP and real VSP data	179
7.2.2	Integration of the corridor stack with surface data	183
7.2.3	Source wavelet estimation using two-way operators.....	185
7.3	Marine dataset (II).....	187
7.4	Marine dataset (III).....	192
7.5	Land dataset (I).....	194
7.6	Land dataset (II)	198
7.7	Land dataset (III).....	201
7.8	Physically modeled dataset	204

8 3-D case studies 211

8.1	Introduction	211
8.2	SEG/EAGE 3-D Overthrust model and dataset	213
8.3	Watertank model and dataset	223
8.4	3-layered model and dataset	229

Appendix A	Data matrix notation	237
Appendix B	Optimized wave field extrapolation operators	241
Appendix C	Processing of VSP data	247
References		257
Summary		263
Samenvatting		265
Curriculum Vitae		267

Symbols and Definitions

Some definitions, transformations, abbreviations and notations that are used in this thesis, will be introduced below.

Definitions

Any scalar function in the *space time domain* is denoted by a lower case symbol, $p(x, y, z, t)$. This function is written in terms of the spatial variables x , y , and z and time t . The corresponding function in the *space frequency domain* is denoted by the corresponding upper case symbol $P(x, y, z, \omega)$. The corresponding function in the *wavenumber frequency domain* is denoted by the corresponding upper case symbol with a tilde \sim above the symbol, $\tilde{P}(k_x, k_y, z, \omega)$. Vector quantities are denoted with an arrow above the symbol, $\vec{p}(x, y, z, t)$. The corresponding vector in the *space frequency domain* is denoted by $\bar{P}(x, y, z, t)$ and in the *wavenumber frequency domain* by $\tilde{\bar{P}}(x, y, z, t)$. Matrices are denoted in the *space time domain* by a bold lower case symbol, \mathbf{p} . The same matrix is denoted in the *space frequency domain* by a bold upper case symbol, \mathbf{P} and in the *wavenumber frequency domain* with a tilde \sim above the symbol, $\tilde{\mathbf{P}}$. The notation convention for the various domains that play a role in this thesis is summarized in Table 1.

Table 1 Notation convention for the different domains that play a role in this thesis.

domain	space-time	space-frequency	wavenumber-frequency
domain, symbol variable	(x, y, z, t)	(x, y, z, ω)	(k_x, k_y, z, ω)
function	$p(x, y, z, t)$	$P(x, y, z, \omega)$	$\tilde{P}(k_x, k_y, z, \omega)$
scalar	p	P	\tilde{P}
vector	\vec{p}	\bar{P}	$\tilde{\bar{P}}$
matrix	\mathbf{p}	\mathbf{P}	$\tilde{\mathbf{P}}$

The transpose of a vector (or matrix) is denoted with a superscript T , the complex conjugate with a superscript $*$.

Transformations

The *forward* temporal Fourier transformation of a (space and) time dependent function is defined by :

$$F(x, y, z_m, \omega) = \int_{-\infty}^{\infty} f(x, y, z_m, t) e^{-j\omega t} dt, \quad (1)$$

The *inverse* transformation is defined as :

$$f(x, y, z_m, t) = \frac{1}{2\pi} \int_{-\infty}^{\infty} F(x, y, z_m, \omega) e^{j\omega t} d\omega, \quad (2)$$

where $f(x, y, z_m, t)$ represents a real-valued three-dimensional function at datum level $z=z_m$ and $\omega=2\pi f$ denotes the angular frequency. Throughout this thesis only positive frequencies are considered, thus $\omega \geq 0$. The inverse temporal Fourier transformation can be reformulated as :

$$f(x, y, z_m, t) = \frac{1}{\pi} \Re \left[\int_0^{\infty} F(x, y, z_m, \omega) e^{j\omega t} d\omega \right], \quad (3)$$

with \Re denoting the real part of the term between the brackets.

The spatial Fourier transformation of the function $F(x, y, z_m, \omega)$ from the space frequency domain to the wavenumber frequency domain is defined as :

$$\tilde{F}(k_x, k_y, z_m, \omega) = \int_{-\infty}^{\infty} \int_{-\infty}^{\infty} F(x, y, z_m, \omega) e^{jk_x x} e^{jk_y y} dx dy, \quad (4)$$

and its inverse as:

$$F(x, y, z_m, \omega) = \left(\frac{1}{2\pi} \right)^2 \int_{-\infty}^{\infty} \int_{-\infty}^{\infty} \tilde{F}(k_x, k_y, z_m, \omega) e^{-jk_x x} e^{-jk_y y} dk_x dk_y. \quad (5)$$

Abbreviations

AVA	Amplitude Versus Angle	CFP	Common Focus Point
CDP	Common Depth Point	CMP	Common Mid Point
CRG	Common Receiver Gather	CSG	Common Shot Gather
CWS	Crosswell Seismic	SNR	Signal to Noise Ratio
FT	Fourier Transform	RT	Radon Transform
ISD	Integrated Seismic Display	SWD	Seismic While Drilling
MSL	Mean Sea Level	VSP	Vertical Seismic Profile
NMO	Normal MoveOut	RVSP	Reversed VSP
SRME	Surface-Related Multiple Elimination	VSP-CDP	VSP-CDP transformed data
WLSQ	Weighted Least SQuare	1-D	1-Dimensional
P-wave	Compressional wave	2-D	2-Dimensional
S-wave	Shear wave	3-D	3-Dimensional

Throughout the thesis several variables are used which are described below :

Table of Notation

c_p	compressional-wave velocity [m/s]	c_s	shear-wave velocity [m/s]
$\delta(x)$	spatial delta function	f	temporal frequency [Hz=1/s]
k_x, k_y, k_z	wavenumbers [1/m]	K	bulk compression modulus [N/m ²]
λ, μ	Lamé coefficients [N/m ²]	p	slowness [s/m]
p	acoustic pressure [Pa=N/m ²]	ρ	volume density of mass [kg/m ³]
t	time [s]; also used as 'two-way time' [s]	σ	Poisson's ratio
t'	'one-way time' [s]	$\Delta t, \Delta t'$	sampling interval in 'two-way time' [s], respectively 'one-way time' [s]

t_{VSP}	VSP travel time [s]	τ	intercept time [s]
τ_{xz}, τ_{zz} , etc.	shear and tensile stresses [N/m ²]	v_x, v_z	horizontal respectively vertical component of the particle velocity [m/s]
x, y, z	cartesian coordinates [m]	$\Delta x, \Delta y, \Delta z$	sampling interval along x -axis, y -axis and z -axis [m]
ω	angular frequency ($2\pi f$) [rad/s]	z_r, z_s	receiver respectively source level [m]
$W^+(z_m, z_0)$	extrapolation matrix for downgoing wave fields from z_0 to z_m	$W^-(z_0, z_m)$	extrapolation matrix for upgoing wave fields from z_m to z_0
$F^+(z_0, z_m)$	inverse extrapolation matrix for downgoing wave fields from z_m to z_0 $= [W^+(z_m, z_0)]^{-1}$ $\approx [W^-(z_0, z_m)]^*$	$F^-(z_m, z_0)$	inverse extrapolation matrix for upgoing wave fields from z_0 to z_m $= [W^-(z_0, z_m)]^{-1}$ $\approx [W^+(z_m, z_0)]^*$
$R^+(z_m)$	matrix representation of the reflection operator at depth level z_m	$P(z_0)$	matrix representation of seismic data at depth level z_0 (see Appendix A)
$\bar{F}_j(z_0, z_m)$	focusing operator, where j denotes the lateral position of the focus point in <i>focusing in emission</i>	$\bar{F}_i^\dagger(z_m, z_0)$	focusing operator, where i denotes the lateral position of the focus point in <i>focusing in detection</i>
\bar{P}_j	CFP gather for <i>focusing in emission</i>	\bar{P}_i^\dagger	CFP gather for <i>focusing in detection</i>

Chapter 1

Introduction

1.1 The seismic method

Today, geophysical exploration plays an important role in the ever increasing demand for energy resources. For the oil and gas industry, geophysics contributes to an economic exploration and exploitation of hydrocarbon (oil and/or gas) reservoirs. Several methods are being used in geophysical exploration, but the seismic exploration method is by far the most important one.

Seismology is the science that deals with the propagation and reflection of elastic waves in the earth's interior. In earthquake seismology, the waves excited by an earthquake are recorded and investigated for a better understanding of the generation of earthquakes and the propagation of the resulting waves as a means of understanding the global structure of the earth. The aim of the seismic exploration methods is to produce images of the earth's subsurface (down to approximately 7 kilometers) and to obtain physical properties from data recorded at the surface. In seismic exploration man-made sources are used, which emit seismic waves into the subsurface.

In the most often used seismic exploration techniques both sources and detectors are placed near or at the surface, at land as well as in marine environments. On land, dynamite and seismic vibrators are commonly used to generate the source wave field. In general for the marine case, airgun sources are used. The response is measured at the surface by a distribution of geophones (land) or hydrophones (marine).

Figure 1.1 illustrates three types of seismic surveys. At the left-hand side of the illustration, the acquisition of seismic measurements on land is shown. Seismic waves are emitted into

the earth by a seismic source (here a dynamite source). These waves propagate through the subsurface. However, whenever changes in the subsurface parameters occur, a part of the wave field gets reflected and propagates upwards to the surface. At the surface the waves are detected by geophones, yielding recorded seismic signals. The result of each seismic experiment is a shot record containing the registrations (as a function of travel time) of reflected wave fields at each detector. The seismic experiments are repeated many times, in which the sources and receivers are placed at different surface locations, in order to obtain a good image quality. At the right-hand side of Figure 1.1, the experiment is shown for a marine acquisition where hydrophones are used to detect the wave field originating from an airgun source array.

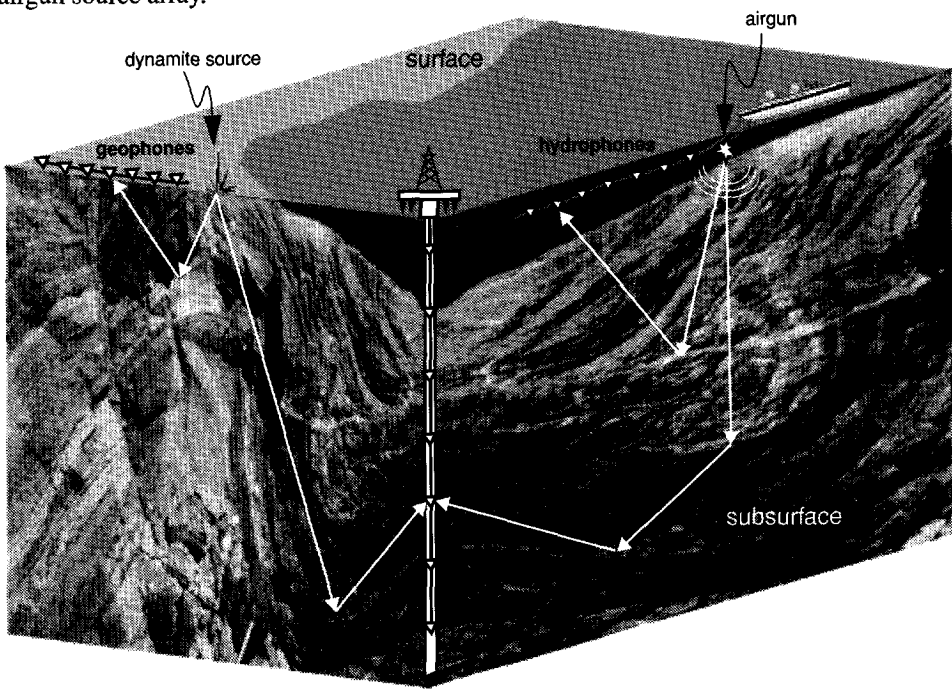


Figure 1.1 The principle of acquisition of seismic measurements in different seismic exploration configurations :

- ***acquisition on land** (left) - Seismic waves which are generated by the seismic source (generally a dynamite source), propagate through the subsurface, get reflected by the layer boundaries and propagate back to the surface. Geophones at the surface are used to measure the response of the seismic waves as a function of time;
- ***acquisition at sea** (right) - Hydrophones along the surface are used to measure the response from an airgun array near the surface;
- ***acquisition in a borehole** (middle) - A tool with geophones and/or hydrophones is lowered in a well to measure the response from a source at the surface.

To obtain more information about a potential reservoir and to investigate the characteristics of the layers from nearby, a well can be drilled. The existence of a borehole allows the seismic method to be applied with sources and/or detectors in the borehole. With these type of surveys extra information can be obtained in the neighbourhood of the borehole, particularly in the target zone (the area where oil and gas reservoirs are found or expected to exist). Placing sources and/or receivers in boreholes helps reservoir engineers in accurately mapping reservoirs. This type of data acquisition where receivers are located in a borehole is also illustrated in Figure 1.1 (in the middle). Note that here an offshore configuration is shown for a vertical well. The acquisition of the data where sources are placed at the surface and receivers in a borehole is called a Vertical Seismic Profiling (VSP) recording. A complementary configuration called reverse-VSP (RVSP) is obtained by placing the sources in the well and receivers at the surface.

In Figure 1.2a a preprocessed surface shot record is shown. The preprocessing consists of 1)interpolation of the missing near offsets, 2)removal of the direct waves (the direct wave consists of energy emitted by the source that travels along the surface of the earth directly to the receivers) and 3)elimination of the surface-related multiples (these multiple reflected waves have traveled more than one time through the subsurface of the earth). Figure 1.2b shows a preprocessed VSP record after common level stacking and noise removal. The main upgoing reflected waves are indicated by the arrows.

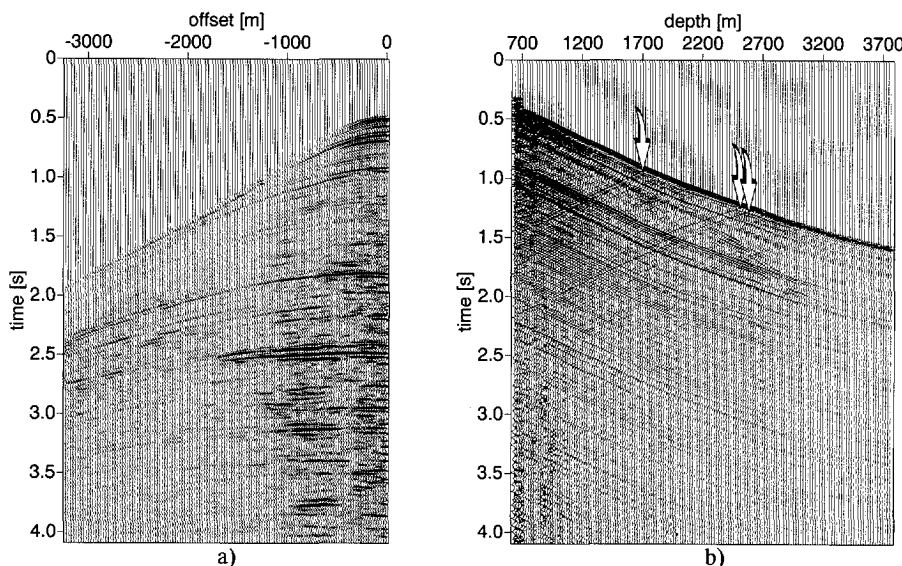


Figure 1.2 a)Preprocessed seismic surface shot record (marine acquisition) and b)preprocessed Vertical Seismic Profiling (VSP) record (note the upgoing reflected waves shown by the arrows).

In this thesis a method is presented for the transformation of surface seismic data into pseudo VSP data or, more generally, pseudo borehole data. This transformation is performed numerically and results in seismic data as if they were “measured” in the subsurface, instead of the measurements recorded at the earth’s surface. In the remaining part of this section, a brief description will be given of the seismic method for obtaining a structural image of the subsurface. The main advantages of borehole data will be discussed together with the motivation and aim of the research.

Recorded waves contain information about the earth along the paths the waves have traveled. In the seismic processing phase, the measured quantities need to be transformed into a model describing the relevant properties of the subsurface and into sections in space and time (or space and depth) of the subsurface. These sections need then to be interpreted in order to obtain structural images of the subsurface. In other words, in the seismic method information is extracted about the earth from the seismic measurements with the objective to present it in terms of geological structure and material properties. With this information geologists may decide to choose an optimum location for drilling. A correct image (with respect to the lateral and depth positioning of the structures as well as the strength of the reflectors) is important for a correct delineation of the reservoir.

The method for transforming the seismic measurements into a structural representation of the subsurface is called seismic *imaging* or *seismic migration*. Imaging requires knowledge of the way seismic waves have propagated in the earth’s subsurface (wave theory).

Prior to obtaining the reflection information at the target zone, the propagation parameters of the overburden (=part of the subsurface above the target zone) have to be estimated. This description is generally referred to as the *macro model* of the subsurface. The macro subsurface model is a sparse model since it does not contain detailed information (e.g. thin layers). If these parameters of the overburden have been estimated accurately, it is possible to correct for the propagation properties of the overburden, yielding the reflection information (*seismic migration*).

Wave field extrapolation lies at the basis of seismic migration methods. The seismic migration method can be formulated as the computational process reconstructing the wave fields below the surface from data at the surface. In this way, data acquisition can be simulated at any desired depth level in the subsurface. Wave field extrapolation removes the propagation effects between the surface and the new depth level. From the extrapolated data, the local reflection properties are estimated by applying the imaging principle (time coincidence of an upgoing wave field with a downgoing wave field, Claerbout (1971)).

The method presented in this thesis, aims at the generation of pseudo borehole data from surface recorded data, using wave field extrapolation algorithms.

The generated pseudo borehole data can then be integrated with migrated seismic data for a better understanding of the images.

1.2 Seismic borehole data

In this section a brief overview is given on data acquisition surveys with receivers or sources in a borehole. The borehole data being discussed here are the Vertical Seismic Profiling (VSP) and the Crosswell Seismic (CWS) data.

1.2.1 Vertical Seismic Profiling

The ever increasing costs of drilling has pushed geophysicists to come up with new techniques to reduce the number of mispositioned boreholes and to improve the field development planning. Vertical Seismic Profiling (VSP) is one of the geophysical techniques responding to this demand of more successful planning. The basic aim of all exploration methods is to obtain a consistent image of the subsurface of the earth, securing future oil- and gas supply, and to keep exploration and production profitable. Vertical Seismic Profiling is a technique where sources are placed at the surface and receivers in a borehole for investigating the characteristics of the structures from nearby. A complementary configuration is obtained by placing the source in the well and the receivers at the surface. The latter is the reverse-VSP (RVSP) configuration. VSP adds a depth dimension to seismic data and allows a more detailed seismic view of the subsurface. This offers the potential for better interpretation of the surface seismic data. The interest in the performance of Vertical Seismic Profiles (VSP) has increased more and more for the last decade. Since all or part of the measurement and observation of VSP takes place inside the earth, one can observe the attenuation and distortion of a surface generated pulse progressing through the earth (downgoing source wave field). The reflection and refraction of the pulse can be observed and also how it is converted to shear and/or pressure waves. Multiples can be a major problem in surface seismic data processing. Therefore the understanding of the multiple generation and reflection mechanism is very important and the way in which they may obscure the primary reflections in the vicinity of the well.

The identification of multiples and their origin in seismic data can be seen very clearly in VSP data.

Vertical seismic profiling has been accepted as a useful tool to solve many uncertainties appearing in the surface seismic data around wells. For the last two decades a lot of research was carried out in the field of real VSP and synthetic VSP modeling and their applications. The lowering of a recording device down a borehole for seismic investigation purposes was first reported by Fessenden (1917). This was the basis for borehole seismic development and was followed by many authors including Gal'perin (1974).

Several authors (Kennett et al. (1980), Wyatt (1981), Balch et al. (1982), Hardage (1983), Balch and Lee (1984), Dillon and Thompson (1984), Fitch (1984), Cassell (1984), Toksöz and Stewart (1984), Aminzadeh and Mendel (1985), Oristaglio (1985), Stewart and DiSiena (1989), Dupal et al. (1993), Hinds et al. (1996)) showed the various advantages of VSP data over surface seismic measurements, around the borehole.

The major advantages of VSP data over surface seismic data may be summarized as follows:

- Identifying different wave types : primaries, multiples and *P*- and *S*- wave conversions.
- Recording of both up- and downgoing waves at a sequence of depth levels, enabling to observe reflected and transmitted wave fields through the geological section.
- Separation and removal of up- and downgoing waves leading to better multiple recognition.
- Because of the close proximity of the receivers to the target zone, today the VSP data are generally characterized by a better SNR and a higher resolution (compared with the equivalent surface seismics) offering a more detailed seismic view of the subsurface. This increases the reliability of the geological interpretation.
- Lithology can be correlated with the processed VSP data, permitting the prediction of lithologies ahead of the drill bit and around the borehole.

In short, the application of Vertical Seismic Profiling proves to be a useful tool for better seismic interpretation.

1.2.2 Crosswell Seismic Profiling

In areas where more than one borehole is available, it is possible to put the sources into one well, and the receivers into another well. In this way it is possible to use relatively high frequencies because both sources and receivers can be positioned near the target zone and beneath the attenuating shallow section (depending on the distance between the boreholes).

1.3 Motivation and aim of research

Considering the advantages of borehole data recording, a new method is presented in this thesis for the transformation of seismic surface measurements into pseudo borehole data with the objective to obtain a better insight and understanding of the propagation and reflection of the waves in the subsurface. In other words, the schemes discussed in this thesis result in seismic data as if they were measured in the subsurface instead of measurements recorded at the earth's surface. The method is based on wave field extrapolation that is aimed at removing the propagation effects and thus improving the interpretability of the seismic data. The application of the method as proposed in this thesis, is mainly focused in the area of seismic data imaging and interpretation. The pseudo borehole data will be proposed as a tool for integrating surface data with real borehole data, images and well log data. It is important to notice that in the transformation of surface data into pseudo borehole data no new information is created. It is a model-based transformation unlike many other transformations e.g. the Fourier or the Wavelet transformations.

1.4 Importance of data reorganization and wave propagation

As outlined in the previous sections, the measurements of seismic waves can be recorded at the surface or in a borehole (space-time domain). In the following illustrations, different data acquisitions will be shown for a single source, transmitting waves into the subsurface. The wave propagation, reflection and transmission of the seismic waves will be shown on a simple two dimensional acoustic subsurface model as depicted in Figure 1.3.

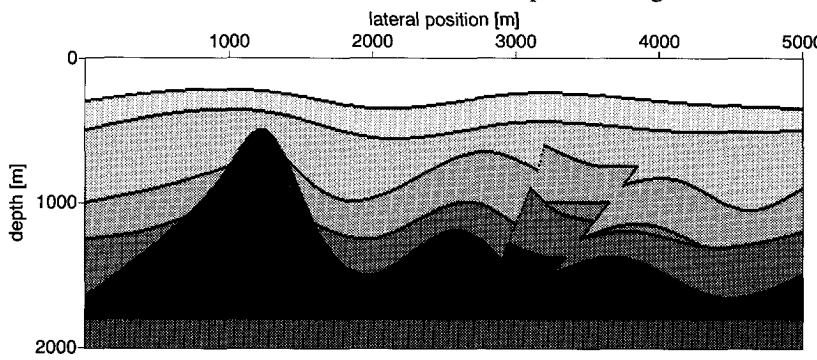


Figure 1.3 Acoustic subsurface model.

Figure 1.4 illustrates three snapshots for a point source at the surface at lateral location $x=2500m$. The three snapshots show for increasing times t_1 , t_2 and t_3 , the propagation of the waves through the subsurface and the reflection and transmission at the layer boundaries.

These snapshots have been modeled using an acoustic finite difference algorithm. From these snapshots it can be easily seen that the seismic source wave field propagates downward and that at each velocity or density contrast, part of the wave field is reflected and transmitted. For increasing times these wave fields may become very complicated so that it will become difficult to understand and identify the various events.

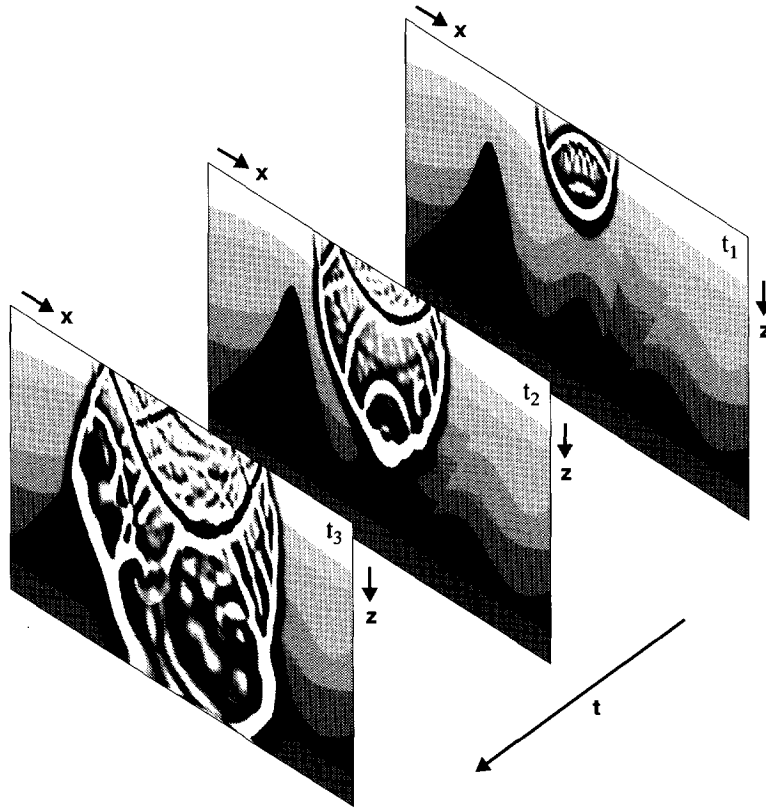


Figure 1.4 Three snapshots for increasing times t_1 , t_2 , and t_3 illustrating the propagation, reflection and transmission of the waves through the subsurface.

For subsequent times, a series of snapshots can be stored on top of each other and form a cube of data (x, z, t) . Figure 1.5 illustrates the registration of the wave field in the different planes. By recording the wave field at the surface with some detectors, a shot record (x, t) is obtained representing the reflected upgoing wave field at the surface along lateral position x for subsequent times t (Figure 1.5a).

From this cube of data (x, z, t) , the wave field (t, z) can be extracted at each depth level z for subsequent times t (at a particular location x).

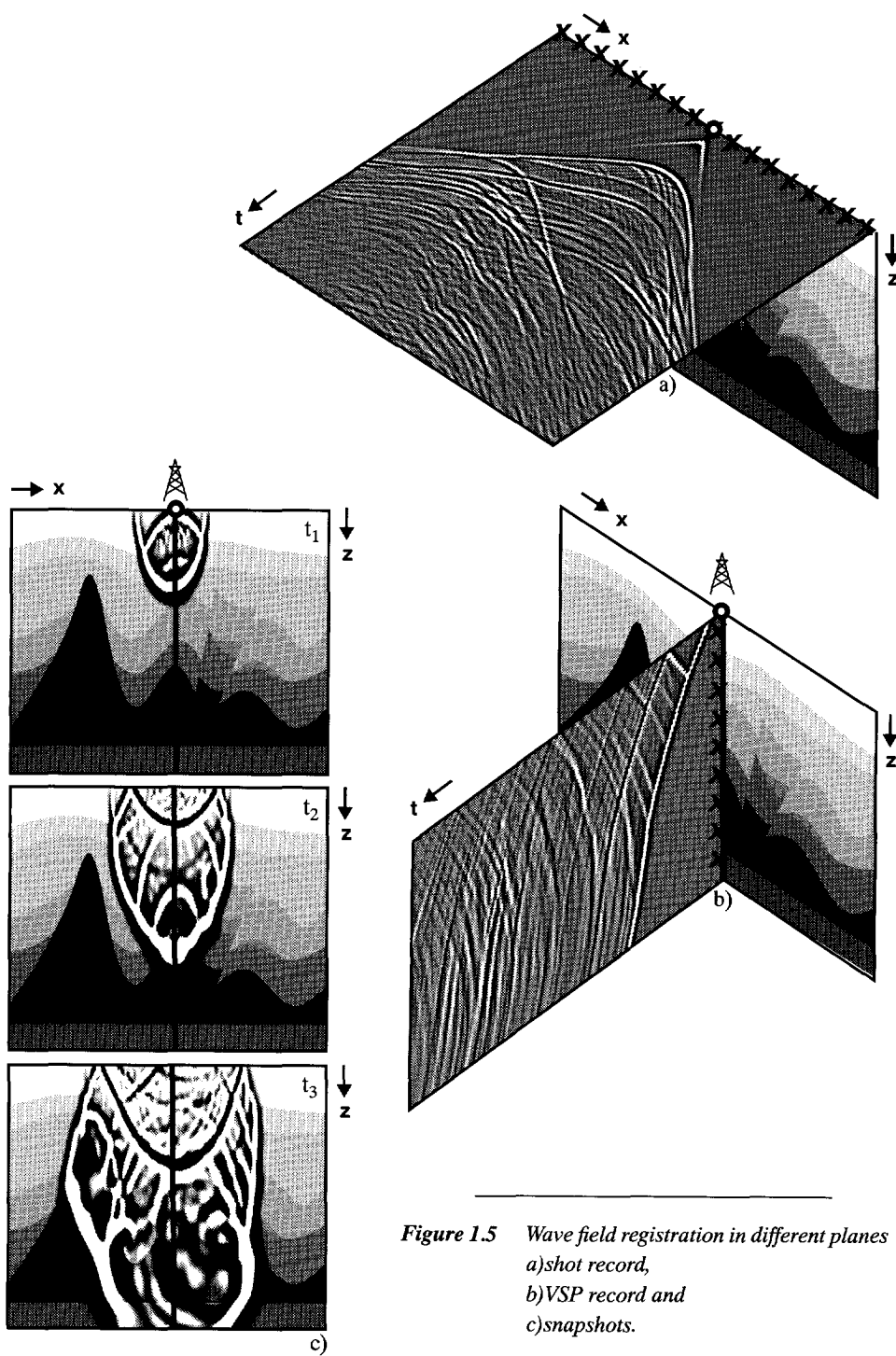


Figure 1.5 Wave field registration in different planes
a) shot record,
b) VSP record and
c) snapshots.

The obtained data representation Figure 1.5b, is then similar to a VSP recording containing the up- and downgoing wave fields at the various depth levels. The lateral location of the “well” is also indicated in the snapshots (see Figure 1.5c). The VSP display is very useful to analyze the entire wave field propagation since it shows the response of the subsurface model to the source pulse at any depth point in the subsurface.

Figure 1.6a illustrates the cube of data with three different data recordings : shot record (x, t) , VSP (t, z) and snapshot $(x, z, t=t_3)$. This volume of data has been “unfolded” into two dimensions for a better view on the continuity of the different events in the different planes (Figure 1.6b). This figure consists of two parts : the left part shows an integrated shot record-snapshot display (*x*-axis in common) and the right part shows the integrated shot record-VSP display (*t*-axis in common). Finally, the lower part of the figure is an integrated snapshot-VSP display (*z*-axis in common). From this integrated data representation it is clear that the VSP display gives significantly more insight in understanding the wave propagation through the subsurface and facilitates the identification of the events in the shot record.

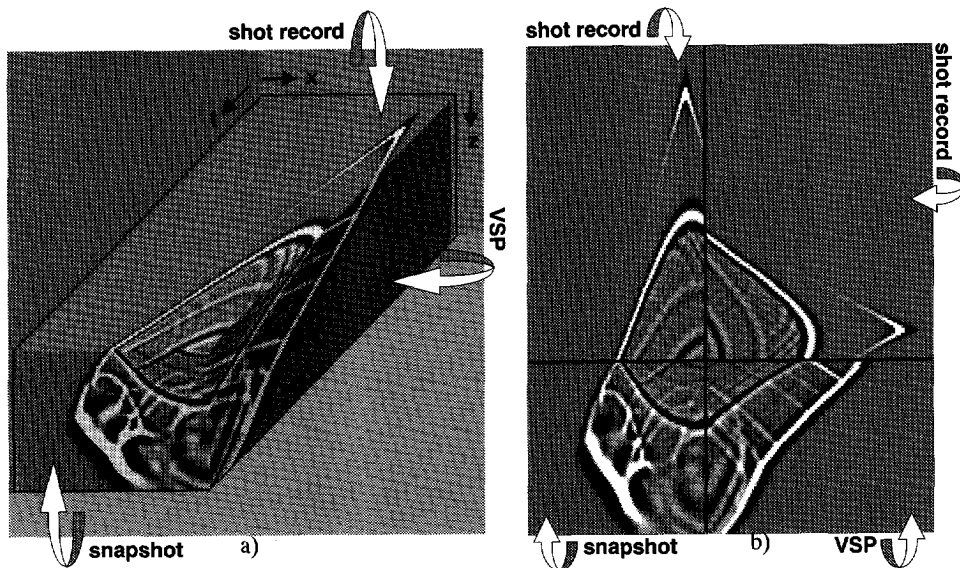


Figure 1.6 Illustration of wave propagation with three different data recordings : shot record, VSP and snapshot $(x, z, t=t_3)$.

This example shows clearly that if in the recording of VSP and surface seismic data the same source is used, both measurement techniques record different cross-sections of the *same* wave field. This important property forms the basis of the idea for transforming surface seismic measurements into pseudo borehole data and underlines the importance of data reorganization.

The generation of pseudo borehole data has a number of applications, predrilling as well as postdrilling. In the *predrilling* stage, pseudo borehole data may be evaluated to optimize the location and the amount of deviation of the borehole. This can be realized by predicting the VSP data that would be measured in the planned well. Well locations are generally chosen on the basis of a geological interpretation of the image of the earth's subsurface obtained from seismic surface data. Therefore, the generation of pseudo borehole data from surface data may assist in designing (deviated) wells to be drilled. Since the pseudo VSP data shows the intermediate stage between the *unmigrated* data and the *migrated* data, the macro model of the subsurface can be easily verified. In addition, taking all the boundary conditions at the seabottom into account and using two-way techniques, source wavelets can be estimated interactively from marine data with all surface-related multiples included. For the generation of pseudo borehole data, the seismic data need to be of higher quality than is common in seismic acquisition. Therefore one or more multi-component seismic shot records could be acquired at the potential well location. Subsequently, these data may be transformed into pseudo borehole data and further processed with the existing borehole inversion tools. The extra costs of the dedicated acquisition should be seen in comparison with the high costs of drilling.

In the *postdrilling* applications, an important aid in the interpretation of borehole data is the comparison with processed surface data related to the same area. The method proposed in this thesis, transforms the surface recorded data into the same "format" as the real borehole data for optimal comparison (Figure 1.7). The comparison of the pseudo borehole data at different locations with the real borehole data extends the structural information laterally for improving the subsurface interpretation.

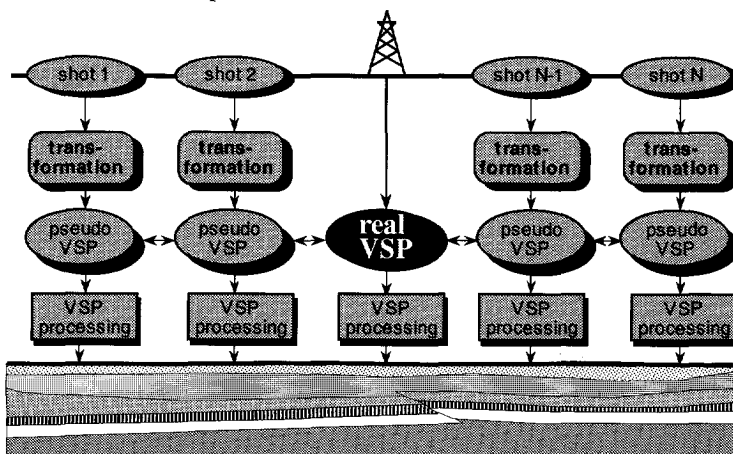


Figure 1.7 Postdrilling : the proposed methodology of pseudo VSP data generation improves the integration of surface data with VSP data.

After a well has been drilled, the VSP acquisition geometry may be designed optimally with the aid of generating pseudo borehole data (e.g. pseudo VSP data may be generated for a series of shot records along the drilled well, to optimally design the acquisition for the VSP recording). For instance, from the generated offset pseudo VSP data, the different illuminations may be studied for an optimum acquisition design to illuminate specific target locations. This may help define the reflectivity as one progresses away from the well (lateral prediction). In this way, the pseudo VSP data can be used to accurately define attributes which could be used to estimate the reservoir properties.

Geologists always infer fault locations through subhorizontal reflector discontinuities. The energy scattered from faults is largely lost in standard processing schemes which emphasize subhorizontal reflectors. The pseudo VSP emphasizes the subvertical reflectors (i.e. faults).

For some geologies, it is sometimes quite difficult to acquire VSP data for all the depth levels. The pseudo VSP data can be generated from the surface data along the well to bridge gaps in real VSP data. In other words, the pseudo VSP data can be used to insert the missing depths in real VSP and integrate real VSP data with surface data. This may have also important applications in prediction ahead of the drillbit. Finally, if a real VSP and a surface shot record are available, recorded with almost the same shot location, the pseudo VSP can be generated and compared with the real VSP data, and offers possibilities to obtain information on the source and receiver characteristics used in both acquisition recordings. The single source real VSP may then be extended to a multi source pseudo offset VSP data to include the angle-dependent properties away from the well.

In this thesis it will be shown how pseudo borehole data can be used in imaging structures along pseudo wells.

1.5 Outline of this thesis

In this thesis a method is discussed for the transformation of seismic surface data into pseudo borehole data.

The body of this thesis is divided into three main parts :

- A)Introduction, theoretical considerations and formulations of the pseudo VSP method (Chapter 2 and 3),
- B)Relations of the pseudo borehole data generation and the Common Focus Point Technology and single-fold imaging using multi-offset, common-well and multi-well, common-offset pseudo borehole data (Chapter 4, 5 and 6), and
- C)2-D and 3-D case studies (Chapter 7 and 8).

In Chapter 2, the formulation of the propagation and reflection of waves through a subsurface is briefly reviewed. Starting from the acoustic wave equation, the two-way representation of wave fields is determined and compared with the one-way wave fields. The various wave field extrapolation algorithms are discussed using two-way and one-way operators in acoustic and elastic media. The forward model for seismic data is briefly reviewed.

Chapter 3 discusses the formulation for the transformation of surface data into pseudo VSP depth records. Some numerical examples illustrate the importance of pseudo VSP data, demonstrating the link between the unmigrated data and the migrated data (using one-way as well as two-way techniques).

In Chapter 4 the Common Focus Point (CFP) technology is discussed briefly. The relation between the construction of CFP gathers and the generation of pseudo VSP data is presented. It is shown how pseudo VSP data can be generated as function of the one-way time t' instead of generating the response at each depth level z . All the examples shown in Chapters 4 to 6 are based on one-way operators.

Chapter 5 discusses how single-fold images are built up with multi-offset, common-well pseudo VSP data. The contribution of various shot records to the image points at a fixed well location is shown by generating a series of varying offset pseudo VSP data. The single-fold images can be stored in a composite gather : the image gather. Similar to pseudo VSP data where the sources are at the surface, pseudo borehole shot records can be constructed by simulating virtual sources in pseudo wells using the CFP technology.

In Chapter 6, the construction of *two-way* and *one-way* common-offset sections is discussed. *Two-way* common-offset sections refer to the conventional common-offset (source-receiver offset; two-way offset) sections. This in comparison with *one-way* common-offset sections which refer to single-fold images obtained using multi-well, common-offset pseudo VSP data (source-well offset; one-way offset). These one-way common-offset sections show the illumination of structures from various angles defined by the borehole/detector configuration. The construction of *two-way time*, *one-way time* and *depth* common-offset sections will be shown on synthetic and field datasets.

In Chapter 7 some 2-D case studies are presented on field data examples and physically modeled data.

Finally in Chapter 8 some 3-D case studies are presented on various 3-D numerical and physically modeled data.

The used matrix notation can be found in Appendix A. Appendix B discusses the construction of the optimized spatial convolution operators. Finally Appendix C illustrates some of the main VSP processing schemes applied on a field dataset.

Chapter 2

Formulation of propagation and reflection

2.1 Introduction

In a seismic experiment the wave field is registered at a number of locations at the surface or in a well. For studying the behaviour of the wave fields at various depth levels, it is necessary to use operators which describe the mathematical relationship between the recorded seismic measurements and the geophysical properties of the earth. This forward model representation, which describes the seismic reflection experiments, forms an essential basis in formulating the methodology of generating pseudo borehole data from seismic surface measurements. The methodology of transforming surface data into pseudo VSP data will be presented in Chapter 3. The transformation of surface measurements (space time domain) to the subsurface structures (space depth domain) requires knowledge of wave theory, describing the *propagation* and *reflection* of waves in the earth. In this chapter a review will be presented on the formulation of the *propagation* and *reflection* of wave fields.

The reflection response of a wave field measured at the surface depends on more parameters than the reflection characteristics of the reflector itself. The source wave field propagates down into the subsurface, reflects at the layer boundaries, and the reflected wave field propagates up to the surface. Therefore the seismic response that is measured at the surface contains a mixture of propagation (up- and downward) and reflection information of the subsurface. The behaviour of the reflected waves are determined by two properties of the medium. The *propagation* properties which are primarily determined by the macro layering of the subsurface (they depend on the global acoustic properties of the medium such as aver-

age velocity and average absorption). As a second property, the *reflection* properties, which are determined by the layering of the subsurface (they depend on the local spatial changes of the acoustic properties of the medium). The principal objective of the seismic processing method is to deduce from seismic measurements, the structure of the subsurface and correctly position the true amplitude reflectivity.

The appropriate method that eliminates the propagation effects from the seismic measurements is called *seismic migration*. For the elimination of the propagation effects, a macro model of the subsurface is needed. The process of seismic migration can also be formulated as bringing the up- and downgoing waves into focus at the reflecting boundaries.

Wave field extrapolation lies at the basis of the seismic migration method and can be formulated as the computational process which transforms the recorded data (using the wave equation) into a series of new recordings representing the simulated registrations at new locations. In forward extrapolation, propagation effects are added to the seismic data. In inverse extrapolation, wave propagation effects are removed from the data.

After extrapolating the wave field downwards into the subsurface, at each depth point the local reflection properties are estimated (imaging principle). The imaging principle is based on the time coincidence of an upgoing wave field with a downgoing wave field (Claerbout, 1971).

In Section 2.2 a review is given on the two-way and one-way wave equations. Starting from the acoustic wave equation, the two-way representation of wave fields is determined and compared with its decoupled representation, being the up- and downgoing one-way wave fields. Both representations are used in the forward model and data description. Some attention will be paid to the formulations for elastic waves. Section 2.3 summarizes the wave field extrapolation algorithms using two-way and one-way operators in acoustic and elastic media. Finally in Section 2.4, the one-way forward model ('WRW model') is briefly discussed. Here the matrix notation is used for describing the seismic wave field. The matrix notation for seismic wave fields has been introduced by Berkhou (1982) and will be used throughout this thesis. An overview of the data matrix notation in the forward model can be found in Appendix A.

2.2 Review of the two-way and one-way wave equations

In this section the representation of two-way and one-way wave fields is briefly discussed. Some of the main expressions of the various wave field extrapolation operators and their relation to each other are presented. In the formulation of the two-way wave field extrapo-

lation operators, the total acoustic wave field is considered. Both up- and downgoing waves are extrapolated simultaneously. Since the total wave field is continuous across acoustic impedance contrasts, the boundary conditions are included implicitly in recursive schemes. Thus transmission effects and multiple reflections are incorporated. A drawback of extrapolation techniques based on the two-way wave equation is the sensitivity to model errors.

In the one-way wave field extrapolation, the total wave field is decomposed into up- and downgoing waves. For an overview of recent references on one-way wave theory, the reader is referred to Wapenaar (1996). In this thesis, for convenience the up- and downgoing waves are supposed to propagate *independently* in the macro layers. The one-way wave field extrapolation techniques are very robust with respect to model errors. A slightly erroneous macro model causes only a small distortion in the extrapolated wave field. At acoustic impedance contrasts coupling of up- and downgoing waves occurs. The boundary conditions and optionally, the multiple reflections should be included explicitly.

The use and formulation of the different wave field extrapolation operators employed in this thesis are extensively discussed by Berkhout (1982) and Wapenaar and Berkhout (1989).

For loss-less inhomogeneous fluids the linearized equation of motion reads (for the source-free situation) :

$$-\nabla p = \rho \frac{\partial \vec{v}}{\partial t}, \quad (2.1a)$$

and the linearized stress-strain relation reads :

$$-\nabla \cdot \vec{v} = \frac{1}{K} \frac{\partial p}{\partial t}, \quad (2.1b)$$

where $p=p(x,y,z,t)$ represents the acoustic pressure as a function of the spatial coordinates (x,y,z) and time t , $\vec{v}=\vec{v}(x,y,z,t)$ represents the particle velocity as function of space and time, $\rho=\rho(x,y,z)$ describes the space dependent mass density in equilibrium and $K=K(x,y,z)$ describes the space dependent bulk compression modulus.

Next, a formulation in the angular frequency domain is chosen because it allows independent extrapolation of monochromatic wave fields (Berkhout, 1982).

In the frequency domain (see Symbols and Definitions), differentiations with respect to time are replaced by multiplicative factors, e.g. :

$$\frac{\partial \vec{v}}{\partial t} \xrightarrow{FT} j\omega \vec{V}. \quad (2.2)$$

Equations (2.1a) and (2.1b) can, respectively, be rewritten in the space frequency domain as:

$$\frac{1}{\rho} \nabla P = -j\omega \vec{V} \quad \text{and} \quad K \nabla \cdot \vec{V} = -j\omega P, \quad (2.3)$$

where $P = P(x, y, z, \omega)$ represents the temporal Fourier transform of the acoustic pressure, $\vec{V} = \vec{V}(x, y, z, \omega)$ denotes the temporal Fourier transform of the particle velocity and $j = \sqrt{-1}$.

The equations in (2.3) can be combined into the frequency domain representation of the two-way acoustic wave equation :

$$\rho \nabla \cdot \left(\frac{1}{\rho} \nabla P \right) + k^2 P = 0 \quad \text{or} \quad \nabla^2 P + k^2 P = \nabla \ln \rho \cdot \nabla P, \quad (2.4)$$

where $k = \omega/c$, with $c = \sqrt{K/\rho}$. $c = c(x, y, z)$ describes the space dependent propagation velocity and k represents the wavenumber. The wave field can be described along the depth coordinate if the z -derivatives in Equation (2.4) are separated from the x - and y -derivatives as:

$$\rho \frac{\partial}{\partial z} \left(\frac{1}{\rho} \frac{\partial P}{\partial z} \right) = -k^2 P - \rho \frac{\partial}{\partial x} \left(\frac{1}{\rho} \frac{\partial P}{\partial x} \right) - \rho \frac{\partial}{\partial y} \left(\frac{1}{\rho} \frac{\partial P}{\partial y} \right). \quad (2.5)$$

Seismic data are always bandlimited, therefore Equation (2.5) can be rewritten in terms of space-variant spatial convolutions as :

$$\rho \frac{\partial}{\partial z} \left(\frac{1}{\rho} \frac{\partial P}{\partial z} \right) = -H_2 * P, \quad (2.6)$$

with $H_2(x, y, z, \omega)$ (2.7)

$$= \left[k^2 d_0(x, y) - \frac{\partial \ln \rho}{\partial x} \delta(y) d_1(x) + \delta(y) d_2(x) - \frac{\partial \ln \rho}{\partial y} \delta(x) d_1(y) + \delta(x) d_2(y) \right].$$

The filters $d_v(x)$ and $d_v(y)$ represent for $v=1,2$ bandlimited first and second order differentiation operators with respect to x and y . $d_0(x, y) = \delta(x)\delta(y)$ represents a spatial delta function. k^2 , $\partial \ln \rho / \partial x$ and $\partial \ln \rho / \partial y$ are space-variant weighting factors. The asterisk $*$ denotes a space-variant spatial convolution along the x - and y - coordinate.

Using $\partial P / \partial z = -j\omega \rho V_z$, the two-way wave equation (2.6) can be reformulated as the following matrix equation :

$$\frac{\partial}{\partial z} \begin{bmatrix} -P \\ V_z \end{bmatrix} = \begin{bmatrix} 0 & j\omega \rho d_0 * \\ -\frac{1}{j\omega \rho} H_2 * & 0 \end{bmatrix} \begin{bmatrix} -P \\ V_z \end{bmatrix} \quad \text{or} \quad \frac{\partial \bar{Q}_l}{\partial z} = A_l \bar{Q}_l. \quad (2.8)$$

Note that Equation (2.8) is a first order two-way wave equation in the space frequency domain for the wave vector $\bar{Q}_l = [-P, V_z]^T$.

The subscript l refers to liquids. The minus sign on P is introduced because, in the full elastic case, the traction will be considered rather than the pressure. Equation (2.8) is now suitable for wave field extrapolation in depth z since it represents an easily manageable first order differential equation in z for the wave vector \tilde{Q}_l .

An important simplification occurs if there are no lateral medium variations. In horizontally layered media (1-D media) it is attractive to perform wave field extrapolation in the wavenumber frequency domain. Following the approach of Berkhout (1982), differentiation in the space frequency domain can be represented by multiplication in the wavenumber frequency domain. One of the properties of the Fourier transform pair is the multiplication with *respectively* $-jk_x$ and $-jk_y$ (in the wavenumber frequency domain) which corresponds to the differentiation with respect to x and y (in the space frequency domain) :

$$\begin{aligned} \frac{\partial F(x, y, z_m, \omega)}{\partial x} &\Leftrightarrow -jk_x \tilde{F}(k_x, k_y, z_m, \omega) \text{ and} \\ \frac{\partial^n F(x, y, z_m, \omega)}{\partial x^n} &\Leftrightarrow (-jk_x)^n \tilde{F}(k_x, k_y, z_m, \omega), \\ \frac{\partial F(x, y, z_m, \omega)}{\partial y} &\Leftrightarrow -jk_y \tilde{F}(k_x, k_y, z_m, \omega) \text{ and} \\ \frac{\partial^n F(x, y, z_m, \omega)}{\partial y^n} &\Leftrightarrow (-jk_y)^n \tilde{F}(k_x, k_y, z_m, \omega). \end{aligned} \quad (2.9)$$

Equation (2.8) can be reformulated in the wavenumber frequency domain, as the acoustic two-way wave equation for laterally invariant media, as follows :

$$\frac{\partial}{\partial z} \begin{bmatrix} -\tilde{P} \\ \tilde{V}_z \end{bmatrix} = \begin{bmatrix} 0 & j\omega\rho \\ -\frac{1}{j\omega\rho} \tilde{H}_2 & 0 \end{bmatrix} \begin{bmatrix} -\tilde{P} \\ \tilde{V}_z \end{bmatrix} \text{ or } \frac{\partial \tilde{Q}_l}{\partial z} = \tilde{A}_l \tilde{Q}_l. \quad (2.10)$$

Operator \tilde{H}_2 is defined as $\tilde{H}_2 = k_z^2 = k^2 - k_x^2 - k_y^2$. From here onward a homogeneous layer is assumed between z_{m-1} and z_m . A solution of the Equation (2.10) can symbolically be described as (Ursin, 1983):

$$\tilde{Q}_l(z_m) = \tilde{W}_l(z_m, z_{m-1}) \tilde{Q}_l(z_{m-1}), \quad (2.11)$$

in which the matrix $\tilde{W}_l(z_m, z_{m-1})$ is symbolically equal to :

$$\tilde{W}_l(z_m, z_{m-1}) = \exp(\tilde{A}_l \Delta z), \quad (2.12)$$

with $\Delta z = z_m - z_{m-1}$. Equation (2.11) is a description of the two-way acoustic downward wave field extrapolation in the wavenumber frequency domain, where the acoustic wave vector \tilde{Q}_l contains two-way monochromatic wave fields (pressure \tilde{P} and vertical component of the particle velocity \tilde{V}_z). Both quantities are continuous across the layer interfaces.

If the square-root operator \tilde{H}_1 is defined such that $\tilde{H}_2 = \tilde{H}_1^2 \Rightarrow \tilde{H}_1 = k_z$,

$$\text{with } k_z = \sqrt{k^2 - k_x^2 - k_y^2} \quad \text{for } k_x^2 + k_y^2 \leq k^2 \quad (\text{propagating waves}) \quad (2.13)$$

$$k_z = -j\sqrt{k_x^2 + k_y^2 - k^2} \quad \text{for } k_x^2 + k_y^2 > k^2 \quad (\text{evanescent waves}) \quad (2.14)$$

then the eigenvalue decomposition applied to operator \tilde{A}_l yields :

$$\tilde{A}_l = \begin{bmatrix} 1 & 1 \\ -k_z & k_z \\ \omega\wp & \omega\wp \end{bmatrix} \begin{bmatrix} -jk_z & 0 \\ 0 & jk_z \end{bmatrix} \frac{1}{2} \begin{bmatrix} 1 & -\omega\wp \\ 0 & k_z \\ 1 & \omega\wp \end{bmatrix} = \tilde{L}_l \ \tilde{\Lambda}_l \ \tilde{L}_l^{-1} \quad , \quad (2.15)$$

where matrix $\tilde{\Lambda}_l$ is a diagonal operator matrix¹. The acoustic two-way wave field extrapolation operator $\tilde{W}_l(z_m, z_{m-1})$ can then be defined as :

$$\begin{aligned} \tilde{W}_l(z_m, z_{m-1}) &= \exp(\tilde{A}_l \Delta z) = \exp\left(\tilde{L}_l \ \tilde{\Lambda}_l \ \tilde{L}_l^{-1} \Delta z\right) = \tilde{L}_l \ \exp(\tilde{\Lambda}_l \Delta z) \ \tilde{L}_l^{-1} \\ &= \tilde{L}_l \ \tilde{V}_l \ \tilde{L}_l^{-1} = \tilde{L}_l \begin{bmatrix} \exp(-jk_z \Delta z) & 0 \\ 0 & \exp(jk_z \Delta z) \end{bmatrix} \tilde{L}_l^{-1} \\ &= \begin{pmatrix} \tilde{W}_{PP}(z_m, z_{m-1}) & \tilde{W}_{PV}(z_m, z_{m-1}) \\ \tilde{W}_{VP}(z_m, z_{m-1}) & \tilde{W}_{VV}(z_m, z_{m-1}) \end{pmatrix} \\ &= \begin{pmatrix} \cos(k_z \Delta z) & \frac{j\omega\wp}{k_z} \sin(k_z \Delta z) \\ \frac{jk_z}{\omega\wp} \sin(k_z \Delta z) & \cos(k_z \Delta z) \end{pmatrix}. \end{aligned} \quad (2.16)$$

Substituting Equation (2.16) into (2.11) yields :

$$\begin{pmatrix} -\tilde{P}(z_m) \\ \tilde{V}_z(z_m) \end{pmatrix} = \begin{pmatrix} \tilde{W}_{PP}(z_m, z_{m-1}) & \tilde{W}_{PV}(z_m, z_{m-1}) \\ \tilde{W}_{VP}(z_m, z_{m-1}) & \tilde{W}_{VV}(z_m, z_{m-1}) \end{pmatrix} \begin{pmatrix} -\tilde{P}(z_{m-1}) \\ \tilde{V}_z(z_{m-1}) \end{pmatrix} \quad (2.17)$$

in which for a homogeneous layer the suboperators are given in Equation (2.16). Note that for propagating waves, the suboperators \tilde{W}_{PP} and \tilde{W}_{VV} describe the real part of the phase shift operator $\exp(-jk_z \Delta z)$. \tilde{W}_{PV} and \tilde{W}_{VP} are related to the imaginary part. For evanescent waves the square-root operator $\tilde{H}_1 = k_z$ becomes imaginary. The goniometric functions should then be replaced by hyperbolic functions of the real argument $jk_z \Delta z$.

Equation (2.17) can also be written as :

$$\tilde{Q}_l(z_m) = \tilde{L}_l \tilde{V}_l \tilde{L}_l^{-1} \tilde{Q}_l(z_{m-1}). \quad (2.18)$$

1. Note that this decomposition breaks down for horizontally propagating waves, that is for $\tilde{H}_1 = k_z = 0$.

As will be seen below, the decomposition operator \tilde{L}_l^{-1} describes decomposition of the total field into downgoing and upgoing waves, \tilde{V}_l describes independent one-way wave field extrapolation of down- and upgoing waves, and the composition operator \tilde{L}_l describes composition of the total wave field from its downgoing and upgoing constituents.

The relation in the $k_x\omega$ domain between the total pressure $\tilde{P}(z_m)$ and the vertical velocity component $\tilde{V}_z(z_m)$ at a depth level z_m and the up- and downgoing pressure wave fields, respectively $\tilde{P}^-(z_m)$ and $\tilde{P}^+(z_m)$ reads :

$$\tilde{P}_l(z_m) = \begin{bmatrix} -\tilde{P}_l^+(z_m) \\ -\tilde{P}_l^-(z_m) \end{bmatrix} = \tilde{L}_l^{-1} \begin{bmatrix} -\tilde{P}(z_m) \\ \tilde{V}_z(z_m) \end{bmatrix} = \frac{1}{2} \begin{bmatrix} I & \frac{-\omega_0}{k_z} \\ I & \frac{\omega_0}{k_z} \end{bmatrix} \tilde{Q}_l(z_m). \quad (2.19)$$

The superscript '+' indicates that the wave is traveling downward in the positive z -direction. Likewise, a superscript '-' indicates that a wave is traveling upwards in the negative z -direction. (Note that at the free surface $z=z_0$ the total pressure $\tilde{P}(z_0) = 0$).

Thus, Equation (2.10) can be decomposed easily into two first order differential equations by decomposing the total wave field \tilde{P} into downgoing \tilde{P}^+ and upgoing \tilde{P}^- waves.

Substituting

$$\tilde{P}_l = \tilde{L}_l^{-1} \tilde{Q}_l \Leftrightarrow \tilde{Q}_l = \tilde{L}_l \tilde{P}_l = \tilde{L}_l \begin{bmatrix} -\tilde{P}^+ \\ -\tilde{P}^- \end{bmatrix} \quad (2.20)$$

into Equation (2.10) yields the set of decoupled one-way wave equations :

$$\frac{\partial}{\partial z} \begin{bmatrix} -\tilde{P}^+ \\ -\tilde{P}^- \end{bmatrix} = \begin{bmatrix} -jk_z & 0 \\ 0 & jk_z \end{bmatrix} \begin{bmatrix} -\tilde{P}^+ \\ -\tilde{P}^- \end{bmatrix} = \tilde{\Lambda}_l \tilde{P}_l. \quad (2.21)$$

The solution of the one-way equation is given by the phase shift operator.

Similarly to Equations (2.10) and (2.11) the solution of Equation (2.21) is equal to :

$$\tilde{P}_l(z_m) = \tilde{V}_l(z_m, z_{m-1}) \tilde{P}_l(z_{m-1}) \quad (2.22)$$

in which the matrix $\tilde{V}_l(z_m, z_{m-1})$ is symbolically equal to $\tilde{V}_l(z_m, z_{m-1}) = \exp(\tilde{\Lambda}_l \Delta z)$, see also Equation (2.15) and (2.16) for a description of the matrices.

Hence, the one-way acoustic downward wave field extrapolation is described in the wave-number frequency domain by :

$$\begin{pmatrix} -\tilde{P}^+(z_m) \\ -\tilde{P}^-(z_m) \end{pmatrix} = \begin{pmatrix} \tilde{W}^+(z_m, z_{m-1}) & 0 \\ 0 & \tilde{F}^-(z_m, z_{m-1}) \end{pmatrix} \begin{pmatrix} -\tilde{P}^+(z_{m-1}) \\ -\tilde{P}^-(z_{m-1}) \end{pmatrix} \quad (2.23)$$

The forward extrapolation operator $\tilde{W}^+(z_m, z_{m-1})$ (also called the downward propagation operator) from z_{m-1} to z_m is defined as :

$$\tilde{W}^+(z_m, z_{m-1}) = \exp(-j k_z \Delta z). \quad (2.24)$$

The inverse extrapolation operator $\tilde{F}^-(z_m, z_{m-1})$ (also called the inverse of the upward propagating operator) from z_{m-1} to z_m is defined as :

$$\tilde{F}^-(z_m, z_{m-1}) = (\tilde{W}^-(z_{m-1}, z_m))^{-1} \quad (2.25)$$

and is usually approximated by the complex conjugate of the forward extrapolation operator $\tilde{W}^+(z_m, z_{m-1})$ (matched filter approach) :

$$\tilde{F}^-(z_m, z_{m-1}) \approx (\tilde{W}^+(z_m, z_{m-1}))^* \quad (2.26)$$

where the asterisk $*$ denotes the complex conjugate.

2.3 Two-way versus one-way wave field extrapolation

In this section a summary is given on the various wave field extrapolation operators determined in the wavenumber frequency domain. These wave field extrapolation operators are used to extrapolate the data from one depth level to another depth level. Wave field extrapolation methods are either non-recursive or recursive. Figure 2.1 illustrates schematically the difference between non-recursive and recursive wave field extrapolation. In the use of non-recursive schemes the wave field is extrapolated from one depth level to the desired or target depth level in one extrapolation step. On the other hand, in the recursive schemes, the wave field at depth level z_m is determined from the wave field at depth level z_{m-1} . In this thesis only the recursive schemes will be considered. In the remaining part of this section the various wave field extrapolation operators will be summarized for acoustic and elastic media.

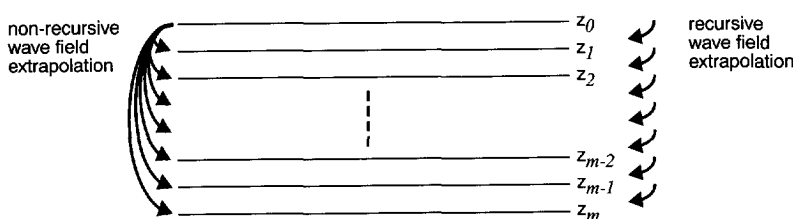


Figure 2.1 Non-recursive and recursive wave field extrapolation.

- The acoustic two-way downward wave field extrapolation can be formulated in the wavenumber frequency domain as a matrix multiplication. For downward extrapolation of the total wave field $[-\tilde{P} \ \tilde{V}_z]^T$ from depth level z_{m-1} to z_m , the following equation holds (assuming a homogeneous layer) :

$$\begin{pmatrix} -\tilde{P} \\ \tilde{V}_z \end{pmatrix}_{z_m} = \begin{pmatrix} \cos(k_z \Delta z) & \frac{j\omega_0}{k_z} \sin(k_z \Delta z) \\ \frac{jk_z}{\omega_0} \sin(k_z \Delta z) & \cos(k_z \Delta z) \end{pmatrix} \begin{pmatrix} -\tilde{P} \\ \tilde{V}_z \end{pmatrix}_{z_{m-1}}. \quad (2.27)$$

Note that with an equivalent operator (with Δz replaced by $-\Delta z$) the upward propagation can be formulated.

- The acoustic one-way wave field extrapolation can be formulated in terms of *forward* extrapolation of the *dowgoing (source)* wave field and *inverse* extrapolation of the *upgoing (reflected)* wave field :

$$\begin{pmatrix} -\tilde{P}^+ \\ -\tilde{P}^- \end{pmatrix}_{z_m} = \begin{pmatrix} \exp(-jk_z \Delta z) & 0 \\ 0 & \exp(jk_z \Delta z) \end{pmatrix} \begin{pmatrix} -\tilde{P}^+ \\ -\tilde{P}^- \end{pmatrix}_{z_{m-1}}. \quad (2.28)$$

Note that with equivalent operators the forward extrapolation of upgoing waves and the inverse extrapolation of dowgoing waves can be formulated :

$$\begin{pmatrix} -\tilde{P}^+ \\ -\tilde{P}^- \end{pmatrix}_{z_{m-1}} = \begin{pmatrix} \exp(jk_z \Delta z) & 0 \\ 0 & \exp(-jk_z \Delta z) \end{pmatrix} \begin{pmatrix} -\tilde{P}^+ \\ -\tilde{P}^- \end{pmatrix}_{z_m}. \quad (2.29)$$

So far it has been illustrated that for a homogeneous layer, the acoustic two-way operator can be written in terms of acoustic one-way processes. In the following some of the main expressions derived from the elastic wave equation will be shown. The derivation of the expressions for the elastic situation are beyond the scope of this thesis. For a further discussion refer to Wapenaar and Berkhouw (1989).

In the acoustic two-way techniques the total wave field has been described in terms of the total acoustic pressure \tilde{P} and the total particle velocity \tilde{V}_z . For the elastic schemes, the total full elastic wave field is defined in terms of the traction $\tilde{T}_z = [\tilde{\tau}_{xz}, \tilde{\tau}_{zz}]^T$ and the particle velocity $\tilde{V} = [\tilde{V}_x, \tilde{V}_z]^T$. For the elastic case, 2-D wave fields are considered.

The two-way elastic downward wave field extrapolation is described in the wavenumber frequency domain by :

$$\tilde{Q}_s(z_m) = \tilde{W}_s(z_m, z_{m-1}) \tilde{Q}_s(z_{m-1}), \quad (2.30)$$

where the elastic wave vectors \tilde{Q}_s contain two-way wave fields (horizontal and vertical components of the particle velocity: \tilde{V}_x and respectively \tilde{V}_z , and the shear and tensile stress on a horizontal plane: $\tilde{\tau}_{xz}$ and respectively $\tilde{\tau}_{zz}$). The subscript s refers to solids.

- The full elastic two-way wave field extrapolation operator \tilde{W}_s describes the relation between the total (two-way) wave fields at two different depth levels. Equation (2.30) is a short notation of :

$$\begin{pmatrix} \tilde{V}_z \\ \tilde{\tau}_{xz} \\ \tilde{\tau}_{zz} \\ \tilde{V}_x \end{pmatrix}_{z_m} = \begin{pmatrix} \tilde{W}_{11} & \tilde{W}_{12} & \tilde{W}_{13} & \tilde{W}_{14} \\ \tilde{W}_{21} & \tilde{W}_{22} & \tilde{W}_{23} & \tilde{W}_{24} \\ \tilde{W}_{31} & \tilde{W}_{32} & \tilde{W}_{33} & \tilde{W}_{34} \\ \tilde{W}_{41} & \tilde{W}_{42} & \tilde{W}_{43} & \tilde{W}_{44} \end{pmatrix} \begin{pmatrix} \tilde{V}_z \\ \tilde{\tau}_{xz} \\ \tilde{\tau}_{zz} \\ \tilde{V}_x \end{pmatrix}_{z_{m-1}}. \quad (2.31)$$

The expressions for the suboperators $\tilde{W}_{11}, \dots, \tilde{W}_{44}$ are beyond the scope of this thesis. Note that these suboperators are defined from depth level z_{m-1} to depth level z_m . The advantages of the two-way techniques are mainly based on the continuity of the field components at layer interfaces. This gives that the boundary conditions at these interfaces are always satisfied and therefore many phenomena are treated correctly without extra effort. As opposed to the one-way schemes, it is important to realize that no assumptions need to be made on the separability of up- and downgoing wave fields. A drawback of the two-way techniques is the sensitivity to model errors, which gives rise to artifacts originating at the boundaries. The four field components in Equation (2.31), that are continuous at layer interfaces, are extrapolated simultaneously. This means that source and reflected wave fields need to be superposed before the downward extrapolation.

The multicomponent seismic data at the surface can be decomposed (similar as in the acoustic case) into separate compressional and shear wave fields (assuming a homogeneous layer). Each wave field can then be handled with similar one-way algorithms as developed for acoustic processing. The elastic one-way and two-way wave fields can be related by the following equation :

$$\begin{pmatrix} \tilde{\Phi}^+ \\ \tilde{\Psi}^+ \\ -\tilde{\Phi}^- \\ \tilde{\Psi}^- \end{pmatrix} = \tilde{L}_s^{-1} \begin{pmatrix} \tilde{V}_z \\ \tilde{\tau}_{xz} \\ \tilde{\tau}_{zz} \\ \tilde{V}_x \end{pmatrix}, \quad (2.32)$$

where \tilde{L}_s^{-1} is a decomposition operator. With Equation (2.32) it is shown that the total elastic wave field \tilde{Q}_s can be decomposed into down- and upgoing *P*- and *SV*- waves by means of the decomposition operator (*P*: longitudinal waves and *SV*: transversal waves with a polarization in the vertical (x, z) plane).

- After the decomposition, the full elastic one-way downward wave field extrapolation is described by:

$$\begin{pmatrix} \tilde{\Phi}^+ \\ \tilde{\Psi}^+ \\ -\tilde{\Phi}^- \\ \tilde{\Psi}^- \end{pmatrix}_{z_m} = \begin{pmatrix} \tilde{W}_p^+ & 0 & 0 & 0 \\ 0 & \tilde{W}_s^+ & 0 & 0 \\ 0 & 0 & \tilde{F}_p^- & 0 \\ 0 & 0 & 0 & \tilde{F}_s^- \end{pmatrix} \begin{pmatrix} \tilde{\Phi}^+ \\ \tilde{\Psi}^+ \\ -\tilde{\Phi}^- \\ \tilde{\Psi}^- \end{pmatrix}_{z_{m-1}}. \quad (2.33)$$

Here $\tilde{\Phi}^+$ and $\tilde{\Psi}^+$ represent the downgoing P - and SV - waves respectively, while $\tilde{\Phi}^-$ and $\tilde{\Psi}^-$ represent the upgoing P - and SV - waves.

The operators on the diagonal in Equation (2.33) have a similar expression as for the acoustic case (see Equation (2.24) and (2.26) with k replaced by k_p or k_s)².

The relation between the two-way and the one-way wave fields (in acoustic and elastic media) in the wavenumber frequency domain are summarized in Figure 2.2. The operators \tilde{L}_l^{-1} and \tilde{L}_s^{-1} indicated in Figure 2.2 are the decomposition operators respectively in acoustic and elastic media. The composition operators are also shown in this figure : \tilde{L}_l and \tilde{L}_s represent the composition operators respectively in acoustic and elastic media.

The wave field extrapolation operators as derived in this chapter form a fundamental tool of the procedure of generating pseudo borehole data from a known wave field at a certain depth level.

Wave field extrapolation can be formulated in general as the construction or reconstruction of the development of a wave field in space and time, from a known field somewhere on a certain time or plane and the characteristics of the medium. With ‘construction’ forward extrapolation is meant and by ‘reconstruction’ inverse extrapolation. The wave field extrapolations can be performed in the wavenumber frequency domain by multiplications. However, the extrapolation operators derived in the wavenumber frequency domain (as summarized in this section) are only correct if the wave field extrapolation is performed in a horizontally layered medium (1 - D medium). For handling more complex models than 1 - D models the wave field extrapolation has to be performed in the space frequency domain by a space-variant spatial convolution.

2. $k_p = \omega/c_p$. In solids the compressional wave propagation velocity is defined in terms of the Lamé parameters λ and μ as : $c_p = \sqrt{(\lambda+2\mu)/\rho}$. $k_s = \omega/c_s$ (with $c_s = \sqrt{(\mu/\rho)}$). The space-dependent bulk compression modulus K can be expressed in terms of the Lamé constants λ and μ as $K = \lambda + 2\mu/3$; the Poisson’s ratio is equal to $\sigma = \lambda/(2\lambda+2\mu)$.

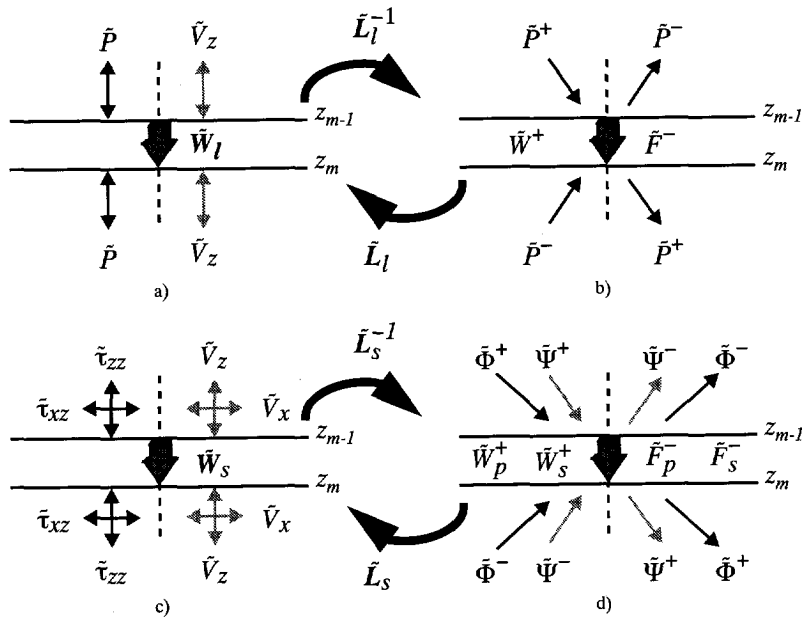


Figure 2.2 Relationship between acoustic a)two-way and b)one-way wave field extrapolation. Relationship between full elastic c)two-way and d)one-way wave field extrapolation.

Therefore the most simple way is to transform the derived operators in the wavenumber frequency domain numerically back to the space frequency domain. This inverse transform is not very efficient because the convolution operators become very long. To avoid the use of very long operators, short wave field operators have been designed which are over a desired wavenumber band, equal or close to the exact formulation of the wave field extrapolation operators in the wavenumber frequency domain (Holberg, 1988, Blacquière, 1989, Thorbecke, 1997). The theory of the short optimized operators is discussed in Appendix B, in which examples are shown for two-way and one-way operators which are used in the implementation. Weighted Least SQuares (WLSQ) techniques have been used in the construction of the short operators. In this formulation it is assumed that the medium is locally homogeneous over the length of the convolution operator. The medium parameter value which is used over the length of the convolution operator is the one from the middle of the convolution operator. The middle value is chosen because it has the most significant contribution to the convolution summation. The application of the short optimized convolution operators is illustrated in Figure 2.3. On the top of Figure 2.3, a part of a lateral inhomogeneous layer is depicted. During the extrapolations in the space frequency domain, local homogeneity is assumed. This is illustrated for three different lateral locations (bottom of Figure 2.3). Note that the local homogeneity assumption can be circumvented by using a modal expansion of

the extrapolation operators. A discussion of this method, which is more accurate, but also much more expensive, is beyond the scope of this thesis. The reader is referred to Grimbergen et al. (1995).

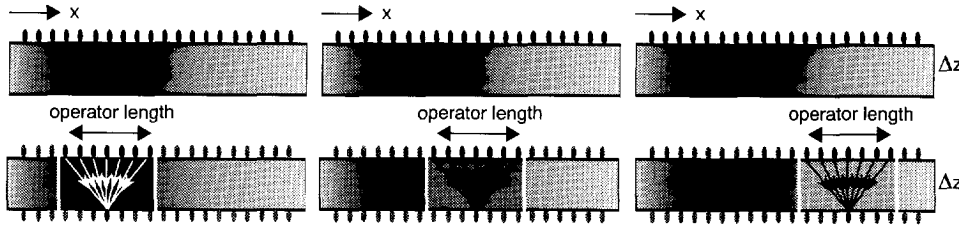


Figure 2.3 The short operator is designed such that local homogeneity is assumed by assigning the middle value of the convolution operator to all values of the extrapolation operator in the aperture of the operator length.

2.4 Review of the one-way forward model ('WRW' model)

In practice, seismic measurements are always discrete in time and space. Consequently, imaging is always a discrete process and therefore the forward model that is used for the description of the surface, effects of propagation and reflection is chosen also to be discrete. In this discrete model, the seismic data is ordered as presented in Appendix A. All the matrices are formulated in the frequency domain (and refer to one Fourier component). It is allowed to represent the model by independent frequency components, since the earth is assumed to be a linear time-invariant medium³. For this reason and taking into account the discrete property, vectors and matrices are pre-eminently suited for the mathematical description of the recorded data. For notational convenience the angular frequency ω in the monochromatic experiments is omitted.

In this section a brief mathematical description for seismic wave fields will be given in terms of matrix operators. The matrix operators were introduced by Berkhout (1982) and quantify the physical process of emission, downward propagation, reflection, upward propagation and detection in inhomogeneous media. For a more detailed description of the forward ('WRW') model, the reader is referred to Berkhout (1985, 1993) and to Wapenaar (1993) for a matrix presentation and an integral representation respectively.

3. For linear wave theory in a time-invariant medium, the imaging problem may be described in the temporal frequency domain. Moreover, as the recording has a finite duration T , a finite number of frequencies N per recorded seismic trace should be considered, where $N = (f_{\max} - f_{\min})T$; $f_{\max} - f_{\min}$ being the temporal frequency range of interest. A typical number of N equals 250.

The forward model consists of a network of various wave field processes.

First the reflection response is discussed for one reflector. The response can be separated into three parts:

- **Downward propagation** - If the vector $\bar{S}^+(z_0)$ represents one Fourier component of the downward traveling source wave field at the data acquisition surface $z=z_0$, then the monochromatic downward traveling source wave field at depth level z_m is given by :

$$\bar{S}^+(z_m) = W^+(z_m, z_0) \bar{S}^+(z_0). \quad (2.34)$$

$W^+(z_m, z_0)$ represents the downward propagation operator from depth level z_0 to z_m ⁴. Operator W^+ is represented by a complex-valued matrix, where each column equals one Fourier component of the impulse response at depth level z_m due to one dipole at the surface z_0 . The propagation direction of the waves is indicated by the superscript : '+' for downward propagation and '-' for upward propagation. Note that for laterally homogeneous media W^+ becomes a Toeplitz matrix, i.e. the elements along the diagonal are constant.

- **Reflection** - At any depth level z_m , reflection may occur. For each Fourier component, reflection may be described by a general linear operator $R^+(z_m)$:

$$\bar{P}_m^-(z_m) = R^+(z_m) \bar{S}^+(z_m). \quad (2.35)$$

$\bar{P}_m^-(z_m)$ is the monochromatic upward traveling reflected wave field at depth level z_m due to the inhomogeneities at depth level z_m only. The reflection operator $R^+(z_m)$ is a matrix describing the reflection properties for downward propagating wave fields : each column describes the monochromatic dipole source response at z_m for one specific grid point at z_m .

- **Upward propagation** - Finally the reflected wave field travels up to the surface.

$$\bar{P}_m^-(z_0) = W^-(z_0, z_m) \bar{P}_m^-(z_m), \quad (2.36)$$

where $\bar{P}_m^-(z_0)$ is one Fourier component of the reflected wave field at data acquisition surface z_0 and $W^-(z_0, z_m)$ equals the upward propagation operator from z_m to z_0 . Each column of W^- equals one Fourier component of the response at z_0 due to one specific dipole at depth level z_m .

4. It can be built up recursively, according to

$$W^+(z_m, z_0) = W^+(z_m, z_{m-1}) W^+(z_{m-1}, z_{m-2}) \cdots W^+(z_2, z_1) W^+(z_1, z_0)$$

Combining Equations (2.34) to (2.36) yields one matrix equation for the reflection response:

$$\bar{P}^-(z_0) = \sum_{m=1}^M \bar{P}_m^-(z_0) = \left[\sum_{m=1}^M W^-(z_0, z_m) R^+(z_m) W^+(z_m, z_0) \right] \bar{S}^+(z_0), \quad (2.37)$$

or for a continuous formulation in z :

$$\bar{P}^-(z_0) = \int_{z_0}^{\infty} [W^-(z_0, z) R^+(z) W^+(z, z_0) dz] \bar{S}^+(z_0). \quad (2.38)$$

In practice, inhomogeneities are present at all depth levels. M denotes the number of depth levels. Note that one depth level does not necessarily coincide with a reflector. Figure 2.4a illustrates expression (2.37) for one point source and one reflection boundary. Note that the reflectivity of the surface is ignored. To Equation (2.37), relations should be added between the induced source function and the downgoing source wave field on the one hand, and the recorded detector signals and the upgoing reflected wave field on the other hand:

$$\bar{S}^+(z_0) = D^+(z_0, z_s) \bar{S}(z_s) \quad \text{and} \quad \bar{P}(z_r) = D^-(z_r, z_0) \bar{P}^-(z_0). \quad (2.39)$$

Matrix operators $D^+(z_0, z_s)$ and $D^-(z_r, z_0)$ are defined by the boundary conditions at the data acquisition surface as well as the type of sources and detectors (velocity or pressure). These operators have been refined by Verschuur (1991) by introducing array properties and buried sources at z_s and buried detectors at z_r .

The vectors $\bar{S}(z_s)$ and $\bar{P}(z_r)$ are defined by the source- and detector patterns and the source and detector signals respectively (see also Figure 2.5).

Equation (2.37) may be rewritten as:

$$\bar{P}^-(z_0) = X_0(z_0, z_0) \bar{S}^+(z_0), \quad (2.40)$$

$$\text{with } X_0(z_0, z_0) = \left[\sum_{n=1}^{m-1} W^-(z_0, z_n) R^+(z_n) W^+(z_n, z_0) \right] + \\ W^-(z_0, z_m) X(z_m, z_m) W^+(z_m, z_0), \quad (2.41)$$

$$\text{with } X(z_m, z_m) = \sum_{n=m}^M W^-(z_m, z_n) R^+(z_n) W^+(z_n, z_m). \quad (2.42)$$

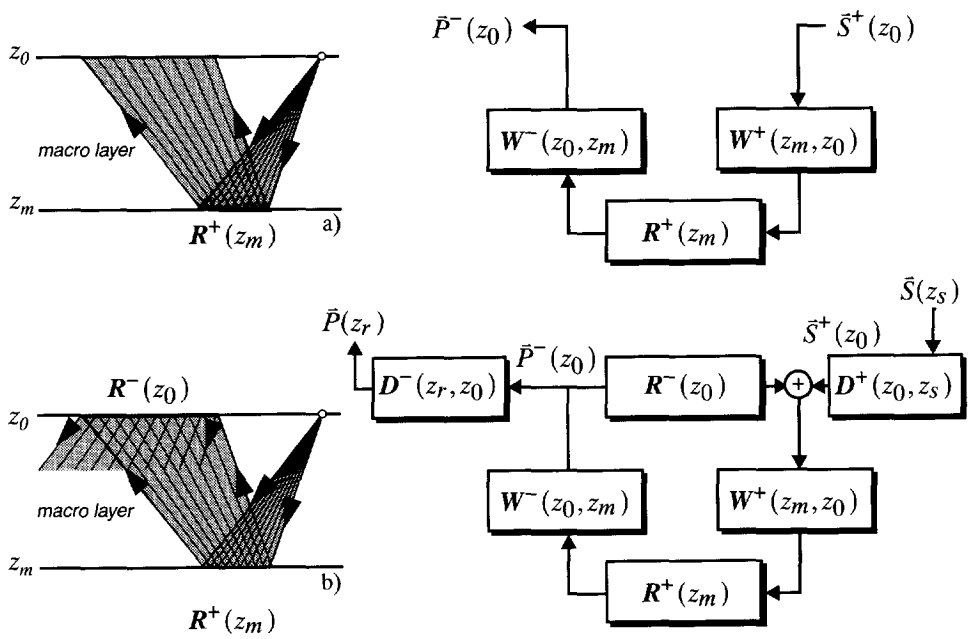


Figure 2.4 a) Propagation and reflection for one point source and one reflecting boundary z_m , ignoring the reflectivity of the surface, b) taking the reflectivity of the surface and source and receiver operators into account.

$X_\theta(z_0, z_0)$ represents the half-space reflection operator at depth level z_0 due to inhomogeneities at $z > z_0$. Note that $X_\theta(z_0, z_0)$ does *not* include the reflection of depth level z_0 . The matrix element (i,j) of $X_\theta(z_0, z_0)$ may be considered as one Fourier component of the reflection response at position $(x,y)_i$ on surface z_0 due to a unit dipole source at position $(x,y)_j$ on the same surface z_0 . For further details see Berkhout (1985).

Similarly, matrix $X(z_m, z_m)$ describes at a detector position at depth level z_m , one Fourier component of the spatial impulse response due to inhomogeneities at $z \geq z_m$ (see Figure 2.5) due to an unit point source (dipole) at z_m . In other words, matrix element $X_{ij}(z_m, z_m)$ may be considered as one Fourier component of the reflection response at position i on surface $z=z_m$, due to a unit point source at position j on the same surface ($z=z_m$).

The vector $\bar{P}^-(z_0)$ represents the detector positions of one seismic experiment (for one frequency). The extension to a multi-experiment can be easily performed. In case of a multi-experiment all vectors of one single experiment are collected into one matrix $\mathbf{P}^-(z_0)$, in which every column describes the response of one single monochromatic experiment.

The formulation of a multi-experiment of Equation (2.40) yields :

$$\mathbf{P}^-(z_0) = \mathbf{X}_0(z_0, z_0) \mathbf{S}^+(z_0). \quad (2.43)$$

In practice the data acquisition surface z_0 is a strongly reflecting boundary and the first equation in (2.39) should be extended to :

$$\bar{\mathbf{P}}^+(z_0) = \mathbf{R}^-(z_0) \bar{\mathbf{P}}^-(z_0) + \mathbf{D}^+(z_0, z_s) \bar{\mathbf{S}}(z_s), \quad (2.44)$$

where $\bar{\mathbf{P}}^+(z_0)$ represents the total downgoing wave field at z_0 and $\bar{\mathbf{P}}^-(z_0)$ contains all the surface-related multiples. In Figure 2.4b the surface reflectivity has been taken into account. Matrix operator $\mathbf{R}^-(z_0)$ defines the surface reflection for upward traveling waves (upward traveling waves are reflected into the subsurface again).

These waves are known as surface-related multiples. Internal multiples in the subsurface can also be incorporated in the model, i.e. in the propagation operators. If Equation (2.37) is formulated in a recursive way, internal multiple scattering can be included in the extrapolation operators, Verschuur (1991).

The surface-related multiples can be best represented by the feedback loop as depicted in Figure 2.4b, where matrix reflection operator $\mathbf{R}^-(z_0)$ defines the surface reflection for upward traveling waves.

Taking the surface-related multiples into account, the total spatial impulse response of the lower space $z \geq z_0$ at the surface z_0 can be extended to :

$$\mathbf{X}(z_0, z_0) = [\mathbf{I} - \mathbf{X}_0(z_0, z_0) \mathbf{R}^-(z_0)]^{-1} \mathbf{X}_0(z_0, z_0) \quad (2.45)$$

This equation forms a fundamental basis of the surface-related multiple removal technology as described by Berkhou (1982) and Verschuur et al. (1992).

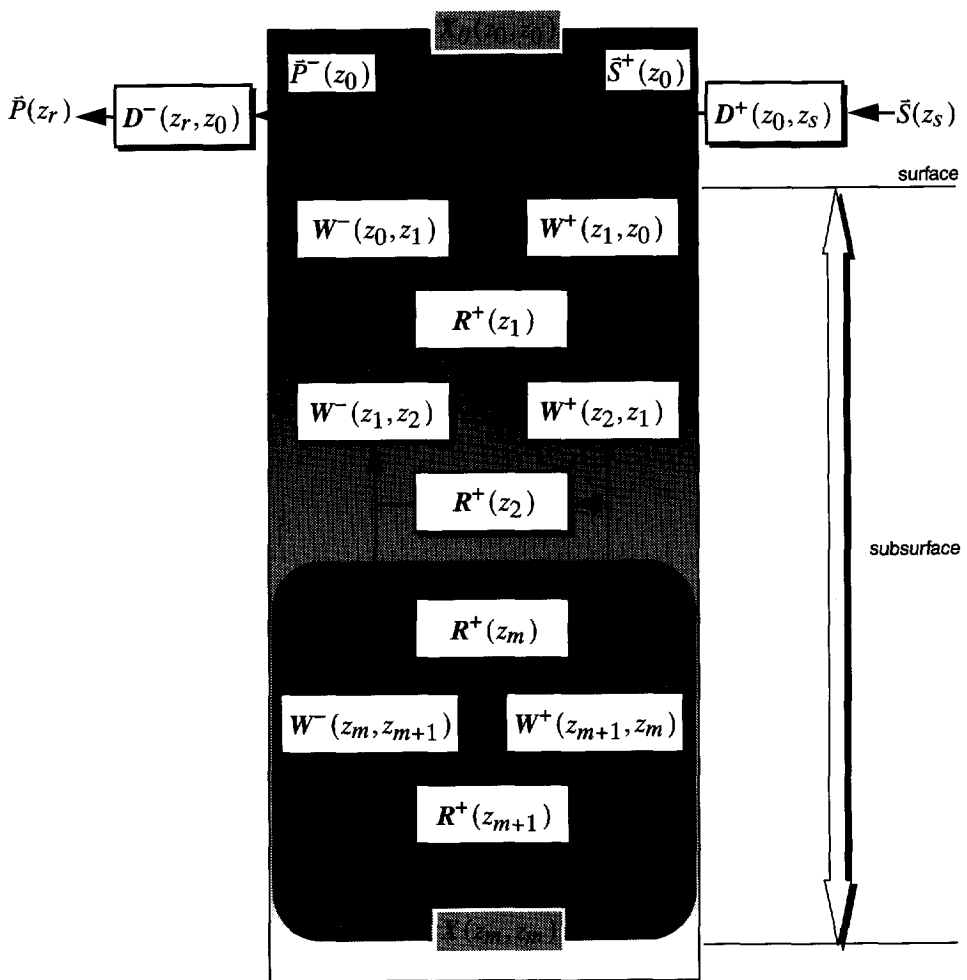


Figure 2.5 Response at the reflection-free surface z_0 due to reflection in half space $z \geq z_0$ ignoring internal multiples and transmission losses. $X_0(z_0, z_0)$ and $X(z_m, z_m)$ are the pulse responses which include the reflection of the depth level z_m

In this chapter, the two-way and one-way wave field extrapolation operators have been determined starting from the acoustic wave equation. The expressions for the different operators in the wavenumber frequency domain have been presented. In the next chapter, the derived wave field extrapolation operators will be used in the methods for generating pseudo VSP data from seismic surface data.

Chapter 3

From surface to pseudo VSP data

3.1 Introduction

In the previous chapter a description has been given on the formulation of waves propagating and reflecting through a subsurface. Following this formulation using the forward model description of seismic data, different wave field extrapolation operators have been formulated in using the one-way and two-way wave equations.

As already discussed in Chapter 1, an important application of Vertical Seismic Profiling (VSP) data recordings is its integration with surface seismic measurements. Considering the various important advantages of VSP data, an algorithm will be presented in this chapter, in which surface seismic measurements are transformed numerically into *pseudo* VSP data.

In transforming receivers along the surface into pseudo receivers placed in a pseudo well, wave field extrapolation techniques play a fundamental role in reconstructing the wave field at predefined pseudo receiver locations. Comparisons will be shown in the use of one-way and two-way wave field extrapolation methods and their applications in generating pseudo VSP data.

It will be shown that the pseudo VSP data acts as an *intermediate* stage which comprehensively demonstrates the way in which the source wave field and the reflected wave field increasingly approach each other (in both using one-way and two-way techniques) and in this way form the image which would be visible in the end stage of a shot record migration without showing the intermediate steps. In this way, pseudo VSP constitutes a tool effectuating the map of surface seismic data into imaged data and operates as a unique link between the unmigrated surface data and the migrated data.

Considering interrelated boundaries of various data types, a 3-D volume representation of integrated data shows the continuity of events through different interrelated planes and improves the interpretation of the wave propagation in time as function of the extension in lateral position and depth of the subsurface. Using the sensitivity of boundary conditions in two-way wave field extrapolation algorithms, pseudo VSP data constitutes as a tool for verifying the correctness of macro subsurface models. In the last part of this chapter some illustrations on the use of different wave field extrapolation methods will be given on synthetic data examples.

In this chapter a formulation will be discussed for the transformation of surface data (shot records) into pseudo VSP data.

3.2 Algorithm for the generation of pseudo VSP depth records

The generation of pseudo VSP data from surface measurements opens a new way of understanding and interpreting seismic events (Alá'i and Wapenaar, 1994). Many events which cannot be identified on seismic surface shot records are rendered easily identifiable through the transformation of surface data into pseudo VSP data by a numerical method. The generated pseudo VSP data contains the same information as the surface data but it is presented in a different format. The presentation of the VSP data brings in a new dimension to looking at different events, giving an easier interpretation. This underlines the importance of data-reorganization as discussed in Chapter 1. When a real VSP is available, the proposed method will improve the integration of surface data with real VSP data since the surface data is transformed into the *same* format as the truly recorded VSP measurements. The computations and comparison of the pseudo VSP data at different locations, where well information is not available, with the real VSP data will enable to extend geological knowledge in all lateral directions and will improve the interpretation of the subsurface model.

The fundamental tool in the transformation of surface data into pseudo VSP data is wave field extrapolation. The main principle of the pseudo VSP data generation is that if the wave field and the source properties are known at the surface, and the wave field extrapolation is carried out correctly (using a correct macro model of the subsurface), then it is possible to reconstruct the wave field at all depths in the subsurface. Wave field extrapolation lies at the basis of advanced seismic processing and reconstructs the field at points in the subsurface. In principle, downward extrapolation can be applied towards any subsurface point in an area below the seismic detectors. Figure 3.1 (left) shows the functional diagram of the method for pseudo VSP generation. The core of the procedure is downward extrapolation of a wave field (acoustic or elastic) from the surface into the subsurface. The technique of pseudo VSP generation requires (high quality) seismic shot records, a description of the source proper-

ties and a macro model of the subsurface. A pseudo VSP dataset can thus be obtained by extrapolating the surface wave field (i.e., the shot record) to a range of detector positions in a potential borehole (see Figure 3.1). On the right of Figure 3.1 it is illustrated that the information of detectors along the surface are focused into pseudo detectors which are placed in a pseudo well.

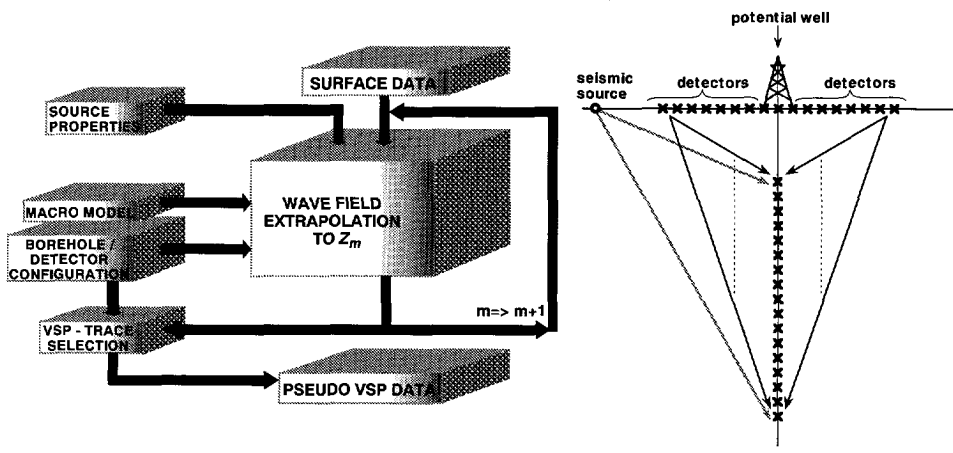


Figure 3.1 Functional diagram for the transformation of surface data into pseudo VSP data.

Note that zero offset as well as non-zero offset VSP data can be obtained in this way. Seismic surface measurements (containing detailed information of the subsurface) are used to generate better VSP results. This in comparison with methods where surface data is not used at all.

The macro model, which defines the propagation properties of the earth, is used to calculate the extrapolation operators. With these operators it is possible to extrapolate the total wave field from one depth level to another. A description of the potential borehole/detector configuration is necessary to make the correct depth step from one detector level to another and to select the correct VSP trace for all depths (Figure 3.2).

The wave field extrapolation is repeated recursively for all depths where detectors are chosen in the potential borehole. The result of one extrapolation step is used as input for the extrapolation of the wave field to the next depth level. The result is a complete pseudo VSP dataset, after all depth steps for the predefined source-receiver VSP survey. Note that with this scheme it is possible to handle all kind of borehole detector configurations.

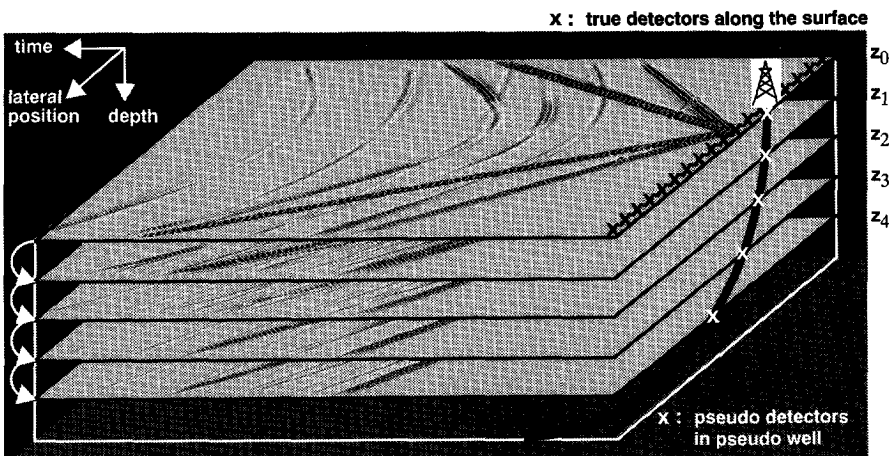


Figure 3.2 Transformation of a seismic shot record into pseudo VSP data. The black crosses represent the true detectors which recorded the surface data; the white crosses denote the pseudo detectors placed in a pseudo well.

3.3 One-way and two-way formulation

In the previous chapter the different wave field extrapolation operators have been discussed briefly. In this section the generation of pseudo VSP data is illustrated in the use of one-way and two-way wave field extrapolation operators. The expressions for the various wave field extrapolation operators have been derived in Chapter 2 from the two-way wave equation. The operators presented in Chapter 2 have been derived in the wavenumber frequency domain. In the formulation of the operators in the frequency domain, the seismic data is decomposed into a number of independent monochromatic wave fields which are extrapolated independently. Figure 3.3 illustrates the seismic measurement matrix for the 2-D single component surface data (see Appendix A for the notation of the data matrix).

In horizontally layered media (1-D media) it is justified to perform wave field extrapolation in the wavenumber frequency domain. However, it is possible to expand the operators which are derived in the wavenumber frequency domain to operators which can handle more structurally complex (2-D and 3-D) subsurface models. The extrapolations need then to be performed in the space frequency domain. In the previous chapter a method has been discussed for transforming the operators from the wavenumber frequency domain to the space frequency domain in an optimized way (see also Thorbecke, 1997). Short operators have been designed such that local homogeneity is created in the aperture of the operator length (see Appendix B for the formulation and illustration of the design of the operators which are per-

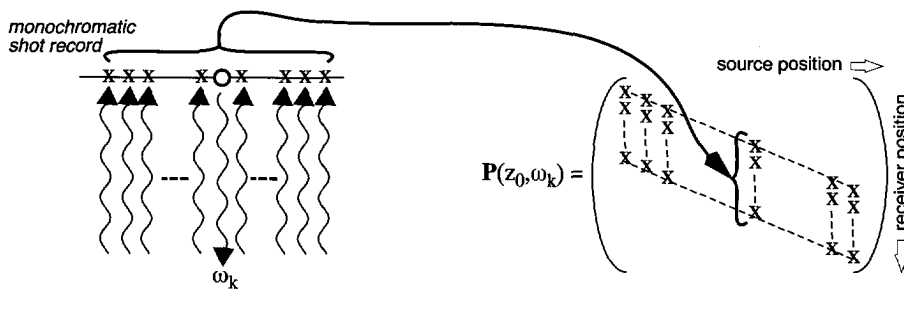


Figure 3.3 The seismic measurement matrix for (2-D single component) surface data. One column refers to one shot record and one element refers to one trace.

formed in the space frequency domain). The general form of operators depends on the domain in which they are derived. In the space frequency domain the operators are convolutions and in the wavenumber frequency domain just simple multiplications.

In the following, four schemes are presented for transforming the surface data into pseudo VSP data. The schemes are illustrated for acoustic two-way and one-way wave field extrapolations applied on surface data with all multiples included and on data after surface-related multiple elimination. The choice of the calculations in the frequency domain has the important consequence that the multi-dimensional forward model for describing the seismic reflection data becomes relatively simple. All matrices refer then to one Fourier component. An important wave field extrapolation method in seismic processing is the one-way method, where the wave field is decomposed into upgoing and downgoing wave fields. These wave fields are separately extrapolated. The two-way approach is another description for wave field extrapolation which takes all boundary conditions into account and fully describes the propagation and reflection of wave fields including multiple reflections. In the formulation of the two-way extrapolation operators, the upward traveling and downward traveling P (and S) wave fields are handled simultaneously, which makes the two-way schemes very sensitive to different parameters of the macro subsurface model. The one-way schemes on the other hand, are robust with respect to errors in the macro subsurface model, but ignore mode conversions (from P to S and vice versa) and internal multiples reflections. A two-way wave field can be decomposed into upward and downward propagating wave fields. If multiple reflections are neglected, the decoupled one-way wave equations describe the up- and downgoing wave modes separately.

For the generation of pseudo VSP data, a wave field $\bar{P}(z_0, \omega)$, representing the subsurface response and a wave field $\bar{S}(z_0, \omega)$, representing the source function is required.

These wave fields are decomposed into upgoing and downgoing waves which can be extrapolated separately for the one-way techniques. In the use of two-way wave field extrapolation operators, the total wave field is used as input to the algorithm. Figure 3.6 illustrates the data flow for respectively the two-way and one-way techniques. Here the monochromatic implementation for generating pseudo VSP data is shown. As an initial process, the surface data is preprocessed and is transformed to the space frequency domain. Based on a gridded macro model defining the propagation properties of the subsurface, extrapolation operators are designed in the wavenumber frequency domain (discretized operators and thus suitable in their performance on sampled data). For the expressions of one-way and two-way wave field extrapolation operators in the wavenumber frequency domain, the reader is referred to Chapter 2.

Extrapolation operators are calculated around every lateral x position in the wavenumber frequency domain (local homogeneity assumption over operator length), which are then mapped into the space frequency domain using an efficient Weighted Least Squares (WLSQ) technique. Operator tables are calculated based on the frequency content of the data and the minimum and maximum velocities of the used macro model. The variable x in Figure 3.6 denotes the variable lateral position over the operator length (opl) which is applied on the data to calculate the value at the next depth level for one lateral position x' (see also Figure 3.4).

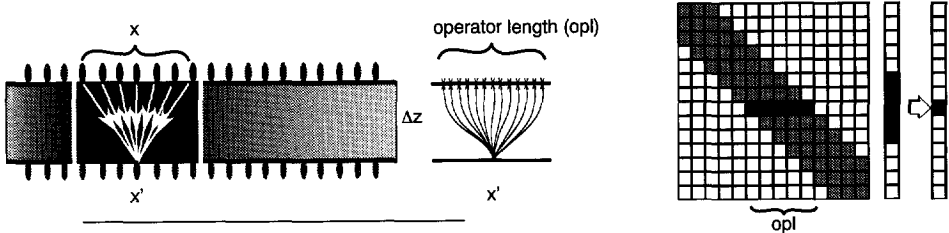


Figure 3.4 Application of the WLSQ short operators. One extrapolation for one lateral position is stored as a row vector in the propagation matrix.

The data is convolved for each depth level with the spatially varying operators, resulting in a new redatumed monochromatic data vector. The wave field extrapolation is performed for all depth where pseudo detectors are positioned in the pseudo well : exactly one element is selected from the data vector and stored to build up the complete pseudo VSP dataset which fulfills the predefined borehole/detector configuration. The algorithm is applied for all frequencies and the pseudo VSP data (ω, z) is transformed back to the space-time domain (t, z) using a temporal Fourier transformation. In the top part of Figure 3.6 the algorithm is shown for the use of two-way operators. Here the total wave field is considered. In using one-way operators the up- and downgoing wave fields are determined separately and added afterwards.

Figure 3.7 illustrates the monochromatic wave field extrapolation which is performed in the space frequency domain using two-way (top) and one-way (bottom) wave field extrapolation operators. According to the predefined borehole/detector configuration, a trace is selected from the extrapolated data which is stored per depth level to obtain after all depth levels a (deviated) pseudo VSP dataset. Note that the data is convolved with the operator over a short operator length and that the selection of the trace may differ along the lateral position (e.g. $P_j(z_l)$ and $P_l(z_m)$ in Figure 3.7, where the indices j and l refer to the lateral position that is selected fulfilling the predefined pseudo VSP geometry).

For the one-way schemes (bottom of Figure 3.7), only the *forward* extrapolation is illustrated for downgoing waves \bar{P}^+ . A similar illustration holds for the *inverse* extrapolation of the upgoing waves \bar{P}^- . For the two-way extrapolations (top of Figure 3.7), two sets of VSP data are created, a pressure field and a velocity field (see also Figure 3.6).

The wave field extrapolation schemes that are discussed in this thesis are applied recursively (see also Figure 3.2). This means that the wave field at a depth level z_{m+1} depends on the wave field at level z_m which depends again from a higher depth level z_{m-1} (Figure 3.5).

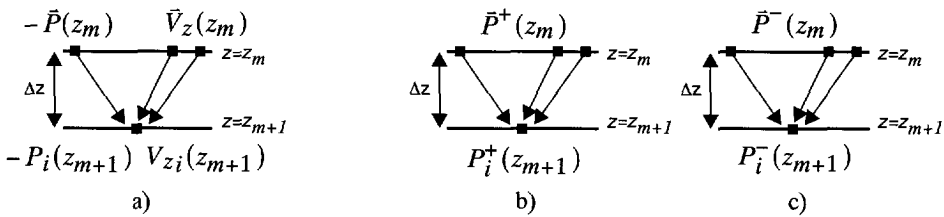


Figure 3.5 The wave field at depth level z_{m+1} depends on the wave field at a higher depth level z_m
 a) two-way scheme (down- and upwaves), b) one-way scheme (downwaves), c) one-way scheme (upwaves).

The expression for the various two-way sub-operators, \tilde{W}_{PP} , \tilde{W}_{PV} , \tilde{W}_{VP} and \tilde{W}_{VV} are given in Equation (2.16) of the previous chapter.

Since the calculations are performed in the space frequency domain (by using WLSQ operators), the two-way wave field extrapolation in the space frequency domain will be noted as :

$$\begin{pmatrix} -\bar{P} \\ \bar{V}_z \end{pmatrix}_{z_m} = \begin{pmatrix} W_{PP} & W_{PV} \\ W_{VP} & W_{VV} \end{pmatrix} \begin{pmatrix} -\bar{P} \\ \bar{V}_z \end{pmatrix}_{z_{m-1}}. \quad (3.1)$$

A similar notation is used for describing the one-way wave field extrapolation.

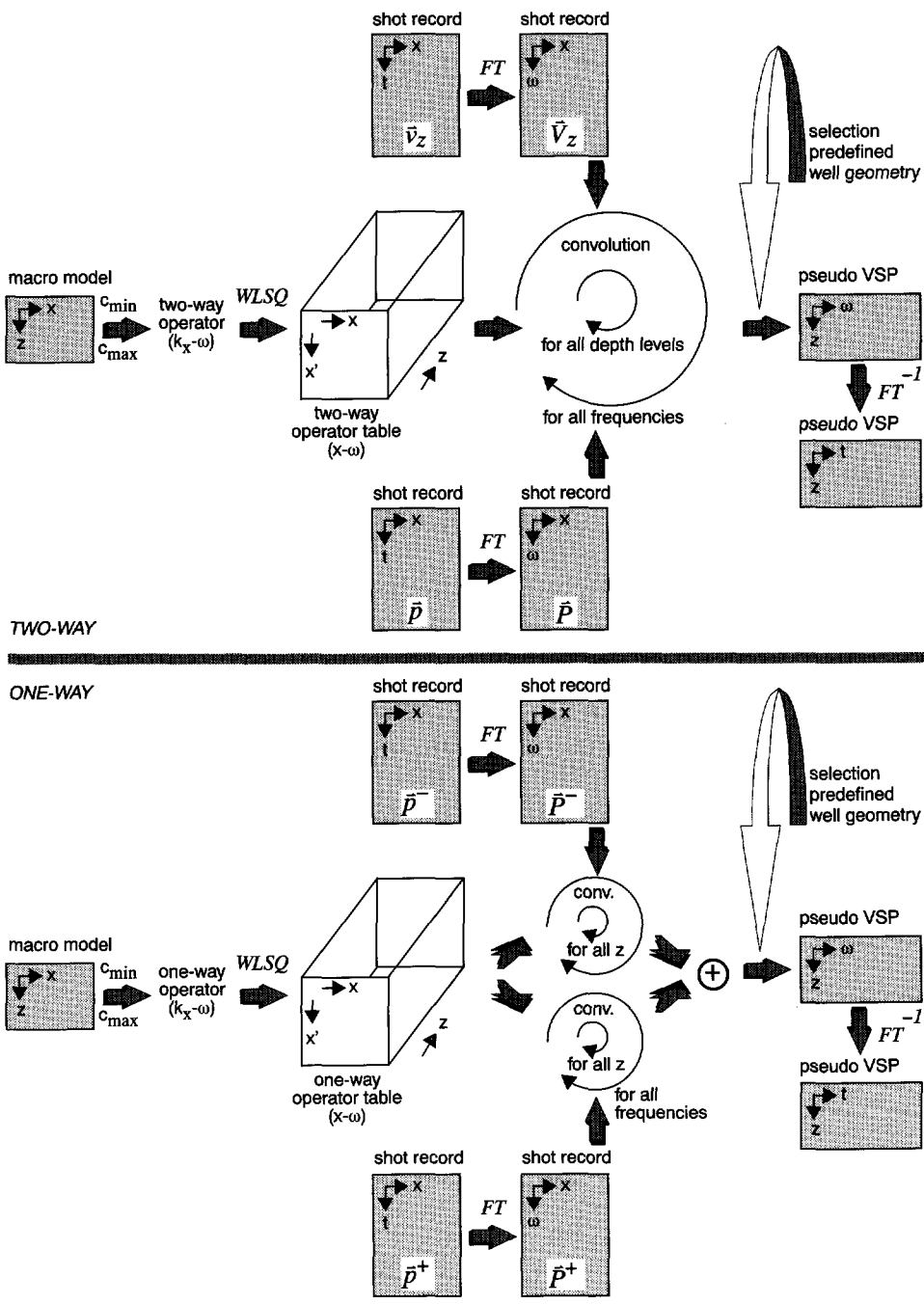


Figure 3.6 Data flow for the transformation of surface data into pseudo VSP data : two-way scheme (top) and one-way scheme (bottom).

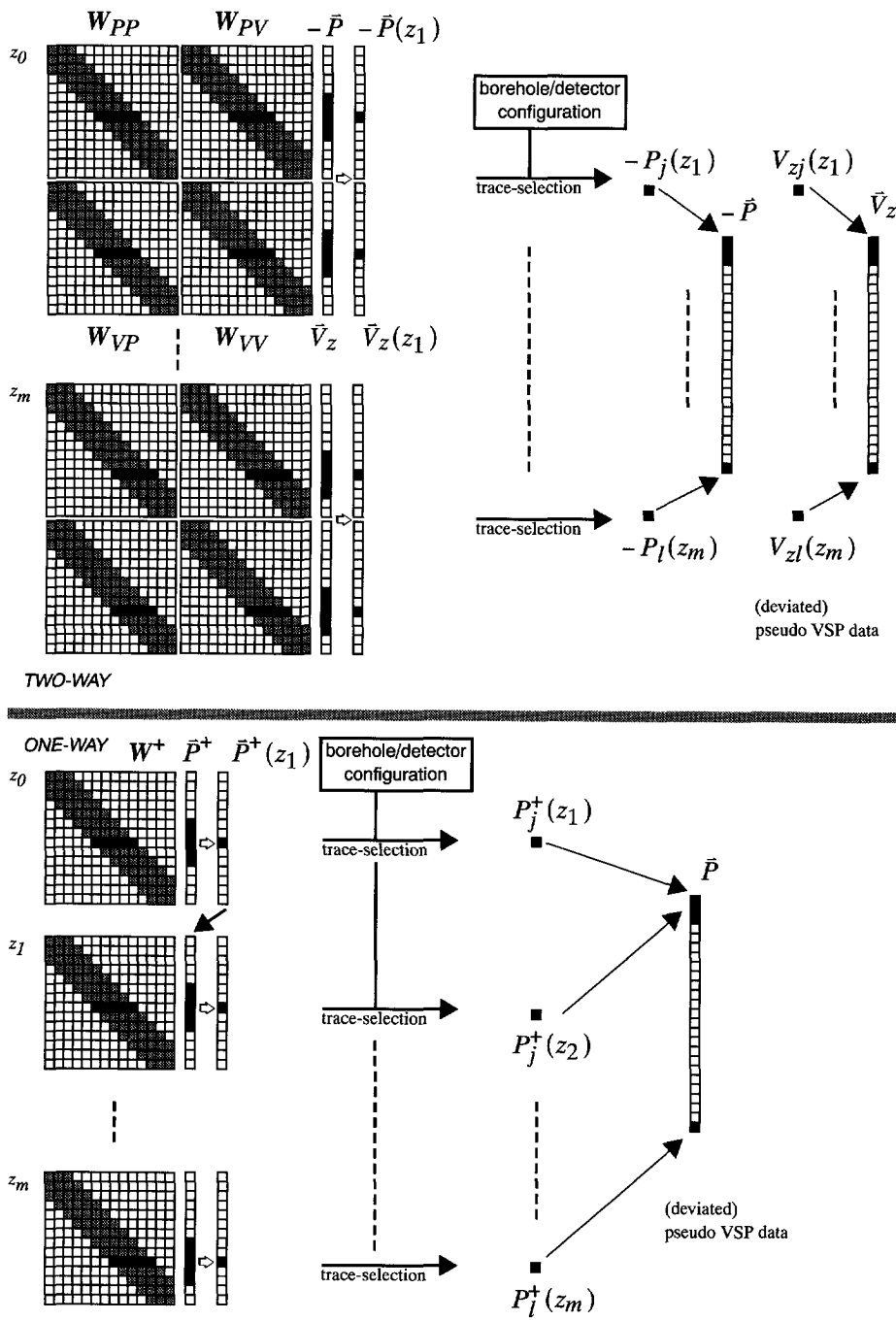


Figure 3.7 Illustration of the monochromatic wave field extrapolation in the space-frequency domain in the two-way (top) and one-way (bottom) pseudo VSP data generation.

Figure 3.8g to j illustrate four schemes in the use of two-way and one-way wave field extrapolation operators. Two shot records are modeled using an acoustic finite difference algorithm for a simple 2 layer model with only a density contrast. The parameters of the model are : $c_{p1}=1500\text{m/s}$, $\rho_1=1000\text{kg/m}^3$, $c_{p2}=1500\text{m/s}$ and $\rho_2=3000\text{kg/m}^3$. c_{p1} and c_{p2} are the acoustic P - wave velocities for respectively the first and second layer and ρ_1 and ρ_2 denote the density. The reflector is positioned at depth $z=200\text{m}$. The modeled shot records (v_z) for a free surface condition is displayed in Figure 3.8a. Note that 5 multiples are visible. In Figure 3.8b the data is displayed after surface related multiple elimination.

Two situations can be considered for two-way techniques :

- The surface multiples in the data generated at the *free surface* are approximated by $-\bar{P}^-(z_0)$ (reflection coefficient is equal to -1, which is a usual assumption for marine data). The pressure and velocity fields read in this case :
 $\bar{P}(z_0) = \bar{S}^+(z_0)$ and $\bar{V}_z(z_0) = \mathbf{K}(\bar{S}^+(z_0) - 2\bar{P}^-(z_0))$. Note that for this acoustic case the vertical component \bar{V}_z is used. $\bar{P}^-(z_0)$ is the recorded wave field and $\bar{S}^+(z_0)$ is the pressure of the source. ($\mathbf{K} \Leftrightarrow (k_z/\omega_0)$; \mathbf{K} is applied in the space frequency domain).
- The surface-related multiples have been removed from the data in the case of a *transparent surface* boundary condition, (assumption : surface z_0 is non-reflective). The total pressure and velocity at the surface can respectively be written as :
 $\bar{P}(z_0) = \bar{P}^-(z_0) + \bar{S}^+(z_0)$ and $\bar{V}_z(z_0) = \mathbf{K}(\bar{S}^+(z_0) - \bar{P}^-(z_0))$.

Similarly, the following situations can be considered for one-way techniques :

- The surface multiples are estimated by $-\bar{P}^-(z_0)$ (assumption of *free surface*). The upgoing respectively downgoing wave fields are described by :
 $\bar{P}^-(z_0) = \bar{P}^-(z_0)$ and $\bar{P}^+(z_0) = -\bar{P}^-(z_0) + \bar{S}^+(z_0)$.
- In the case of a *transparent surface* boundary condition, the surface-related multiples have been removed from the data (assumption : surface z_0 is non-reflective). The upgoing respectively downgoing wave fields (after decomposition and surface-related multiple elimination process) are then given by :
 $\bar{P}^-(z_0) = \bar{P}^-(z_0)$ and $\bar{P}^+(z_0) = \bar{S}^+(z_0)$.

The input data for the different schemes are summarized in Table 1.

Table 1 Input data for the various schemes in generating pseudo VSP data.

two-way	one-way	two-way	one-way
with multiples (free surface)		without multiples (transparent surface)	
$\bar{P} = \bar{S}^+$	$\bar{P}^- = \bar{P}^-$	$\bar{P} = \bar{P}^- + \bar{S}^+$	$\bar{P}^- = \bar{P}^-$
$\bar{V}_z = \mathbf{K}(\bar{S}^+ - 2\bar{P}^-)$	$\bar{P}^+ = -\bar{P}^- + \bar{S}^+$	$\bar{V}_z = \mathbf{K}(\bar{S}^+ - \bar{P}^-)$	$\bar{P}^+ = \bar{S}^+$

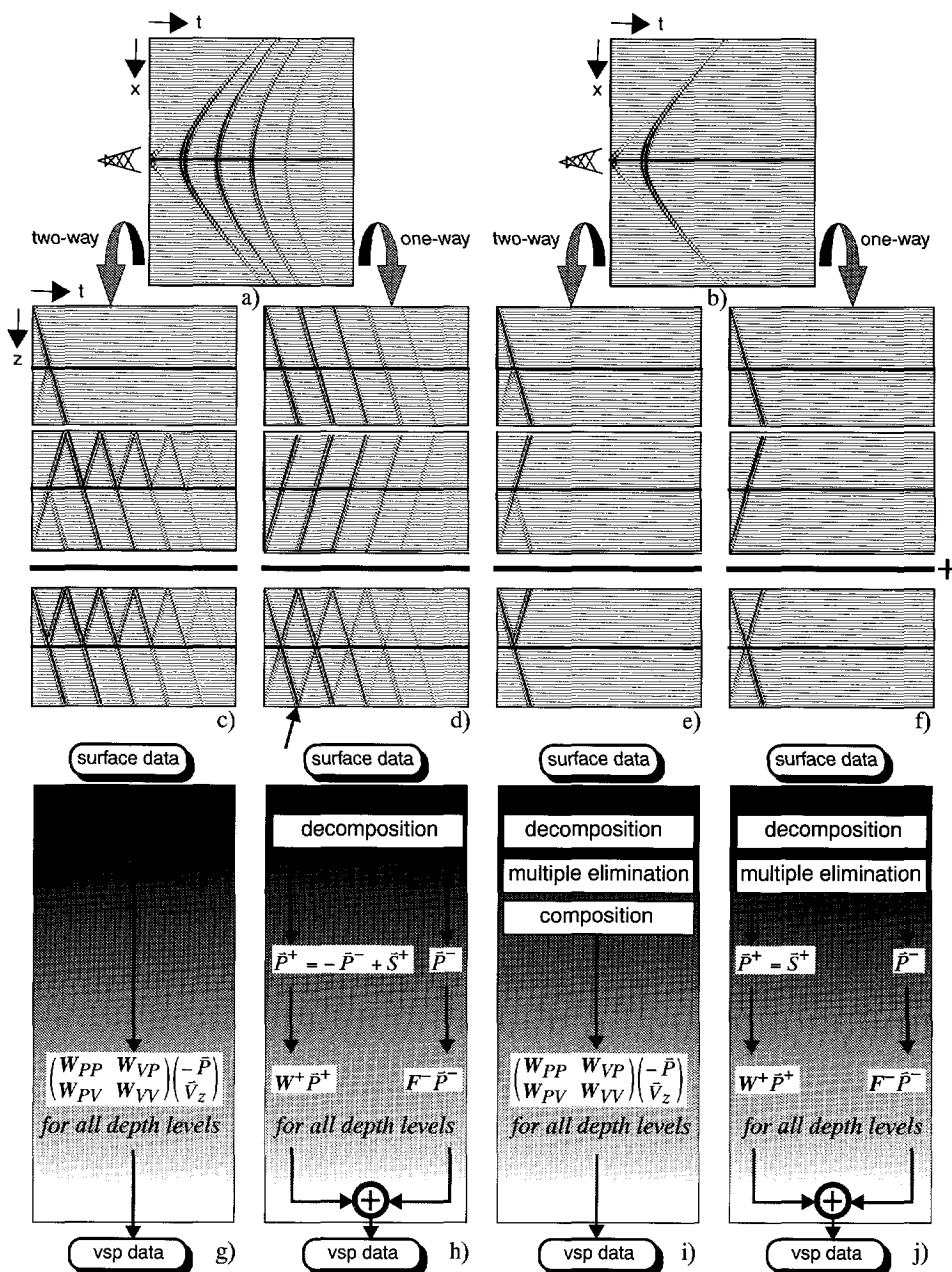


Figure 3.8 Pseudo VSP generation from a) surface data with multiples and b) after surface-related multiple elimination using acoustic two-way respectively one-way wave field extrapolation operators.

Figure 3.8c and d show the result of the acoustic two-way and one-way techniques applied to surface data with multiples.

For the two-way techniques the total wave field is separated into a source wave field and a reflected wave field and both wave fields are extrapolated separately from the free surface. This separation illustrates that for a correct macro model the upgoing non-causal events (which are automatically generated at the reflector in the separate pseudo VSP wave fields) will cancel each other. For the one-way techniques the wave field is decomposed into up- and downgoing pressure wave fields which are extrapolated separately and pseudo VSP data are generated. Addition of the result of these separate wave fields results into a full one-way pseudo VSP. Comparing the results obtained by one- and two-way techniques it can be seen that the extra (incorrect) events in the one-way pseudo VSP (Figure 3.8d) will result in a false image in the shot record migration (see arrow in Figure 3.8d).

Note that the pseudo VSP data acts as an *intermediate* stage which comprehensively demonstrates the way in which the source wave field and the reflected wave field increasingly approach each other and in this way form the image which would be visible in the end stage of a shot record migration without showing the intermediate steps. Summarizing, the pseudo VSP constitutes a tool effectuating the map of surface seismic data into imaged data and operates as a unique link between the unmigrated surface data and the migrated data.

The pseudo VSP is generated also from surface data after surface-related multiple elimination (Figure 3.8b). Figure 3.8e and f show the result of the acoustic two-way and one-way techniques applied to surface data after surface-related multiple elimination. The results are shown in Figure 3.8e for the two-way techniques and in Figure 3.8f for the application of the one-way techniques. Comparing the results of Figure 3.8e and f, a non-causality is observed in the *one-way pseudo* VSP data which is not correct and meaningless (have to be zeroed).

3.4 Data integration

Vertical seismic profiling is a widely used geophysical technique which responds to the demand of more successful planning and improvement of the field development.

The interest in the performance of Vertical Seismic Profiles (VSP) has been increased more and more over the last decade. Since all or parts of the measurement and observation of VSP takes place inside the earth, one can observe the attenuation and distortion of a surface generated pulse progressing through the earth. The reflection and refraction of the pulse can be observed and also how it is converted to shear and/or pressure waves. Multiples can be a major problem in surface seismic data processing. Therefore the understanding of the mul-

multiple generation and reflection mechanism is very important and the way in which they may obscure the primary reflections in the vicinity of the well. The identification of multiples and their origin in seismic data is very useful and can be seen very clearly in the VSP display.

Vertical seismic profiling has been accepted as a powerful tool to solve many uncertainties appearing in the surface seismic data around wells. For the last two decades a lot of research was carried out in the field of real VSP and synthetic VSP modeling and their applications.

It is worthwhile to mention that in the past many authors have modeled VSP data in order to compare them with recorded VSP data.

Given the source properties and a detailed description of the subsurface it is possible to compute the wave field at any position in space (for instance in a borehole) by solving the wave equation numerically (forward modeling). Of course the reliability of the details fully depends on the reliability of the detailed description of the full subsurface model that has to be specified as input for the modeling scheme. For comparison, in the method of the pseudo VSP generation, the details in the resulting VSP data come directly from the measured surface data rather than from the seismic interpreter. This essential difference is illustrated in Figure 3.9.

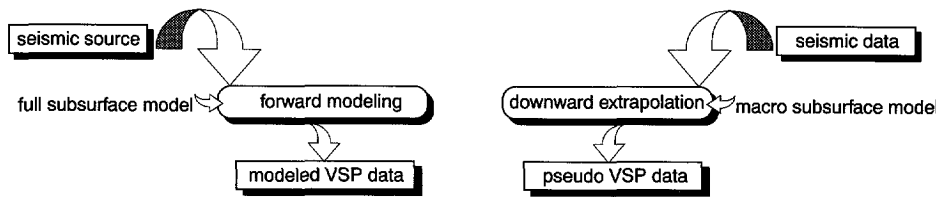


Figure 3.9 Pseudo VSP data generation in comparison with VSP modeling.

In this section some attention is paid to the importance of *reorganization* of data. With the aid of a simple elastic 1-D model, it will be illustrated how different data types can be integrated with each other. In the introduction of this thesis, different data types in Chapter 1 illustrated the wave propagation through a medium. An integration was shown of the recording of the wave field at the surface (shot record) with a macro model through which the waves propagate. The axis that was common for both was the lateral position x . The shot record was displayed as function of the lateral position x and two-way time t . Similarly, integrations were made between the model and snapshots (at increasing times t) which had both axes (lateral location at the surface x and depth z) in common. The snapshots viewed the propagation of the wave fields through a medium as function of increasing times. In the same way, VSP data was integrated with the model; the depth axis z was common to both data types. It was illustrated that in using an equal source in both recording the shot record and VSP data, both data acquisitions would record the same wave field.

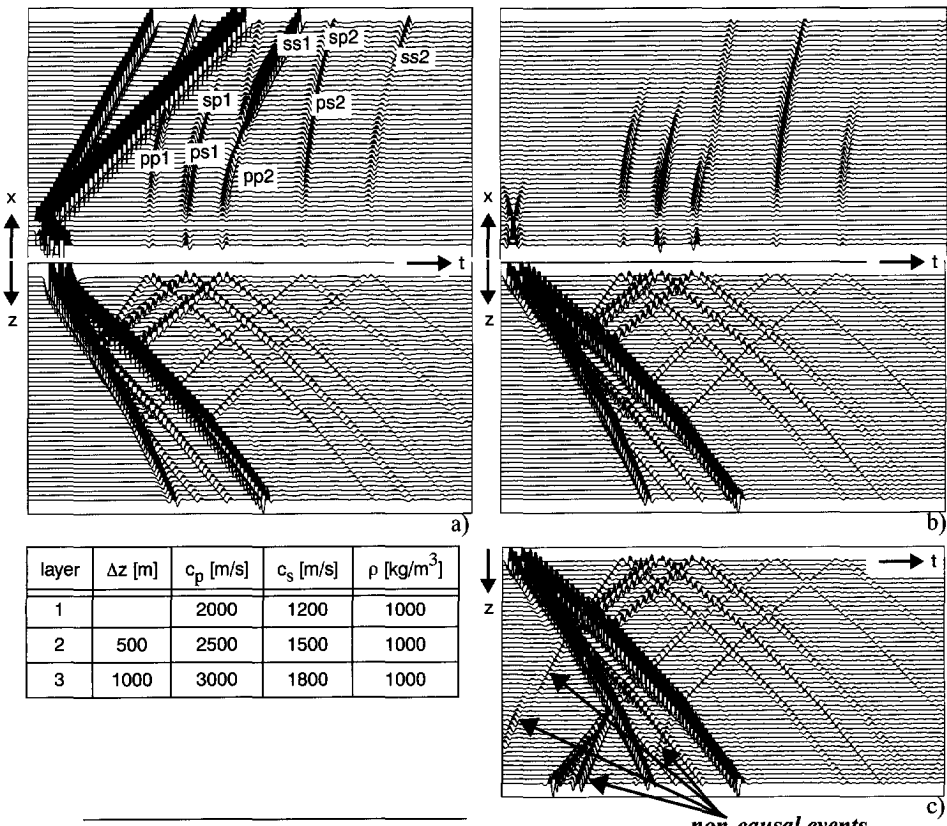


Figure 3.10 Integrated display of modeled data a) shot record and VSP, b) pseudo VSP data generated from the shot record with correct model (see table), c) pseudo VSP data generated with an erroneous model $c_{p2}=2375$ m/s.

Figure 3.10a shows the integration of modeled surface data and offset VSP data using an elastic finite difference algorithm corresponding to a vertical stress source τ_{zz} and horizontal v_x receivers. Note that both datasets have the time axis in common, since they record the same wave field. The display consists of two parts, an upper part and a lower part. The upper part representing the surface data and the lower part representing the VSP data. The source signature is a 60Hz Ricker wavelet, the receiver spacing is 8m and the time sampling is 4ms. Various events are indicated in this figure. Figure 3.10a shows the reorganization of data, by presenting the same information of data in a different format. Both datasets contain the same information but are represented in different formats for an easier interpretation of the various events. The VSP data gives a significant better understanding of the complex events e.g. multiples and wave conversions. Figure 3.10b shows the pseudo VSP data, computed from the surface data. Note the time-coincidence of the events by comparing the surface data with the VSP data.

Two-way full elastic wave field extrapolation operators have been used which were applied in the wavenumber frequency domain. The surface data has been preprocessed in order to correctly locate it within the window of the propagating waves for any layer. The same macro model is used as for the VSP modeling. Figure 3.10c illustrates the pseudo VSP generated from the preprocessed surface data in Figure 3.10b, using an erroneous macro model (5% error in the velocity of the second layer). The compressional velocity of the second layer has been taken $c_{p2}=2375\text{m/s}$ instead of the correct velocity of $c_{p2}=2500\text{m/s}$ (the subscript 2 refers to the second layer). This gives rise to many non-causal P - and S - events. Note that these effects accumulate with depth and do not influence the events of the layer above. This illustrates the potential of the pseudo VSP method for macro model verification which will be discussed in the next section.

In this example the VSP is modeled and generated for one offset (112m) in a vertical well. This can be extended to modeling VSP data for increasing offsets and for the same shot position (offset VSP data contain information about the reflection and transmission properties of the earth laterally away from the well). Figure 3.11 illustrates offset VSP data for increasing offsets on both sides of the single shot position (v_z receivers for a vertical stress source τ_{zz}). A 3-D volume of data can be constructed by collecting the series of offset VSP data in a cube.

Figure 3.12 shows various views and slices through the 3-D volume of modeled data (v_x receivers). Figure 3.12a shows some snapshots which can be also used to build up the volume of data. Figures 3.12b to d show some slices out of the volume illustrating the continuity of the different events in the various shot record, VSP and snapshot planes.

Figure 3.13a and b show a 3-D volume of data (v_x receivers) illustrating the different cross sections (shot record, VSP and snapshot). This 3-D data volume has been built by a series of offset VSP data (see also Figure 3.11). This 3-D volume of data can also be built by a series of downward extrapolated shot records or by a series of snapshots.

Figure 3.13a illustrates clearly the different planes (x,t) , (x,z) and (t,z) of this volume, which represent in fact the shot record, the snapshot and the VSP respectively. The continuity of the events in the different planes adds another *dimension* to the interpretation of the events. A remarkable event in Figure 3.13a is the headwave (see arrows in the snapshot and VSP). With this 3-D volume of data it is possible to take slices of it, to identify different events.

The 3-D data volume can be unfolded and pasted into two dimensions which makes the continuity of the different planes more identifiable (see Figure 3.14).

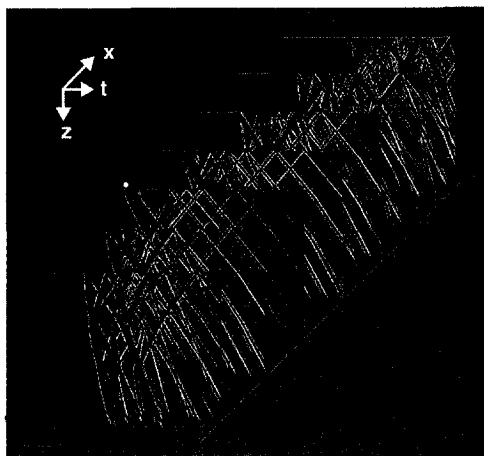
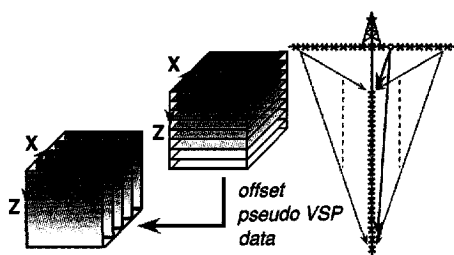
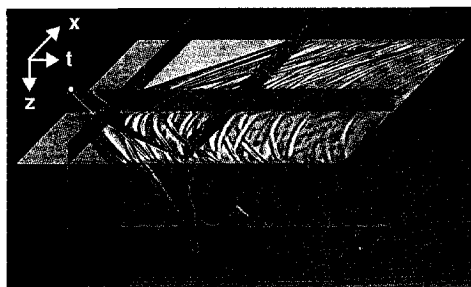


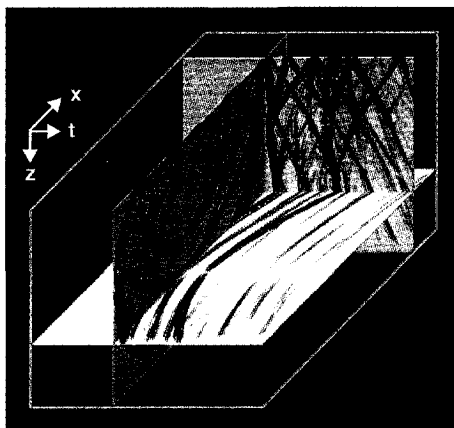
Figure 3.11 Construction of a 3-D volume of data by a series of offset VSP data or downward extrapolated shot records.



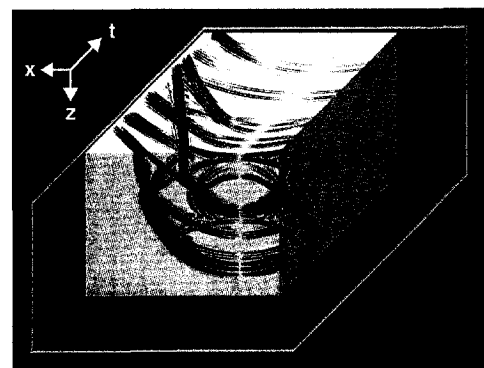
a)



b)

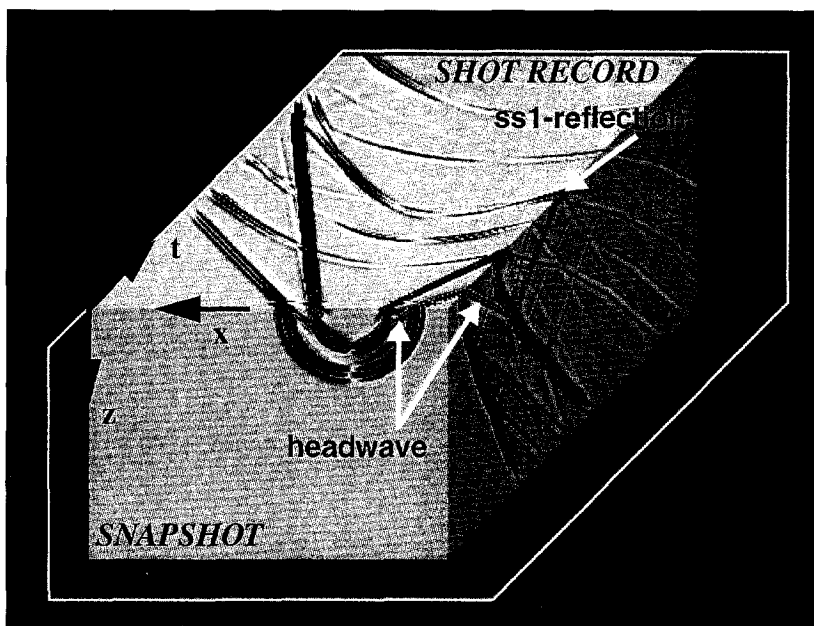


c)

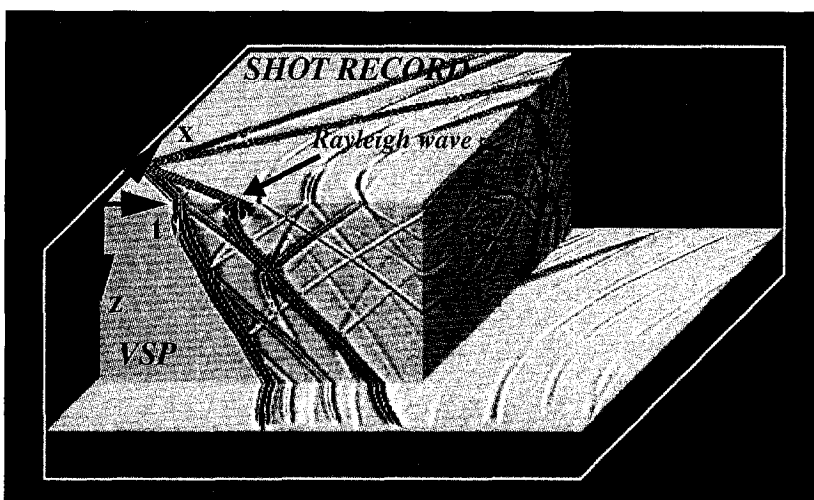


d)

Figure 3.12 Various slices through the 3-D volume of modeled data (snapshots, shot records and VSP data).



a)



b)

Figure 3.13 3-D volume of data illustrating the different cross sections (shot record, VSP and snapshot : v_x registrations for a τ_{zz} source).

Figures 3.14a to c show the unfolded 3-D volume of data, representing three pictures of the wave propagation for increasing times t_1 to t_3 . Each figure consists of two parts. The left part shows the shot record in combination with the snapshot (x-axis in common). The lateral position of the well is displayed in these figures. The right part illustrates the integrated shot record-VSP display at the position of the well (the time axis is common to both the datasets). Finally the lower part of each figure is an integrated snapshot-VSP display (z-axis in common). From this integrated data representation it is clear that for increasing times t_1 to t_3 , the VSP display gives much more insight in understanding the wave propagation through the subsurface and facilitates the identification of the events in the shot record.

It is common practice to use the snapshots to understand the complexity of a shot record. The investigation of snapshots gives insight but to understand what is really going on it is proposed to generate VSP data. By generating VSP data, much more insight will be gained into the different events because all the complex events become identifiable. This is a powerful method of studying complex shot records. This way of looking at the data underlines the important application of vertical seismic profiles. VSP establishes a unique link between the geological interface in depth and its time event on the surface seismic section.

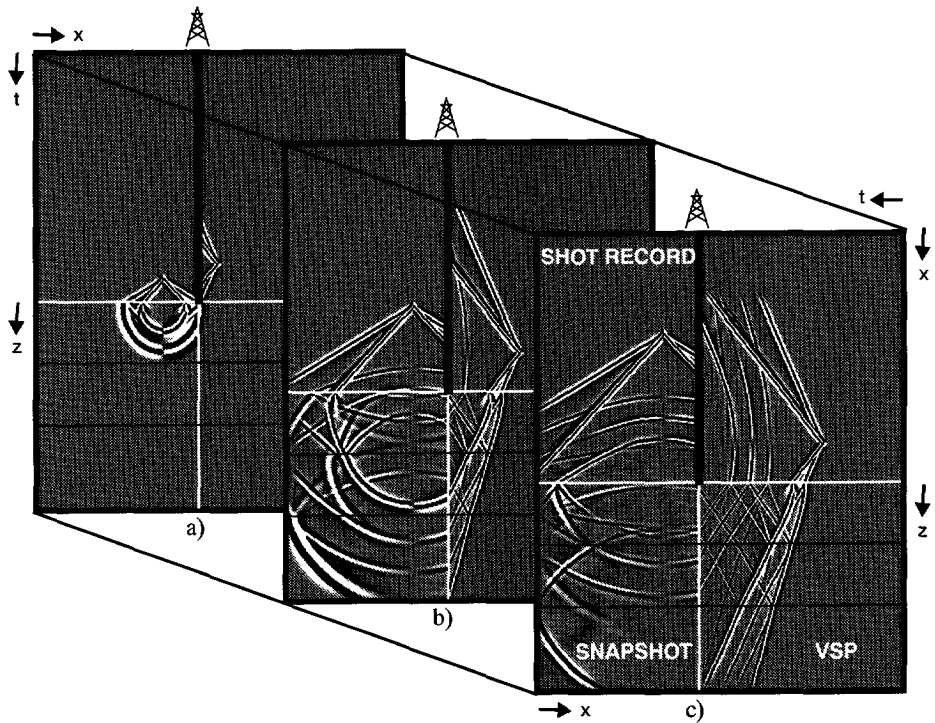


Figure 3.14 Snapshots, VSPs and shot records illustrating the wave propagation for increasing times t_1 to t_3 .

3.5 Boundary conditions

If the total (acoustic or elastic) wave field is known and full knowledge of the medium parameters is gained, every boundary condition can be met throughout the complete extrapolation process and optimal reconstruction of the wave field propagating in the earth can be achieved. When some parts of the required knowledge as pointed out above are not available, then some unwanted components of the wave field are generated. These unwanted components can not be avoided, due to inaccuracies in specified medium parameters, which are inevitable in velocity estimation and migration. The strength of these unwanted components, the non-causal events, is related to the reflection coefficient of the erroneously positioned contrast causing the generation of these components. Two-way wave field extrapolation techniques are sensitive to errors specified in medium parameters. This *sensitivity* can be used in the extrapolation to introduce a new criterion for the verification of the correctness of the macro model. In this section some examples show the verification of the parameters of macro subsurface models in using two-way operators.

The information on a macro model of the subsurface is present in the seismic shot record in the arrival times of the reflections. If an erroneous model is used as input for a two-way wave field extrapolation algorithm, non-causal solutions are observed, because the arrival times are not properly handled due to a wrongly specified depth or layer velocity. In two-way wave field extrapolation techniques downgoing and upgoing waves are handled simultaneously. Therefore the source and reflected wave fields need to be superposed before downward extrapolation. The basic principle of macro model verification lies on the sensitivity to errors in the macro model. The automatic fulfillment of the boundary conditions at layer boundaries is illustrated in Figure 3.15 using two-way wave field extrapolation techniques.

For a better understanding of the coupling between the up- and downgoing waves, they have been split at the surface into incident downgoing and reflected upgoing waves and the effects of two-way downward extrapolation is analyzed on the down- and upgoing waves independently. The upgoing waves below the interface (dashed arrows) in Figure 3.15a and b are automatically generated to fulfill the boundary conditions at the layer interface. The boundary conditions are automatically fulfilled because the total wave field is continuous for all depths. Addition of these two separate parts will result in a correct coupling in case of a correct model; the dashed arrows cancel each other, because they are of same amplitude but opposite in phase (see Figure 3.15c). Extrapolating with an erroneous macro model will result in an incorrect upgoing wave (see upgoing dashed arrow in Figure 3.15d). Here the difference is shown between correct and incorrect coupling between up- and downgoing waves. In other words, surface data extrapolated with a slightly wrong macro model, will result in incorrect coupling between up- and downgoing wave fields at the layer interfaces.

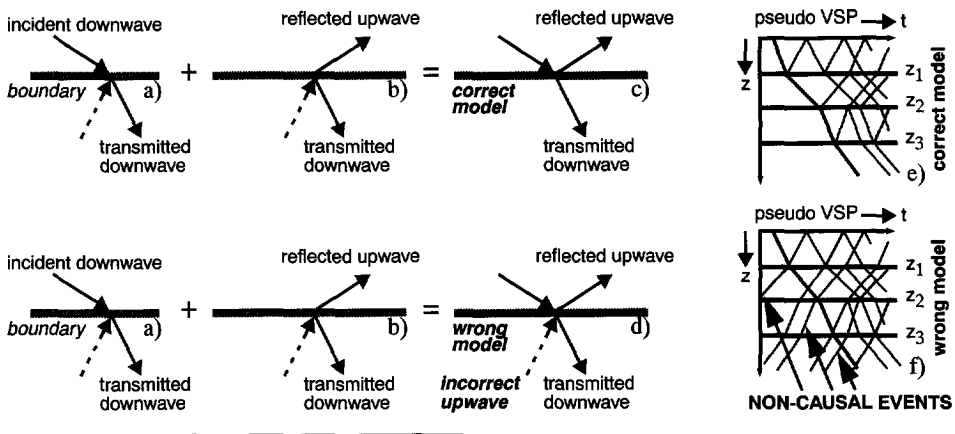


Figure 3.15 Boundary conditions at interface for a) an incident downgoing wave and b) a reflected upgoing wave, c) superposition of a) and b) for correct coupling and d) incorrect coupling. e) Pseudo VSP data using a correct macro model and f) the occurrence of non-causalities in the pseudo VSP data using an erroneous model in the wave field extrapolations.

Upgoing wave fields would then arrive earlier at the detectors than downgoing primaries, which is not possible for configurations where sources are positioned at the surface.

A possible updating procedure (Figure 3.16) may be used for the verification and estimation of the macro model of the subsurface, starting with an initial macro model : the initial pseudo VSP may be inspected on the occurrence of non-causal events. In the presence of non-causal events, the procedure of transformation and inspection may be repeated iteratively until non causal events disappear.

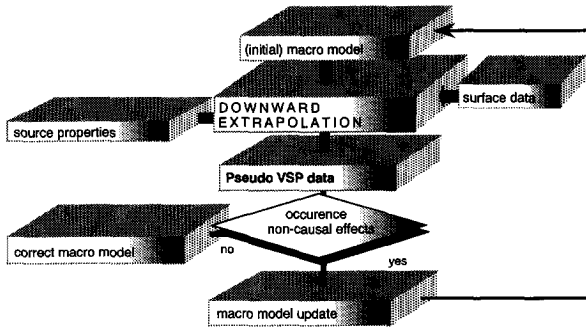


Figure 3.16 Proposal for an iterative macro model updating procedure using two-way techniques.

In the following, some examples on the macro model verification are illustrated on synthetic modeled data based on an elastic horizontally layered subsurface model. The updating procedures using pseudo VSP data are beyond the scope of the thesis.

The elastic layer parameters of the macro model are given in Figure 3.17. Figure 3.17a shows the shot record (v_z registration) that is modeled in the wavenumber frequency domain. The source used for this experiment is a vertical τ_{zz} source at the free surface. Here a similar approach is used as in Figure 3.8c, where the total wave field is separated into two wave fields, i.e. the source- and the reflected wave field. The wave fields are separately extrapolated downward using full elastic two-way operators, see Equations (2.30) and (2.31). The extrapolation is performed in the wavenumber frequency domain. Both wave fields have been extrapolated with the correct macro model. The upgoing waves below the interface are automatically generated to fulfill the boundary conditions at the interface. These upgoing waves below the interface are the so-called non-causal compressional and shear wave events. The separately generated pseudo VSP data (source wave field : 3.17b) and (reflected wave field : 3.17c) show the transmission and reflection of P - and S - waves. Addition of Figure 3.17b to Figure 3.17c results in a “correctly generated” pseudo VSP (Figure 3.17d). The non-causalities cancel each other because they are of equal amplitude but opposite in phase. The pseudo VSP data have been generated to a depth of 700m. This example manifests clearly the fulfillment of the boundary conditions at the interface in using two-way extrapolation operators. Here the pseudo VSP generation constitutes an effective tool for a better understanding of boundary conditions at interfaces. The separately extrapolation of source and reflected wave fields gives a clear view and understanding of the elastic boundary conditions. Note that for the generation of pseudo VSP data the 4 components of the elastic wave field (v_z , τ_{xz} , τ_{zz} , v_x) are computed at each depth level. The generated τ_{zz} response is depicted in Figure 3.17e. The other components v_x and τ_{xz} are shown in Figure 3.18. Similar to Figure 3.17 the wave fields for the v_x component has been treated separately. From Figure 3.18b and c it is clearly seen, that the upgoing non-causal S - waves are better identifiable. Addition of Figure 3.18b and c gives the result which is depicted in Figure 3.18d. Note the *higher S*- wave energy in all the panels in comparison with those in Figure 3.17.

The appearance of the non-causalities is illustrated with the following examples which show the behaviour of the different non-causalities appearing by wrongly specified parameters of the macro model. Figure 3.19a represents the pseudo VSP data generated from the surface data (v_z and v_x registrations for a vertical τ_{zz} stress source; depicted above the pseudo VSP data) for the correct macro model using two-way elastic wave field extrapolation operators. The same elastic horizontally layered model has been used as depicted in Figure 3.17 and Figure 3.18. Figures 3.19b to e show the generated pseudo VSP data using erroneous macro models. In Figure 3.19b the pseudo VSP data are shown with an error of 10m in the depth (first reflector). This gives rise to many non-causal events in comparison with the correct VSP data (Figure 3.19a). Figure 3.19c shows the results for an error in the P - wave velocity (c_p) of the first layer : 100m/s has been subtracted.

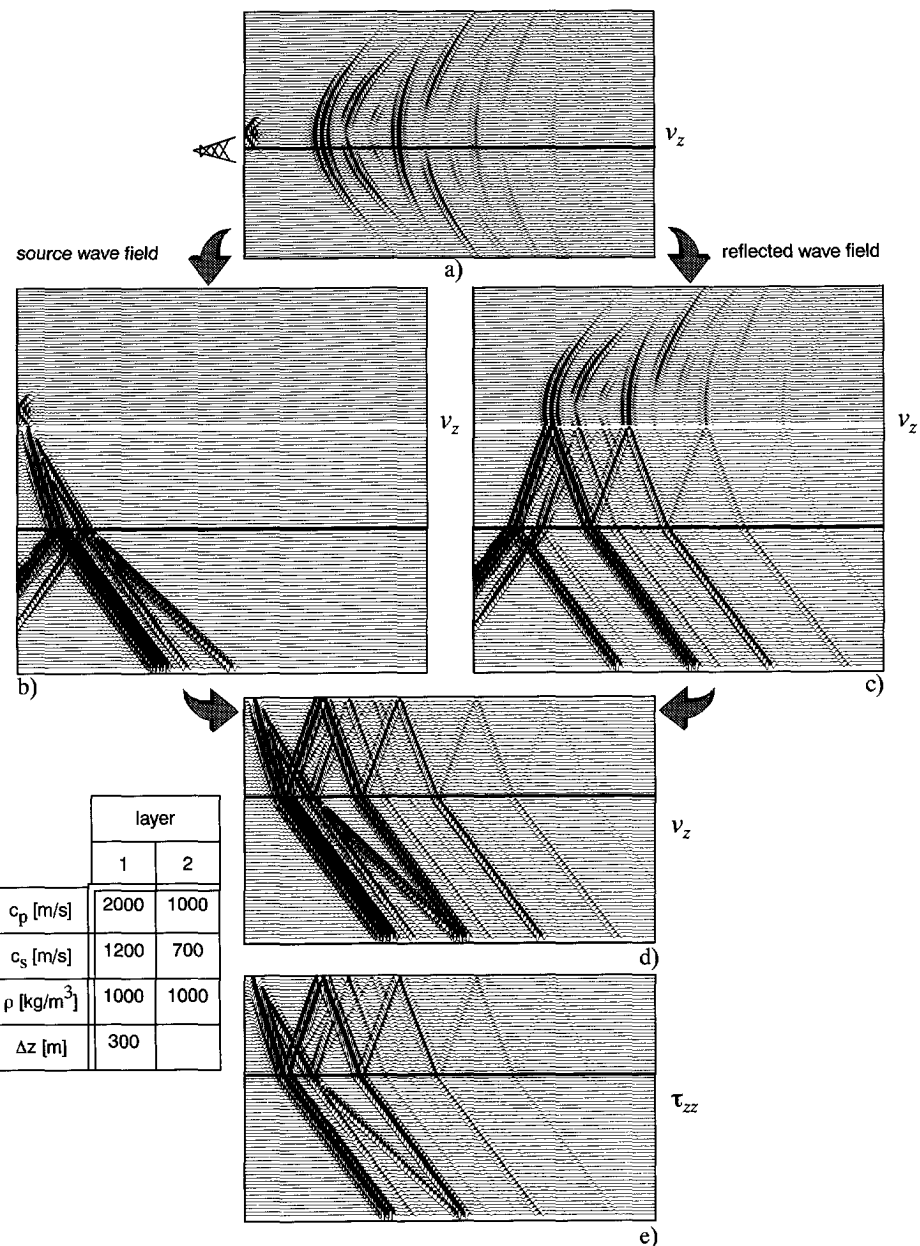


Figure 3.17 Transformation of elastic surface data into elastic pseudo VSP data. The different figures show the various components of the data for a τ_{zz} source at the free surface. Note that the pseudo VSP data have been generated at 112m offset with respect to the shot location.

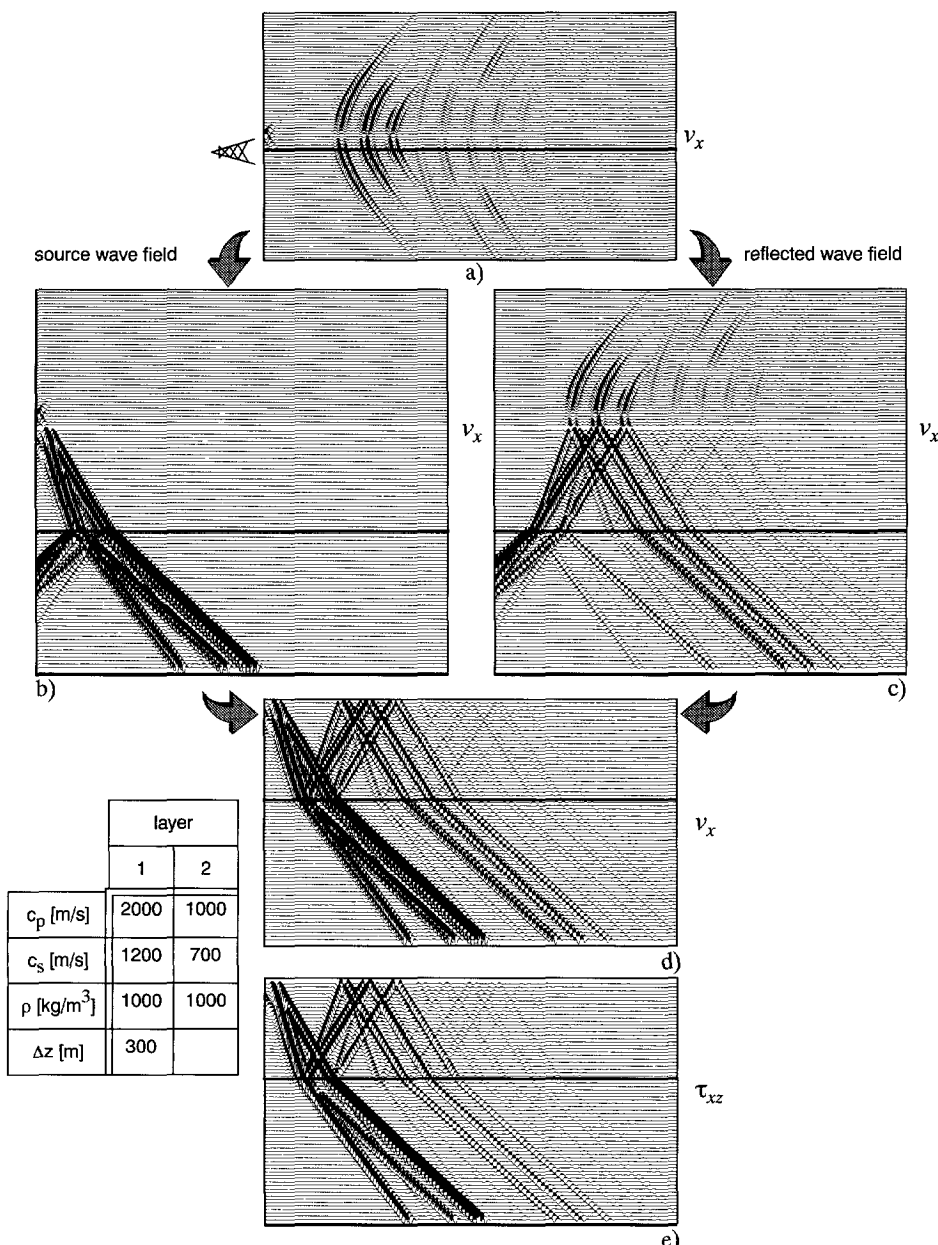


Figure 3.18 Transformation of elastic surface data into elastic pseudo VSP data. The different figures show the various components of the data for a τ_{zz} source at the free surface. Note that the pseudo VSP data have been generated at 112m offset with respect to the shot location.

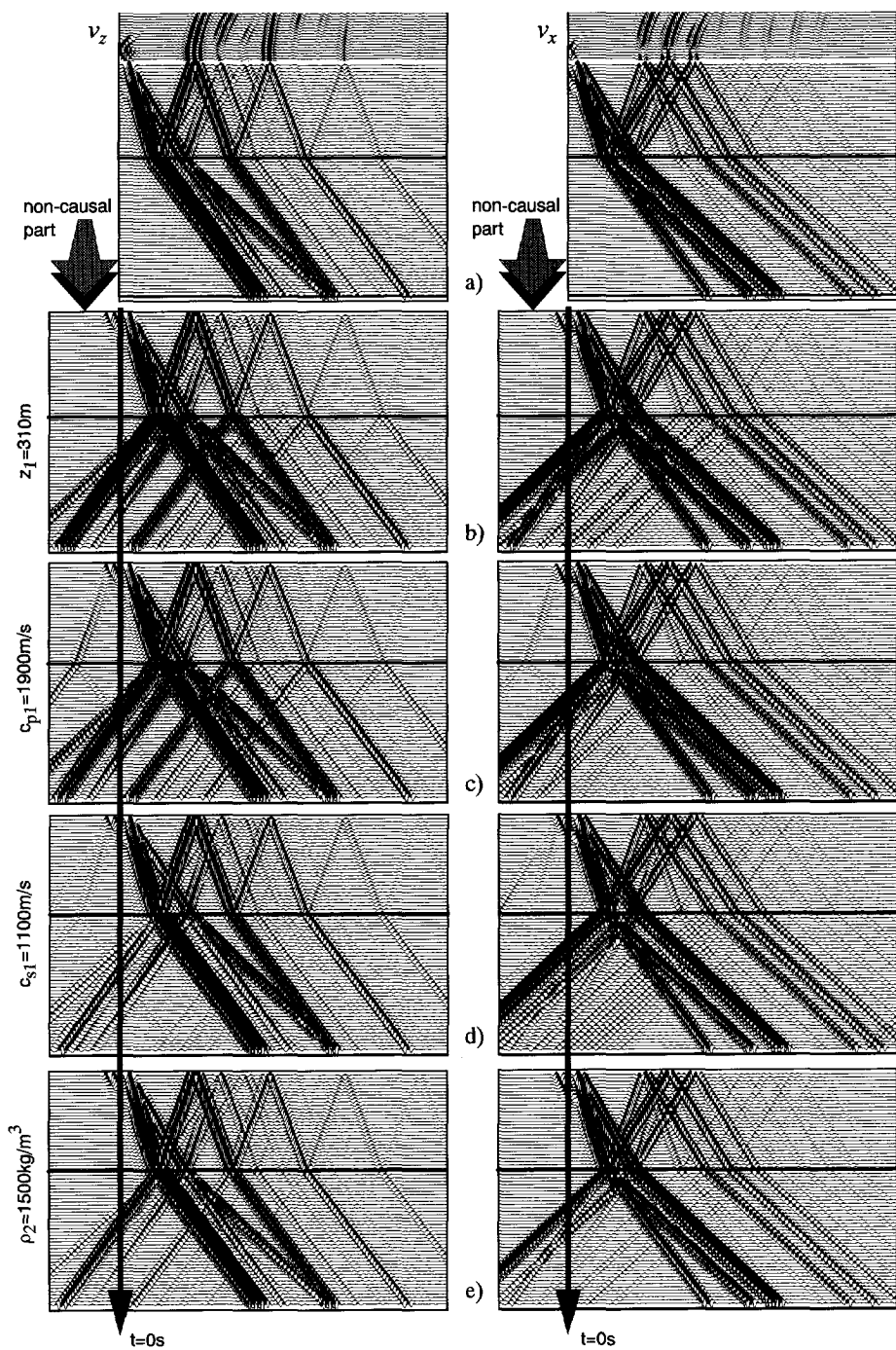


Figure 3.19 The effect of elastic two-way pseudo VSP generation with incorrect input parameters.

Figure 3.19d shows the effect if the velocity of the S -waves in the first layer have been decreased by 100m/s. Figure 3.19e shows the pseudo VSP data generated with an error in the density of the second layer: 500kg/m³ has been added to the density of the second layer. Comparing the results it is clear that the effect of the unwanted field components is repeated downwards and an error in e.g. the second layer will of course not influence the events of the layers above. Finally Figure 3.20a shows the effect on the generated pseudo VSP data with an error in the source amplitude. The amplitude of the source wave field (part of the input to the algorithm) has been increased by 10% of the original amplitude of the source wave field. An important point to note in these experiments is that whenever the amplitude of the source wave field is not correct, the non-causalities appear only at the direct wave (compare with Figure 3.20). Therefore the best strategy for the macro model verification and update is to correct first for the errors in the specified parameters of the macro model and then finally correct for the amplitude of the source wave field.

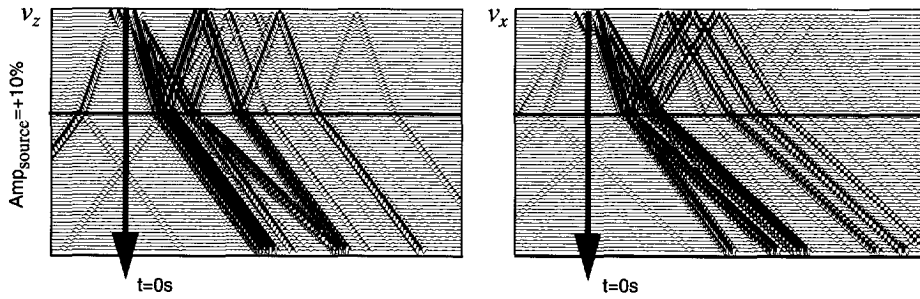


Figure 3.20 The effect on the generated pseudo VSP data with an error in the source amplitude.

To get a better insight into the different non-causalities, the following experiments investigate the appearance of these unwanted events in more detail. Figure 3.21a (top) shows the shot record generated for the simple situation of a plane wave (at normal incidence) at the free surface for the given acoustic model (see Figure 3.21). Figure 3.21 shows the behaviour of the non-causalities in the generated pseudo VSP with errors respectively in the depth, velocity and density of the macro model. For each type of error, three pseudo VSP data are shown. Upwards the results are shown for a negative error and downwards for a positive error in depth. Note that the pseudo VSP data in the middle is correct. The experiment (Figure 3.21a) is performed with 7 negative and 7 positive errors, with each time an extra error of 20m in depth. For the velocity and density, 2 negative and 2 positive errors have been made. Furthermore the last trace of each pseudo VSP is plotted to study the behaviour of the noncausalities. One thing to notice for the depth error is that 2 non-causalities are generated (one originating at the correct depth, i.e. $z=300m$, and the other a shifting non-causality). Note that the polarity of the non-causalities changes in passing from the negative errors to the positive ones. Studying the last traces of the velocity error panel, a phase shift can be

observed in the direct wave of the generated pseudo VSP data. Similar to the above explained figures, the effect of errors in the density of the macro model is that the shape of the non-causalities remains the same but the amplitudes are increased with an increased error in the density. Combination of errors will produce more complicated pictures.

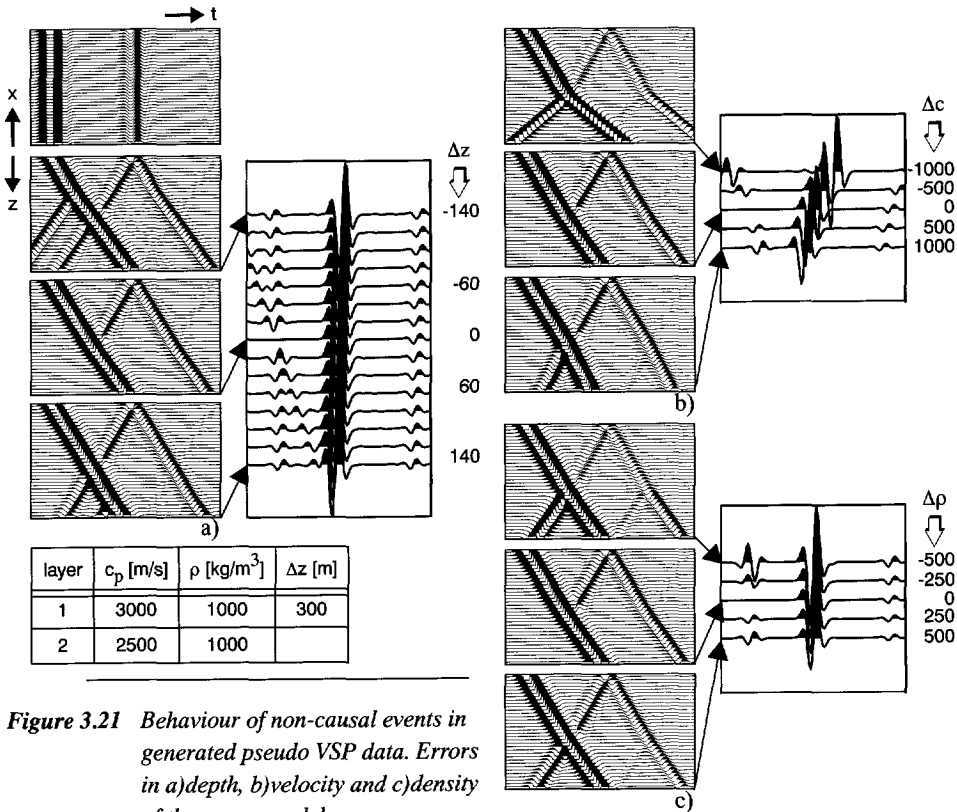


Figure 3.21 Behaviour of non-causal events in generated pseudo VSP data. Errors in a) depth, b) velocity and c) density of the macro model.

For acoustic boundaries there are two conditions : 1)the pressure must be continuous and 2)normal component of the particle velocity must be continuous. The angle dependent reflection and transmission coefficients for a fluid-fluid boundary are given in Figure 3.22. For the derivation of the different boundary conditions for different interfaces e.g. fluid-fluid, solid-fluid, solid-solid etc. the reader is referred to Berkhout (1987). Figure 3.23 illustrates the acoustical interface equations for two-way wave field extrapolation. R is the angle dependent reflection coefficient (see also Figure 3.22).

$$R_{pp}^+ = \frac{\rho_2 c_{p2} \cos \alpha - \rho_1 c_{p1} \cos \beta}{\rho_2 c_{p2} \cos \alpha + \rho_1 c_{p1} \cos \beta} \quad T_{pp}^+ = \frac{2 \rho_2 c_{p2} \cos \alpha}{\rho_2 c_{p2} \cos \alpha + \rho_1 c_{p1} \cos \beta}$$

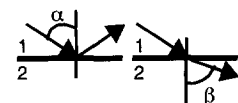


Figure 3.22 Angle dependent reflection and transmission coefficients for fluid-fluid boundaries.

In the case of correct coupling, the following equation holds : $P_1^- = RP_1^+$ and for incorrect coupling : $P_1^- = \check{R}P_1^+ + (1 - \check{R})P_2^-$. \check{R} represents the reflection coefficient in the incorrect macro model. Combining both equations shows that the amplitude of the non-causal event P_2^- is given by :

$$P_2^- = \left(\frac{R - \check{R}}{1 - \check{R}} \right) P_1^+ \quad (3.2)$$

Note that for $\check{R} = R$ the non-causal event disappears (correct coupling).

$$P_1^- = RP_1^+ + (1 - R)P_2^- \quad \text{and} \quad P_2^+ = (1 + R)P_1^+ - RP_2^-$$

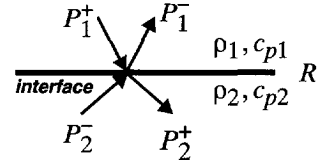


Figure 3.23 Acoustical interface equations for both upgoing and downgoing waves.

3.6 Illustrations on synthetic data

3.6.1 The Marmousi model and dataset

So far, some examples were shown for the application of the pseudo VSP generation method to surface measurements with horizontally layered models. To handle also a structurally more complex geology the following example is given. In this example pseudo VSP data will be generated from the well-known Marmousi dataset. The Marmousi model is based through the North Quenguela trough in the Cuanza basin (Angola) as described in Verrier and Branco (1972).

The data is modeled with an acoustic, second order finite difference scheme. The acquisition geometry is a moving end of spread configuration containing 96 geophone groups, with an initial offset of 200m. The number of shots is 240. The spacing of the sources and receivers is 25m. The data has a sampling interval of 4ms (length of data : 4s). The first and last shot positions are positioned respectively at 3000 and 8975 meters. For a more detailed description of the model and dataset see Versteeg and Grau (1991).

Analogous to the 3-D volumes given in the example of Figure 3.13, a 3-D volume of data is built for the Marmousi dataset. The 3-D data volume is illustrated in Figure 3.24. The 3-D volume is further mapped into two dimensions for a better identification of the continuity of the events in the different planes. Figure 3.25b shows the wave propagation through the Marmousi model at a time t_1 . The positions of the well and the source are indicated in the Marmousi model and the correspondence of the data in depth can be verified with the model.

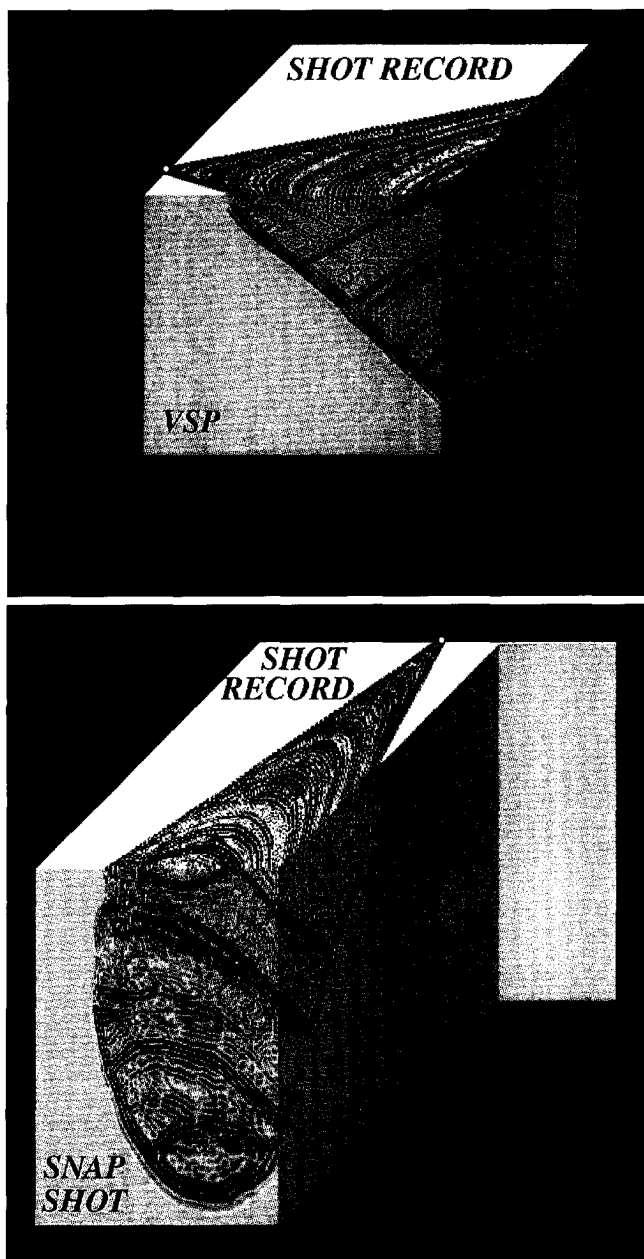


Figure 3.24 Wave propagation through the Marmousi model in the different planes (shot record, snapshot and VSP).

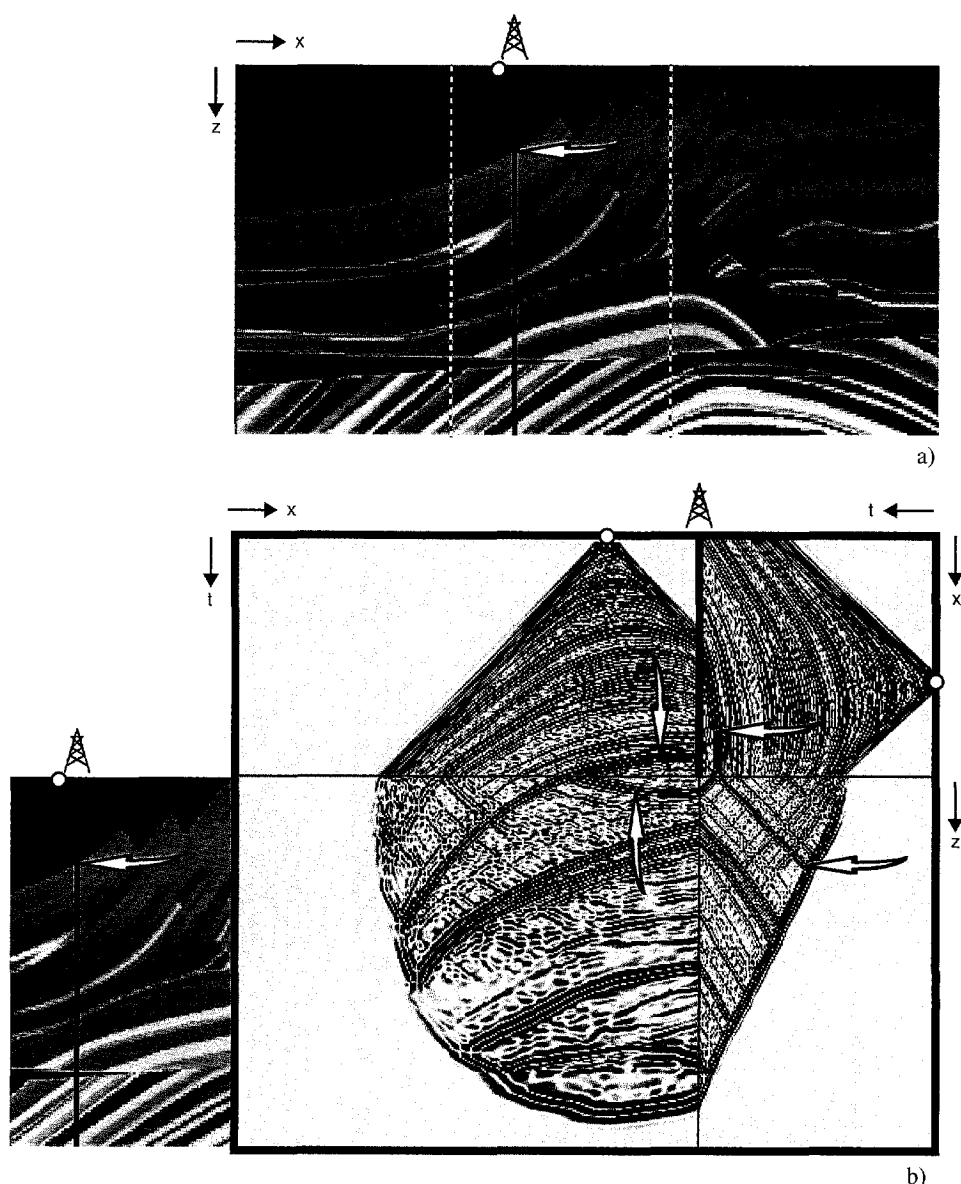


Figure 3.25 a) The Marmousi model and b) wave propagation through the Marmousi model.

Figure 3.25b consists of two parts. The left part shows the current technology to use snapshots to understand the complexity of the shot record. The right part illustrates the objective of the research presented in this thesis. It is clear that the events in the VSP are much better identifiable than the complex events in the snapshot.

In other words, the pseudo VSP gives much more insight into the identification of the different complex events in surface seismic data. Note that the development of the pseudo VSP algorithm allows insight into the entire wave propagation problem. The VSP data can not only identify e.g. the surface-related multiple (see arrow in Figure 3.25b), but it can also illustrate how the multiple is created and which path the source wave field took through the model layers. Placing the model next to the VSP data allows a fast interpretation of the surface multiple and the layers in which the events are generated.

From the first shot gather of the Marmousi dataset, a pseudo VSP data is generated at 725m offset. The thin water layer reverberations have been removed from the shot gather and the missing near offsets were interpolated using a CMP interpolation technique. The removal of the water layer reverberations improved the data significantly. The sharpening of the wavelet (due to removal of the thin layer reverberations) can be observed in the comparison of Figure 3.26a and b.

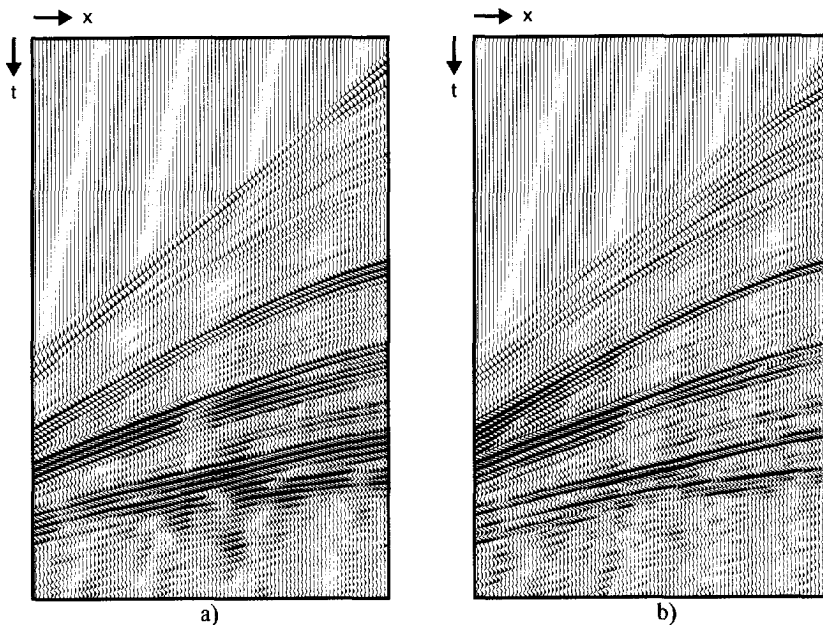


Figure 3.26 a) Shot #1 of the Marmousi dataset and b) shot #1 after the removal of the thin layer reverberations.

Figure 3.27 shows an Integrated Seismic Display (ISD) of the first shot gather of the Marmousi dataset, the modeled VSP data at $725m$ offset and the Marmousi model. The vertical axis of the model has been exaggerated to match it with the depth of the modeled VSP data. The modeled VSP is computed with an acoustic finite difference algorithm.

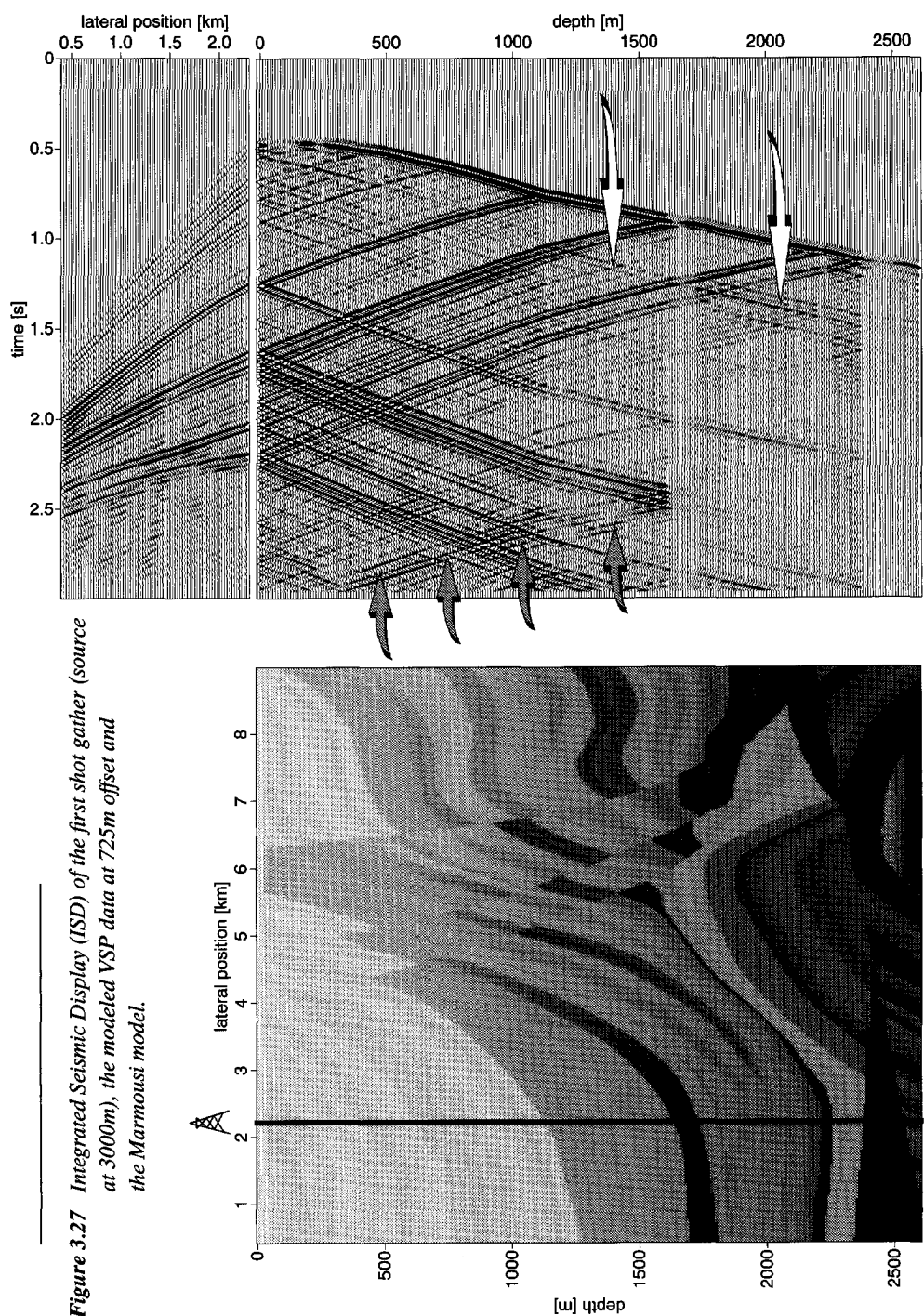
The integrated shot record / VSP display allows an easy interpretation of the different events (as shown in Figure 3.27). Following an event in the shot record and the VSP through to the macro subsurface model enables to have a clear interpretation of the different events.

For comparison, a pseudo VSP data, related to the same area of interest, is generated from the first shot gather of the Marmousi dataset using two-way wave field extrapolation operators. The pseudo VSP is generated by downward extrapolation of the wave field in the space frequency domain (lateral variations can be handled properly). In the space frequency domain the operators are applied by spatial convolutions.

Figure 3.28 shows an Integrated Seismic Display (ISD) of the first shot gather of the Marmousi dataset, the generated pseudo VSP data at $725m$ offset (two-way), the velocity profile at the well and the depth image after full prestack migration. The full prestack depth migration has been performed in the space frequency domain using the true velocity model. The Marmousi watergun wavelet is used in the pseudo VSP generation (see Figure 3.28) and modeling (see Figure 3.27) and is obtained by digitizing a near field signal which has been filtered with a trapezoid frequency filter ($0, 10, 40, 60$ Hz).

Comparing the results of the generated pseudo VSP with that of VSP modeling it is clear that the internal multiples up to the first order are handled correctly (see white arrows in Figure 3.27 and Figure 3.28). Due to some numerical errors some non-causalities appear at the layer interfaces. The non-causalities that appeared before the direct wave have been zeroed because they are not correct and meaningless.

A remarkable difference between the generated pseudo VSP and the modeled VSP are the multiples at the left (see grey arrows in Figure 3.27) which are not present in the generated pseudo VSP (Figure 3.28). The absence of the internal multiples in the pseudo VSP is due to the limited registration time in the surface shot data.



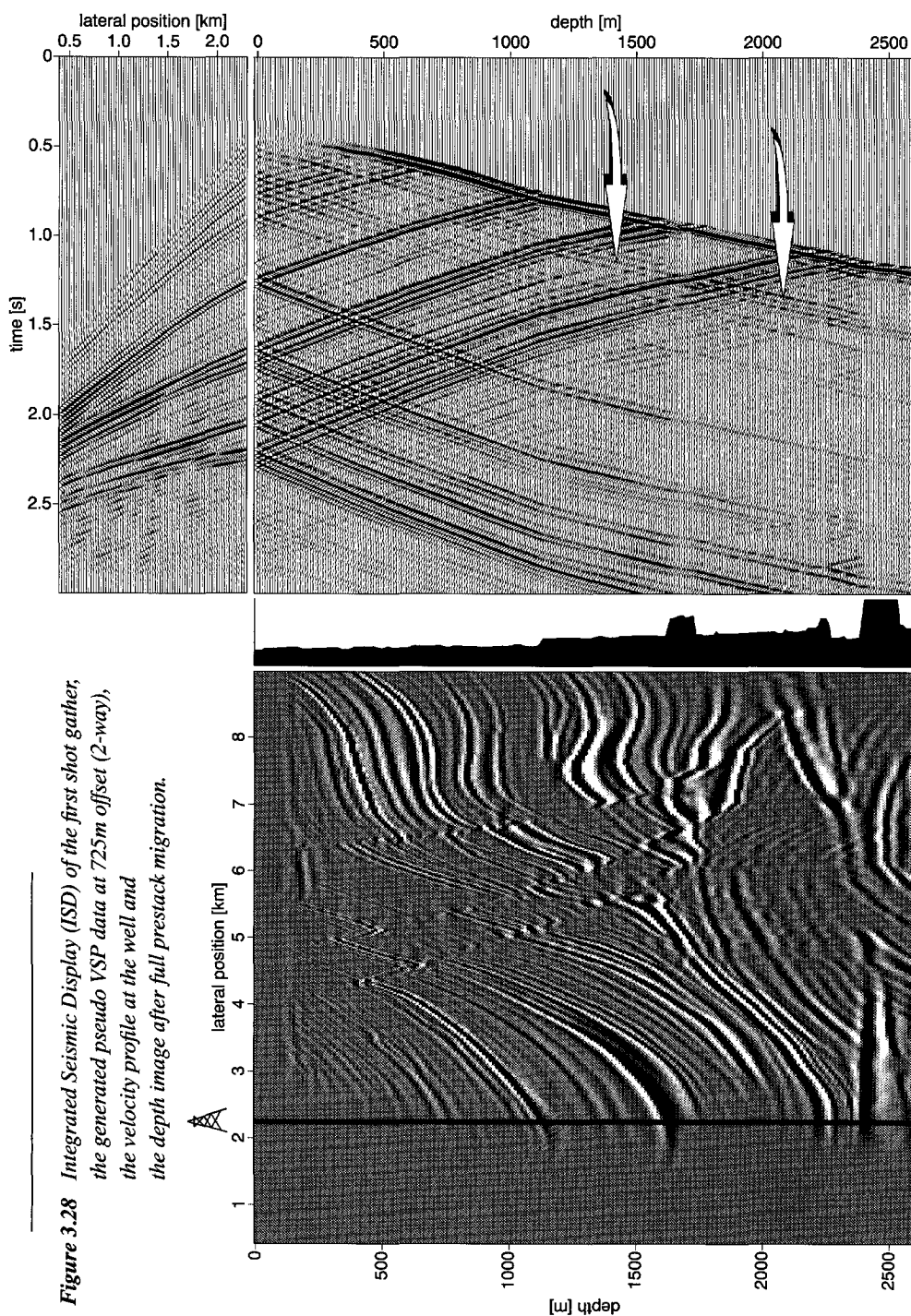


Figure 3.28 Integrated Seismic Display (ISD) of the first shot gather, the generated pseudo VSP data at 725m offset (2-way), the velocity profile at the well and the depth image after full prestack migration.

3.6.2 Aliasing issues

For the generation of the pseudo VSP a shot record is used as input. It may be that shot records which are not aliased at all will result in a pseudo VSP data that is spatially aliased. Spatial aliasing occurs in surface data if the sampling of the data $\Delta x \geq (c_{xmin}/2f_{max})$. Temporal aliasing occurs in surface or VSP data if the sampling time of the data $\Delta t \geq (1/2f_{max})$. To avoid spatial aliasing in the generation of pseudo VSP data, the following conditions should be put into attention for choosing the sampling interval of the pseudo receivers : $\Delta z \leq (c_{zmin}/2f_{max})$, where f_{max} denotes the maximum frequency. Figure 3.29 illustrates that spatial aliasing may occur if the above described criteria is not met. Figure 3.29a shows the response + source wave field at the surface of a horizontally layered model with 1 boundary at 200m depth. The parameters of the acoustic model are : $c_{p1}=1500\text{m/s}$, $\rho_1=1000\text{kg/m}^3$, $c_{p2}=1000\text{m/s}$ and $\rho_2=3000\text{kg/m}^3$. The dimensions of the model are 1000m lateral and 400m depth with an equally sampled grid of 10m. The $f-k$ spectrum of the data shows a maximum frequency content of 60Hz. Figure 3.29b shows the pseudo VSP data with its spectrum. The frequency content of the response has been increased to a maximum of 120Hz, but the source wave field has still a frequency content of 60Hz (Figure 3.29c). Generation of a pseudo VSP data from the shot record in Figure 3.29c shows that the data becomes spatially aliased for the higher frequencies (Figure 3.29d). Note the non-causal event that is created due to unbalanced frequency.

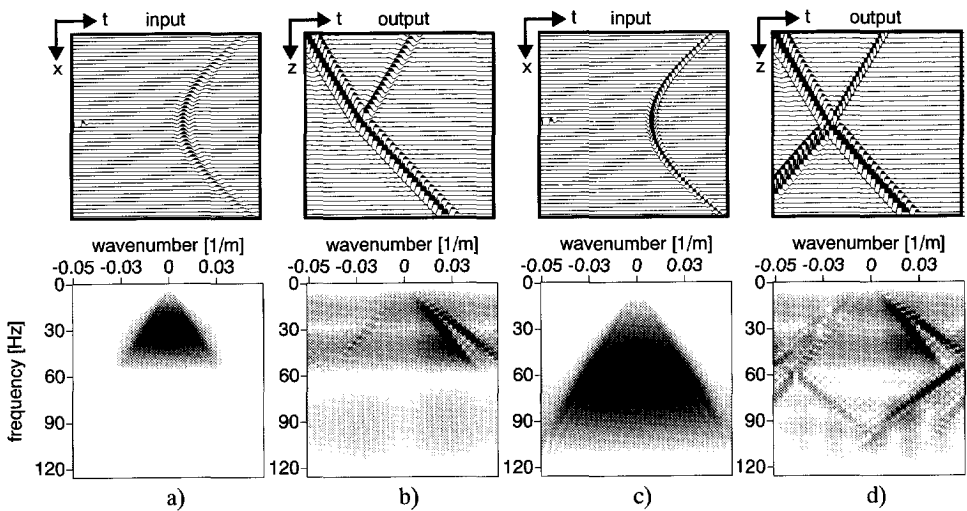


Figure 3.29 Illustration of spatial aliasing occurring in pseudo VSP data. Data and their related wavenumber frequency spectra : a) shot record ($f_{max}=60\text{Hz}$) + source wavelet ($f_{max}=60\text{Hz}$), b) pseudo VSP generated from (a), c) shot record ($f_{max}=120\text{Hz}$) + source wavelet ($f_{max}=60\text{Hz}$) and d) pseudo VSP generated from (c).

3.6.3 Laterally invariant subsurface model

The experiment that will be discussed here is based on the acoustic subsurface model given in Figure 3.30, with an irregular water bottom. The length and depth of the model are respectively 2700m and 2000m.

The spacing of the sources and receivers is 15m. The wavelet used in this example has a frequency band of 0-50Hz with a central frequency at 25Hz. The shape of the spectrum of the used wavelet is a cosine square. The acoustic layer parameters of the subsurface model are given in Figure 3.32b. Figure 3.30a shows a simulated shot record (p registration) for the indicated source position in Figure 3.30, with all multiples included. Figure 3.30b shows the shot record after surface related multiple elimination, in which the four primaries can be easily observed. Due to synclinal shapes the multiple behaviour is very complex.

Since the free surface is a very strong reflector, the surface-related multiples can completely mask the primary reflections from deeper interfaces. This can be observed in the migration result of one shot record as shown in Figure 3.31. The multiple elimination procedure consists of an adaptive inversion process, see Verschuur et al. (1992). It uses the prestack data itself in the multiple prediction operator and therefore requires no knowledge about the subsurface. By the adaptive application of the surface-related multiple elimination process, the original source signature is estimated in a true amplitude sense. This multiple-free dataset will be used to generate pseudo VSP data. The VSP is in this case situated at zero offset. The pseudo VSP generation method is applied as well on the data with multiples as on data after surface multiple elimination. The pseudo VSP is generated with the one-way and two-way extrapolation operators respectively. The wave field extrapolation is performed in the space frequency domain using the exact subsurface model. Figure 3.30c and d show the one-way respectively two-way pseudo VSP generation from the shot record with all multiples included. Note that the data parameters as given in Table 1 on page 60, are used to fulfill the surface boundary conditions. The surface data has been pasted next to the generated pseudo VSP at the position of the well for an easier interpretation of the different events. Figure 3.30d shows that most of the multiple energy remains in the first layer.

Figure 3.30e and f show the one-way respectively two-way pseudo VSP generation from the shot record after the surface-related multiple elimination method is applied to it. Figure 3.30e shows that internal multiples are not handled correctly and in this way cause an incorrect intersection with the downgoing source wave field. Internal multiples can be clearly identified in Figure 3.30d and f (see arrows). Due to numerical errors some non-causal effects occur because the two-way extrapolation is very sensitive. The non-causalities that appeared before the direct wave have been zeroed because they are not correct and meaningless. The shots were modeled with a space-frequency algorithm using a limited aperture.

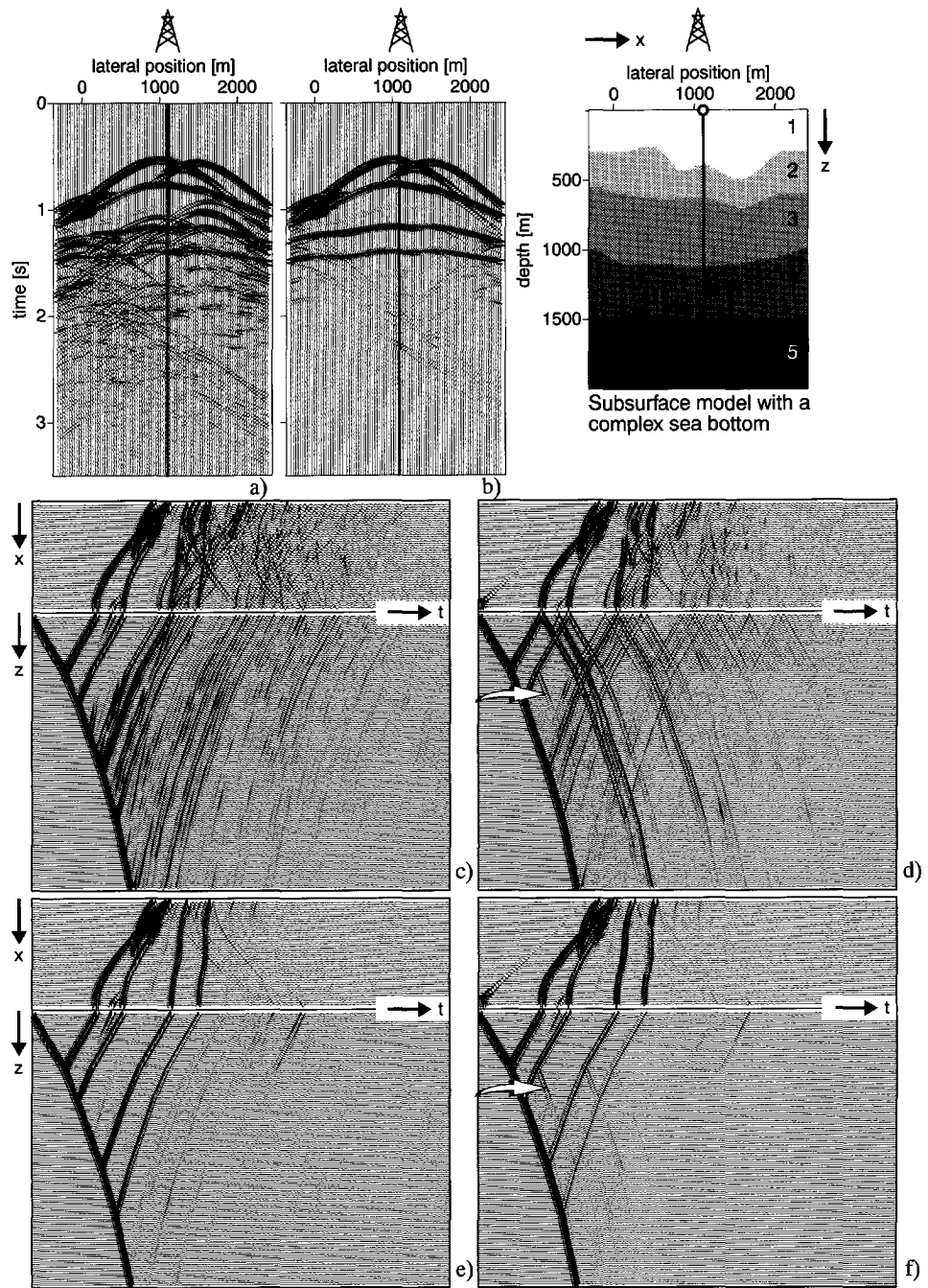


Figure 3.30 Pseudo VSP generation from a shot record a) with multiples and b) after surface-related multiple elimination, using one-way (c and e) and two-way operators (d and f).

Figure 3.30e and f show that the boundary artifacts from aside fade away in depth (out of plane events). The internal multiples are still visible and are handled correctly in the generated pseudo VSP. It is important to notice that the generation of the pseudo VSP provides us with an unambiguous tie between seismic events on a time section and their geological interface in depth.

Figure 3.31 shows the 2-D shot record migrations for the shot with all multiples included (Figure 3.31a) and for the shot after surface-related multiple elimination has been applied to it (Figure 3.31b). Note that the internal multiples still cause false images in Figure 3.31b (see the arrow). Figure 3.32a shows the VSP modeling using an acoustic finite difference algorithm (v_z -registration including all multiples). The comparison of the one-way methods and the two-way methods reveals the presence of *internal multiples* in the generated pseudo VSP (in using two-way wave field extrapolation operators).

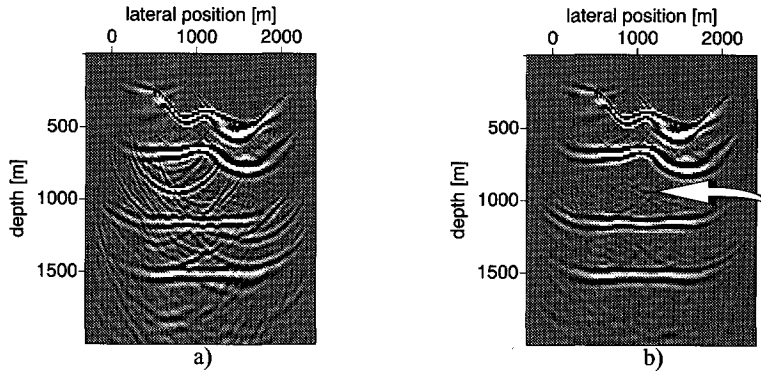


Figure 3.31 Shot record migration of a single shot record a) with all multiples included and b) after surface-related multiple elimination.

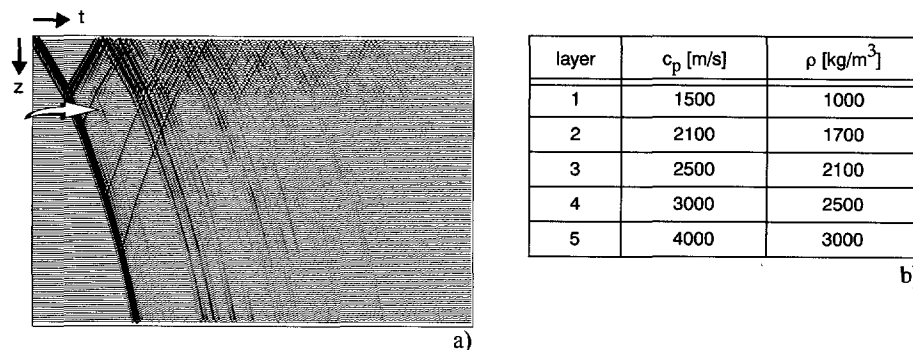


Figure 3.32 a) Finite difference modeling of the vertical zero-offset VSP (v_z) with the source at 1050m, b) acoustic layer parameters of the subsurface model.

3.6.4 Accuracy aspects

Next some remarks will be given on the accuracy of generated pseudo VSP data. Figure 3.33 shows the order of the errors appearing in a generated pseudo VSP (two-way wave field extrapolation, not exact macro model), after surface multiple elimination. It is shown that the errors in the “non-causal area” are equal to $O(R)$ and in the “causal area” are equal to $O(R^3)$. From this figure it follows that the wave fields in the VSP are handled correct in the “causal area” to $O(R^2)$, even when the macro model is not exact.

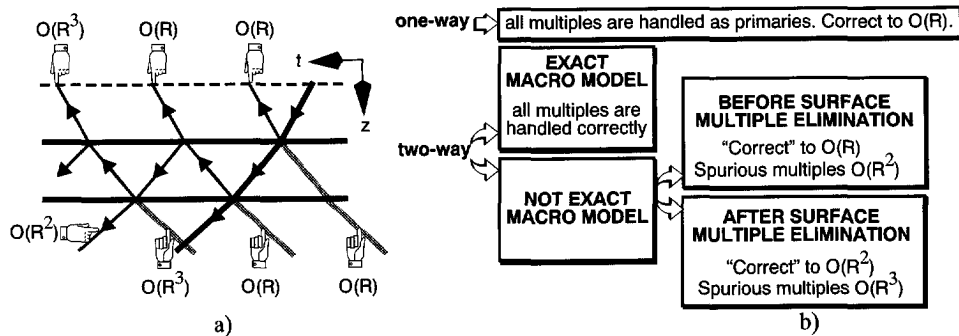
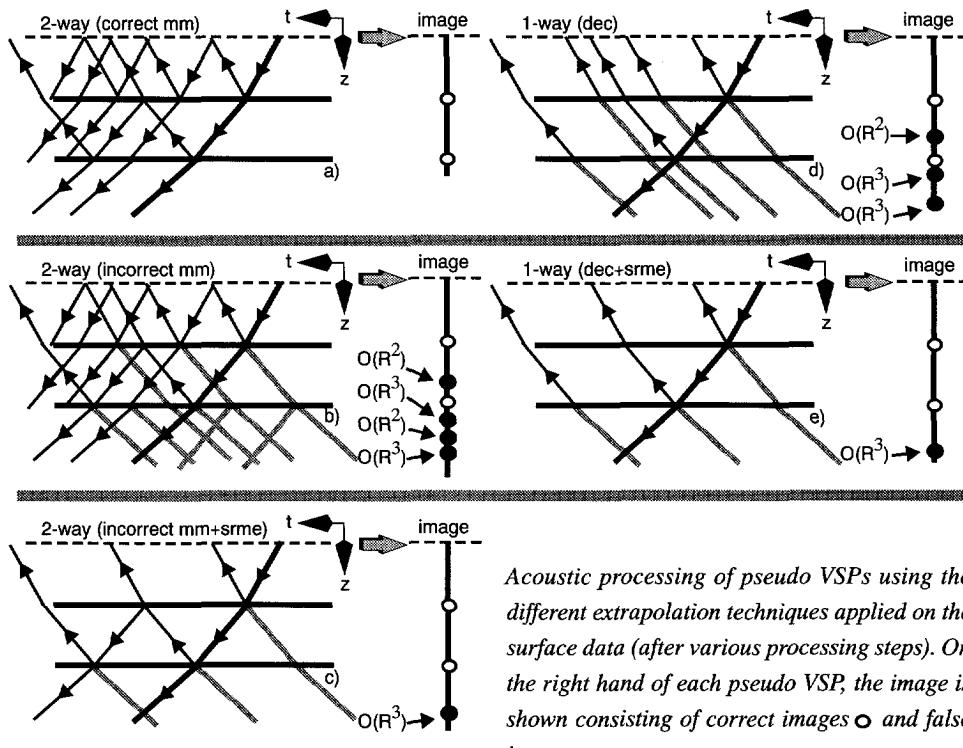


Figure 3.33 a) Illustration of the order of errors appearing in two-way pseudo VSP data (after surface related multiple elimination) using a wrong macro model. b) Illustration of the order of errors in different situations.

Structural information can be obtained both from surface data and from VSP data by seismic migration. The principle of migration consists of (Berkhout, 1984) : forward extrapolation of downgoing source wave field to a depth z_m , inverse extrapolation of detected upgoing wave fields to depth z_m and correlation at z_m . Figure 3.34 shows some schematic experiments with pseudo VSP data generated from the surface data in different situations. Figure 3.34a shows schematically the results of the two-way pseudo VSP with a correct macro model. This result with respect to the imaging is correct. Some minor macro model changes will introduce false images. The pseudo VSP generated with an incorrect model (after srme) results in a false image due to the incorrectly positioned internal multiple reflections. All multiples are handled as primaries in the *one-way* wave field extrapolation which introduce false images, but less than two-way. They can be removed before the downward extrapolation. In Figure 3.34e it is shown that false images may occur due to *internal* multiple reflections. Note that these errors are of the same order as in the situations using two-way schemes.



Acoustic processing of pseudo VSPs using the different extrapolation techniques applied on the surface data (after various processing steps). On the right hand of each pseudo VSP, the image is shown consisting of correct images \circ and false images \bullet .

Figure 3.34 a) 2-way pseudo VSP generated with correct macro model (mm), b) 2-way using an incorrect mm, c) 2-way pseudo VSP using an incorrect mm from surface data after surface-related multiple elimination (srme), d) 1-way pseudo VSP from surface data after decomposition (dec) of the total wave field into up- and downgoing waves and separate extrapolation of these and e) 1-way pseudo VSP from surface data after dec and srme.

3.6.5 Numerical example on internal multiples

The following example is a synthetic data example in which data is modeled through a 5 layered model as depicted in Figure 3.36e. The model parameters are given in Figure 3.35.

layer	c_p [m/s]	ρ [kg/m^3]
1	1500	1000
2	1900	1700
3	2500	2100
4	3500	2750
5	2500	2100

Figure 3.35 Parameters of the 5 layered acoustic model.

Figure 3.36a shows the integrated pseudo VSP and the shot record. The data does not contain surface-related multiples due to the absent of a free surface. The data have been modeled with a raytracing algorithm. The pseudo VSP data have been generated with the acoustic two-way wave field extrapolation algorithm.

In this example the objective is to trace the propagation paths of the internal multiples by studying the pseudo VSP data. The downgoing seabottom reflection (internal multiples generated by the two-way algorithm) can be clearly identified. Furthermore Figure 3.36d shows a blow up of Figure 3.36a for a better view on the internal multiples.

The different arrows in Figure 3.36d illustrate the internal multiples which are generated in the pseudo VSP data. It should be noticed that the non-causalities appearing prior to the direct wave have been zeroed (the source wave field is missing).

The pseudo VSP offers a very simple tool for understanding the wave propagation through the model and the paths the “internal” waves took to reach the surface. The data have been modeled also without internal multiples (data is displayed at the top of Figure 3.36b). The difference between the shot record (including the internal multiples) and the shot record (modeled without internal multiples) is depicted at the top of Figure 3.36c (the internal multiples).

The pseudo VSP data have been generated also from the shot records shown in the Figures 3.36b and 3.36c for a better understanding of the internal multiples. Figure 3.36c (lower part) shows the pseudo VSP data generated from the shot record (internal multiples) for a better understanding in which layers the internal multiples are generated. Note that the upgoing non-causal events are generated because of the missing downgoing wave fields.

Figures 3.36f, g and h show respectively the full prestack depth migration results of the shot records shown on the top of Figures 3.36a, b and c. Comparing the results, it can be clearly seen that the internal multiples cause “false” images in the full prestack depth migration results.

In this chapter, the algorithms for generating pseudo VSP data have been illustrated on different models using different wave field extrapolation operators. Furthermore, some analysis was performed on the behaviour of non-causal events which appeared in using two-way wave field extrapolation operators with erroneous models. From the examples in this chapter it is clear that by showing an Integrated Seismic Display (ISD), a fast interpretation may be obtained between events recorded in the surface seismic data and the corresponding reflectors in the subsurface via the pseudo VSP data generation and integration.

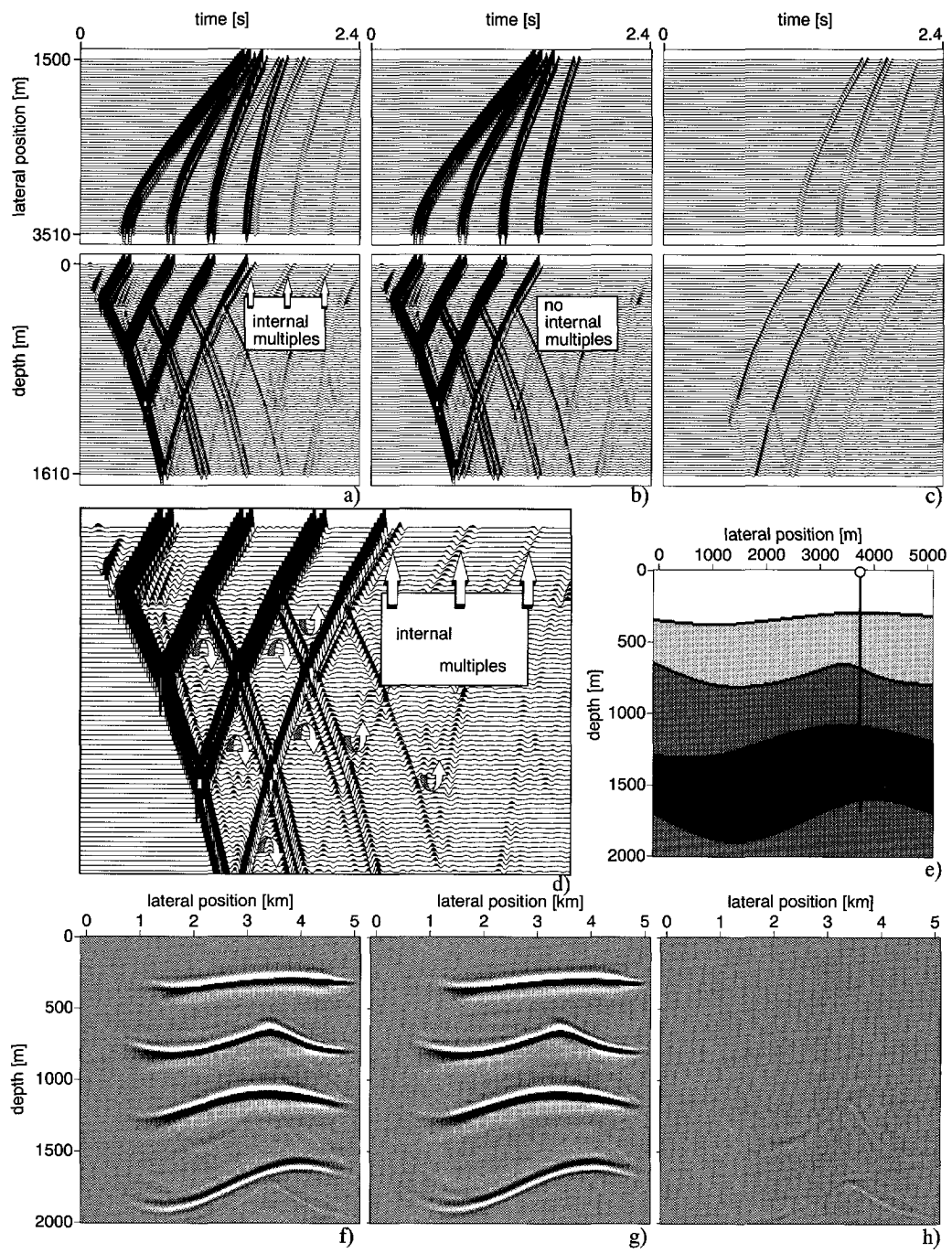


Figure 3.36 The influence of internal multiples in surface seismic data on the generation of pseudo VSP data and full prestack depth migrations.

Chapter 4

Pseudo VSP data and Common Focus Point technology

4.1 Introduction

In this chapter the relation between the construction of Common Focus Point (CFP) gathers and the generation of pseudo Vertical Seismic Profile (VSP) data is presented. The construction of CFP gathers (which represents the response of a synthesized areal source that aims at the illumination of one subsurface focus point) represents a numerical focusing process. The basic pseudo VSP algorithms on the other hand, as described in the previous chapter, transform the surface data into pseudo VSP data by downward wave field extrapolation. By showing that one trace of a CFP gather is equivalent to one trace from a pseudo VSP for a specific depth point, pseudo VSP data can also be derived from CFP gathers. Since the CFP technology is based on the one-way schemes, the pseudo VSP data shown in this chapter are also based on the one-way wave equation. In this chapter it will be shown how pseudo VSP data can be generated as function of the one-way time t' . Selecting one trace from the CFP gathers results finally in the generation of pseudo VSP data as function of the one-way time t' . It enables an easier comparison with truly recorded borehole data which can be also mapped into a “*two-way time t versus one-way time t' display*”. Similar to pseudo VSP data where the sources are at the surface, pseudo Crosswell Seismic (CWS) data can be constructed by simulating virtual sources in pseudo wells using the CFP technology. Reverse VSP (RVSP) and Crosswell Seismic (CWS) surveys are similar to VSP data in the sense that they record both upgoing and downgoing wave fields, but they differ with respect to source and receiver configurations.

Integration of multi-offset, common-well pseudo VSP data, forms so-called image gathers which will be discussed in the next chapter. In Chapter 6 multi-well, common-offset pseudo VSP data along seismic lines will illustrate the illumination of subsurface structures from various angles.

4.2 Common Focus Point technology

As discussed in the previous chapter, for the generation of pseudo VSP data it is essential to have a description of the propagation properties of the subsurface, high quality shot records (preferably multi-component) and the properties of the source. The nucleus of the pseudo VSP generation technique is based on downward extrapolation of a wave field at the surface into the subsurface. The validity of the pseudo VSP data depends on the description of the macro velocity model. If the macro model is correctly defined then the up- and downgoing waves in the VSP will intersect each other at the correct depth.

Berkhout and Rietveld (1994) presented a method for macro model estimation and verification based on controlled illumination. The method of controlled illumination generates areal shot records by combining the field shot records in such a way that the related areal source wave field has a pre-defined shape at a pre-defined position at the target. A very attractive way of controlled illumination is defined by a focusing operator (Berkhout, 1992). Synthesis with focusing operators yields so-called CFP gathers. The resulting CFP method involves a new way of depth migration, circumventing the estimation of the macro model prior to migration. In the first part of this chapter, the CFP method will be briefly described and its relation will be shown with the generation of pseudo VSP data. For a detailed description of the theory and the various applications of the CFP technology, the reader is referred to Berkhout (1997a and 1997b) and Thorbecke (1997).

The CFP method explains migration in terms of two separate focusing steps : *1)focusing in emission* and *2)focusing in detection*. In this way, the insight in the complex process of prestack migration will be significantly improved leading to a two-step formulation of prestack migration. Focusing in emission transforms shot records into CFP gathers. On the other hand, focusing in detection transforms CFP gathers into prestack migration results. The second step involves weighted stacking of the traces within each CFP gather and gives the double focusing result which results into a seismic image. The result of the first focusing step is suitable for velocity and AVO analysis. Note that the focusing in emission and focusing in detection can be performed in reverse order.

For obtaining the structure of the subsurface the propagation parts of the data have to be removed. In the WRW formulation this means that the downgoing propagation and upward

propagation are removed (*W-operators*) in order to obtain information on the reflectivity of the subsurface (*R*). In the previous chapter it was shown that the pseudo VSP data generation acts as an intermediate stage and illustrates how the downgoing source wave field approaches the upgoing reflected wave field and thus how an image is formed from surface seismic data. However, the CFP method is based on a synthesis process. This constitutes to a formulation of the migration process with the aid of the *focusing* concept instead of the concept of *wave field extrapolation*. In this chapter it will be shown that the pseudo VSP technology is closely related to the CFP technology.

4.2.1 Designing areal sources

Considering the forward *WRW* model as discussed in Chapter 2, the incident wave field at depth level z_m is given by :

$$\bar{S}^+(z_m) = W^+(z_m, z_0) \bar{S}^+(z_0). \quad (4.1)$$

In Equation (4.1), $W^+(z_m, z_0)$ represents the forward propagation information between the surface z_0 and depth level z_m . Vector $\bar{S}^+(z_0)$ represents one Fourier component of the downward traveling source wave field at the data acquisition surface $z=z_0$.

For a combination of experiments this leads to the following matrix equation :

$$S^+(z_m) = W^+(z_m, z_0) S^+(z_0). \quad (4.2)$$

Notice that one column of $S^+(z_0)$ contains the downgoing source wave field at the surface for one shot position. The corresponding column in $S^+(z_m)$ contains the wave field at depth level z_m for the same shot position.

For a combination of experiments the recorded wave field is given by :

$$P^-(z_0) = \sum_{m=1}^M [W^-(z_0, z_m) R^+(z_m) W^+(z_m, z_0)] S^+(z_0). \quad (4.3)$$

Here it is assumed that the surface-related multiples have been removed from the data and that the data have been decomposed into upgoing and downgoing wave fields. Similar as one column of the matrix $S^+(z_0)$ refers to the downgoing wave field at the surface z_0 for one shot record, the corresponding column in $P^-(z_0)$ contains the reflected wave field.

Considering the different shots to be Huygens' point sources, these sources can be combined to construct an areal source. The specific shape of the wave front is determined by relative amplitudes and timing (Berkhout 1992 and Rietveld 1995). For the construction of the areal

sources, a synthesis operator $\bar{\Gamma}(z_0)$ is necessary. The synthesis operator has to be designed such that it illuminates the target in a desired way. The synthesized wave field at the surface z_0 can be constructed from differently positioned local sources that are related to different experiments :

$$\bar{S}_{syn}^+(z_0) = S^+(z_0) \bar{\Gamma}(z_0). \quad (4.4)$$

The incident wave field due to the areal source at depth level z_m is found by applying the synthesis operator to both sides of Equation (4.2), yielding

$$\bar{S}_{syn}^+(z_m) = W^+(z_m, z_0) \bar{S}_{syn}^+(z_0). \quad (4.5)$$

Here $\bar{S}_{syn}^+(z_0)$ and $\bar{S}_{syn}^+(z_m)$ represent respectively the areal source wave field at the surface z_0 and at depth level z_m . Assuming that the individual dipole sources at z_0 are identical (on a regular grid) according to

$$S^+(z_0) = S(\omega) I, \quad (4.6)$$

the synthesized wave field at z_0 can be simplified to

$$\bar{S}_{syn}^+(z_0) = S(\omega) \bar{\Gamma}(z_0), \quad (4.7)$$

where $S(\omega)$ denotes the contribution of the wavelet in the data and I is the unity matrix. Using Equation (4.6), Equation (4.5) simplifies to :

$$\bar{S}_{syn}^+(z_m) = W^+(z_m, z_0) S(\omega) \bar{\Gamma}(z_0). \quad (4.8)$$

Applying the synthesis operator to both sides of Equation (4.3) results in the following expression of the areal shot record :

$$\bar{P}_{syn}^-(z_0) = \sum_{m=1}^M [W^-(z_0, z_m) R^+(z_m) W^+(z_m, z_0)] \bar{S}_{syn}^+(z_0), \quad (4.9)$$

$$\text{in which } \bar{P}_{syn}^-(z_0) = P^-(z_0) \bar{\Gamma}(z_0), \quad (4.10)$$

denotes the synthesized response due to the synthesized areal source. From Equation (4.10) it can be seen that each shot record (each column in $P^-(z_0)$) is multiplied with the corresponding value of the synthesis operator $\bar{\Gamma}(z_0)$. Hence, in the time domain, each shot record is convolved with one trace of the synthesis operator after which the resulting shot records are stacked per common position. The result is an *areal* shot record.

4.2.2 Controlled illumination

In the previous section it has been shown that many point source responses can be combined to construct one areal source response. The areal source wave field at the surface can be designed such that the incident source wave field at a specific target zone shows a predefined shape. This principle of controlled illumination (Rietveld, 1995) has various advantages in performing prestack depth migration in an efficient and accurate way. The necessary requirements are that one has to predefine areal source properties at a certain target depth level followed by a synthesis operator design for obtaining the requested wave field. The last step is performed by inverting Equation (4.8) :

$$\bar{\Gamma}(z_0) = \frac{\mathbf{F}^+(z_0, z_m) \bar{S}_{syn}^+(z_m)}{S(\omega)} \approx \frac{S^*(\omega) [\mathbf{W}^-(z_0, z_m)]^* \bar{S}_{syn}^+(z_m)}{|S(\omega)|^2 + \varepsilon^2}, \quad (4.11)$$

where $\mathbf{F}^+(z_0, z_m) = [\mathbf{W}^+(z_m, z_0)]^{-1} \approx [\mathbf{W}^-(z_0, z_m)]^*$ denotes the inverse of the downward propagation operator. The operator is approximated with the complex conjugate of the upward propagation operator, as proposed by Berkhou (1982) and Wapenaar and Berkhou (1989), to avoid instability of the inverse propagation operator in the evanescent field and to obtain accurate amplitudes.

The complex conjugate in the frequency domain denotes a time reversal in the time domain. Equation (4.11) shows that a synthesis operator can be designed at the surface z_0 from the desired wave field $\bar{S}_{syn}^+(z_m)$ at depth level z_m .

Remark

Controlled illumination can be described as a depth level oriented approach because the areal wave field is prescribed at a particular depth level. In the remaining part of this chapter, this approach is turned into a gridpoint oriented approach (target point). For convenience, in the use of focusing synthesized wave fields the subscript 'syn' will be replaced by a subscript i or j , indicating the lateral position of the focus point.

In addition, the term *synthesis operator* $\bar{\Gamma}(z_0)$ will be replaced by *focusing operator* $\bar{F}_j(z_0, z_m)$, where j denotes the lateral position of the focus point in emission (hence the focusing is source related).

If the focusing is receiver related, the operator $\bar{F}_i^\dagger(z_m, z_0)$ will be used, where i denotes the lateral position of the focus point in detection; the dagger \dagger denotes a row vector.

4.2.3 Focusing in emission

As described in the first part of this section, the CFP method can be described in two consecutive numerical focusing processes : 1)focusing in emission and 2)focusing in detection. In this subsection, the process of focusing in emission (yielding a CFP gather) is described and the next subsection discusses the process of focusing in detection (transforming each CFP gather into a single trace).

An initial focusing operator is necessary for the construction of the CFP gather from all available shot records. The constructed CFP gather represents a multi-offset response of the subsurface that is generated by a focusing source array at the surface. The CFP gather represents the registration of individual receivers at the surface with different positions. This process is called *focusing in emission*.

To achieve illumination of a focus point at z_m , the downgoing source wave field at z_m has to be prescribed to be zero for all the lateral position, except for the location of the focus point :

$$\bar{S}_j^+(z_m) = S(\omega) \bar{I}_j(z_m) = [0, 0, 0, \dots, 0, S(\omega), 0, 0, 0, \dots, 0]^T, \quad (4.12)$$

with $\bar{I}_j(z_m)$ a unit column vector with a 1 at the j^{th} position at depth z_m .

Hence the subscript j denotes the lateral position of the focus point (x_j, z_m) . (Note that the subscript *syn* is replaced by a subscript j). The focusing operator reads (analogous to Equation (4.11)) :

$$\bar{F}_j(z_0, z_m) = [W^-(z_0, z_m)]^* \bar{I}_j(z_m). \quad (4.13)$$

The areal source at the surface can be expressed by (analogous to Equation (4.8)):

$$\bar{S}_j^+(z_0) = S(\omega) [W^-(z_0, z_m)]^* \bar{I}_j(z_m). \quad (4.14)$$

Applying the focusing operator to both sides of Equation (4.3) (with $S^+(z_0) = S(\omega)I(z_m)$) yields :

$$\bar{P}_j^-(z_0, z_m) = \sum_{m=1}^M [W^-(z_0, z_m) R^+(z_m) W^+(z_m, z_0)] \bar{S}_j^+(z_0), \quad (4.15)$$

with $\bar{S}_j^+(z_0) = S(\omega) \bar{F}_j(z_0, z_m)$ and $\bar{P}_j^-(z_0) = P^-(z_0) \bar{F}_j(z_0, z_m)$ describing the areal source and the response of the areal source respectively.

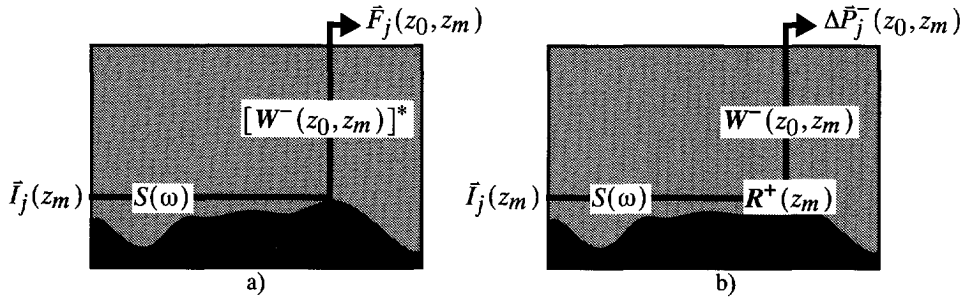


Figure 4.1 Illustration of focusing concept: a) design step for determining the focusing operator; b) visualization of the focus point response; only valid for reflecting level z_m

Applying Equation (4.14) to the right-hand side of Equation (4.15), omitting the summation, yields the response from a single depth level z_m due to the focusing areal source :

$$\Delta \bar{P}_j^-(z_0, z_m) = W^-(z_0, z_m) R^+(z_m) S(\omega) \bar{I}_j(z_m) = W^-(z_0, z_m) \bar{R}_j^+(z_m) S(\omega). \quad (4.16)$$

Here $\bar{P}_j^-(z_0, z_m)$ has been replaced by $\Delta \bar{P}_j^-(z_0, z_m)$ to indicate that the contribution of only one depth level is included : $\Delta \bar{P}_j^-(z_0, z_m)$ denotes the focus point response, representing the response at depth level z_0 due to a source at position x_j of depth level z_m . The reflectivity operator $\bar{R}_j^+(z_m)$ describes the directivity patterns of this source. It represents the j^{th} column of the reflectivity matrix $R^+(z_m)$, which contains the angle dependent reflectivity properties of depth point (x_j, z_m) .

Figure 4.1 shows a graphical illustration between the two separate steps of design and synthesis.

Addition of the out-of-focus responses to Equation (4.16) results into the CFP gather with the focus point at (x_j, z_m) :

$$\bar{P}_j^-(z_0, z_m) = W^-(z_0, z_m) \bar{R}_j^+(z_m) S(\omega) + \bar{\epsilon}_j^{\text{above}} + \bar{\epsilon}_j^{\text{below}}. \quad (4.17)$$

$\bar{\epsilon}_j^{\text{above}}$ and $\bar{\epsilon}_j^{\text{below}}$ represent respectively the contribution from above and below depth level z_m . The time-domain versions of $\bar{\epsilon}_j^{\text{above}}$ and $\bar{\epsilon}_j^{\text{below}}$ represent respectively reflections that arrive earlier and later than the involved focus point response.

4.2.4 Focusing in detection

In the previous subsection, a description has been given on the process of focusing in emission. As discussed, focusing in emission synthesizes areal sources that aim at the illumination of subsurface gridpoints. The involved synthesis process transforms the shot records into CFP gathers which defines an areal shot record that represents the response of a focusing source located on a single gridpoint. In a similar way, the process of focusing in detection can be formulated as synthesizing areal detectors to single subsurface gridpoint responses. The process of focusing in detection transforms CFP gathers into local prestack migration results. In other words, the constructed areal source, “illuminates” only one point in the subsurface and the areal detector “listens” only to the response of one gridpoint. The reader is referred to Berkhout (1997a and 1997b) and Thorbecke (1997), for a thorough description of the CFP method, its integration in prestack migration (in terms of double focusing), velocity estimation and Amplitude Versus Angle (AVA) analysis. Figure 4.2a demonstrates that the directivity of the virtual source is given by a focusing beam : three focusing source beams are used to illuminate one single gridpoint from left, centre and right. Note the significant changes in directivity of the related virtual ‘point’ sources at the focus point. The construction of a CFP focus point is illustrated in Figure 4.2b showing the illumination of a focus point by an areal source array and the detection of the same focus point by an areal detector array.

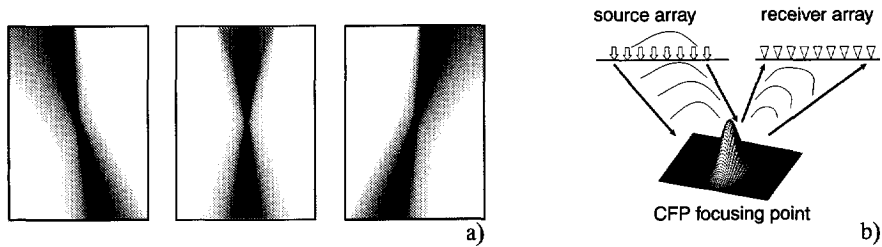


Figure 4.2 Focused illumination: a) three focusing source beams that illuminate one gridpoint from left, centre and right. b) The construction of a common focus point gather.

Similar to the construction of an areal source using a focusing operator, a focusing operator may be used for constructing an areal detector. The expression for this desired focusing operator can be formulated as :

$$\bar{F}_i^\dagger(z_m, z_0) = \bar{I}_i^\dagger(z_m) \bar{F}^-(z_m, z_0), \quad (4.18)$$

where $\bar{I}_i^\dagger(z_m)$ is a unit row vector with a 1 at the i^{th} position at depth z_m ; subscript i denotes the lateral position of the focus point in detection; the dagger \dagger denotes a row vector.

The operator $F^-(z_m, z_0)$ denotes the inverse of the propagation operator $W^-(z_0, z_m)$. Operator $F^-(z_m, z_0)$ may be approximated by the complex conjugate of the propagation operator $W^+(z_m, z_0)$ to avoid instability of the inverse propagation operator in the evanescent field :

$$F^-(z_m, z_0) = [W^-(z_0, z_m)]^{-1} \approx [W^+(z_m, z_0)]^* . \quad (4.19)$$

Substituting Equation (4.19) into Equation (4.18) yields :

$$\bar{F}_i^\dagger(z_m, z_0) = \bar{I}_i^\dagger(z_m) [W^+(z_m, z_0)]^* , \quad (4.20)$$

Note that the focusing operator for focusing in emission was a column vector (Equation (4.13)), while in this case the focusing operator represents a row vector.

Applying the focusing operator $\bar{F}_i^\dagger(z_m, z_0)$ to Equation (4.16) yields the double focusing result from one single depth level z_m :

$$\Delta P_{ij}(z_m) = \bar{F}_i^\dagger(z_m, z_0) \Delta \bar{P}_j^-(z_0, z_m) = \bar{I}_i^\dagger(z_m) \bar{R}_j^+(z_m) S(\omega) = R_{ij}(z_m) S(\omega) . \quad (4.21)$$

Considering the out-of-focus responses from all other depth levels gives :

$$P_{ij}(z_m) = R_{ij}(z_m) S(\omega) + \varepsilon_{ij}^{above} + \varepsilon_{ij}^{below} , \quad (4.22)$$

ε_{ij}^{above} denotes the contribution of reflectors above the focusing level, and ε_{ij}^{below} denotes the contribution of reflectors below the focusing level.

In the description of the prestack migration in terms of double focusing, both the angle averaged reflection coefficient and the angle-dependent reflectivity can be obtained very easily. If the focus points for the areal source and areal detector are at the same lateral position ($j=i$) then that situation is referred to as confocal focusing. The confocal focusing leads to angle averaged reflection coefficients, which are used in structural imaging. For situations where the focus points for the areal source and areal detector are not at the same lateral position, the angle dependent reflection coefficients may be obtained (bifocal focusing). The results may be used in the Amplitude Versus Angle (AVA) analysis. Table 2 gives a summary on *confocal* and *bifocal* focusing.

Table 2 Confocal and bifocal focusing (Berkhout, 1997a).

focusing	
confocal	source and detector array focus at the <i>same</i> location
	-> angle averaged reflection coefficients
	structural imaging
bifocal	source and detector array focus at <i>neighbouring</i> locations
	-> angle dependent reflection coefficients
	reservoir characterization

The use of CFP technology is illustrated in Figure 4.3. The model used in this illustration consists of a 2-D slice of the strike direction (dip direction slice $x=200$) from the SEG/EAGE 3-D Overthrust model. For a more detailed description on this model refer to Chapter 8. An initial focusing operator need to be calculated by positioning a point source at the desired gridpoint in the subsurface. In Figure 4.3, a focusing point has been chosen at lateral location $y=14000$ meters and depth $z=3200$ meters.

Next the source response has to be calculated at the surface. The focus point illumination and location of that specific point is illustrated in Figure 4.3b with snapshots, showing the wave fronts focusing into one single point. The focusing operator for this focus point illumination is displayed in Figure 4.3a. The snapshots have been generated performing a forward recursive downward depth extrapolation of the focusing operator through the model. Note that the focusing operator is displayed with one-way time t' .

Figure 4.4b shows some raypaths through the model for the focusing point experiment. Note that the aperture shown here is smaller than used in constructing the focusing operator. A one-way time t' is used in the focusing operator (this is the travel time from the secondary source to the receivers at the surface).

Figure 4.4a illustrates a focusing beams for the focus point illumination experiment. The beam is constructed by performing a forward recursive downward depth extrapolation of the focusing operator through the model and calculating for each depth level the energy of the wave field per lateral position.

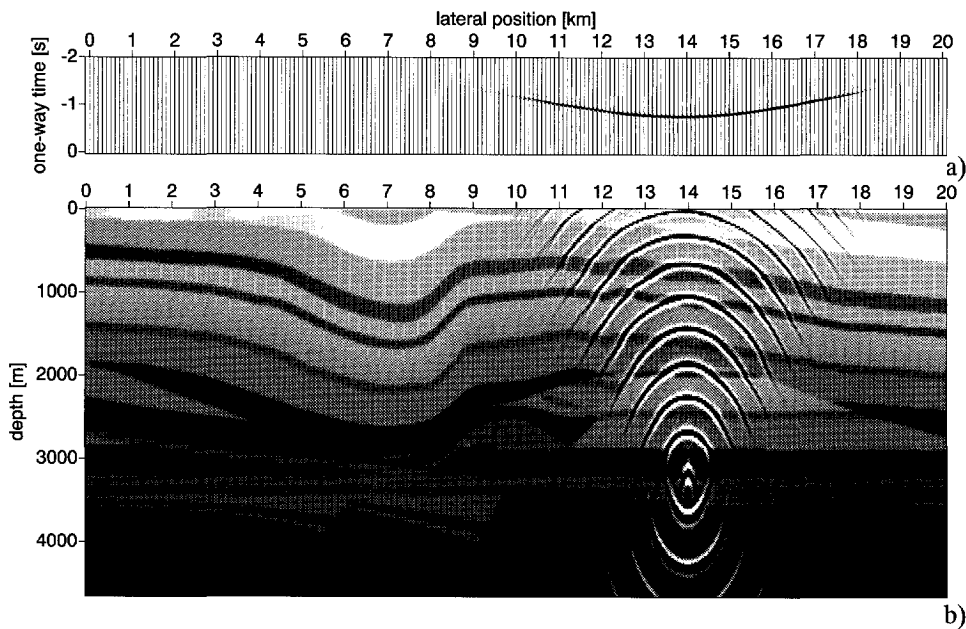


Figure 4.3 Illustration of focusing the recordings at the surface into one single focus point at depth (slice $x=200$ from the SEG/EAGE 3-D Overthrust model). The secondary source is located at $y=14000\text{m}, z=3200\text{m}$. The focusing operator is displayed in a).

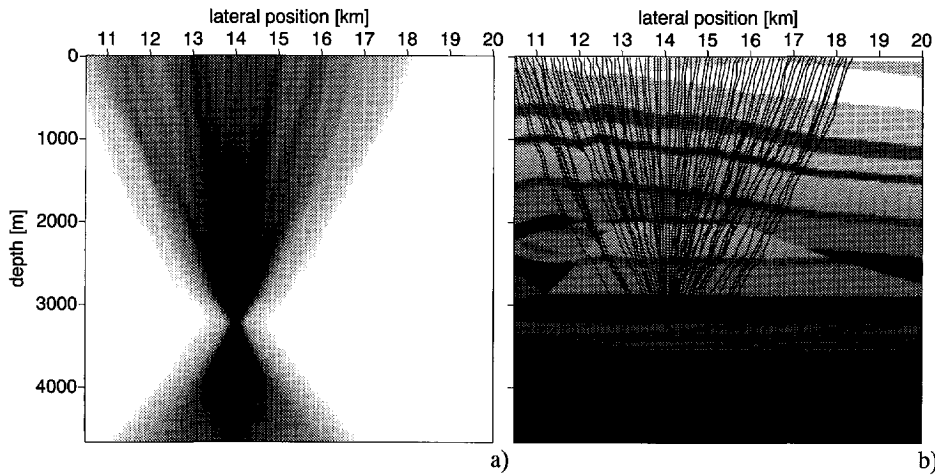


Figure 4.4 a) Focusing beam for the focus point illumination experiment.
b) Rays for the construction of the focusing operator.

4.3 Pseudo VSP generation in relation with Common Focus Point Technology

In the previous chapter it has been shown that the generation of pseudo VSP data is based on a *wave field extrapolation concept*. However, in the first part of this chapter, the CFP technology has been discussed which is based on a *wave field synthesis process*.

In CFP-based prestack migration the focusing operator is reapplied to the focus point response and is integrated to an image at the focus point (this means zero cross correlation). This is based on a formulation of the migration process in terms of a double focusing concept instead of the wave field extrapolation concepts. For the pseudo VSP this means that the direct wave field and the reflected wave fields are combined at their intersection, yielding an image at the focus point for one offset.

In this section it will be shown that both concepts of focusing and wave field extrapolation are interrelated by showing the generation of pseudo VSP data in relation with the construction of common focus point gathers. It will be shown that *one* trace of a CFP gather is equivalent to *one* trace of a pseudo VSP *for a specific depth point* chosen for focus point illumination. Since the CFP technology is based on the one-way wave equation, the pseudo VSP data generated in this chapter will be also based on the one-way equation for an optimal comparison.

For the generation of pseudo VSP data, the offset is *fixed* and the focus point is *variable*. By offset is meant here, the offset of the source position at the surface and the lateral position of the well head. In the CFP method, one point in depth is studied for a series of sources at the surface. That means that the offset is *variable* and the focus point is *fixed*.

Figure 4.5 shows the relation of the generation of pseudo VSP data and the construction of common focus points using the CFP technology. The schematic flow illustrates the main difference in the approach between both methods. Here it is shown that multi-source pseudo VSP data equals multi-focus CFP data.

The generation of pseudo VSP data from surface data can be performed in two ways: the pseudo VSP data can be generated from shot gathers by wave field extrapolation operators (left column of Figure 4.5). On the other hand, pseudo VSP data can be generated from receiver or shot gathers by focusing operators used for common focus point illumination. The result is a multi-focus CFP data (middle and right column of Figure 4.5).

As described in the previous section, the double focusing result for one depth level z_m consists of 2 steps:

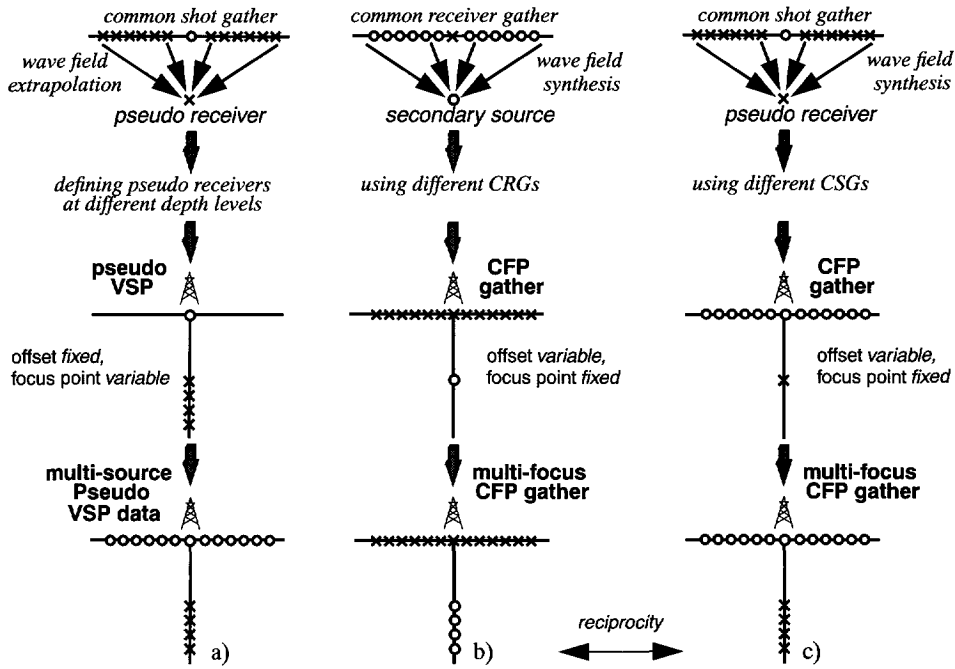


Figure 4.5 A multi-source pseudo VSP data equals a multi-focus CFP gather.

$$\text{focusing in } \underline{\text{emission}}: \bar{P}_j^-(z_0, z_m) = P^-(z_0) \bar{F}_j(z_0, z_m) \text{ and} \quad (4.23a)$$

$$\text{focusing in } \underline{\text{detection}}: P_{ij}(z_m) = \bar{F}_i^\dagger(z_m, z_0) \bar{P}_j^-(z_0, z_m). \quad (4.23a)$$

Figure 4.6 illustrates a visualization for the double focusing result. For $i=j$ (confocal focusing), the following equation holds for the estimation of the reflectivity :

$$\langle R_{ii} \rangle = \sum_{\omega} P_{ii}. \quad (4.24)$$

The generation of pseudo VSP data can analogous to Equations (4.23a) and (4.23a), be described in terms of focusing operators as :

$$\underline{\text{downgoing}}: P_{ik}^+(z_m, z_0) = \bar{I}_i^\dagger(z_m) W^+(z_m, z_0) \bar{P}_k^+(z_0) = \bar{W}_i^\dagger(z_m, z_0) \bar{P}_k^+(z_0) \quad (4.25a)$$

and

$$\underline{\text{upgoing waves}}: P_{ik}^-(z_m, z_0) = \bar{I}_i^\dagger(z_m) F^-(z_m, z_0) \bar{P}_k^-(z_0) = \bar{F}_i^\dagger(z_m, z_0) \bar{P}_k^-(z_0). \quad (4.25b)$$

The symbol i indicates the lateral position of the predefined well for the pseudo VSP data generated from a shot record with the shot at lateral location k . Remember that each type of well configuration can be designed in this way (e.g. a deviated well).

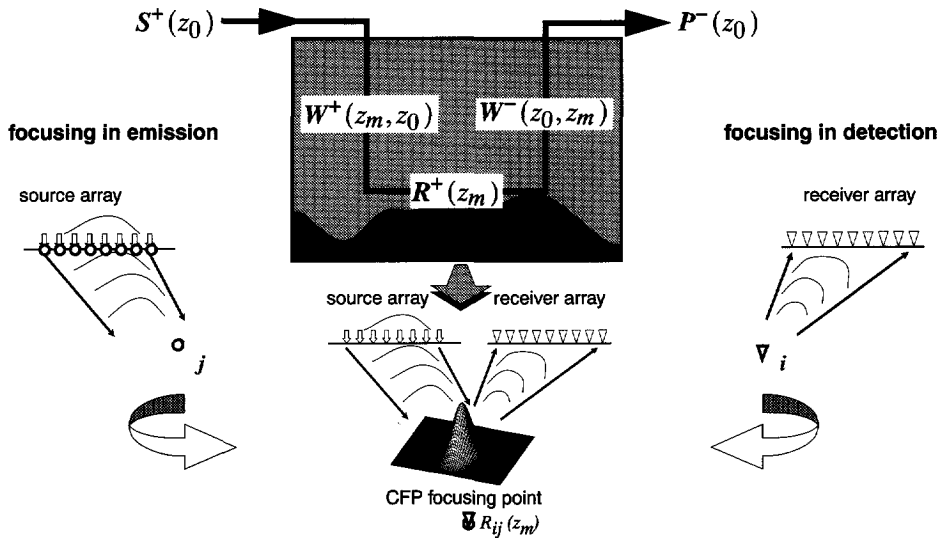


Figure 4.6 Visualization of the double focusing result for one reflecting depth level by combining source and receiver arrays. Note that in this case $i=j$.

This scheme can be performed recursively, as discussed in Chapter 3. In a pseudo VSP, the intersections of the upgoing wave fields and the downgoing source wave field are called the “image points”.

The reflectivity at an image point, generated from a shot record with shot location at k , can be theoretically written as :

$$\begin{aligned} \langle R_{ii,k}(z_m) \rangle &= \sum_{\omega} \frac{P_{ik}^-(z_m, z_0)}{P_{ik}^+(z_m, z_0)} \\ &= \sum_{\omega} \left[\bar{F}_i^\dagger(z_m, z_0) \bar{P}_k^-(z_0) \right] \left[\bar{W}_i^\dagger(z_m, z_0) \bar{P}_k^+(z_0) \right]^{-1}, \end{aligned} \quad (4.26)$$

where k represents the lateral shot location. The subscript ii denotes the focusing of the receivers to lateral location i (first index), and the focusing of the source information to lateral location i (second index) at depth level z_m . Note that the inverse term in Equation (4.26) can be approximated by the matched filter approach as discussed in Chapter 2. Note that for the full illumination of a “depth point”, all the other shot records contributing to the image point, have to be taken into account. The result (obtained by averaging all $\langle R_{ii,k} \rangle$) can then be written as $\langle R_{ii} \rangle$. The subscript k has been omitted to indicate the contribution of all the shot records recorded along the surface. Figure 4.7 shows an illustration for the source and receiver configurations. Figure 4.8 shows schematically the imaging with the aid of the pseudo VSP method and its comparison with the CFP method.

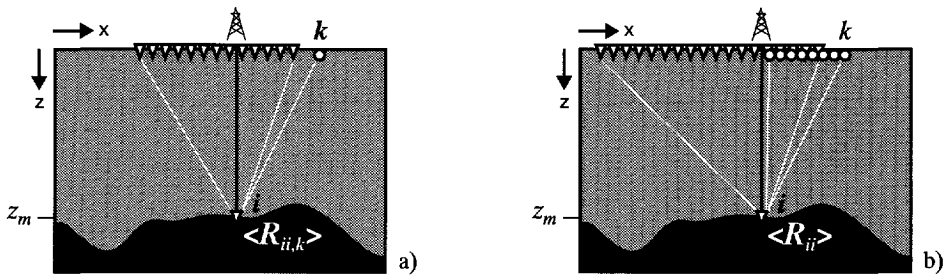


Figure 4.7 Illustration for the generation of pseudo VSP from the surface data : a) the extrapolated wave field at z_m is extracted at the lateral well location i , the source being located at lateral position k . b) The contributions from the different sources to the image point are added to obtain the reflectivity $\langle R_{ii} \rangle$ at z_m .

The main difference in using both approaches is that in the generation of pseudo VSP data, all the depths along a pseudo well are taken into account for a single shot record (the dataset is built up for one source-well configuration giving a limited illumination for all depth levels, see Figure 4.8a).

In a later stage, the contribution of all the sources at the surface have to be taken into account for an optimal illumination to the images at the well. In the CFP technology, *one single depth point* is studied for all the source contributions, and in a later stage, the algorithm is applied to other depth points (for a full image at the well the number of focus points need to be extended). The method of CFP imaging (see also Figure 4.8b) and illustrations have been extensively discussed by Thorbecke (1997).

In principle, the same result of imaging should be obtained with both methods, since the only difference is the sequence of processes applied to the surface data. From Figure 4.8 it is clear that the full images at the well are built up in different sequences.

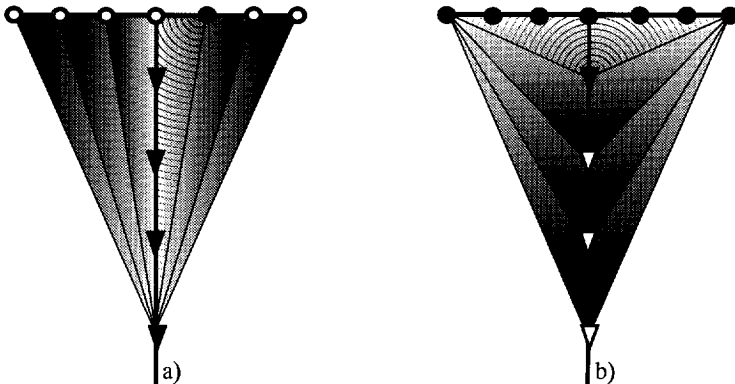


Figure 4.8 Imaging of data with the aid of the a) pseudo VSP method and b) CFP method.

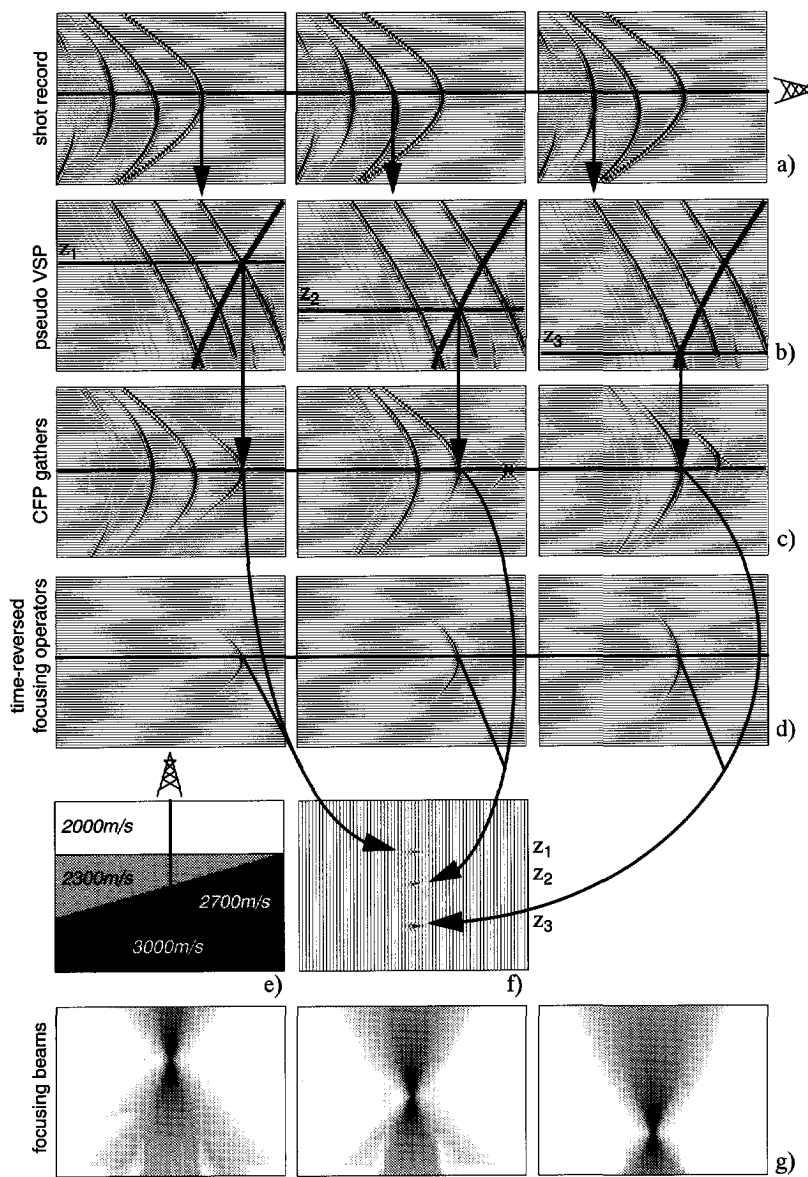


Figure 4.9 The construction of images around the three focus points by correlation of CFP gathers with the related focusing operators.

Figure 4.9 illustrates an example on the construction of three focus points at reflecting boundaries z_1 , z_2 and z_3 for the simple macro subsurface model depicted in Figure 4.9e. Figure 4.9a illustrates three times the same shot record which is transformed to zero-offset

pseudo VSP data (Figure 4.9b) and to the CFP gathers for the focusing points at the three boundaries z_1 , z_2 and z_3 respectively (Figure 4.9c).

The process of synthesizing converts the two-way times of the data (shot records) into a mixture of one- and two-way times. The time-reversed focusing operators, constructed from the correct macro model, are depicted in Figure 4.9d. Note that only the event in the CFP gather corresponding with the time-reversed focusing operator (focus point response) is located at the one-way time t' . It is important to notice that for a correct macro model the time-reversed focusing operator and the related focus point response have equal travel times. Figure 4.9f visualizes the migrated images around the three focus points. Finally in 4.9g the three focusing beams are illustrated for the focused points in the construction of the CFP gathers.

Figure 4.10a illustrates the pseudo VSP generated at 150m offset for the correct macro model. The CFP is constructed for a focusing point on the first reflector ($z=z_1$). Note the correspondence between the pseudo VSP data and the CFP gather: the trace in the pseudo VSP at z_1 is equal to the trace from the CFP gather at the offset of 150m. In Figure 4.10 the pseudo VSP, CFP gather and migrated section were constructed with the correct macro model. It can be clearly seen in the migrated section that a focus point image is constructed at the first reflector (Figure 4.10c). Note that the traveltimes of the focus point response (Figure 4.10b) and the time-reversed focusing operator (Figure 4.10d) are equal. In case of an erroneous focusing operator (due to a wrong macro model) the traveltimes between the focus point response and the time-reversed focusing operator would not be equal and would show a mismatch. This can be illustrated by the following example (Figure 4.11).

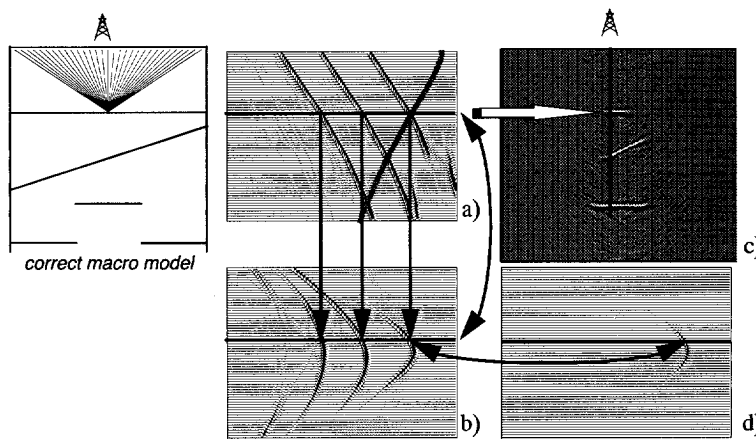


Figure 4.10 a) 150m offset pseudo VSP data in relation with the b) CFP gather, c) migrated depth section (1 shot) and d) time-reversed focusing operator.

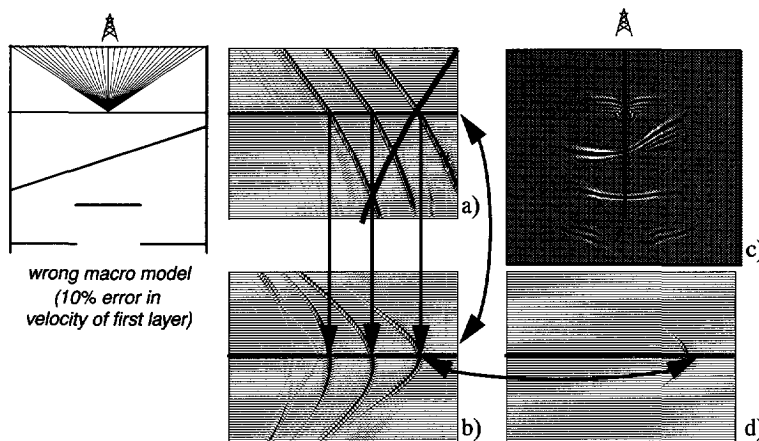


Figure 4.11 a)Zero offset pseudo VSP data in relation with the b)CFP gather, c)migrated depth section and d)time-reversed focusing operator.

An error in the macro model is made in the propagation velocity of the first layer: 10% lower than the original propagation velocity. It can be clearly seen in the pseudo VSP data (Figure 4.11a) that there is a mismatch at the first reflector: the intersection of the upgoing and downgoing waves takes place on a smaller depth than the reflecting boundary. This mismatch can also be clearly identified in the CFP gather: the focus point response in the CFP gather (Figure 4.11b) does not coincide with the time-reversed focusing operator (Figure 4.11d). Of course, the effect of the erroneous focusing operator and erroneously positioned focus point response can be also seen in the migrated section (see Figure 4.11c): an erroneous macro model does not result into a correct focus point image. It can be shown that the correct focusing operator is situated between the erroneous time-reversed focusing operator and the erroneous focus point response.

The following example illustrates in a step by step approach, the relation between the construction of a CFP gather and the generation of pseudo VSP data. The used model in this example is the “syncline model” (Figure 4.12) which will be used also in Chapter 5 and 6. The numerical data was modeled by forward modeling with an acoustic finite difference algorithm. The model consists of four interfaces and one diffractor at $x=750m$, $z=1000m$. The model includes a negative reflection coefficient for the wedge located in the right part of the model. The dipole source used in the modeling of the data is given by a Ricker wavelet with a peak frequency of 26.4Hz. The numerical data is modeled with a fixed acquisition spread and 512 time samples. The lateral shot distance between successive shot points (201 shot records each with 201 receivers) $\Delta x=15m$. The source locations are defined at each successive receiver location.

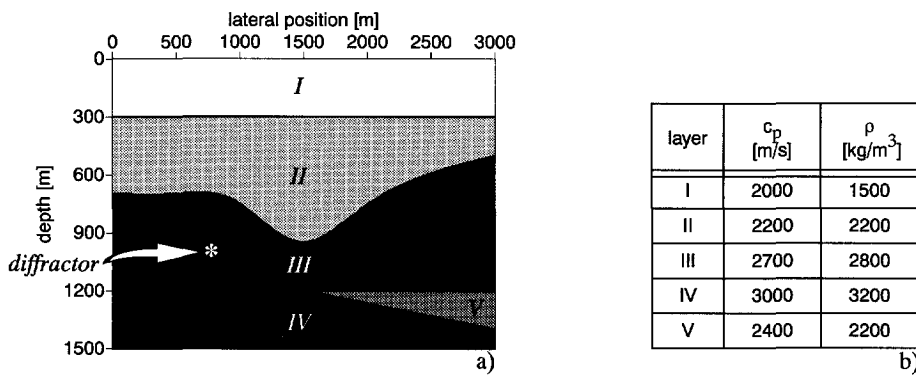


Figure 4.12 a) Subsurface "syncline" model and b) parameters of the model.

Figure 4.13 (top) shows five shots from the 201 modeled shot records along the line. The data have been modeled without surface-related multiples. The source positions for the shots are respectively 0m, 750m, 1500m, 2250m and 3000m.

In Figure 4.13 (middle-left) the zero offset section (containing surface-related and internal multiples) is illustrated in comparison with the zero-offset section (without surface-related multiples). A deghosting have been performed on the data with all multiples included, to make an optimal comparison possible with the data without surface-related multiples. The four primary reflections are indicated with an arrow. At the bottom of Figure 4.13, the image results are shown after full prestack depth migration. The left panel shows the migration result where the data contained all multiples and the right panel shows the result of the migration applied on the data which was modeled without surface-related multiples. The recursive depth migration is carried out with the same *WLSQ* extrapolation operators as used in the generation of pseudo VSP data. The construction of these operators is discussed in Appendix B.

The configuration that is used in this example is a walkaway VSP configuration where a fixed well is chosen and the sources are moved along the surface away from the well. The well is located at 1650m (see for the model Figure 4.12).

The various sources in this experiment are ranging from 900m to 2400m (largest offset : 750m).

Figure 4.14 shows the raypaths for the above described experiment with the shot locations respectively at 1050m, 1350m, 1650m, 1950m and 2250m and the well is located at 1650m.

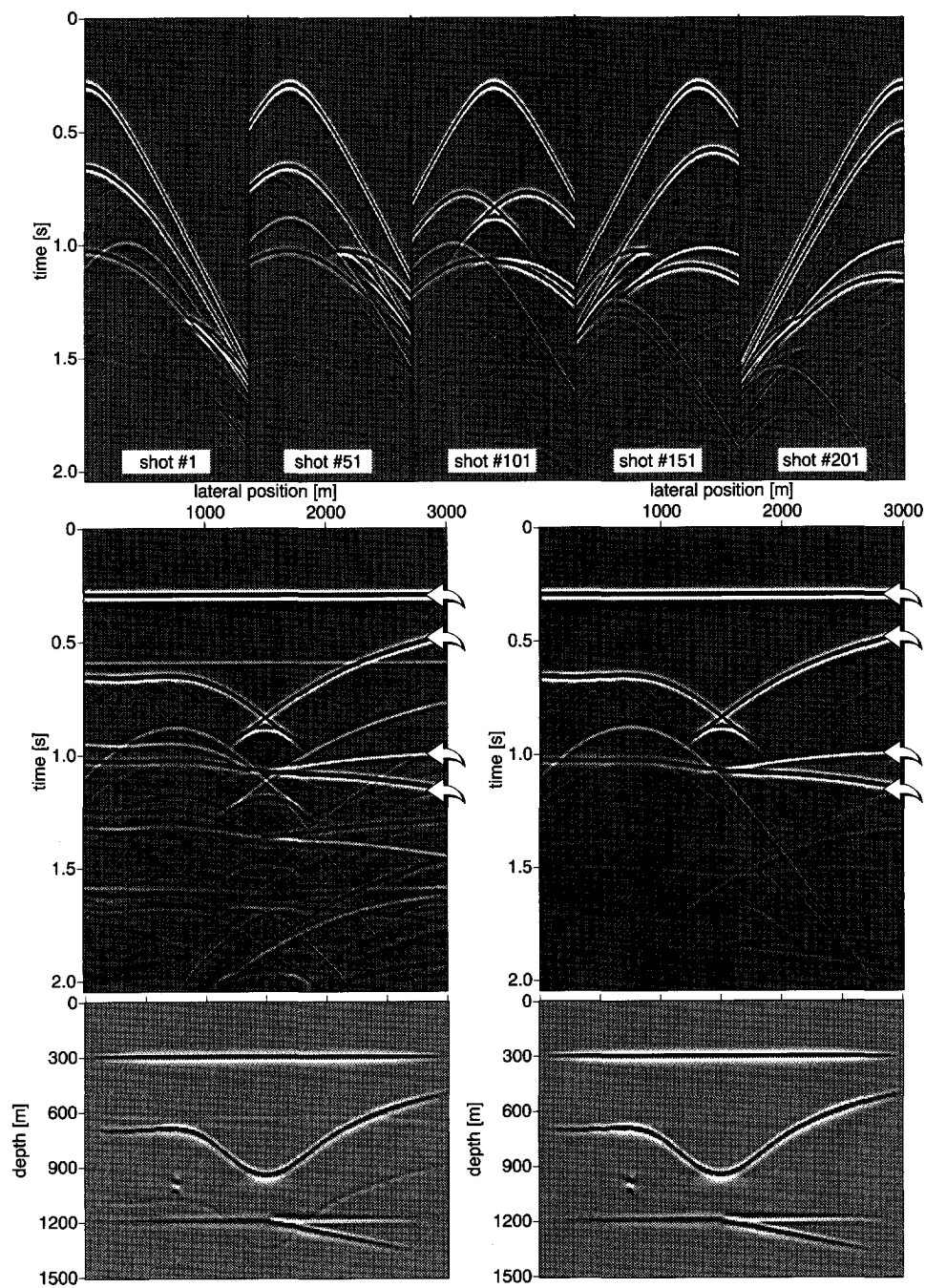


Figure 4.13 5 shots without surface-related multiples (top), zero offset data (middle) and prestack migration depth result (bottom) (data with and without surface-related multiples).

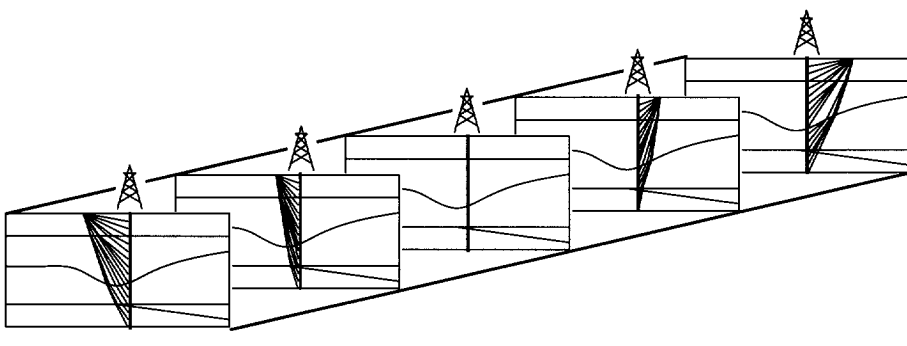


Figure 4.14 Raypaths for the experiment, well at 1650m, sources respectively at 1050m, 1350m, 1650m, 1950m and 2250m.

If the pseudo VSP data are generated from the shots (without surface-related multiples), a series of pseudo walkaway VSP data is obtained which form together a cube of data. Figure 4.15 shows 2 views of the 3-D volume of data obtained in this way. This experiment shows clearly the relation of the generation of pseudo VSP data with the construction of CFP data. The pseudo VSP data have been generated using the one-way wave field extrapolation operators (this in relation with the construction of CFP gathers which are also based on the one-way wave equation). Each depth slice through this volume represents a CFP gather. The upper layer slice represents a common receiver gather. Note that the intersections in the pseudo VSP data of the source wave field and the reflected wave field map the unmigrated events from the surface into depth images. It can be clearly seen that the multi-valued bowtie event (indicated by a pointer in upper picture) which is visible at the upper layer (common receiver gather) turns into single-valued imaged events at the reflectors.

This volume has been built by a series of walkaway pseudo VSP data and each depth slice represents a CFP gather. In a similar way, this volume can be constructed using CFP gathers for focusing in detection. The various focus points are located at the different depth levels in the subsurface. Selection of one lateral position from the constructed volume results into a pseudo VSP data for that lateral position. The figures at the right of Figure 4.15 show that offset VSP data can be obtained by taking slices from the cube of data at various lateral positions. Similarly CFP gathers can be obtained by taking slices at different z levels.

Figure 4.16 shows the connection of the shot record (shot position at 1650m) and the CFP gathers for the three layer boundaries z_1 , z_2 and z_3 . The focus points for the CFP gathers are positioned at the intersection of the pseudo well with the 3 boundaries. The pseudo VSP data are generated at 450m offset with respect to the shot location. The left part of each panel shows the shot gather, the middle part of each panel shows the pseudo VSP generated from the shot record to respectively depth $z_1=300m$, $z_2=945m$ and $z_3=1200m$.

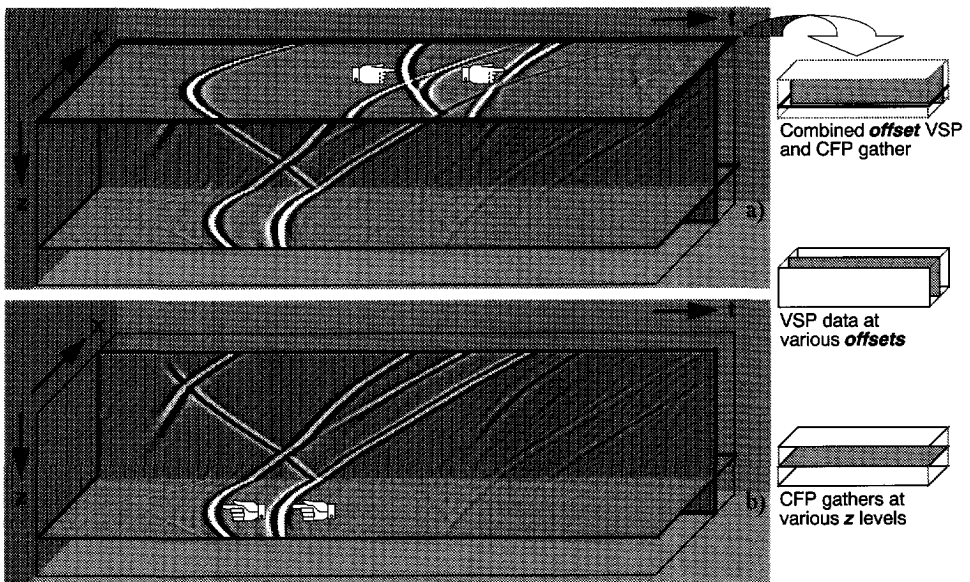


Figure 4.15 Slices of the 3-D volume. The 3-D volume consists of a series of walkaway VSP data. The VSP data are generated from modeled data without surface-related multiples.

z_1 , z_2 and z_3 represent respectively the depth of boundary 1, 2 and 3. The right part of each panel shows the three CFP gathers (starting with the trace at the position of the shot record at the surface z_0). The pseudo VSP data shows that only one branch of the triplication in the

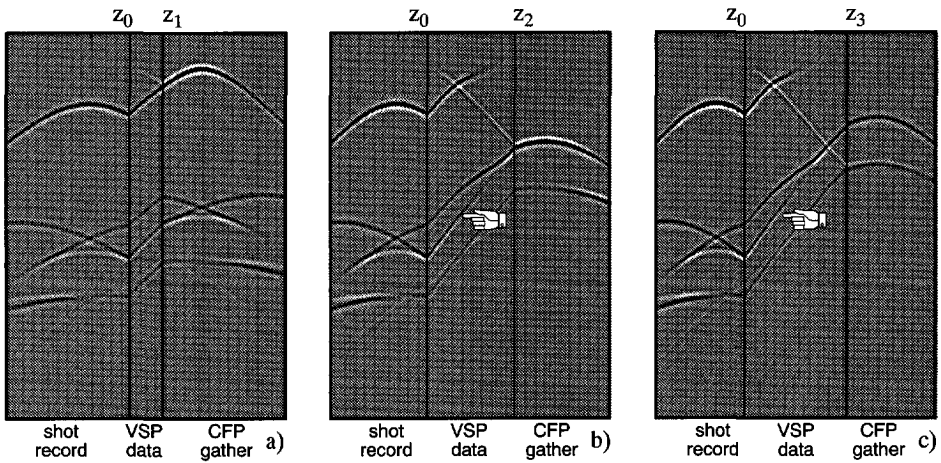


Figure 4.16 From shot record to CFP gathers via the pseudo VSP data : a) pseudo VSP data generated at 450m offset from depth z_0 to $z_1=300m$, b) same offset VSP from z_0 to $z_2=945m$ and c) same offset VSP from z_0 to $z_3=1200m$. Note the imaging of the data from the surface to their reflection points at the boundaries at depth levels z_1 , z_2 and z_3 .

shot record is propagated to the depth position of the focus point. The triplication originates from the syncline structure in the model. The pseudo VSP acts here as a tool to distinguish which events are reflections from aside the well and which reflections cross the pseudo well. The pointer in Figure 4.16b and c shows that the event is fading away. These events come from aside the syncline structure and are slowly losing their energy for the deeper depth levels. The event in the pseudo VSP data which travels from the top left to the right, represents the first break crossing the 3 focusing points at z_1 , z_2 and z_3 . The events appearing above the first break are non-causal events, which are also observed in the CFP gathers. In other words Figure 4.16 shows the link of the surface data with the CFP gathers via the pseudo VSP data. The pseudo VSP data gives insight in the illumination properties of the construction of CFP gathers.

4.4 Pseudo VSP data in one-way time : (t, t') display

In this section a method is presented for a new display of pseudo VSP data : data display as a function of the one-way time t' instead of depth z . The presentation of the pseudo VSP data in one-way time t' allows an easier way of identifying events. The pseudo VSP display as function of t' illustrates the propagation paths of waves through a medium as function of the one-way time t' . The pseudo VSP data (t, t') can be constructed using the CFP method or by a method as described in Section 4.5. Figure 4.17 shows a diagram for the construction of pseudo VSP data (t, t') . For subsequent depth levels (crossing a pseudo well) different focus points are selected. The corresponding time-reversed focusing operators are calculated. For regular depth levels, an irregular depth step in the one-way time $\Delta t'$ is created. The time-reversed focusing operators are then interpolated for every one-way equal time step $\Delta t'$. The interpolated operators are used for the construction of the corresponding CFP gathers. In this way a series of CFP gathers is constructed for increasing one-way time steps $\Delta t'$. According to the well geometry, a trace-selection is made from each CFP gather and in this way the upgoing wave field in the pseudo VSP (t, t') is constructed. Similarly, according to the borehole/detector configuration, a trace-selection is made from each time-reversed focusing operator resulting in the downgoing wave field of the pseudo VSP (t, t') . Addition of the upgoing and the downgoing wave field results finally in the total pseudo VSP (t, t') .

In the following example, a pseudo VSP (t, z) data is generated from a shot record along the seismic line. The data was provided by Mobil Exploration and Producing Technical Center Dallas, U.S.A.. In addition, this pseudo VSP (t, z) data is transformed to pseudo VSP (t, t') data display. Figure 4.18 shows respectively a shot after surface-related multiple elimination, the pseudo VSP generated (t, z) data and the pseudo (t, t') VSP data. The sampling in the one-way time direction $\Delta t'$ is chosen the same as for the two-way time sampling Δt .

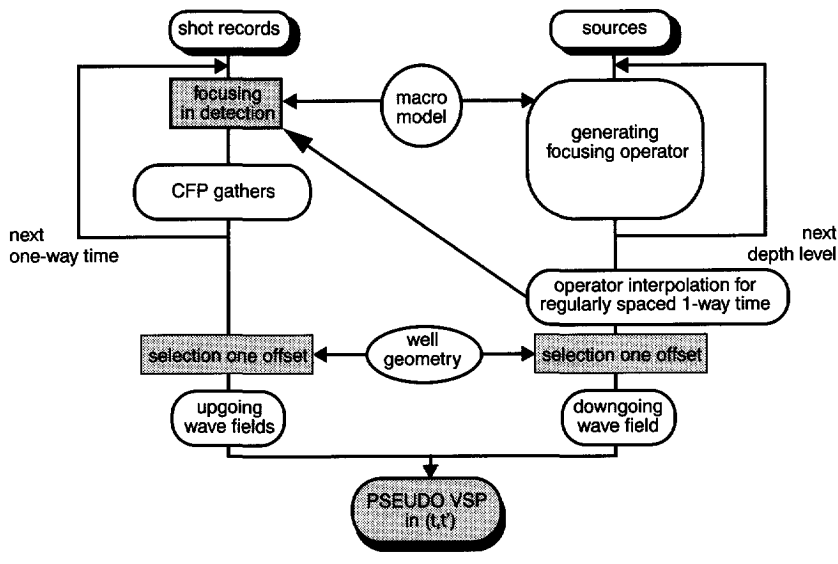


Figure 4.17 Diagram showing the construction of pseudo VSP (t,t') data.

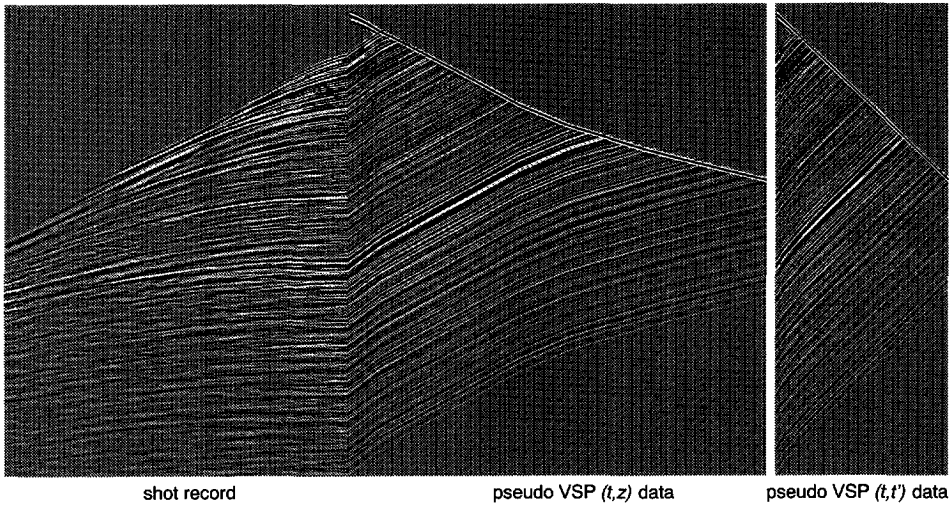


Figure 4.18 From surface shot record data to pseudo VSP (t,z) data and to pseudo VSP (t,t') data.

For the generation of the pseudo VSP data, one-way operators were used. The pseudo VSP data has been generated using the scheme shown in Figure 4.17. Note that the non-causal events before the first break have been zeroed. The pseudo VSP (t,t') can also be constructed by stretching the pseudo VSP (t,z) along the first break. This method will be described in Section 4.5. The mapping of the VSP data (t,z) into a display VSP (t,t') data has the advantage that additional processes can be carried out at the reflection points.

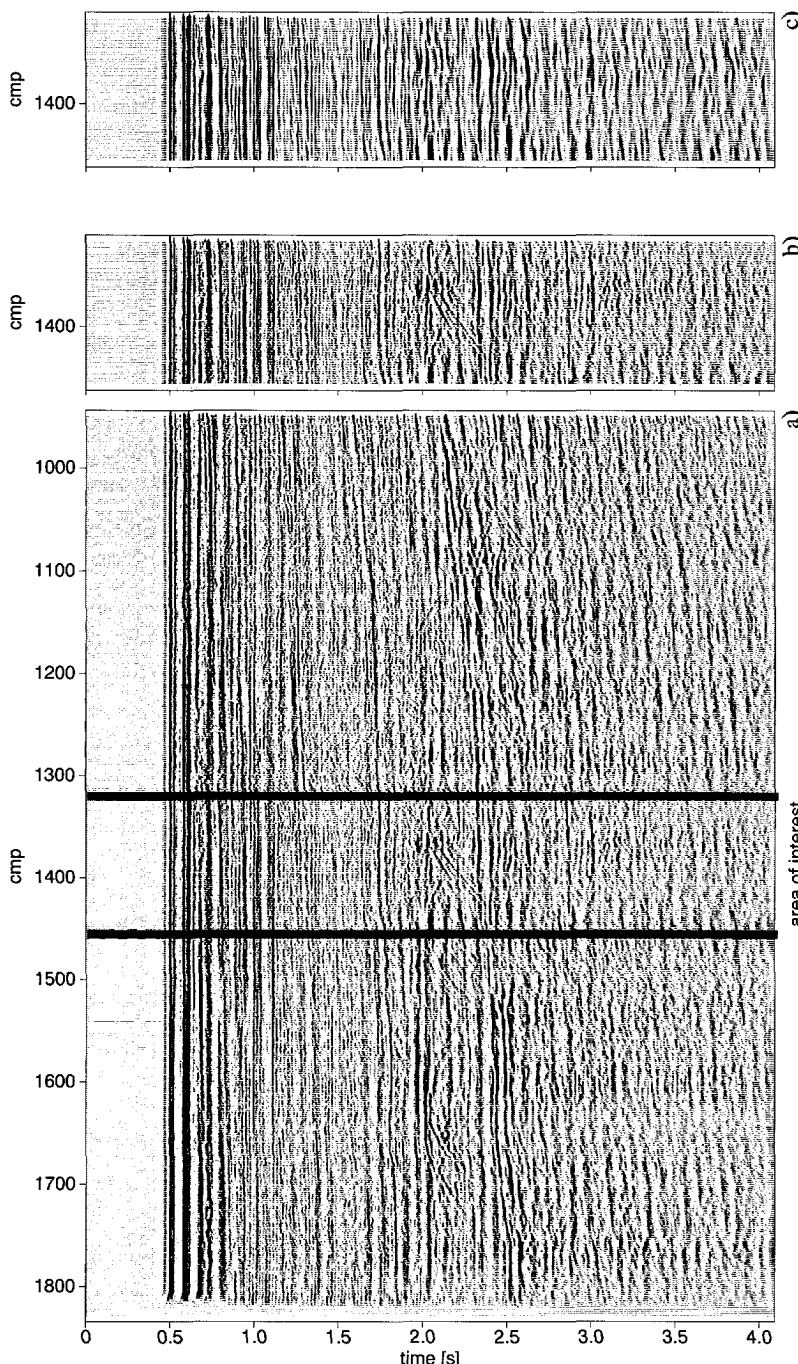


Figure 4.19 a)Zero-offset section (data was provided by Mobil Exploration and Producing Technical Center Dallas U.S.A.),
b)zero-offset section for area of interest and c)result of preprocessing and single-fold imaging in (t, t') .

Such a process is illustrated in Figure 4.19. Figure 4.19a shows the zero-offset section along the Mobil seismic marine line with a part indicated as “area of interest”. The area of interest

is also depicted in Figure 4.19b. Figure 4.19c shows the result of preprocessing and single-fold imaging in (t, t') . The shot records have been mapped into zero-offset pseudo VSP (t, t') data for a vertical well and the data is stacked at the reflection points along 45° and in this way all the events which have not traveled along the zero-offset are suppressed. Note that the section depicted in Figure 4.19c is a one-way time t' display and the data is single-fold imaged. This is in comparison with Figure 4.19b where the unmigrated data is displayed as function of the two-way time t .

4.5 Real VSP data in one-way time : (t, t') display

In this section a method is proposed for a new display of real VSP data : in t' (similar as discussed for the pseudo VSP data in the previous section). Figure 4.20 illustrates the transformation of VSP data from (t, z) to (t, t') using the first break as stretching function. An important application of this transform is the identification of waves traveling through a medium with a different velocity profile. The events which have traveled along the same ray-paths as the first break (borehole/detector configuration) will be aligned at an angle of 45° (for sample rate $\Delta t' = \Delta t$). All other events that traveled along different rays will not be aligned. The aligned events (with the first break) can then easily be removed. Finally all other events including 3-D effects will remain which can be tied to the surface seismic data.

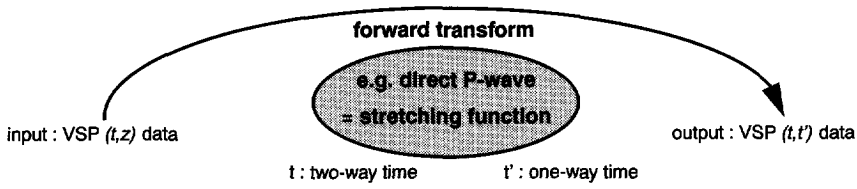


Figure 4.20 Transformation of VSP data from the (t, z) display into the (t, t') display.

4.5.1 Marine data example

The objective is to transform the VSP display which is generally a display as function of depth z into a display which is function of the one-way time t' . Figure 4.21 illustrates the transformation from the VSP (t, z) display to the VSP (t, t') on real data. The dataset was obtained from Mobil Exploration and Producing Technical Center Dallas U.S.A., containing marine seismic data and well log measurements. Figure 4.21a shows a part of the pre-processed VSP data at well B (VSP along the seismic line). Note that the two-way time axis t is replaced by the VSP time (t_{VSP}). For a more detailed description of the dataset and the processing on this dataset the reader is referred to Chapter 7 and Appendix C. Figure 4.21b shows the reorganization of the data as function of the one-way time t' .

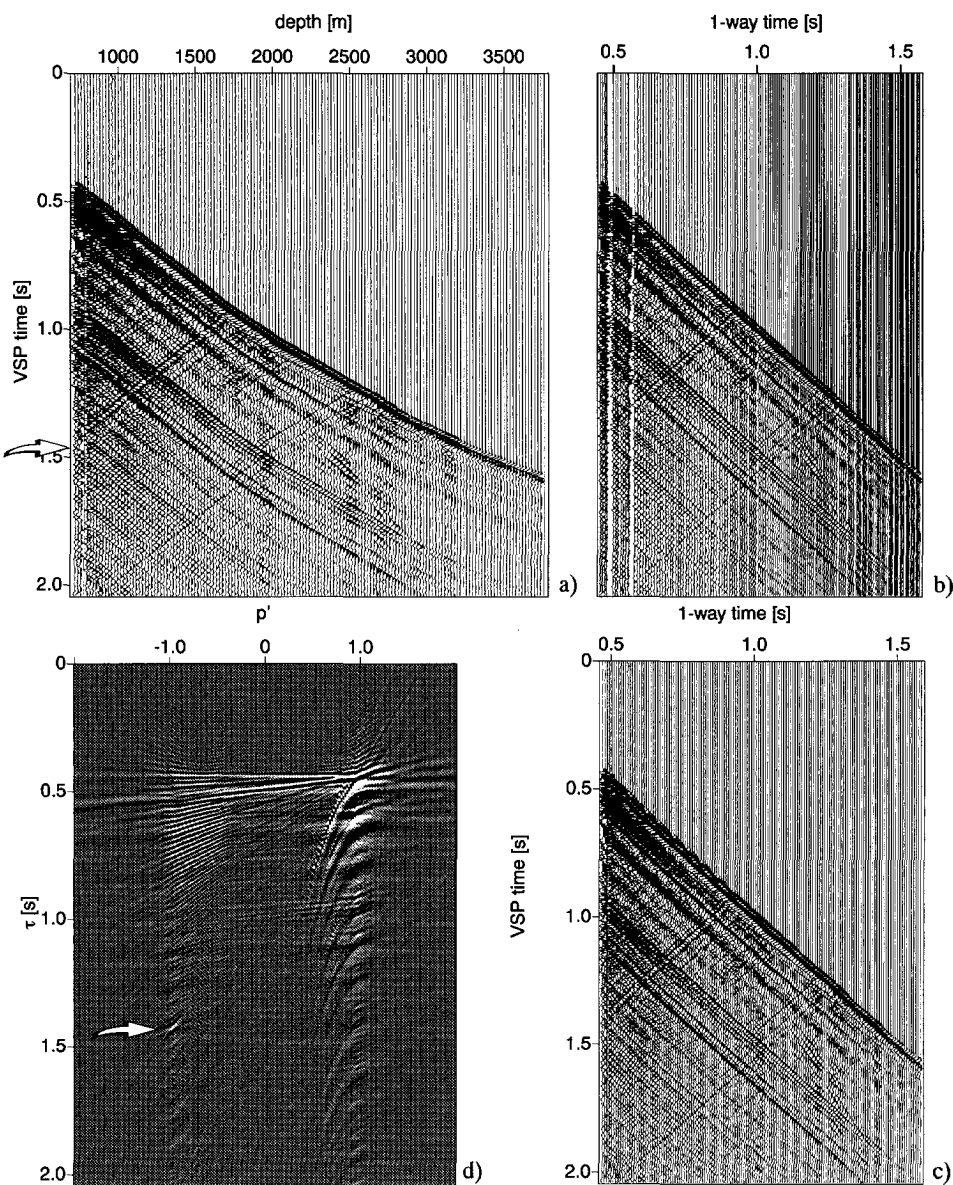


Figure 4.21 From depth to one-way time: a) preprocessed marine VSP data and b) after mapping to one-way time axis, c) VSP (t_{VSP}, t') regularized in subsequent one-way time steps $\Delta t'$ and d) linear Radon transform of Figure 4.21c.

As noticed, the spacing in t' is irregular. The regularized VSP (t_{VSP}, t') after interpolation is displayed in Figure 4.21c. Furthermore a linear Radon transform of Figure 4.21c is depicted in Figure 4.21d where the arrow indicates the primary reflection in the negative p' range.

4.5.2 Land data example (I)

In the following, an example is illustrated on a land dataset. The example presented here shows the application of the VSP (t, t') display in the suppression of S -wave modes in VSP data. Figure 4.22 shows the scheme which is used, for the forward and backward transform in the suppression of the S -waves. Notice that with this scheme each unwanted event can be removed easily.

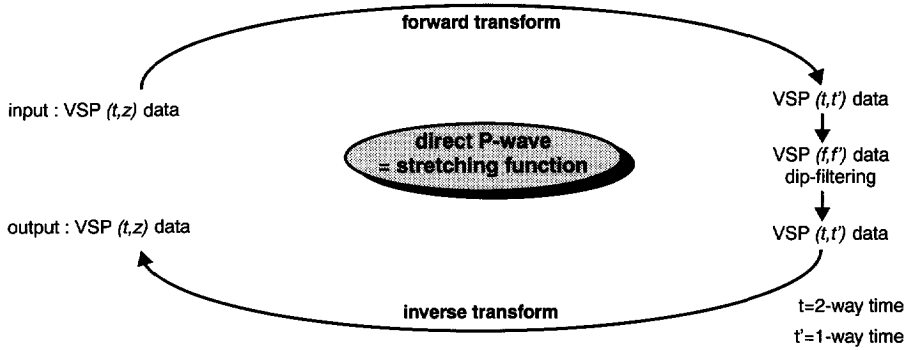


Figure 4.22 Scheme for the suppression of S -wave modes in real VSP data.

Figure 4.23a shows a preprocessed offset VSP land data with the P - and S -waves visible. The VSP data was recorded in the Middle East. This VSP is also displayed in the VSP (t_{VSP}, t') display (see Figure 4.23b). The (t_{VSP}, t') display is obtained by picking the first break (direct P -wave), stretching the data along the first break pick and interpolating the missing times t' . Notice that the sample rate for t' is chosen the same as the sample rate for the VSP time t_{VSP} (direct P -wave crosses the t_{VSP} axis at an angle of 45°). Figure 4.23d and e show the result of the VSP data (t_{VSP}, z) and (t_{VSP}, t') after transformation to respectively the (f, k) and (f, f') domain. It can be clearly seen from Figure 4.23e how the P -wave energy is aligned. Furthermore it can be seen from this picture that the S -wave is also aligned but in an other angle. This (f, f') plot gives also a clear indication on the behaviour of the Poisson's ratio through a medium. A constant Poisson's ratio through a model should also indicate a sharp S -wave image line in the (f, f') plot (in case stretching is applied on the P -wave first break velocity profile). One could describe it as follows: the quality of the focus of S -waves in the (f, f') plot gives an indication on the behaviour of the Poisson's ratio through a medium. In the following step, the data has been filtered in the (f, f') plot along the P -wave curve (dip filter) and transformed back to the (t_{VSP}, t') display. The result is shown in Figure 4.23c. From this picture it can be clearly seen that the S -wave energy is suppressed. Note that the $S-P$ transmission indicated with the arrow in Figures 4.23b and c is visible in both displays.

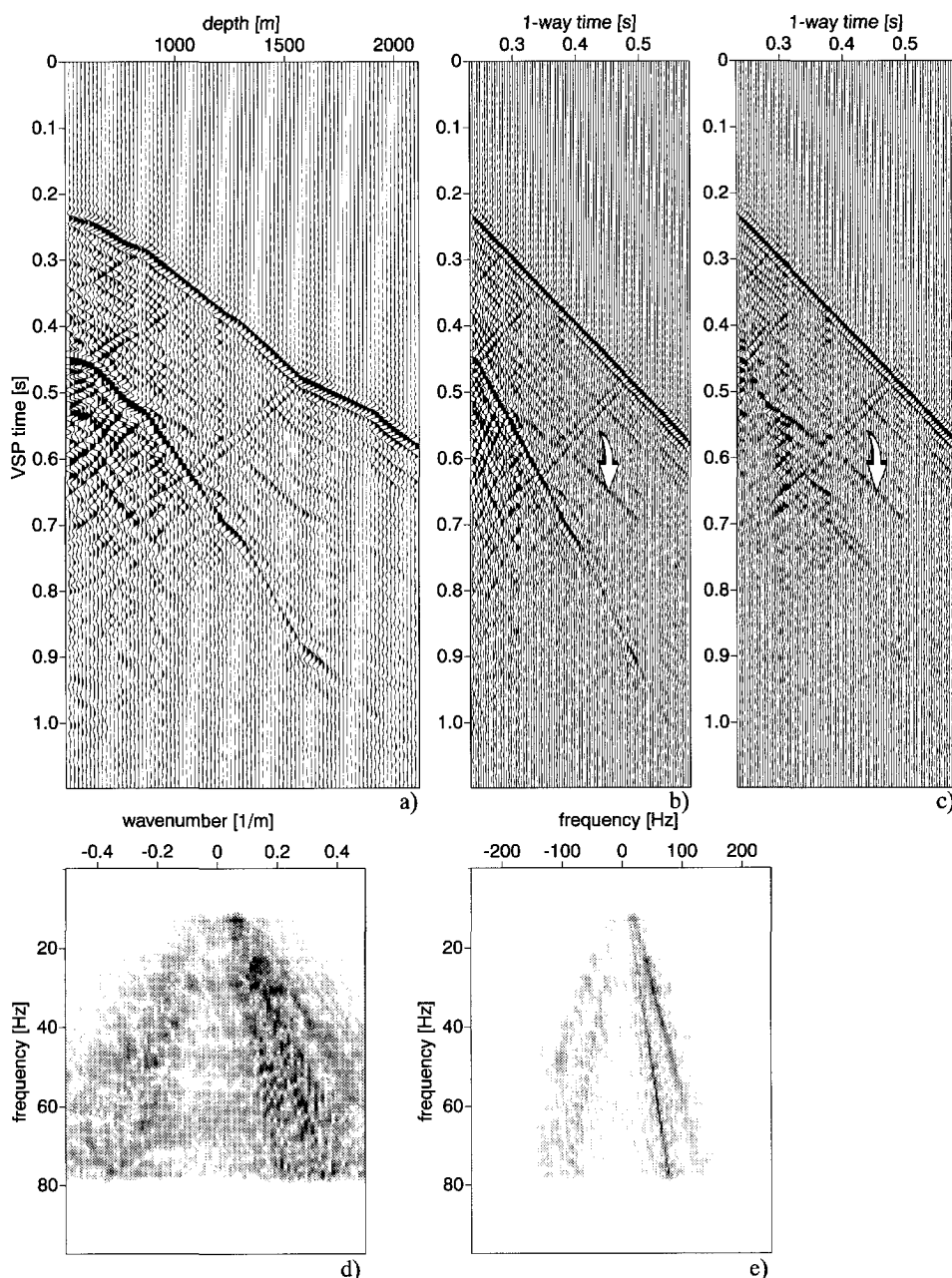


Figure 4.23 The transformation of the depth axis into the one-way time axis applied on land data
 a) $VSP(t_{VSP}, z)$. The data was recorded in the Middle East,
 b) $VSP(t_{VSP}, t')$ and c) $VSP(t_{VSP}, t')$ filtered in the (f, f') domain.
 d) $VSP(f, k)$ and e) $VSP(f, f')$.

Furthermore the dip-filtered VSP (t_{VSP}, t') is transformed again to the (t_{VSP}, z) display to be compared with the original unfiltered VSP data (t_{VSP}, z). The result for this experiment is displayed in Figure 4.24. Note that the S- wave energy is suppressed. The arrow in Figure 4.24b indicates the S to P transmission through the model which can be clearly identified.

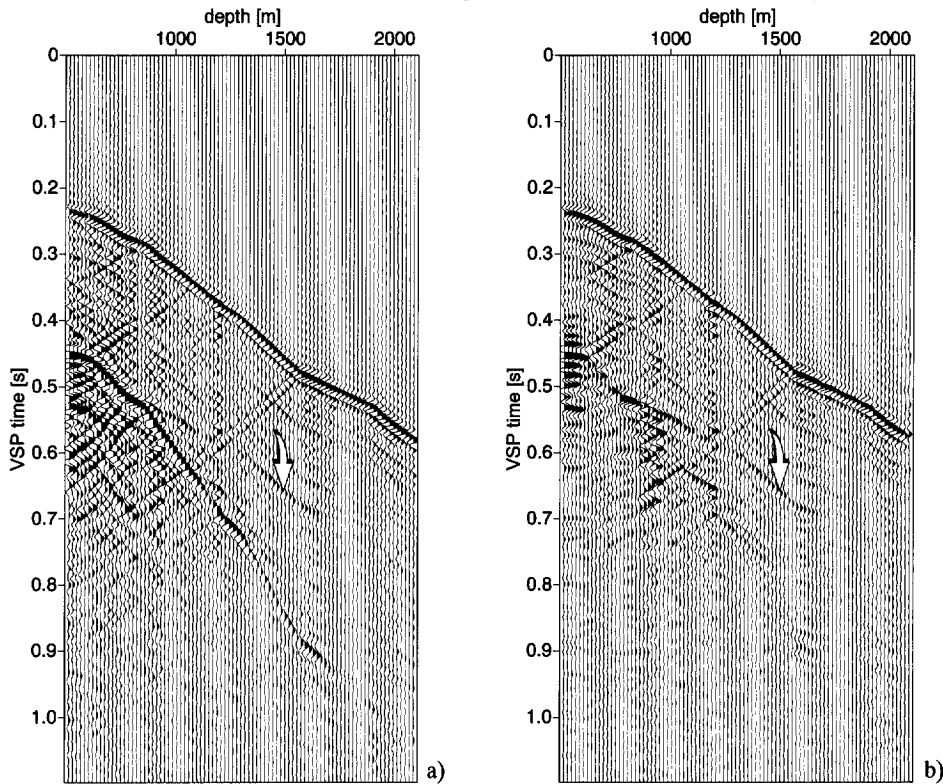


Figure 4.24 VSP data (t_{VSP}, z) a) before and b) after filtering in the (f, f') domain.

Figure 4.25 shows respectively the linear Radon transform of the VSP data from Figure 4.23a and b. The linear Radon transform shows a clear separation of the up- and downgoing events. The upgoing events from Figure 4.23a are mapped to the negative p values and the downgoing events Figure 4.23a are mapped to the positive p values. Note the different p values because of the different angles. However in Figure 4.25b only two main different p' values can be distinguished because of the stretching of the data along the P- wave first break (the downgoing P- wave first arrivals show a sharp focused point and the downgoing S- wave first arrivals show an unfocused point). Here again the quality of the focus of the downgoing S- wave (indicated with arrow) gives an indication of the Poisson's ratio. If the point (indicated with arrow) in Figure 4.25b is well focused, then that would be an indication for the constant Poisson's ratio throughout the medium.

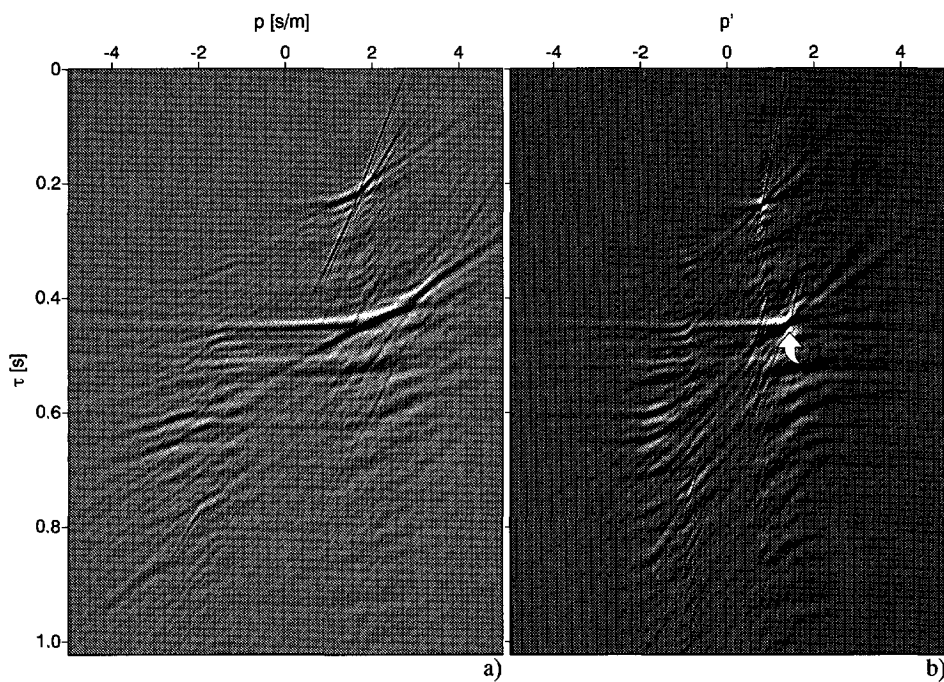


Figure 4.25 Linear Radon transform respectively applied on Figure 4.23a and b.

4.5.3 Land data example (II)

Next an example is shown of another VSP which is a land data from the Canadian Foothills. The data was provided by Husky Oil Canada. The preprocessed VSP data is displayed in Figure 4.26a and its corresponding (t_{VSP}, t') display in Figure 4.26b. The P - wave energy is dominant over the S - wave energy. Note the alignment of the events propagating with different velocity in Figure 4.26b. Studying the VSP data, a very strong upgoing wave can be identified (see white arrows in Figure 4.26a and b). For the prediction ahead of the drillbit and predicting the originating reflector for this strong upgoing wave, the pseudo VSP data (in depth z or in one-way time t') may be generated from the surface data and the velocity model estimated from the surface data. This pseudo VSP data may be used for “extrapolating the recorded VSP data towards depth” to predict the originating reflector. The surface seismic data was not available, but this example shows a proposal for generating pseudo VSP data to be used in bridging the missing gap to the originating reflector. This is schematically shown in Figure 4.26a and b.

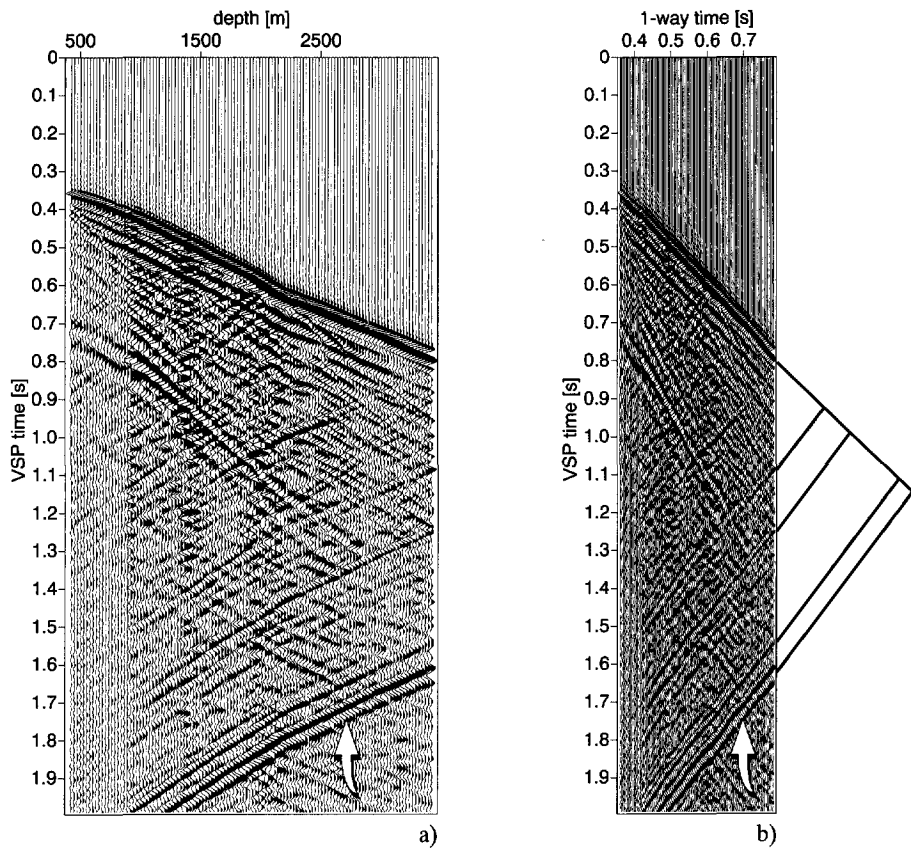


Figure 4.26 a)Real VSP data (t, z) and b)after stretching (one-way time display instead of depth). (courtesy Husky Oil Canadian Foothills Data). Here it is proposed to use a pseudo VSP data for the prediction ahead of the drillbit.

If the VSP velocity is consistent with the surface seismic data, then the surface seismic data can be used to generate pseudo VSP data for the prediction ahead of the drillbit. However, a mismatch between both datasets may give a new velocity profile which can then be used in the surface seismic processing and pseudo VSP data generation.

In this chapter, the relation was shown between the generation of pseudo VSP data and the construction of CFP gathers. It was shown that the pseudo VSP data gives insight into the illumination properties of CFP gathers and integrates the events in the shot record to the events in the constructed CFP gathers. A method has been proposed for a new display of VSP data (in one-way time t' instead of depth z). This new domain is less sensitive to velocity errors and linearizes the reflection events. Furthermore, by displaying the VSP data in one-way time t' , new opportunities are created for the analysis of real and pseudo VSP data.

Chapter 5

Imaging with multi-offset, common-well pseudo VSP data

5.1 Introduction

In this chapter some of the aspects of imaging with multi-offset (source-well offset; one-way offset), common-well pseudo VSP data will be discussed. In other words, the contribution of a range of single shot records along the surface is studied for the imaging of structures at one virtual well.

In the first part of this chapter, it will be shown how images are constructed using pseudo VSP data. The generation of pseudo VSP *depth* and *one-way time* records will be shown in Section 5.2. In Section 5.3, a series of multi-offset pseudo VSP data are generated from a series of shot records at the surface, for a common-well.

In this way image gathers can be built up which show the contribution of various sources to the image points at a virtual well. The image gathers are constructed as function of *depth z* and/or *one-way time t'*.

The construction of depth and/or one-way time image gathers will be discussed and illustrated. All the examples shown in this chapter are based on one-way operators.

5.2 From surface to pseudo VSP depth and one-way time records

In Chapter 3 of this thesis, the pseudo VSP data generated from seismic surface data has been illustrated as a tool for integrating unmigrated (single shot) data with migrated data. It was shown that the pseudo VSP data display helps to establish the relationship between events in the original shot gather and the migration sections. Furthermore the pseudo VSP generation was formulated in relation with the CFP method. The most important difference between both imaging methods has been shown : in the pseudo VSP method, single surface shot records are transformed into pseudo VSP data. On the other hand, in the CFP method only the response (of one depth point) is studied for a range of sources at the surface. In this section it will be illustrated how surface data (i.e. a shot record) can be transformed to pseudo VSP depth and/or one-way time images. The generation of a pseudo VSP depth record is illustrated on the syncline model dataset. For a description of the synclinal model and dataset see Section 4.3.

In Figure 5.1a, the pseudo VSP data has been generated at zero offset from a shot record (shot at $x=1650m$) after surface-related multiple elimination. The black line in the shot record (Figure 5.1a) indicates the well location. The upgoing waves have been inversely extrapolated and the first break times have been calculated with a raytracing algorithm to form the pseudo VSP data. The intersection of the first break line and the upgoing waves yields the “*image points*” in the pseudo VSP data. Note that the contribution of all the shot records to these image points will give the same result as the full prestack migration at the well location (the black line in the migrated section shown in Figure 5.1a indicates the location of the well). The “*image points*” from the pseudo VSP data can be selected and mapped towards the depth axis or the one-way time axis.

The selection procedure for the image points is performed as follows : as a first step, the wave field is inversely extrapolated and selected according to the predefined borehole/detector configuration; the first break is determined for the well configuration by a raytracing algorithm. Next, unit values are assigned to the first break arrival times. This dataset is then multiplied with the data containing the upgoing waves. In this way the upgoing events at the first break times are selected. These *image points* can be mapped to the *depth* axis and also to the *one-way time* axis resulting in a single trace as function of *depth* z or *one-way time* t' . An example of mapping the image points (in pseudo VSP data) to the *depth* or *one-way time* is illustrated in Figure 5.1b. The white arrows show the image points. Note that the non-causal part before the direct arrival has been zeroed. These image points have been determined and mapped to *depth* (top of Figure 5.1b) and mapped to *one-way time* (left of Figure 5.1b); the resulting trace have been reproduced 5 times for display purposes. It should be noticed at this point that for an optimal comparison with the full prestack migration the

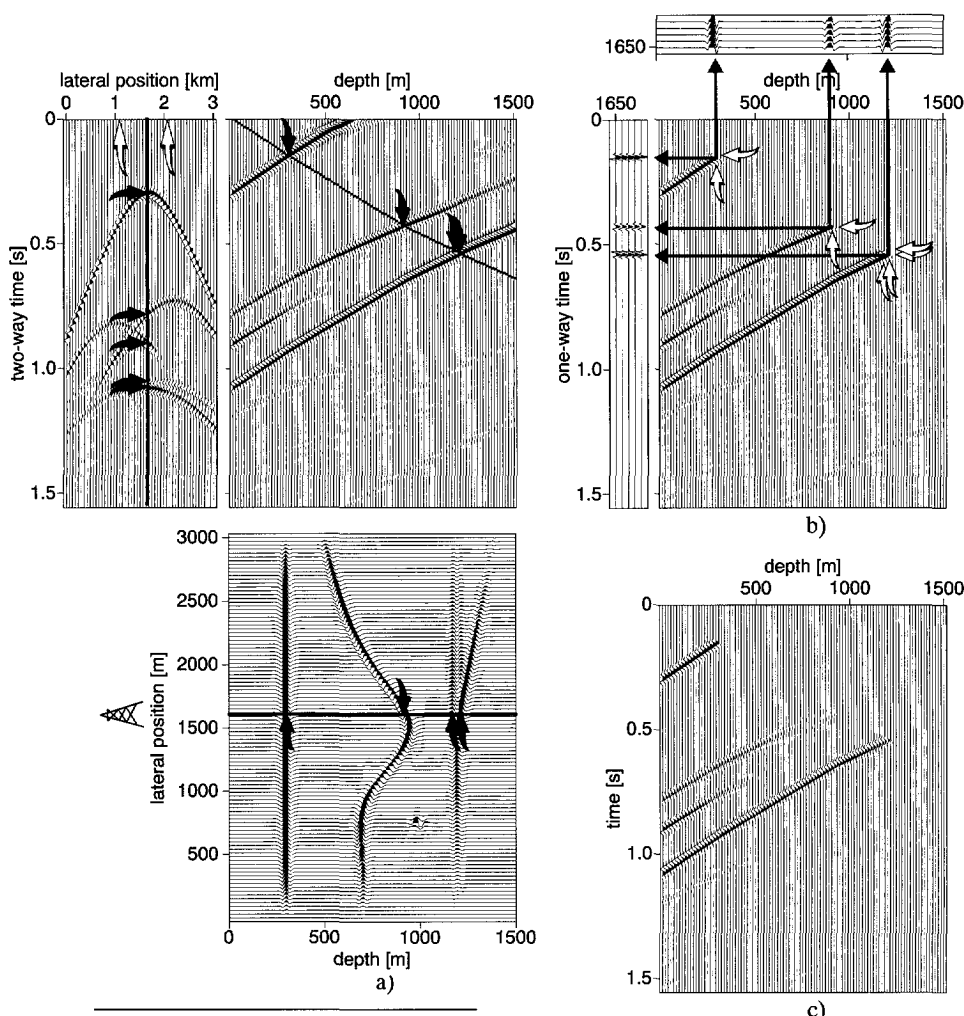


Figure 5.1 The effect of limited aperture on the image points constructed from pseudo VSP data. For a wide aperture the image points are better determined.

a) Integrated Seismic Display (ISD) of shot record with shot at $x=1650\text{m}$, pseudo VSP at zero offset and prestack migrated depth section, b) pseudo VSP generated from the shot for which all offsets were used and c) pseudo VSP generated from the shot with a limited aperture of 600m at each side of the shot record (arrows in the shot record show the limited aperture).

“image points” should be corrected in amplitude and phase by $1/\sqrt{j\omega}$ and also for the propagated source wavelet. Furthermore it is important to use a large aperture of receivers such that the image points are best determined. A limited aperture results into a poor image as illustrated in Figure 5.1c. The pseudo VSP of Figure 5.1b has been generated from a shot record with 201 receivers. On the other hand the pseudo VSP shown in Figure 5.1c has been

generated using only 81 receivers (600m maximum offset on both sides of the well). The arrows in Figure 5.1a show the limited aperture that was used in generating the pseudo VSP of Figure 5.1c. Comparison of Figure 5.1c with Figure 5.1b shows that the image points are not correctly determined for a limited aperture. This example shows that pseudo VSP image points can be restored correctly for a wide aperture (and a correct model). Therefore, a split spread shot gather is preferred rather than using the end of spread shot records. According to the theorem of reciprocity (Rayleigh, 1896, and Fokkema and Van den Berg, 1993), Figure 5.2 shows that a split spread shot gather can be constructed from a series of end of spread shot records. Reciprocity is applied on shot k to p to construct a full split spread shot record j (left). A sparser split spread gather j can be constructed from shots k to m if the source spacing is larger than the receiver spacing (right).

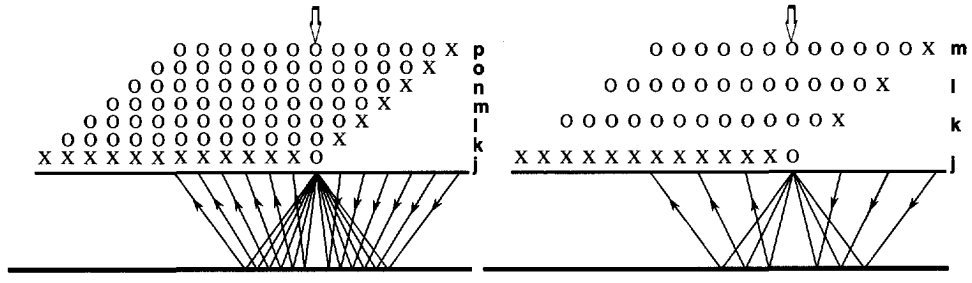


Figure 5.2 Procedure for constructing a split spread shot gather from a series of end of spread shot records using the principle of reciprocity.

In the previous chapter, the relation was shown between the generation of pseudo VSP data and the construction of CFP gathers using the CFP technology. From the relation between the pseudo VSP and the CFP gathers it is clear that the full images at a pseudo well can be built up in different ways. In the pseudo VSP method, the images are built up for one source-well configuration (limited illumination but detectors at all depth levels). The contribution of other sources have to be taken into account for an optimal illumination: extension to multi sources. On the other hand, in the CFP technology only one point is illuminated for all sources. For a full image at the well, the number of focus points need to be extended.

5.3 Construction of depth and one-way time image gathers

In this section the construction of image gathers will be discussed. The image gather represents a composite gather built from the contribution of all the sources to the image points at a well location. In Figure 5.3a a schematic illustration is given that may be used for the construction of image gathers. The objective of constructing image gathers is to study the influence of the various shot records to the image points at a predefined borehole/detector

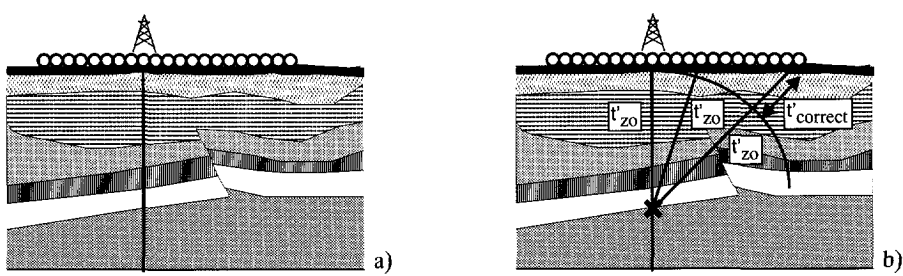


Figure 5.3 a) Geometry that may be used in the construction of image gathers : the contribution is studied of the various sources to the image points at the well location.
 b) Illustration for the time that has to be corrected per detector level with respect to the source : moving the sources virtually to the well-head.

configuration. Note that each type of well configuration can be used (e.g. a deviated well). The image gathers can be constructed by mapping the image points from pseudo VSP data as described in Figure 5.1, to the depth axis or to the one-way time axis. In this way *depth* and/or *one-way time* image gathers can be built up. Note that for the construction of the one-way time image gathers, a moveout correction has to be applied to the resulting gathers (see Figure 5.3b, t'_{zo} is the zero offset one-way time and $t'_{correct}$ represents the correction time). The moveout correction means that each source is shifted *virtually* to the well head.

5.3.1 From pseudo VSP depth records to *depth* image gathers

Figure 5.4 shows a configuration for a fixed well and a series of shot records at the surface. If the image points from the generated multi-offset, common-well pseudo VSP data are mapped to the depth axis and a correct macro model is used, then each event in the resulting image gather should be horizontally aligned regardless the structure in the subsurface. Figure 5.4 (right) shows the depth image gather that is constructed from the image points obtained from generated pseudo VSP data.

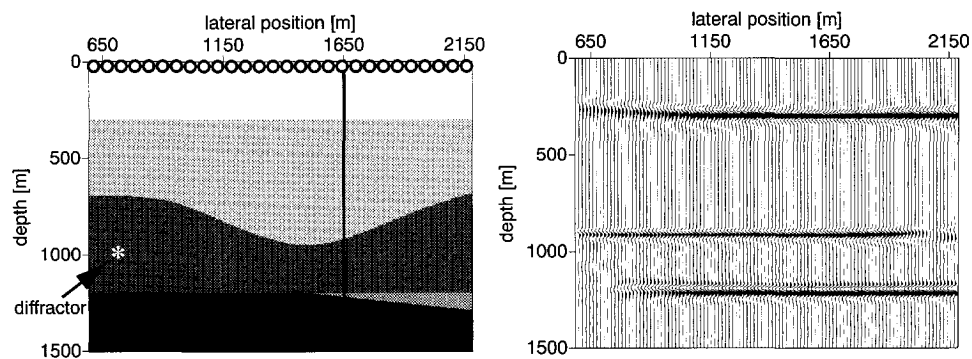


Figure 5.4 The construction of a depth image gather from pseudo VSP depth records.

Since the image gather is a composite gather in which the different shot records are individually migrated at the well location, the contributions should be all aligned if a correct model is used (Berkhout, 1984; Al-Yahya, 1989, Lafond and Levander, 1993). The non-alignment of the events in Figure 5.4 at the edges of the images is due to a limited acquisition range. The different shot records give individually their contribution to the image at a virtual well location. This means that if the events in an image gather are stacked, the resulting trace is similar to that obtained by prestack depth migration.

5.3.2 From pseudo VSP one-way time records to *one-way time* image gathers

In this section some of the imaging aspects will be discussed for a range of shot records along the surface and detectors vertically distributed in a virtual well. The construction of the image gathers from pseudo VSP (t, t') data will be discussed and illustrated with an example.

- **Construction of *one-way time* image gathers**

In this example, a series of walkaway VSP data is generated from a series of shot records (after surface-related multiple elimination) distributed along the surface of the syncline model. The range of the source locations is from 900m to 2400m with a step of 15m. The well is located at 1650m.

As discussed in the previous chapter, for the construction of the pseudo VSP (t, t') data, a series of CFP gather responses can be constructed for various focus points chosen in depth. For the construction of the pseudo VSP (t, t') data, the response of the wave fields have to be extracted for each successive one-way time step t' . Following the scheme of Figure 4.17, a series of time-reversed focusing operators can be calculated for a range of focus points in the pseudo well at 1650m. The time-reversed focusing operator related to a focus point at the first boundary ($z=300m$) is depicted in Figure 5.5a. The corresponding CFP gather is shown in Figure 5.5b. Note that because a correct model has been used here, the event of the time-reversed focusing operator and the corresponding event in the CFP gather (focus point response) are time-coincident. This is based on the principle of equal traveltimes (Rietveld, 1995, Berkhout, 1997a and 1997b). In other words, for a correct macro velocity model the arrival times of the focus point response are given by the traveltimes of the involved time-reversed focusing operator. The focus point response is defined as the coherent event in the CFP gather, representing the reflection response from the involved focus point. For a thorough discussion on the macro model aspects the reader is referred to Berkhout (1997b) and Thorbecke (1997). The focus point response is indicated with an arrow in Figure 5.5b. The construction of the CFP gathers refers to the first focusing steps. In the second focusing step,

the information of the CFP gather is added and positioned at the one-way time (in the second focusing step, the CFP gather has to be moveout corrected).

This is performed by a *1-D* convolution between the time-reversed focusing operator and the corresponding CFP gather. The *1-D* convolution has to be performed in time. The result of this convolution is the alignment of the focus point response at $t=0s$ (for a correct macro model). Figure 5.5d shows the moveout corrected CFP gather with the aligned focus point response at $t=0s$. Figure 5.5c shows the same as Figure 5.5d but an additional shift (to the one-way time) has been applied. Similar type of panels have been shown by Cox (1991) who called them common depth point gathers and showed that the alignment of the events contains information that can be used for macro model estimation.

For the construction of the pseudo VSP (t, t') data, a series of one-way time operators is needed. As a first operation some distributed focus points are chosen for which time-reversed focusing operators are calculated. This is illustrated in Figure 5.5e. Note that there is no need to distribute the focus points regularly. The operators are then interpolated in time for a regular one-way time step and the result is depicted Figure 5.5f. For each time step $\Delta t'$, the CFP gathers are constructed and one trace is selected per CFP gather related to the well configuration. The constructed zero offset pseudo VSP (t, t') data is depicted in Figure 5.5g. Remember that zero offset refers to the zero distance between the well head and the corresponding source location at the surface.

Note that the upgoing events are cut at the first break times. The data can also be selected from the moveout corrected CFP gathers. The result is shown in Figure 5.5h (moveout corrected pseudo VSP (t, t') data), where a stretching is visible of the events to the zero time. The moveout correction means that each source is shifted *virtually* to the well head. If the procedure of constructing pseudo VSP (t, t') data is repeated for all the offsets, a cube of data (x, t, t') can be constructed.

Figure 5.6 shows some generated pseudo VSP (t, t') data for various offsets. The offsets selected from the CFP gathers are respectively : $-600m$, $-300m$, $0m$, $300m$ and $600m$.

It is important to notice from this figure that all the “imaged points” (i.e. points from the upgoing wave field muted at the first break) are all positioned at equal one-way times t' although the shot records (input) correspond to different source locations. The events which have traveled along the borehole are all straight. The events from aside the synclinal structure which were recorded in the shot record fade away by approaching the “imaged points”. The pseudo VSP (t, t') data after moveout correction (see also Figure 5.5h) are stored in a cube as shown in Figure 5.7a (data without surface-related multiples) and Figure 5.7b (all the multiples are included).

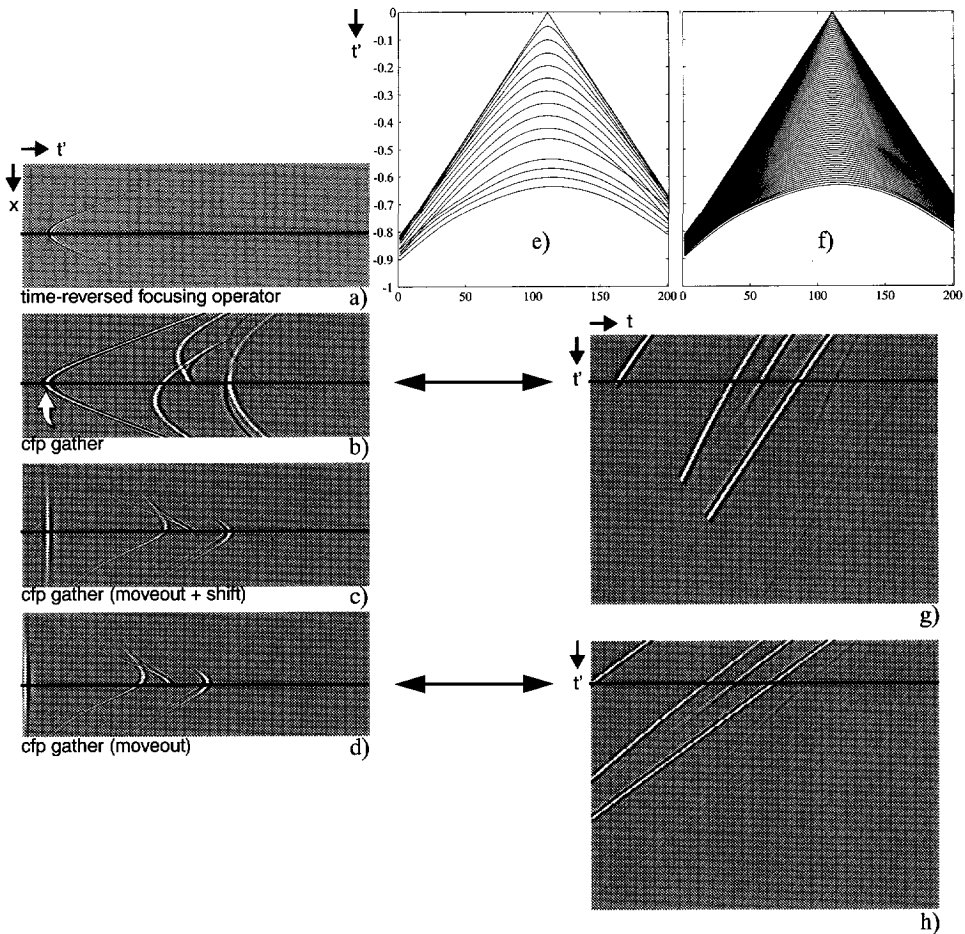


Figure 5.5 The different steps in the construction of pseudo VSP (t, t') data. The moveout corrected pseudo VSP (t, t') forms the image for one single shot contribution.

Figure 5.8 gives an explanation of the constructed cube of data for interpretation purposes. Figure 5.8 is based on the data without the surface-related multiples. The vertical slices along the lateral x -axis represent the moveout corrected pseudo VSP (t, t') data (Figure 5.8a). The moveout corrected pseudo VSP (t, t') at zero offset is depicted below Figure 5.8a. The horizontal slices (Figure 5.8b) through the volume represent the moveout corrected CFP gathers which have been constructed for subsequent one-way time steps $\Delta t'$. The moveout corrected CFP gather corresponding to the first boundary ($z=300m$) is depicted below Figure 5.8b. Note that the focus point response is aligned and positioned at $t=0s$. The black line represents the same trace as depicted in the pseudo VSP (t, t') data of Figure 5.8a. The front side of the cube shows a composite gather : the so-called *one-way time image gather*.

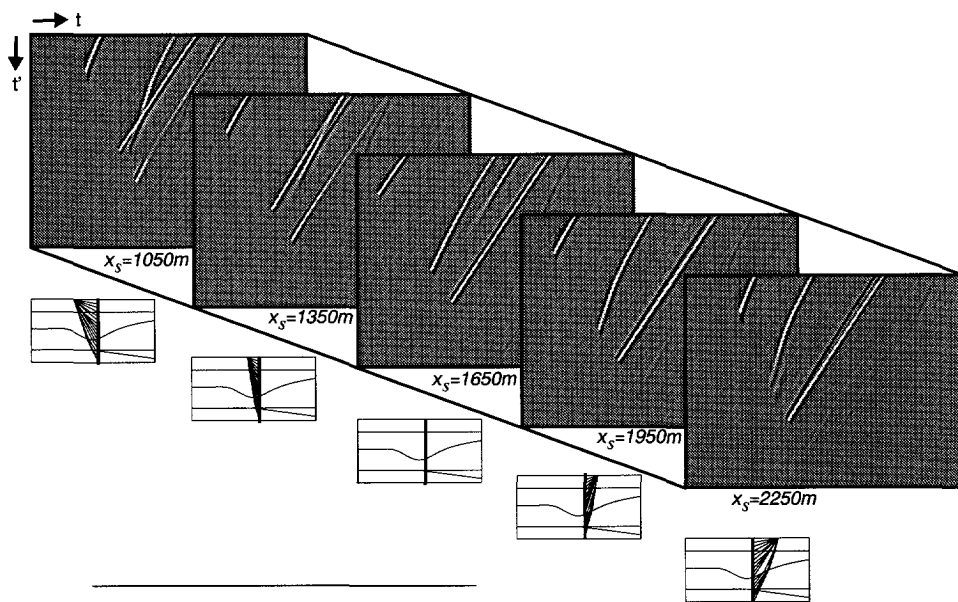


Figure 5.6 Constructed pseudo VSP (t, t') data for various offsets with respect to the well at $x_s = 1650m$. The shot locations for the shot records (x_s) that contribute to the pseudo VSP (t, t') data are shown below each panel.

The image gather at $t=0s$ (shown below Figure 5.8c) shows the “image points” of the generated pseudo VSP (t, t') data (for a common-well at $1650m$) with the contribution of all the shot record with shot locations at the surface ranging from $900m$ to $2400m$. All the events corresponding to the reflection of the layer boundaries are aligned at $t=0s$ (for correct model). Note that the straight line corresponding to the synclinal reflector becomes unfocused as indicated with the arrow.

The reason for that (critical angle) can be explained with the following figure. Figure 5.9 shows some raypaths for the source at $x_s=2400m$. Here the top of the right flank of the syncline structure starts acting as a diffraction point (indicated with arrow) and most of the energy is propagating along the flank. The propagation from the energy from the diffraction point is also visible in the pseudo VSP (t, t') data of Figure 5.6 ($x_s=2250m$). It can be clearly seen (in Figure 5.6, $x_s=2250m$) that at a particular t' , energy is growing and approaching the second reflector and this energy results into a “false image” at the first break times. If the pseudo VSP (t, t') data are generated from the data with all multiples included, a resulting cube (x, t, t') is obtained as shown in Figure 5.7b. Note that the events corresponding to the primary events are all horizontally aligned except the surface-related multiple events which have a bending shape. Comparison of Figure 5.7a and b shows a phase shift of the data with multiples. The surface data with all multiples included have to be deghosted to obtain the same phase as the data without surface-related multiples.

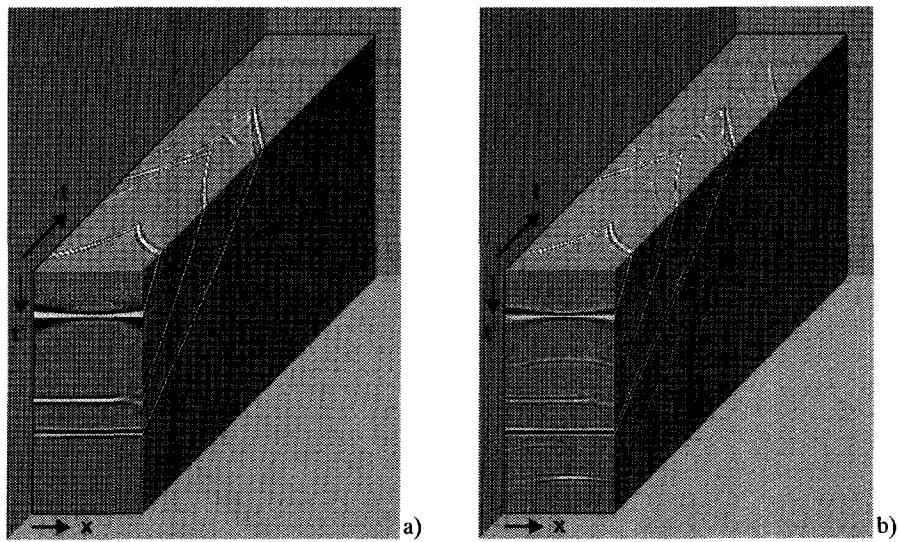


Figure 5.7 Image gathers constructed from pseudo VSP (t, t') data using the correct velocity :
 a) surface data without surface-related multiples and
 b) data including the surface-related multiples.

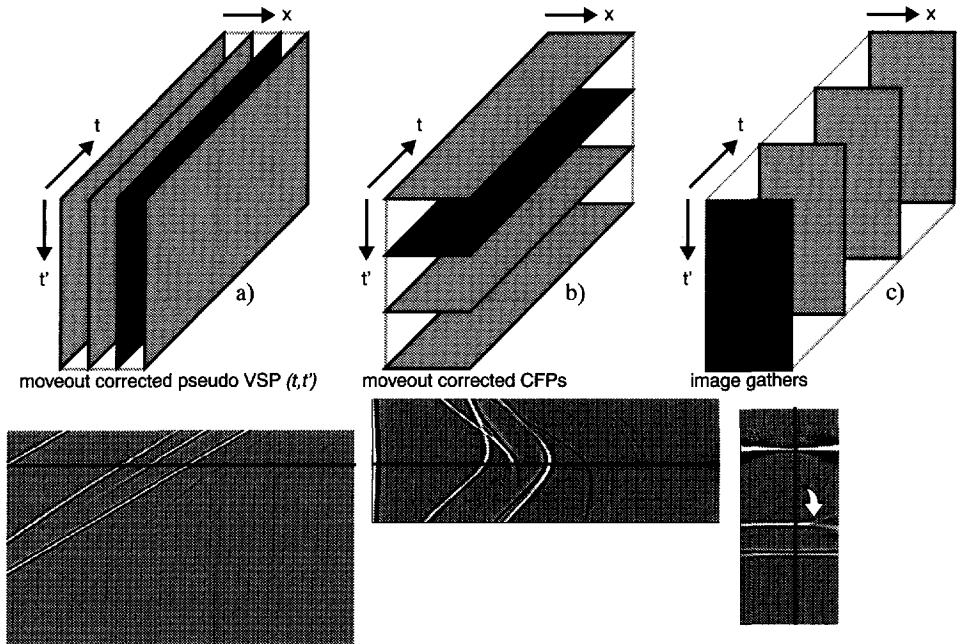


Figure 5.8 Various slices from the 3-D cube of data (x, t, t') .

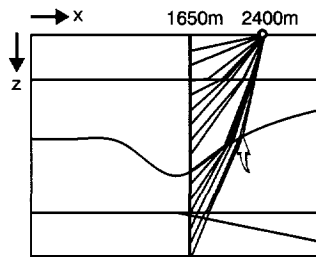


Figure 5.9 Raypaths for the source at $x_s=2400m$.

Figure 5.10 illustrates some slices from the cube (x, t, t') without surface-related multiples (see also Figure 5.7a): the picture on the top shows the moveout corrected CFP data (+shift) at the three boundaries.

At the bottom some gathers are shown for increasing times $t=0.0s$, $t=0.26s$, $t=0.52s$, $t=0.78s$ and $t=1.04s$. These slices are snapshots showing how the different events are aligned at time $t=0s$ (one-way time image gather). The image gathers give an illustration of the angle-dependent illumination of a particular depth point at a boundary illuminated from a series of sources along the surface.

As discussed earlier, if the macro velocity model is correct it means that correct operators have been used in the construction of the CFP gathers and all the events in the image gather ($t=0s$) should be aligned horizontally. If there are errors in the macro model the different images will not line up horizontally.

To illustrate the construction of the one-way time image gathers with a wrong macro velocity model, the following experiment has been done. In the construction of the cubes (x, t, t') , a *wrong* velocity has been used, leading to *incorrect* time-reversed focusing operators.

Figure 5.11a and b show respectively the construction of the cubes from data without surface-related multiples and with all multiples included. Incorrect velocities have been used in the construction of the cubes : a velocity of 200m/s too low has been taken in each layer. The resulting image gathers show an *upward* curvature of the primary events.

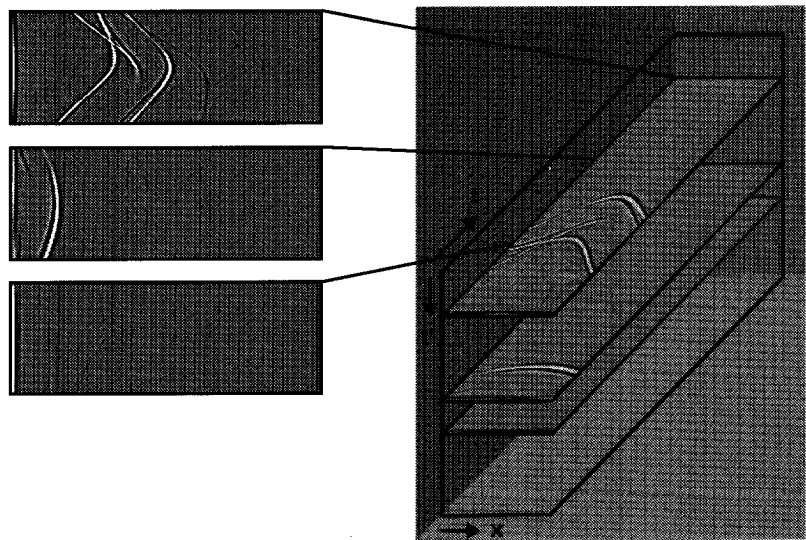
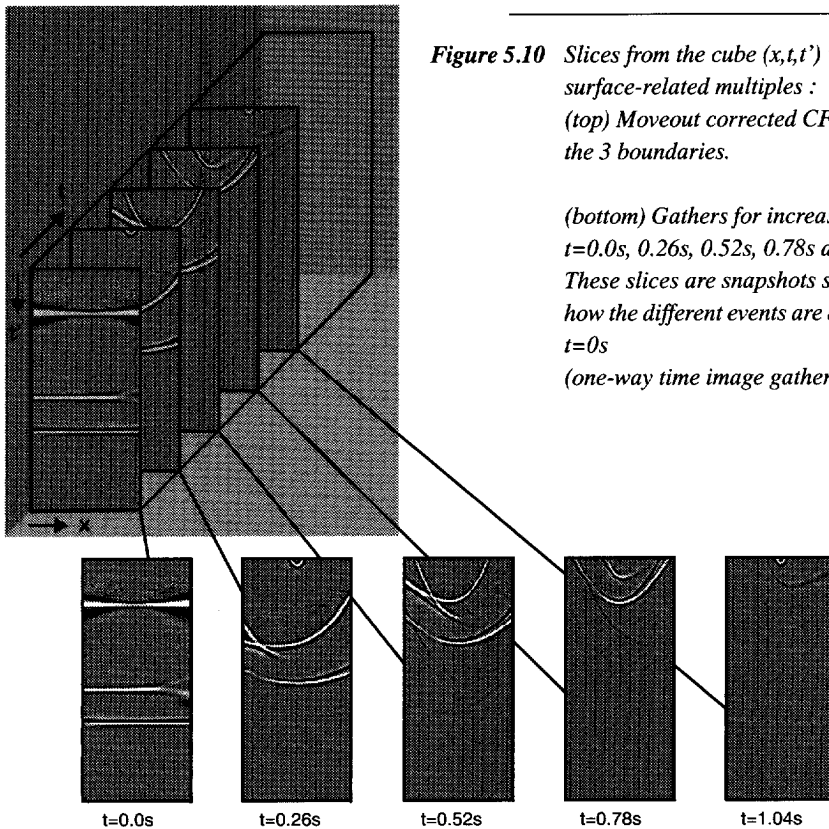


Figure 5.10 Slices from the cube (x, t, t') without surface-related multiples :
 (top) Moveout corrected CFP data at the 3 boundaries.

(bottom) Gathers for increasing times
 $t=0.0s, 0.26s, 0.52s, 0.78s$ and $1.04s$.
 These slices are snapshots showing
 how the different events are aligned at
 $t=0s$
 (one-way time image gather).



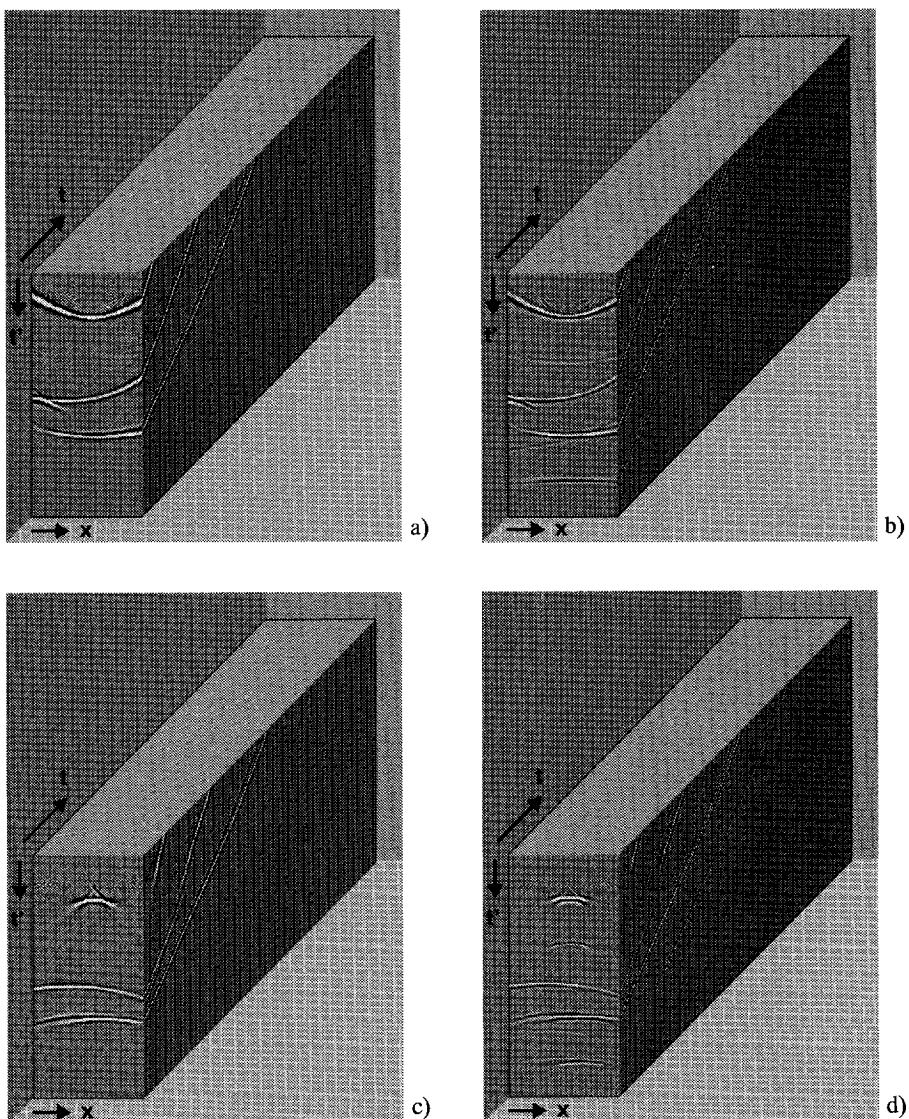


Figure 5.11 Data mapped into one-way time image gathers with pseudo VSP (t, t') data using wrong velocities. a) Data without surface-related multiples: a lower velocity of 200m/s has been taken in each layer, b) data including surface-related multiples, velocity in each layer : -200m/s, c) data without surface-related multiples: a higher velocity of 200m/s has been taken in each layer, and d) data including surface-related multiples, velocity in each layer : +200m/s (Note that the fresnel zone is moving out of the aperture of the data).

In the generation of pseudo VSP data, the source positions are still at the surface. Hence, if a secondary source is constructed somewhere in depth using the CFP technology as discussed in Chapter 4, then any type of pseudo shot record can be simulated in a (virtual) borehole. This idea offers the possibility to create pseudo Crosswell data from CFP gathers (2-step process). If the pseudo borehole data is created for the same focus points as chosen to build up the CFP gathers maximum energy will be obtained at the reflecting boundaries for a correct macro model. The aforementioned way of constructing pseudo seismic borehole data (or well-to-well data) from surface measurements has another interesting feature. If the virtual borehole is chosen along a raypath and the zero-offset pseudo borehole data is constructed, then the traveltimes of the reflected events are minimum and the amplitudes are maximum. Hence, if the velocity model is not correct then the raypath is not correct and the wave field energy does not travel along the (virtual) borehole.

In Chapter 4 it was shown that numerical focusing may be seen as simulating virtual sources anywhere in the subsurface. Hence, the measurements of any source-detector configuration in the subsurface can be constructed from surface measurements. The potential of this capability will be discussed with the following example. For a correct velocity model the traveltimes of the source event and the related reflection event in the CFP trace are equal (principle of equal traveltimes). A pseudo shot record in a borehole ('*borehole shot record*') can be easily computed by generating a pseudo "VSP" record from a CFP gather. Figure 5.12 shows an Integrated Seismic Display (ISD) of a synthesized borehole shot record from a CFP gather together with the CFP-related focusing operator. Note the focusing point at the second boundary at $t=0$ s (maximum energy). Figure 5.12f shows the amplitude contour plot of the borehole shot record. A focusing beam related to the focusing point chosen in Figure 5.12c, is displayed in Figure 5.12e. Incorrect focusing can be very well studied with this type of Integrated Seismic Displays (ISD).

Figure 5.13 illustrates how pseudo borehole shot records can be generated for the imaging of steep flanks. Real source positions at the surface can be mapped to virtual source positions in depth at the (virtual) borehole. Next pseudo borehole shot records may be generated in the (virtual) borehole. This procedure may be an effective tool to image steep flanks. Optionally, the virtual borehole may be chosen along a raypath such that the traveltimes of the reflected events are minimum and the amplitudes are maximum. The wave field energy does not travel along the virtual borehole if the velocity model and thus the raypath is not correct.

Of course, the sources and detectors may also be positioned in *different* wells; the result will then be pseudo well-to-well data.

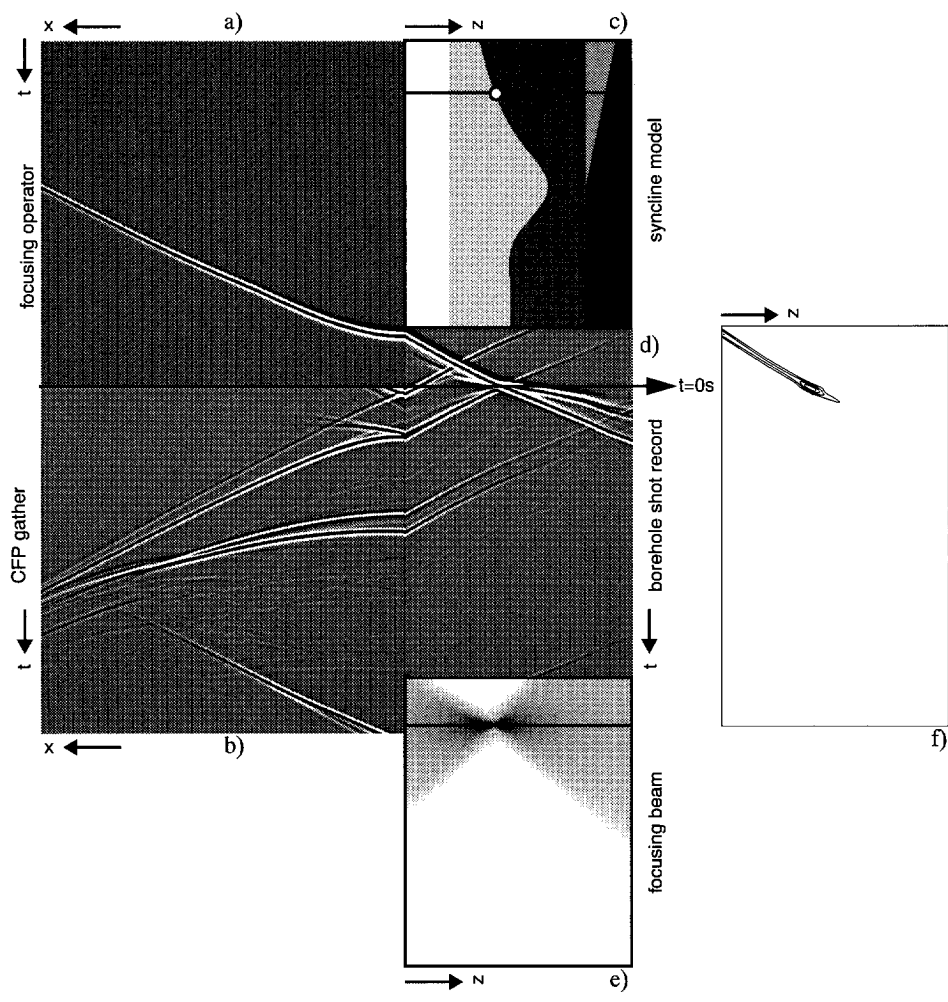


Figure 5.12 From CFP gather to pseudo seismic borehole data.

Note the very nice visualization of the focusing effect at the focus point.

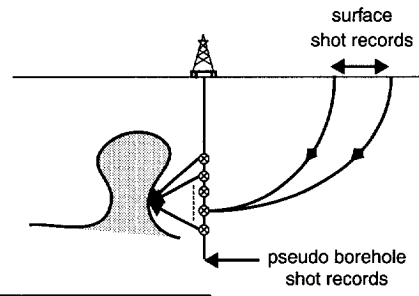


Figure 5.13 Two-fold double focusing for controlled imaging of very steep flanks.

5.4 Picocol model and dataset

In the following example the Picrocol model has been used. The dataset and model was provided by the Institut Français du Pétrole (IFP). The Picrocol geological model contains a salt diapir that pierces horizontal sedimentary layers, folding and uprising them near the flanks and breaking them in and above the “cap rock”. The sedimentary layers are nearly symmetric on the two sides of the salt body (the bases of these layers are almost at the same depth in the regions where the layers are horizontal) and are made up in the shallow parts by shaly-sandy detrital sediments and in the deeper parts by carbonates. The base of the salt is horizontal, slightly faulted and situated at about 3300m depth. The Picrocol structural model is based on a real dataset shot over a salt dome in the southern North Sea (Ehinger, 1994) and is shown in Figure 5.14 in which various layers are numbered. The dimensions of the model are 16km (length) by 4km (depth).

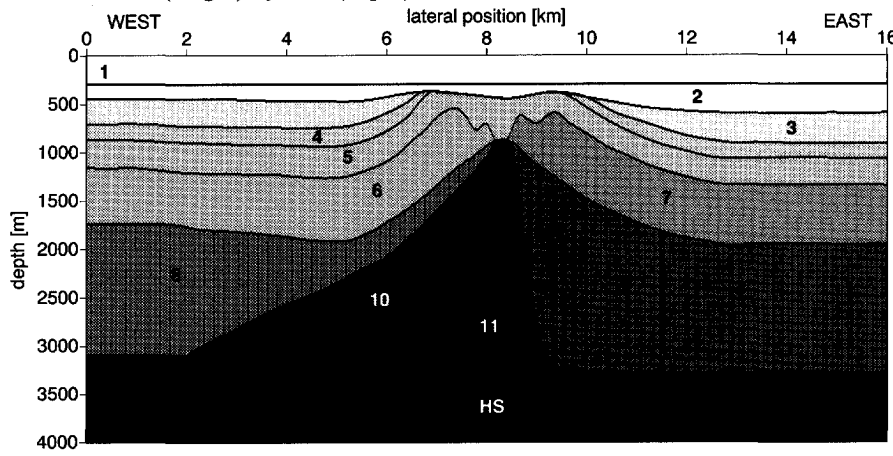


Figure 5.14 The Picrocol structural model.

The velocities c_p [m/s] of each layers are respectively defined as follows : 1) 1700, 2) 1800, 3) 2000, 4) 2200, 5) 2310, 6) 2450, 7) 2800, 8) 3200, 9) 3500, 10) 4200, 11) 4500 and HS) 5000. The corresponding densities ρ [kg/m³] are respectively defined as : 1) 2000, 2) 2100, 3) 2100, 4) 2200, 5) 2200, 6) 2250, 7) 2300, 8) 2400, 9) 2450, 10) 2550, 11) 2200 and HS) 2700. The acquisition parameters for the seismic survey were : • number of shots: 501, shot from west to east, • first shot at 3000m last shot at 13000m, • distance between shots: 40m, • receivers: symmetric array with first trace at offset 2500m west of shot location, • number of receivers: 251, receiver spacing 4m and • number of samples per trace: 1001; sampling interval: 0.004s (recording time 4s). The synthetic seismic data have been generated using a 2-D finite difference acoustic wave propagation modeler (*SIERRA*™). The source consisted of 5 guns with a total spread of 32m, the interval between guns being 8m and the depth of the guns 8m.

The “shot point” is in the middle of the spread. The 5 guns were “fired” at the same moment. The source signature is the first derivative of a Gauss function with a central frequency of 22.5Hz. The data have been preprocessed and the surface-related multiples have been removed (Verschuur, 1991). Figure 5.15a shows the zero offset section from the data after surface-related multiple elimination. The depth image after recursive full prestack depth migration has been depicted in Figure 5.15b. Note that the right flank of the salt dome is not properly imaged.

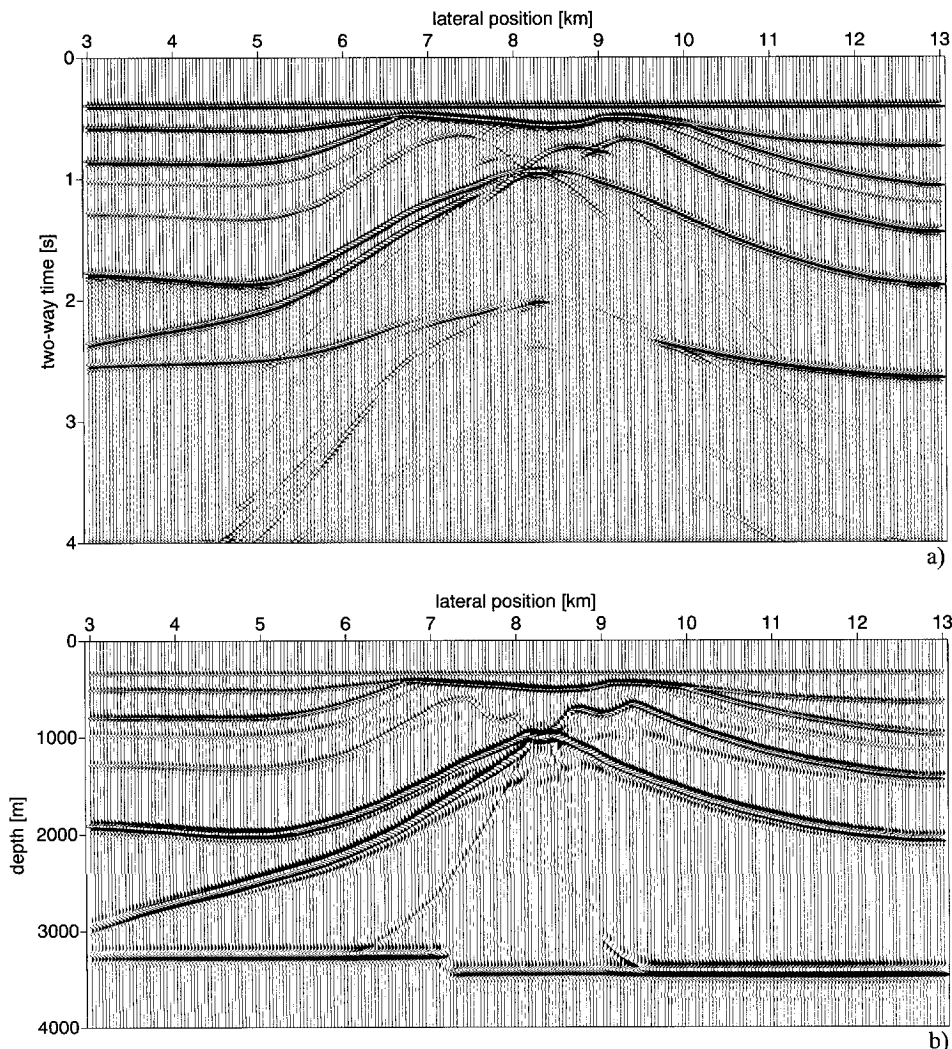


Figure 5.15 a)Zero offset section of the Picrocol dataset across the salt dome and b)depth image after full prestack depth migration.

The construction of image gathers using pseudo VSP data is illustrated in Figure 5.16. A vertical well has been located at 7km and the contribution of the shot records at the surface is studied. Figure 5.16a shows the configuration of the well at 7km. The image points are determined as discussed before (see also Figure 5.1), by the multiplication of the first break arrival times (unit amplitude) with the data. Figure 5.16b shows the resulting depth image gather (here the image points have been mapped to the depth axis). It is interesting to identify that the steep flank indicated with the arrow in Figure 5.16a is imaged (in depth) mostly from the contribution of the shot records at the left. All the events corresponding to a boundary have been horizontally aligned because a correct model was used. The single-fold images related to the steep flank are indicated with an arrow in Figure 5.16b. Note that for obtaining the full prestack image at the well location, the traces in the image gathers have to be stacked. The result of the stacking is shown respectively in Figure 5.16c for the well at $x=7\text{ km}$. The resulting trace has been reproduced 5 times for display purposes. If the image points are mapped to the one-way time axis, a gathers is obtained as depicted in Figure 5.16d. Note that to obtain the one-way time image gather, an additional time shift (moveout) has to be applied to the data (see also Figure 5.3b).

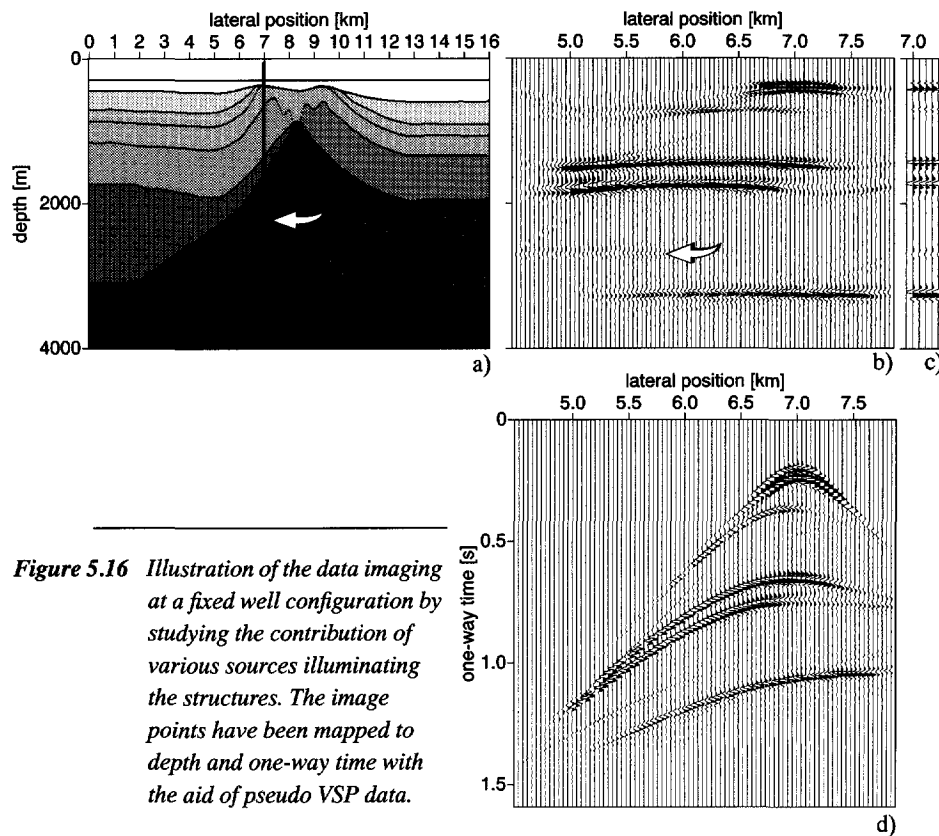


Figure 5.16 Illustration of the data imaging at a fixed well configuration by studying the contribution of various sources illuminating the structures. The image points have been mapped to depth and one-way time with the aid of pseudo VSP data.

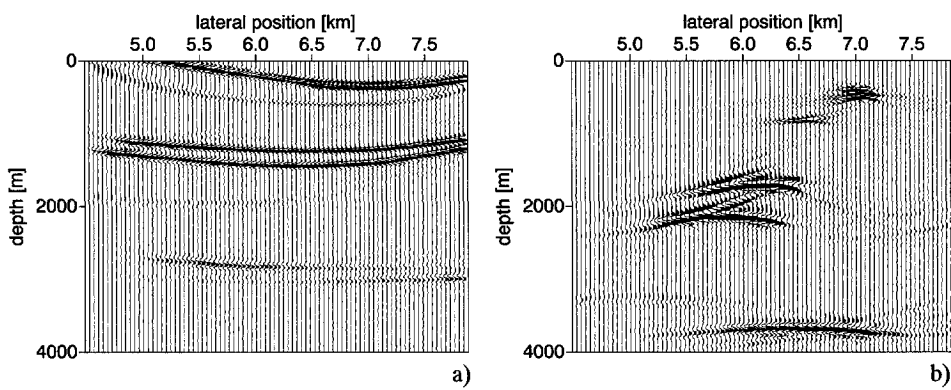


Figure 5.17 Constructed depth image gathers using erroneous velocity models.
The velocities in each layer are chosen a) 200m/s too low and b) 200m/s too high.

So far it has been shown that for a correct model the events in the image gathers will be horizontally aligned regardless the structure of the model. To illustrate that the image gathers can be used to verify the correctness of the subsurface model, in the following example erroneous velocities have been used (the velocities in the model have been decreased by 200m/s). The result for this experiment is shown in Figure 5.17a. The events in the image gather show an upward curving behaviour indicating that the subsurface model is incorrect.

Figure 5.17b shows the result in using an incorrect model (the velocity of each layer has been increased by 200m/s). If a larger velocity is used than the correct velocity, the events in the image gather show a downward curving behaviour and due to the higher velocity the Fresnel zone moves outside the aperture of the data (in the construction of this gather, the Fresnel zone moves outside of the aperture of the shot record data and for larger offset pseudo VSP data this becomes visible). The depth image gather may also be constructed for a deviated well. This is shown in Figure 5.18a where a deviated well is chosen and the contribution of the various shot records is investigated. The result is shown in Figure 5.18b.

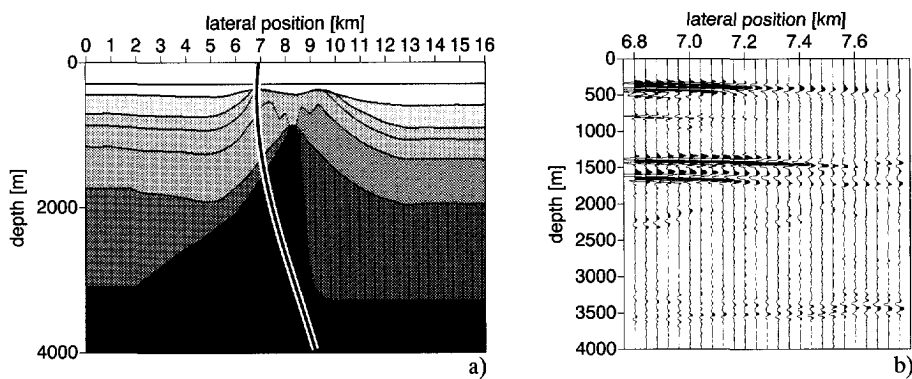


Figure 5.18 The construction of depth image gathers for a deviated well configuration : a)geometry of the deviated well and b)result of the image gather.

For an optimal display the result of Figure 5.18b has to be shifted laterally along the coordinates of the pseudo well, to locate the images at their correct lateral position.

In the following experiment, some focusing beams have been constructed and the energy have been calculated from the corresponding CFP gathers. The results are depicted in Figure 5.19 a to d. The focus points have been respectively chosen ($x=10\text{ km}$ $z=830\text{ m}$), ($x=6.8\text{ km}$ $z=750\text{ m}$). The beams of Figure 5.19a and b, are constructed by performing an inverse recursive downward depth extrapolation of the time-reversed focusing operators through the model and calculating for each depth level the energy of the wave field per lateral position. Using the time-reversed focusing operators, two CFP gathers have been constructed. These CFP gathers have been used to calculate the energy of the wave field per depth level by inverse recursive downward depth extrapolation. The results are illustrated in Figure 5.19c and d.

From these figures it can be clearly seen that the energy is focused at the focus points and a direction is shown for the events of the next or previous layers. By studying the Figures 5.19c and d, pseudo wells can be designed along the raypaths such that the maximum energy is followed and pseudo borehole data are generated. Note that in this way pseudo borehole data is generated from CFP gathers (response of a common focus point in depth).

The advantage of using CFP gathers to generate borehole data is that reflections from faults and other structures become better identifiable in the CFP gather which are then used as input to generate pseudo borehole seismic data. Figure 5.20a illustrates a shot record with the shot at ($x=6.8\text{ km}$, $z=0\text{ m}$). A CFP gather has been constructed from all the shot records along the line and the result is shown in Figure 5.20c. The focus point for the construction of the CFP gather was placed at $x=6.8\text{ km}$ at a depth level of 750 m .

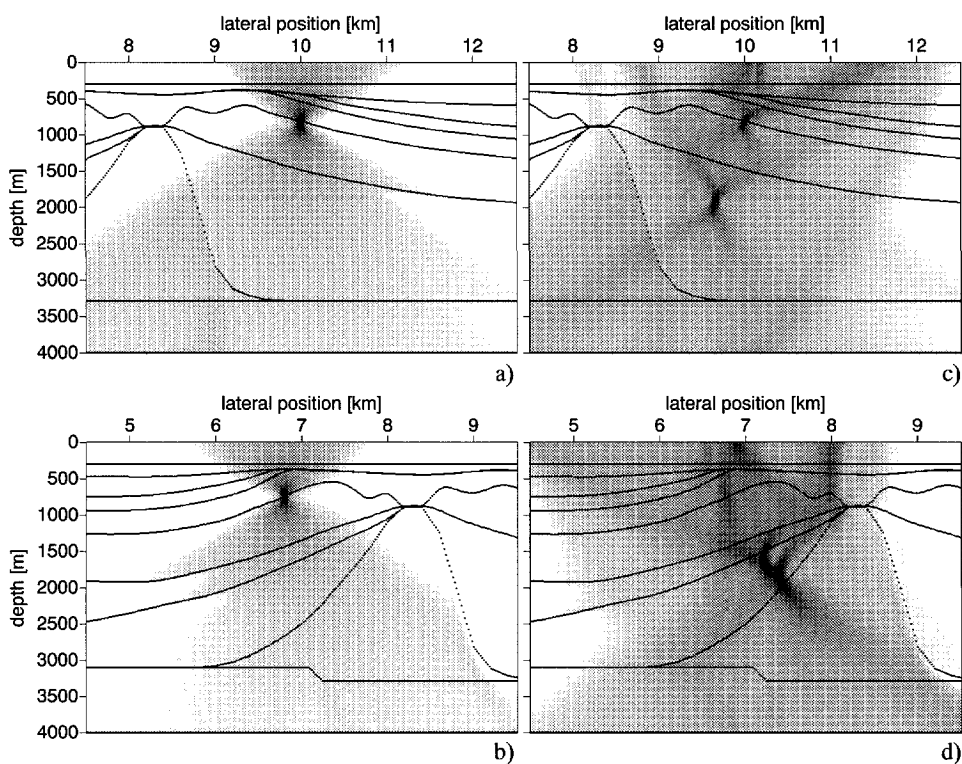


Figure 5.19 a) and b): Focusing beams at different positions. c) and d): Energy calculation per depth level for corresponding CFP gathers.

The configuration of the well that is used in this experiment is depicted in Figure 5.20b. The location of the focus point has been indicated in this figure (see also Figure 5.19b and e).

From the CFP gather with the focus point at ($x=6.8\text{ km}$, $z=750\text{ m}$) it can be seen that the reflection from the flank of the salt is better visible than in the shot record. This event is indicated in Figure 5.20c with an arrow. From the CFP gather in which some of the reflections are clearly visible, a VSP depth record has been generated according to the borehole/detector configuration as shown in Figure 5.20b. The result of the generation of the VSP depth record is depicted in Figure 5.20d. The black line indicates the first break times calculated with raytracing.

Using the CFP gather as input to the pseudo borehole data generation has the advantage that the various events will be focused in depth. Figure 5.20e shows a contour plot of the envelope of the upgoing waves from Figure 5.20d. From the contour plot it can be seen that the energy of the event (indicated with the arrows in Figure 5.20d and e) is focused at the depth level $z=750\text{ m}$. The focus point was placed at $x=6.8\text{ km}$, $z=750\text{ m}$.

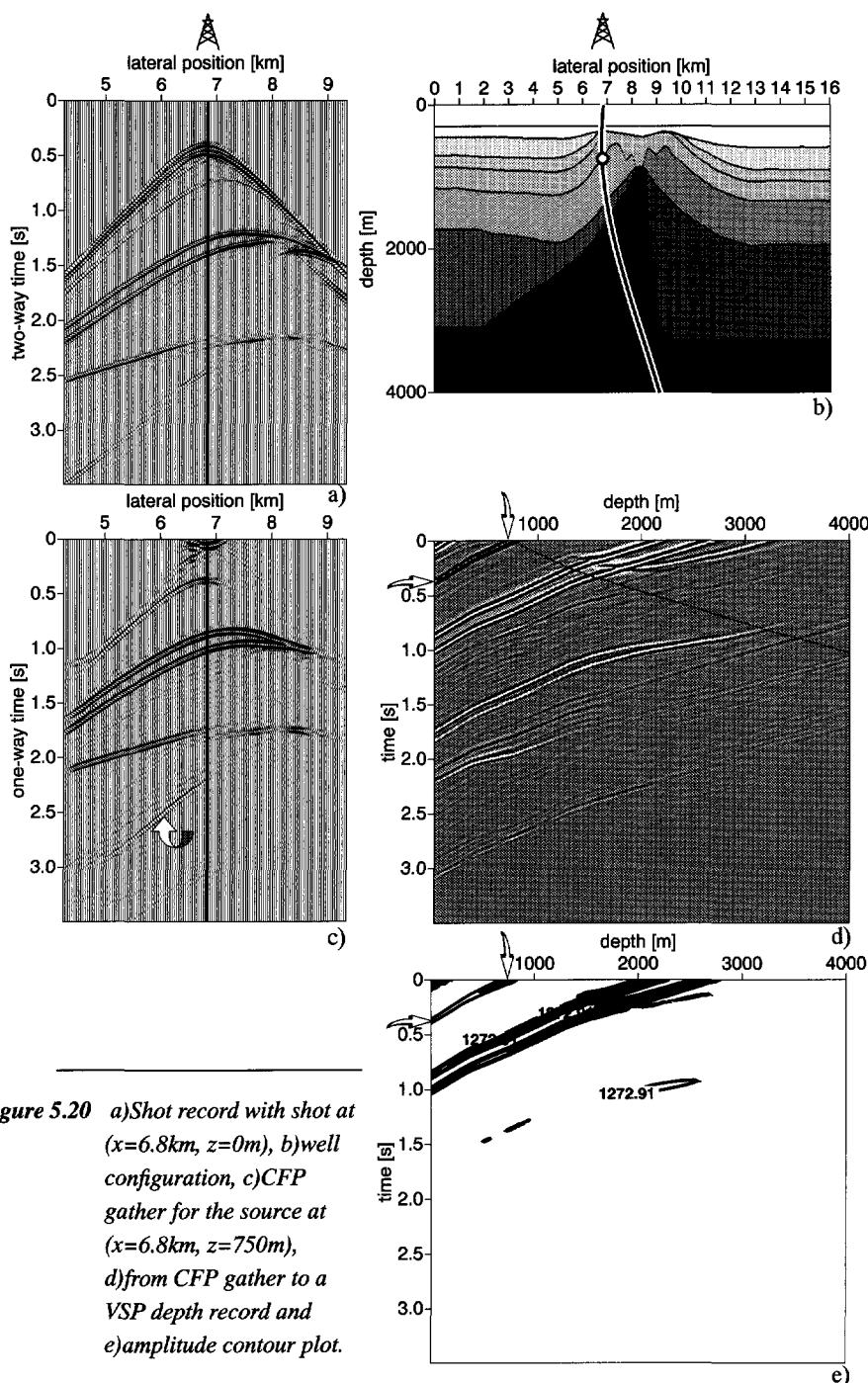


Figure 5.20 a) Shot record with shot at ($x=6.8\text{ km}$, $z=0\text{ m}$), b) well configuration, c) CFP gather for the source at ($x=6.8\text{ km}$, $z=750\text{ m}$), d) from CFP gather to a VSP depth record and e) amplitude contour plot.

The reflection corresponding to the focus point (“the so-called focus point response”) will be focused at the depth of the focused point using a correct model. According to the results of Figure 5.19b and d, some of the other events in the CFP gather will be also focused at particular depth levels. Here it should be noticed that in the generation of a VSP depth record from a CFP gather, only the event corresponding with the “common focus point response” will be focused at its correct depth (using a correct macro model).

Similar panels like in Figure 5.20e can be found in Cox (1991) who called them focus panels and used them for macro model velocity analysis. Other references are Yilmaz and Chambers (1984) and Faye and Jeannot (1986) who used the focus panel approach (maximum amplitude of depth points should be located at zero time).

From the previous examples it may be concluded that the pseudo VSP image points can be mapped to the *depth* or *one-way time* axis for a common-well and a series of shot records along the line. The results of the imaging with multi-offset, common-well pseudo VSP data are respectively called *depth image gather* and *one-way time image gather*. The events in an image gather will be aligned horizontally regardless the structure of the subsurface model, assuming the used velocity model is correct. A lower velocity shows an upward curvature. A higher velocity shows a downward curvature. The construction of the pseudo wells may be chosen along zero offset rays to include an optimal imaging and illumination of structures.

Furthermore it has been shown that by simulating virtual sources using the CFP technology, pseudo borehole shot records (with a virtual source chosen somewhere in depth) can be generated from CFP gathers. The macro model can be verified and optimum pseudo wells can be constructed by showing the energy flow in the subsurface. These energy flows can be shown by displaying the energy of downward extrapolated CFP gathers. For a correct macro model the energy will be maximum at the correct boundaries.

Chapter 6

Imaging with multi-well, common-offset pseudo VSP data

6.1 Introduction

In the previous chapter it was shown how various shot records along a line contribute to the image of the reflecting boundaries at one pseudo well location. Examples have been shown on the construction of depth and one-way time image gathers. It has been shown that with the construction of image gathers, the correctness of the macro velocity model of the subsurface can be verified. For a correct macro model the contributions from the different sources will be horizontally aligned in the image gather regardless the structure of the subsurface.

In this chapter it will be shown how single-fold images are built up using multi-well, common-offset pseudo VSP data. The availability of virtual multi-wells along a seismic line enables the lateral imaging with the aid of common-offset pseudo VSP data. The advantage to illustrate the imaging of structures with the aid of pseudo VSP data is that particular structures can be illuminated from various angles defined by the borehole/detector configuration. For an optimum illumination, the borehole/detector configuration can be chosen raypath oriented. This means that the borehole/detector configuration can be chosen along raypaths (raypath imaging). The result of the imaging with the aid of multi-well, common-offset pseudo VSP data leads to a composite section, the common-offset (source-well offset) section.

The *two-way* common-offset sections refer to the conventional common-offset (source-receiver offset; two-way offset) sections. This in comparison with *one-way* common-offset sections which refer to the multi-well, common-offset (source-well offset; one-way offset) sections.

The pseudo VSP data shown in this chapter, are generated in the space-frequency domain using the one-way wave field extrapolation operators. One-way common-offset sections with a *fixed* offset refer to *vertical* wells. Similarly, one-way common-offset sections with a *variable* offset refer to sections constructed from *deviated* wells. In Section 6.2 the construction of one-way common-offset sections will be discussed. Examples will be shown on synthetic (Section 6.3) and field data (Section 6.4). The one-way common-offset sections illustrate the contribution of various sources to the images along predefined borehole/detector configurations and clearly reveal possible acquisition deficiencies for the coverage of data given a source and receiver configuration. In other words, one-way common-offset sections reveal which shot records do not contribute to the image of a specific subsurface grid-point. The construction of *two-way time*, *one-way time* and *depth* common-offset sections will be discussed.

6.2 From image gathers to common-offset sections

In the previous chapter it was shown how image gathers can be built up from multi-offset, common-well pseudo VSP depth and one-way time records. In this section the single-fold images are built up using multi-well, common-offset pseudo VSP data. A fixed configuration is moved laterally for the various sources and pseudo VSP data are generated to determine the image points. Figure 6.1 shows that for a fixed source-well configuration the “*image points*” can be mapped to construct depth and/or one-way time common-offset sections. Note that the source-well offset can be either negative or positive.

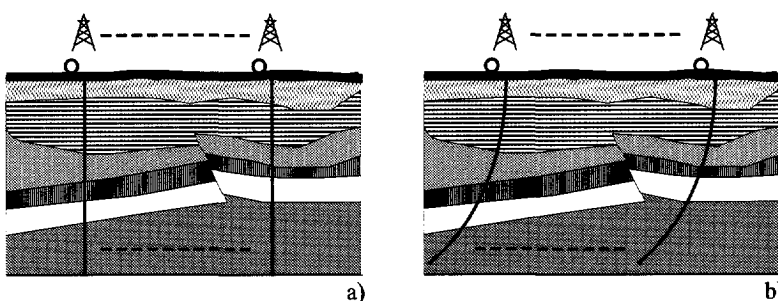


Figure 6.1 The construction of one-way common-offset (source-well offset) sections for a)fixed offset (vertical wells) and b)variable offset (deviated wells).

One-way common-offset sections illustrate the illumination of structures at the pseudo well location for specific borehole/detector configurations. Each trace from a common-offset section represents the result of *one single source*. However, for an optimal illumination of subsurface structures with the aid of pseudo VSP data, it is necessary to take into account all the sources (at the surface) contributing to the image at a particular pseudo well.

By constructing one-way common-offset sections, a series of single-fold imaged (half-migrated) sections using multi-well, common-offset pseudo VSP data are obtained, each showing different illuminations and thus another view on the imaged structures in the subsurface. These one-way common-offset sections can be used to obtain a better interpretation of different imaged structures by choosing specific pseudo wells.

6.2.1 Construction of *two-way* and *one-way* common-offset sections

In this section the construction of two-way and one-way common-offset sections will be discussed. In the midpoint technology, Common Mid Point (CMP) gathers (two-way) can be reordered to *two-way* common (source-receiver) offset sections (offset definition in Figure 6.2a). It is important to notice that the two-way common-offset sections contain unmigrated data.

This in contrast with the *one-way* common-offset sections in which the events are half-migrated. These one-way common (source-well) offset sections can be obtained by imaging with multi-well, common-offset pseudo VSP data (offset definition in Figure 6.2b). The resulting one-way common-offset sections can be displayed in depth or one-way time. The one-way common-offset sections clearly reveal possible acquisition deficiencies for the coverage of data given a source and receiver configuration. *One-way* common-offset sections can be determined by re-ordering one-way image gathers. Alternatively, *one-way* common-offset sections can be constructed by mapping pseudo VSP image points to the depth (result : *depth* common-offset section) or to the *one-way* time axis (result : *one-way time* common-offset section) for multi-well, common-offset configurations.

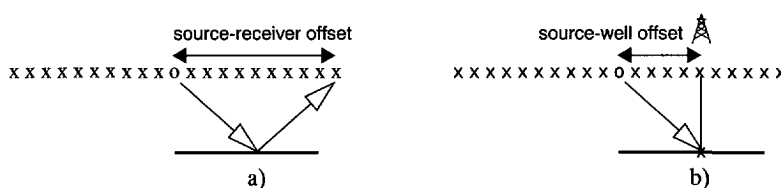


Figure 6.2 Definition of a) source-receiver offset (two-way offset) and b) source-well offset (one-way offset).

Table 3 shows the comparison between the construction of two-way and one-way common-offset sections.

Table 3 Construction of two-way and one-way common-offset sections (Berkhout, 1997a).

<i>two-way</i> common-offset section	<i>one-way</i> common-offset section
orientation : midpoint	orientation : gridpoint
offset : source-receiver offset (two-way)	offset : source-well offset (one-way)
procedure : sorting from surface data	procedure : sorting from one-way image gathers
result : in two-way time	result : in one-way time or depth
data : unmigrated data	data : half-migrated data (single-fold images)

6.3 Synthetic data examples

6.3.1 Syncline model and dataset

In the following example, the synclinal model is used to illustrate the construction of different common-offset sections. For a description of the syncline model and data the reader is referred to Section 4.3. Figure 6.3a illustrates the construction of the two-way conventional common-offset sections. The two-way offsets are respectively $0m$, $750m$ and $1500m$. In Figure 6.3b the result are shown of the constructed one-way time common-offset sections. The one-way offset used here are $0m$, $375m$ and $750m$. Note that the data is half-migrated. For comparing the one-way common-offset sections with each other an additional time correction need to be performed before adding the different common-offset sections with each other. The structures in the different one-way time sections should then be aligned (for a correct model). The depth common-offset sections have been depicted in Figure 6.3c. The importance of these common-offset sections is that for a correct subsurface model, the corresponding structures in all the different sections need to be comparable and located at the same (x, z) location. Furthermore it is important to notice that addition of the different common-offset sections should give the full prestack migration result as shown in Figure 6.4.

The depth and one-way time common-offset sections may show some artifacts due to incomplete illumination (single-fold images obtained from single shot records). A part of Figures 6.3c have been blown up for a better view of the artifacts and is depicted in Figure 6.3d. As can be identified the artifacts (around the diffraction point) appear at different angles. In this example vertical wells have been used. All other kind of deviated wells may be used for positive and negative one-way offsets.

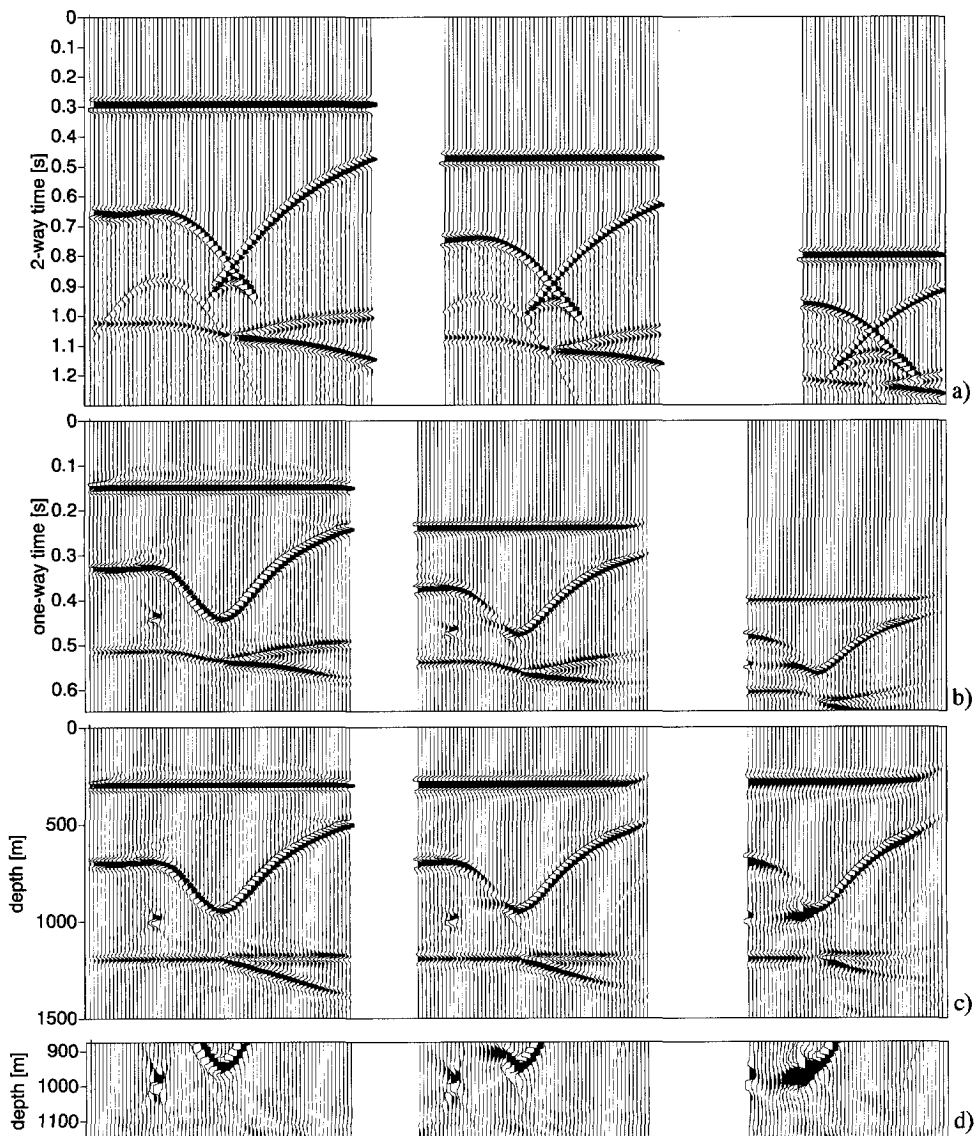


Figure 6.3 a) Two-way time common-offset sections of the syncline model for respectively the two-way offsets : 0m, 750m and 1500m. b) One-way time common-offset sections for respectively the one-way offsets : 0m, 375m and 750m and c) depth common-offset sections for the one-way offsets : 0m, 375m and 750m.
d) Blow up of a part of (c).

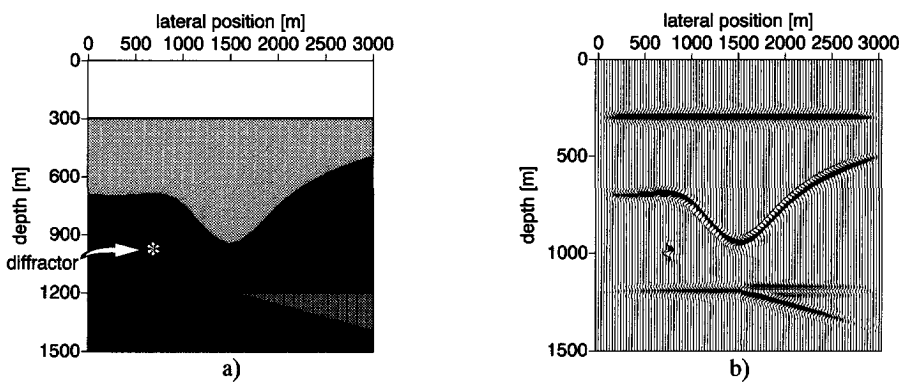


Figure 6.4 a) Syncline model and b) depth image after full prestack depth migration.

6.3.2 Picrocol model and dataset

In the following illustrations, the Picrocol model has been used. The Picrocol model and its dataset have been discussed in the previous chapter. The dataset and model were provided by the Institut Français du Pétrole (IFP).

For the Picrocol data, various one-way time common-offset sections for vertical wells and deviated wells have been constructed. The various source-well configurations have been depicted on the right of Figure 6.5. In a similar way, corresponding depth common-offset sections have been constructed (see Figure 6.6).

From the common-offset sections it can be seen that the different borehole/detector configurations result into different illuminations of the structures. Furthermore the correspondence between the events in the one-way time and the depth common-offset sections is remarkable. Note the velocity pull-up effect below the salt dome in Figure 6.5 and its mapping and its corresponding imaging in the depth common-offset section shown in Figure 6.6. Some artifacts appear in the common-offset sections because of the incomplete imaging (*only one* shot record is used each time). These artifacts would be less in the use of more shot records.

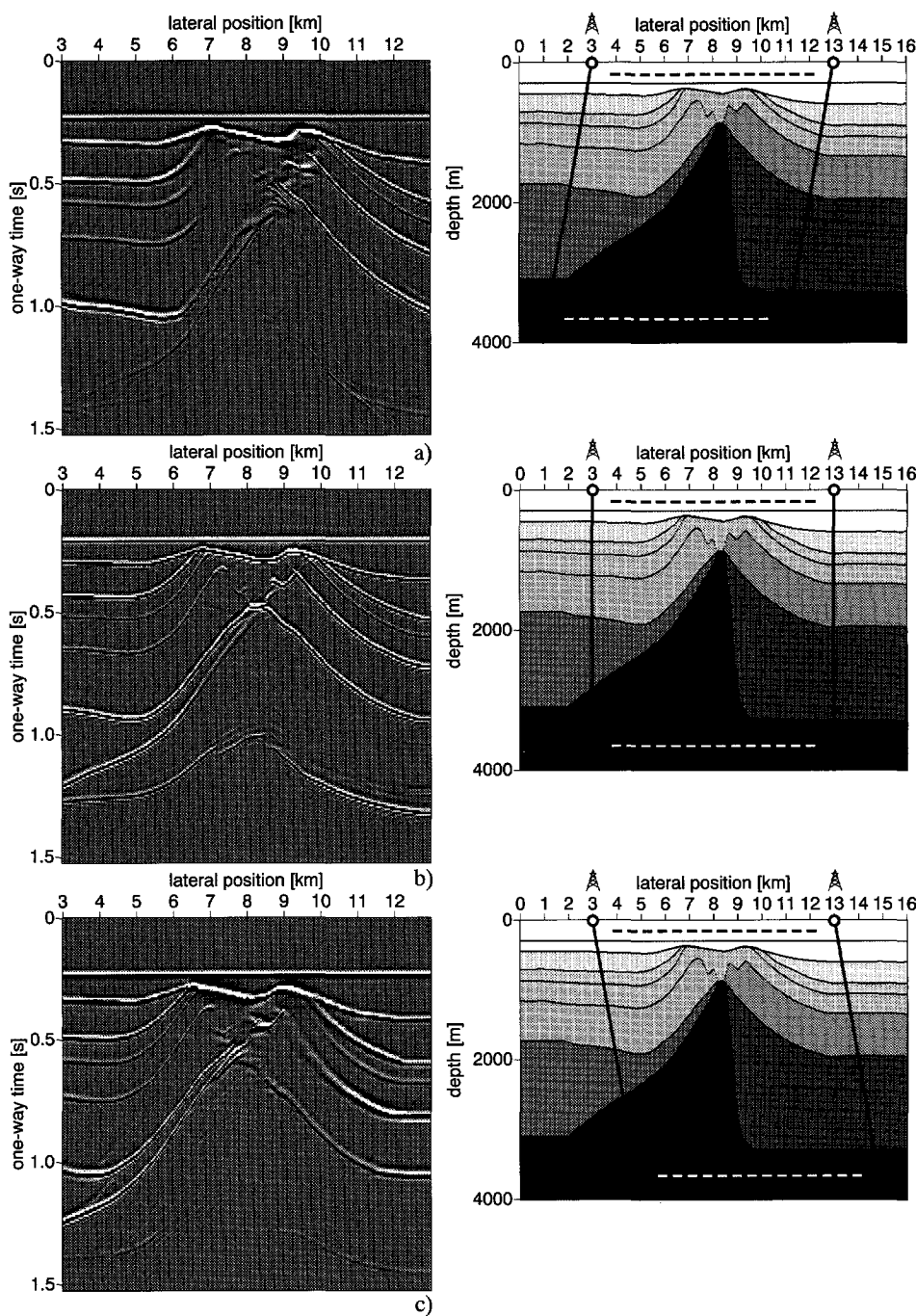


Figure 6.5 One-way time common-offset sections for vertical and deviated wells.

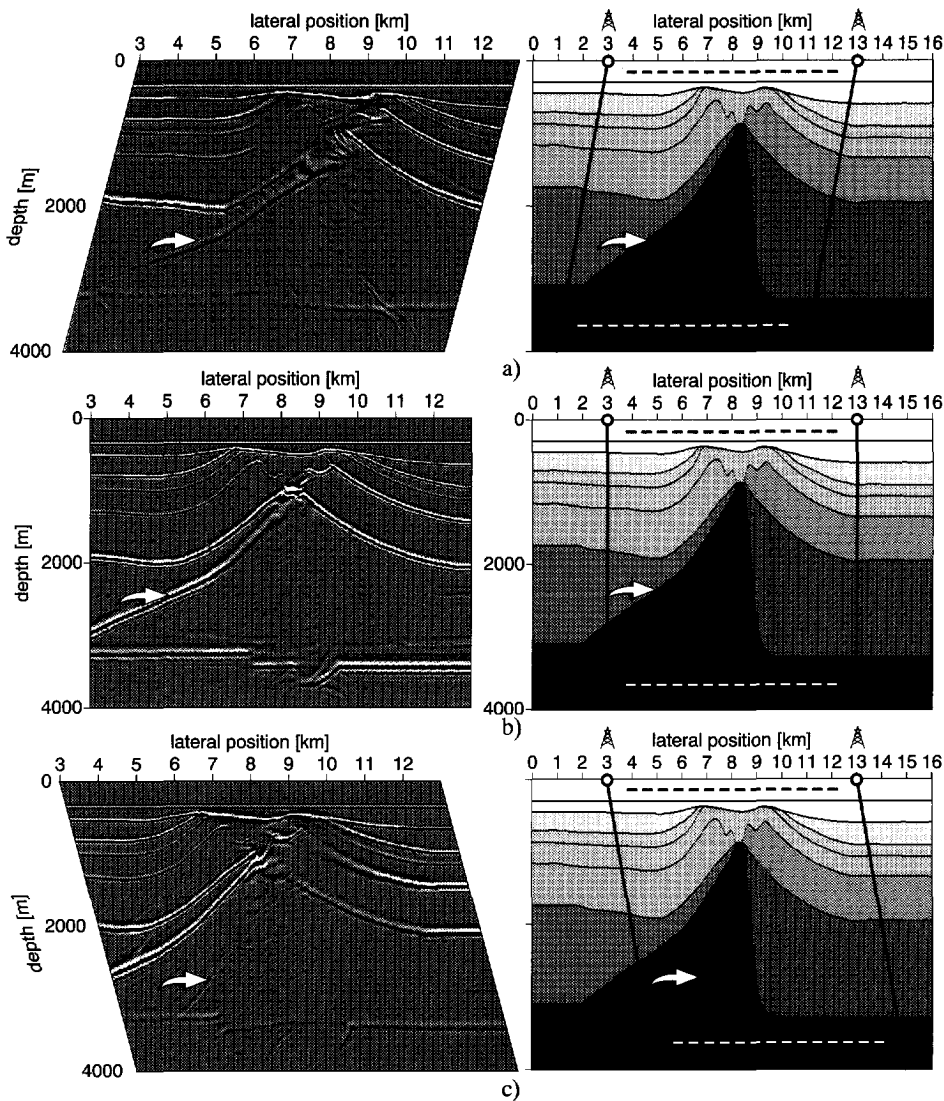


Figure 6.6 Depth common-offset sections for vertical and deviated wells.

In the following, an example will be shown on a *sector scan* configuration. Here the illumination is shown from one specific surface point to many different directions. A series of pseudo wells are used as shown in Figure 6.7a. The shot record with the shot location at $x=7\text{ km}$ is shown in Figure 6.7b. Figure 6.7c illustrates the shot record migration for the single shot. The image points of the pseudo VSP data have been determined and mapped to the depth axis. The result is depicted in Figure 6.7d. The triangle in this figure shows the area (x, z) in which the image points have to be mapped.

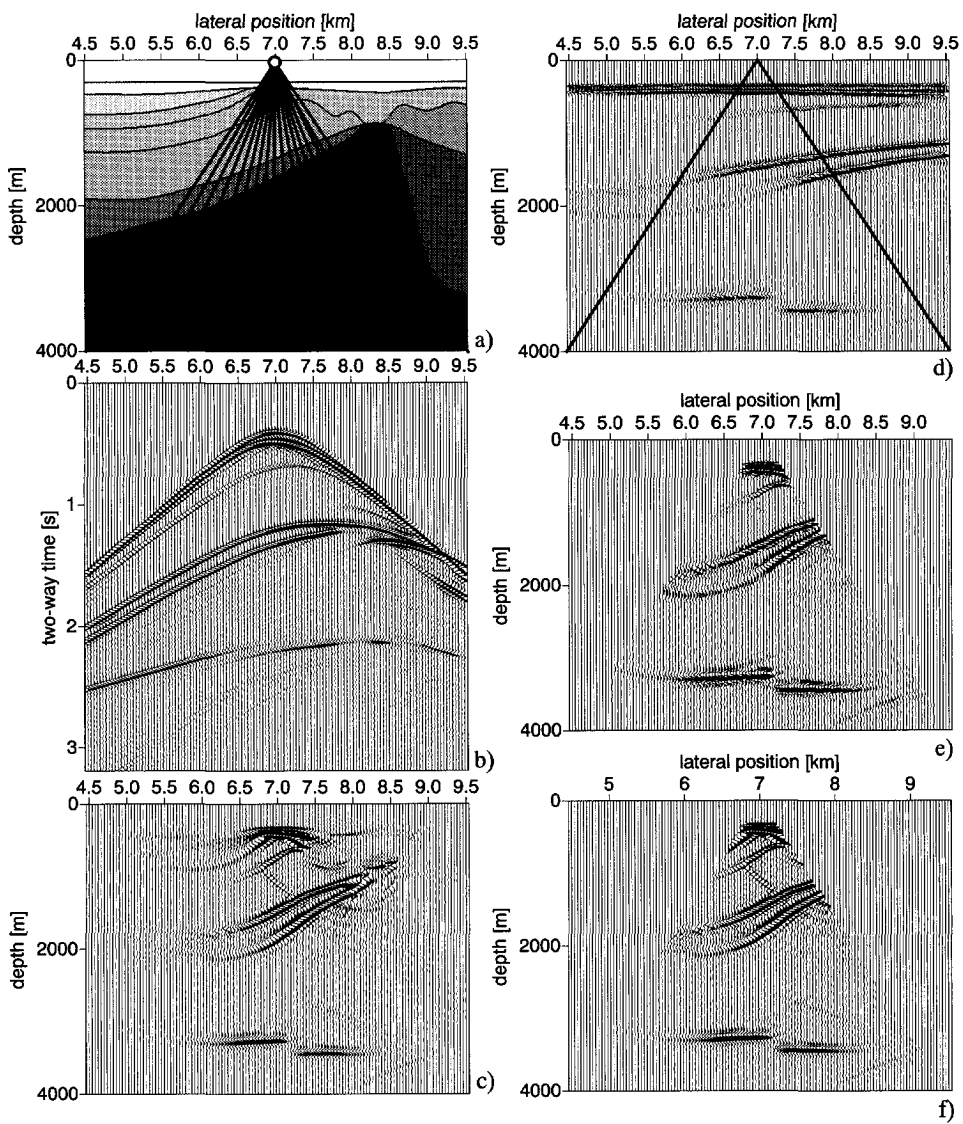


Figure 6.7 Sector scan : a) configuration of the wells, b) shot record with source at 7 km, c) prestack single shot record depth migration, d) image constructed from the pseudo VSP image points (in depth), e) localizing Figure 6.7d into the correct triangle (resampling the data laterally) and f) mute of Figure 6.7c to make an optimal comparison possible with Figure 6.7e.

This is done in Figure 6.7e in which the data have been resampled laterally. To make a comparison of Figure 6.7e with the shot record migration, the data of Figure 6.7c has been muted (see Figure 6.7f).

6.3.3 SEG/EAGE Salt model and dataset

In this section the Salt model is used, issued from the joint SEG/EAGE 3-D Modeling Project (SEM). The SEG/EAGE Salt model (Figure 6.8) is one of the geological models that is used for modeling 3-D synthetic seismic datasets. The dimensions of the model are $13.5\text{km} \times 13.5\text{km} \times 4.2\text{km}$. It has been built to address data quality issues encountered around the types of geological salt bodies in the Gulf of Mexico (Aminzadeh et al., 1995).

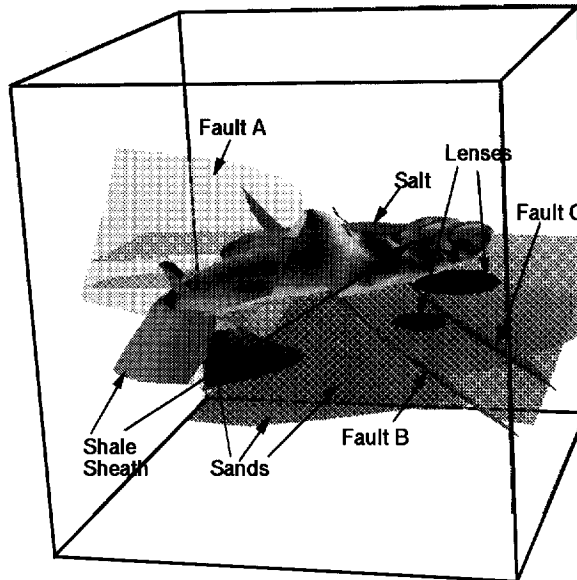


Figure 6.8 SEG/EAGE Salt model with lots of surfaces
(modified after the SEG/EAGE Salt Model Committee).

Figure 6.9a illustrates the A-A' profile. A 2-D seismic line has been modeled along this profile and was provided by Amoco Exploration and Production Technology Group, Tulsa, U.S.A.. The A-A' profile has been used by O'Brien and Gray (1996) for comparing different migration results. The modeled data consists of 325 shot records moving from left to the right. The location of the first shot is at position $x=0\text{m}$ with a receiver line ranging from $x=-4267.2\text{m}$ (-14000ft) to $x=0\text{m}$. The second shot is positioned at 48.768m (160ft). The sampling interval of the receivers is 24.384m (80ft). The maximum frequency content of the data is about 25Hz and the time sampling interval is 8ms. The reflectors in the SEG/EAGE Salt model are constructed by spikes positioned in a smoothly varying background (120% of background velocity). The structure of the salt is presented with a high velocity of $c_p=4480\text{m/s}$. A zero-offset section has been extracted from the modeled data and is shown in Figure 6.9b. From this figure it can be seen that there are many diffraction curves. A depth section after full prestack depth migration is shown in Figure 6.9c.

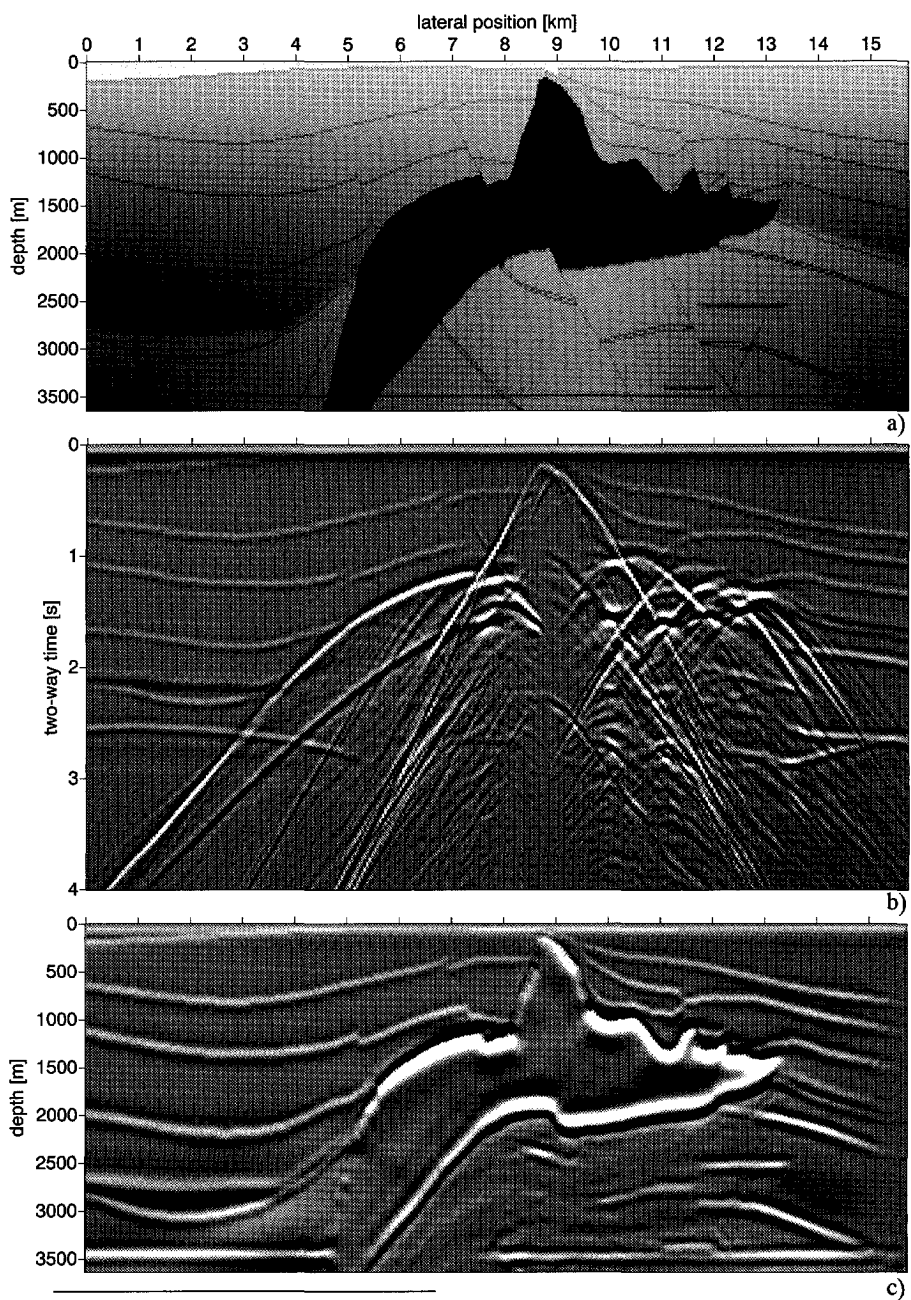


Figure 6.9 a) SEG/EAGE Salt model (A-A' profile), b) zero offset section (the 5s data is displayed here up to $t=4s$). c) Depth section after full prestack depth migration.

Additional zero traces have been added to both sides of the shot records to image energy at large angles.

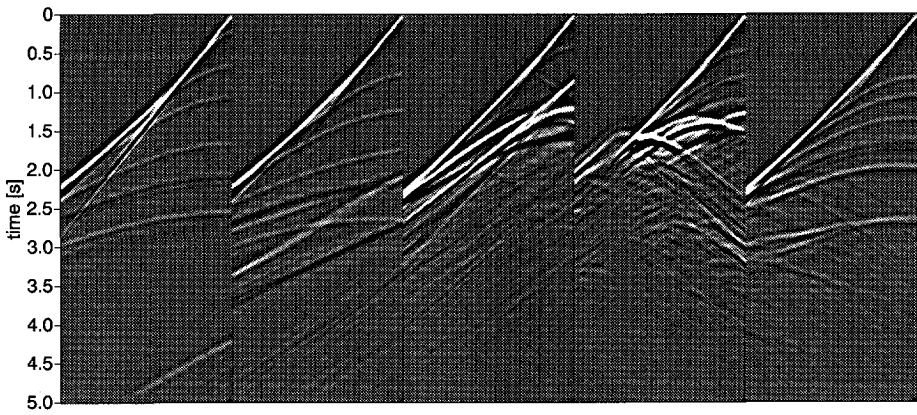


Figure 6.10 Five shot records from the Salt model A-A' profile : shot#1,#82,#163,#244 and #325.

Figure 6.10 shows five shot records (without surface-related multiples) from the 2-D modeled data along the A-A' profile. The image gathers are illustrated in Figure 6.11.

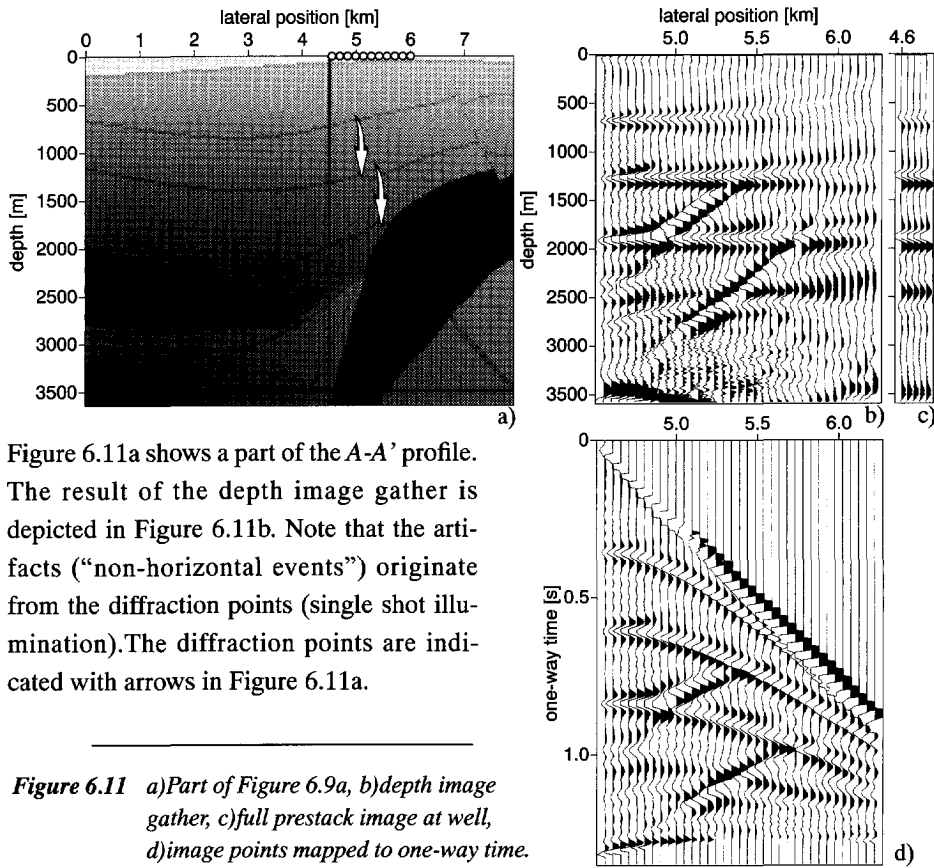


Figure 6.11a shows a part of the A-A' profile. The result of the depth image gather is depicted in Figure 6.11b. Note that the artifacts (“non-horizontal events”) originate from the diffraction points (single shot illumination). The diffraction points are indicated with arrows in Figure 6.11a.

Figure 6.11 a)Part of Figure 6.9a, b)depth image gather, c)full prestack image at well, d)image points mapped to one-way time.

For a full image at the well location, the contribution is necessary of all the sources along the line. A plain stack of Figure 6.11b results into the prestack depth migrated result at the well (see Figure 6.11c; trace has been reproduced 5 times for display purposes). It is important to notice that the horizontal alignment of the events in Figure 6.11b indicates the correctness of the model. Figure 6.11d shows the results for mapping the pseudo VSP image points to one-way time. Note the correspondence of the events in comparison with Figure 6.11b. The data of Figure 6.11d has to be moveout corrected and stacked for a full prestack one-way time image at the well.

Figure 6.12 shows the constructed depth common-offset sections for vertical wells. The one-way offsets are respectively 250m, 1000m and 1500m.

Comparing the sections for different offsets, the right flank of the salt dome (indicated with the arrow in Figure 6.12b) and some structures at the right are well imaged (see for comparison Figure 6.9c). These depth common-offset sections show depth sections with different illuminations of structures. Addition of these sections should give the same result as that obtained by full prestack depth migration. The depth common-offset sections may contain some artifacts (due to single shot illumination on diffractions). It is interesting to see that the fault (fault B in Figure 6.8) is visible in the depth common-offset sections and is not clearly visible in Figure 6.9c. This can be explained as follows. In the full prestack depth migration the structure of the salt dome is dominant in amplitude. Therefore it is quite difficult to identify the weaker structures. Since the depth common-offset sections illustrated the image data for particular pseudo wells, it may be that weaker events become better visible and more dominant events are being suppressed. In other words, the construction of the depth common-offset sections may be useful for the illumination of particular structures such that other dominant reflections are suppressed. Note that each type of deviation of the well can be used for the construction of the depth common-offset sections. Furthermore comparing the sections in Figure 6.12, it is clear that the angle of the artifacts is changed in the different sections. On the other hand, the structures in Figure 6.12 corresponding to the structures visible in the model Figure 6.9a, are mapped to their correct location for a correct model but show different amplitude behaviour. To get a better understanding why the fault indicated with the arrows in Figure 6.12, becomes visible in the common-offset sections, some rays have been calculated from the fault to the surface. A depth has been chosen on the fault of interest and a focusing beam have been constructed (Figure 6.13a).

Furthermore some rays have been shot from the same depth point (Figure 6.13b) for a better understanding of the transmitted energy. As can be seen from Figure 6.13, most of the energy that may illuminate that specific fault, comes from only some shot records along the surface (shot locations around 10km and 11km).

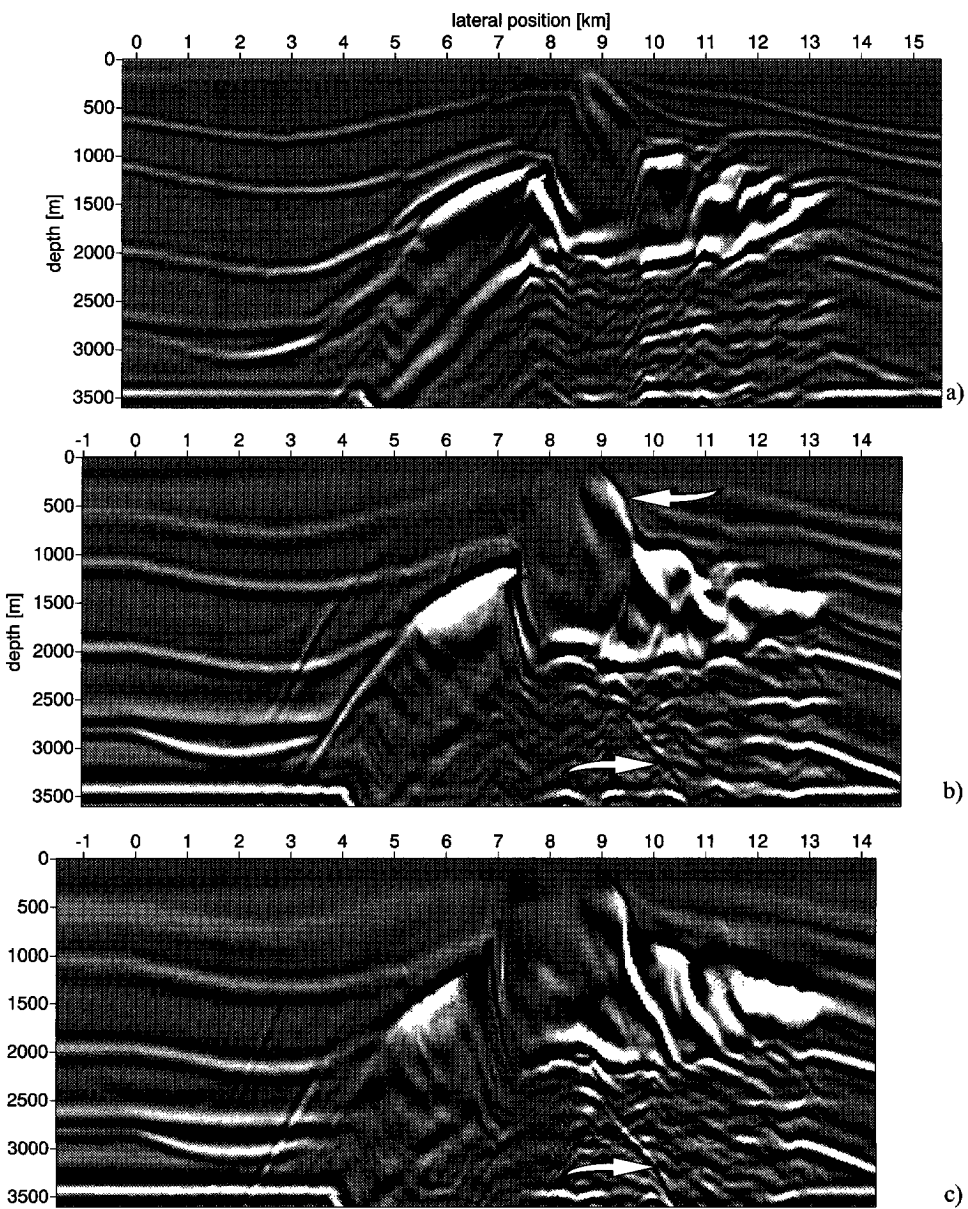


Figure 6.12 Depth common-offset sections for vertical wells. The offsets are respectively a) 250m, b) 1000m and c) 1500m.

Since only some shot records contribute to the image of that specific fault the weak fault reflection is lost in the prestack migrated result, because of the bad quality and SNR of the imaged data below the salt body.

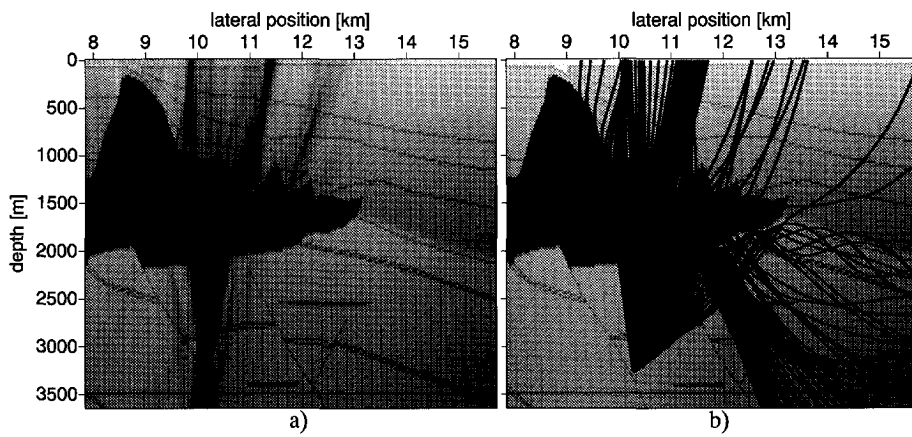


Figure 6.13 a)Focusing beam for a source on the fault and b)calculated rays for same depth point.

The common-offset sections in Figure 6.12, were constructed for positive offsets. In a similar way, a depth common-offset section has been constructed for a negative offset (-500m) and is depicted in Figure 6.14. Zero traces have been added to the end of spread shot gathers to study the steep faults in the resulting section. Note that the left flank of the salt body is imaged and most of the other structures illuminated from the left.

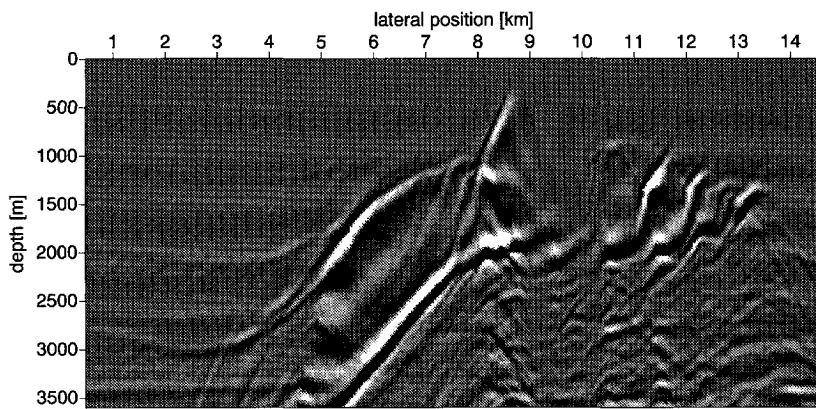


Figure 6.14 Depth common-offset section for vertical wells. The offset is -500m.

Figure 6.15 illustrates a depth common-offset section for deviated wells. Note that the imaged fault is also visible in the result obtained using deviated wells. For comparison, 4 standard common-offset Kirchhoff migrations have been added and the result is depicted in Figure 6.16. Note that the fault is not clearly visible in the result of the stack of the four common-offset Kirchhoff migrations.

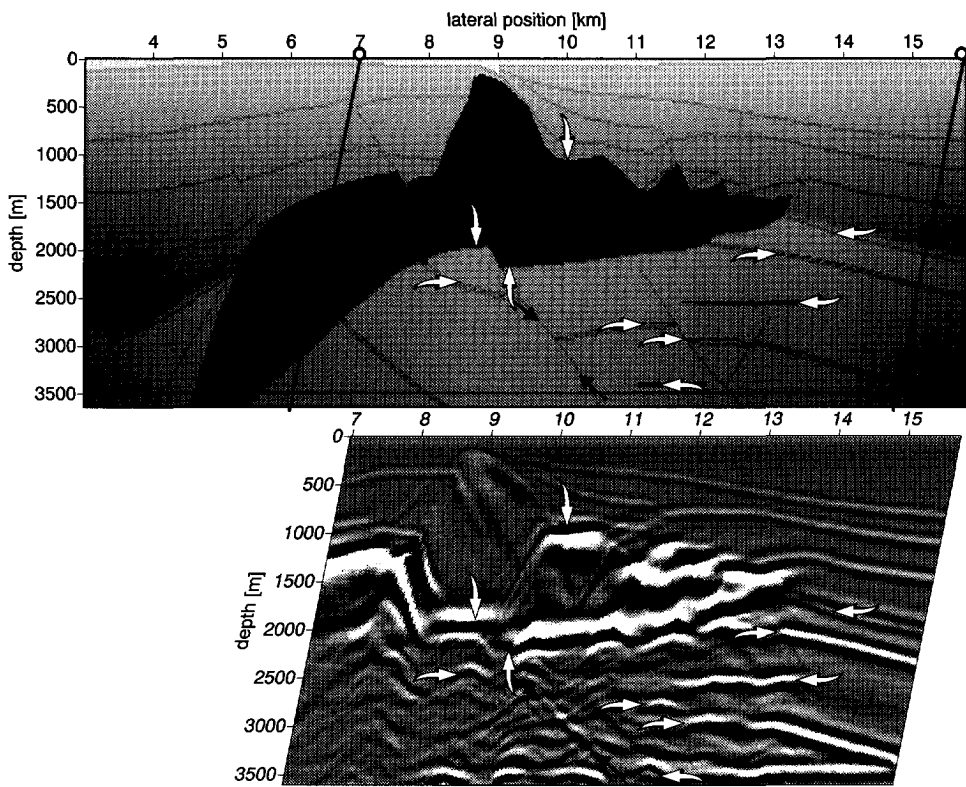


Figure 6.15 Depth common-offset section for deviated wells (offset ranging from 25m to 1000m).

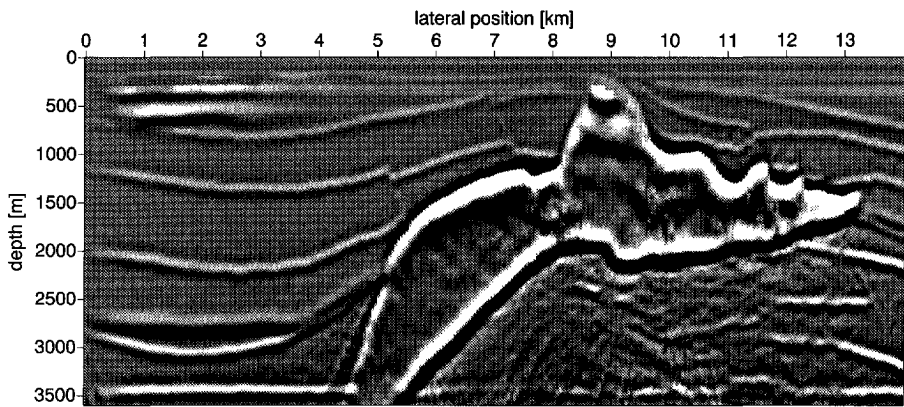


Figure 6.16 Stack of standard common-offset Kirchhoff migrations - offsets : 0m, 500m, 1000m and 1500m.

Figure 6.17 shows the standard common-offset Kirchhoff migration (two-way offset : 2000m) in comparison with the one-way common-offset section (as shown in Figure 6.12b) in which the one-way offset is 1000m. It is interesting to see from Figure 6.17 that the fault indicated in Figure 6.12b with an arrow (fault B in Figure 6.8) is quite difficult to identify.

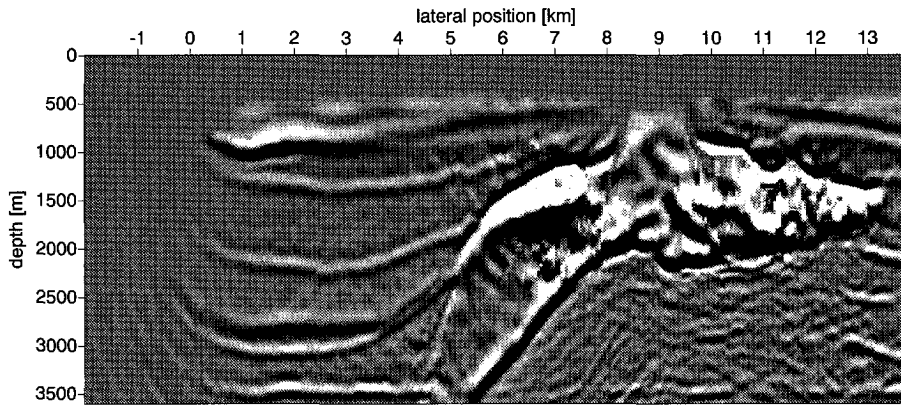


Figure 6.17 Standard common-offset Kirchhoff migration (two-way offset : 2000m).

For a better understanding of the contribution of the shot records to the images formed in the depth common-offset sections, the following experiment is performed. Two focus points have been chosen : one on the left flank of the salt dome and the other on the right flank (see top of Figure 6.18). For both chosen focus points the focusing operator is determined and is displayed in Figure 6.18a for the chosen focus points respectively. Snapshots have been generated performing a forward recursive downward extrapolation of the focusing operator through the model (top of Figure 6.18). The corresponding CFP gathers have been determined and are depicted in Figure 6.18b. Furthermore the CFP gathers have been moveout corrected with the time-reversed focusing operator and the results for both focus points are depicted in Figure 6.18c. The double focusing prestack migration results for the focus points can be obtained by a plain stack of the results moveout corrected CFP gathers (Berkhout, 1997a and 1997b). Note that the events Figure 6.18c are horizontally aligned at $t=0s$ (for a correct macro model the time-reversed focusing operator and the focus point response are time-coincident). From this experiment it can be clearly seen that for the focus on the left of the salt dome most contribution to the image at the left flank comes from the shot records with sources at the left of the focus point. Similarly, for the focus on the right of the salt dome most contribution to the image at the right flank comes from the shot records with sources at the right of the focus point. In other words, for the focus point on the left of the salt dome the Fresnel zone is moving to the left and for the focus point on the right of the salt dome the Fresnel zone is moving to the right.

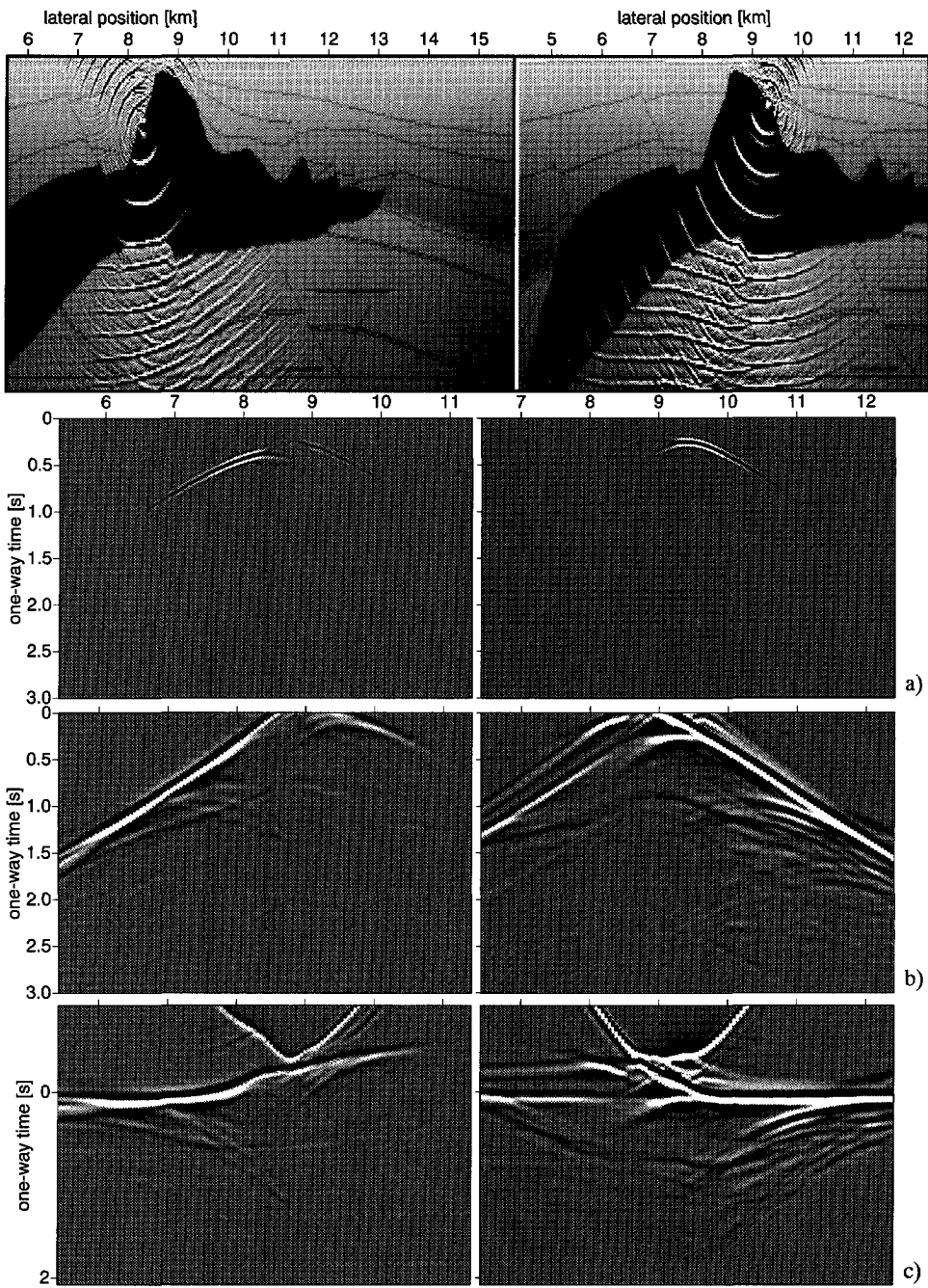


Figure 6.18 Focusing points with corresponding operators, CFP gathers and moveout corrected CFP gathers showing the contribution of the Fresnel zone in the full prestack image.

The moveout corrected CFP gathers can be used for a better understanding of the images which are formed in the depth common-offset sections shown in this section. For a better understanding why the fault in Figure 6.12b and Figure 6.12c are better visible than in the full prestack depth migration and common-offset Kirchhoff migration can be explained with Figure 6.19.

For the same focus point as used in Figure 6.13, the time-reversed focusing operator is constructed and depicted in Figure 6.19a. A CFP gather has been constructed using the focusing operator. The CFP gather has been moveout corrected with the time-reversed operator and the result is depicted in Figure 6.19b.

Figure 6.19 shows the contribution of all the sources at the surface to the prestack migration result at the focus point with coordinates $(x,z)=(10.0\text{km},3.2\text{km})$. For a correct model the contributions of the different sources should be aligned at $t=0\text{s}$. However, in Figure 6.19b it can be clearly seen that only a small number of shot records at the surface contribute to that specific image point (see arrows).

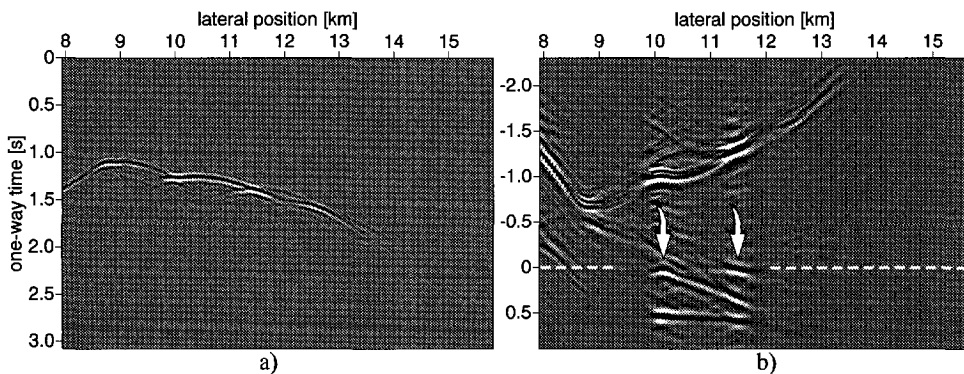


Figure 6.19 a) Time-reversed focusing operator for the same focus point as in Figure 6.13 : $(x,z)=(10.0\text{km},3.2\text{km})$ and b) corresponding moveout corrected CFP gather.

The following can be concluded regarding the differences in imaging the faults below the salt body : geologists always infer fault locations through subhorizontal reflector discontinuities. The energy scattered from faults is largely lost in standard processing schemes which emphasize subhorizontal reflectors. The pseudo VSP emphasizes the subvertical reflectors (i.e. faults).

6.4 Field data examples

In this section some examples are illustrated on two field datasets : a marine and a land dataset, respectively.

6.4.1 ELF model and dataset

The data shown in this section is a marine line consisting of 378 shot records. The data was provided by the Institut Français du Pétrole (IFP) and was owned originally by ELF. The data were made available for the ISI (Integrated Structural Imaging) project of the Joule II program of the European Committee.

A macro subsurface model has been estimated (structure shown in Figure 6.20a; Kabir, 1997). The image result of the full prestack depth migration is shown in Figure 6.20b. The prestack depth migration has been performed in the space frequency domain. The depth step in the recursive wave field extrapolation was chosen $10m$.

Figure 6.21 illustrates an Integrated Seismic Display (ISD) of shot record, pseudo VSP, part of the model and part of the migrated section. The well configuration and source location are indicated in the model and the migrated section. The parameters for the data acquisition were : shot spacing : $40m$, receiver spacing : $26.66m$, sampling rate of the data : $4ms$, total number of samples per trace : 1250 . The offset range of the shot records (120 traces per shot record) ranges from $-187,5m$ to $-3362m$.

The arrows in Figure 6.21 show the integration of events in the shot record, pseudo VSP and the migrated depth section. The pseudo VSP data has been generated for a deviated well. In this way, the events in the shot record (indicated by the 2 pointers) can be followed from the shot record through the pseudo VSP until they make an intersection with the downgoing source wave field (in pseudo VSP). In the use of a vertical well, these events would fade away after some depth steps and would never make an intersection with the downgoing source wave field in the pseudo VSP data.

Another display of the integrated datasets showing the value of the pseudo VSP data as integration is shown in Figure 6.22. Here the integration is shown between the shot record and the generated pseudo VSP (top of Figure 6.22). The integration between the pseudo VSP data and the prestack migration result is illustrated at the bottom of Figure 6.22 (Note the deviation of the well).

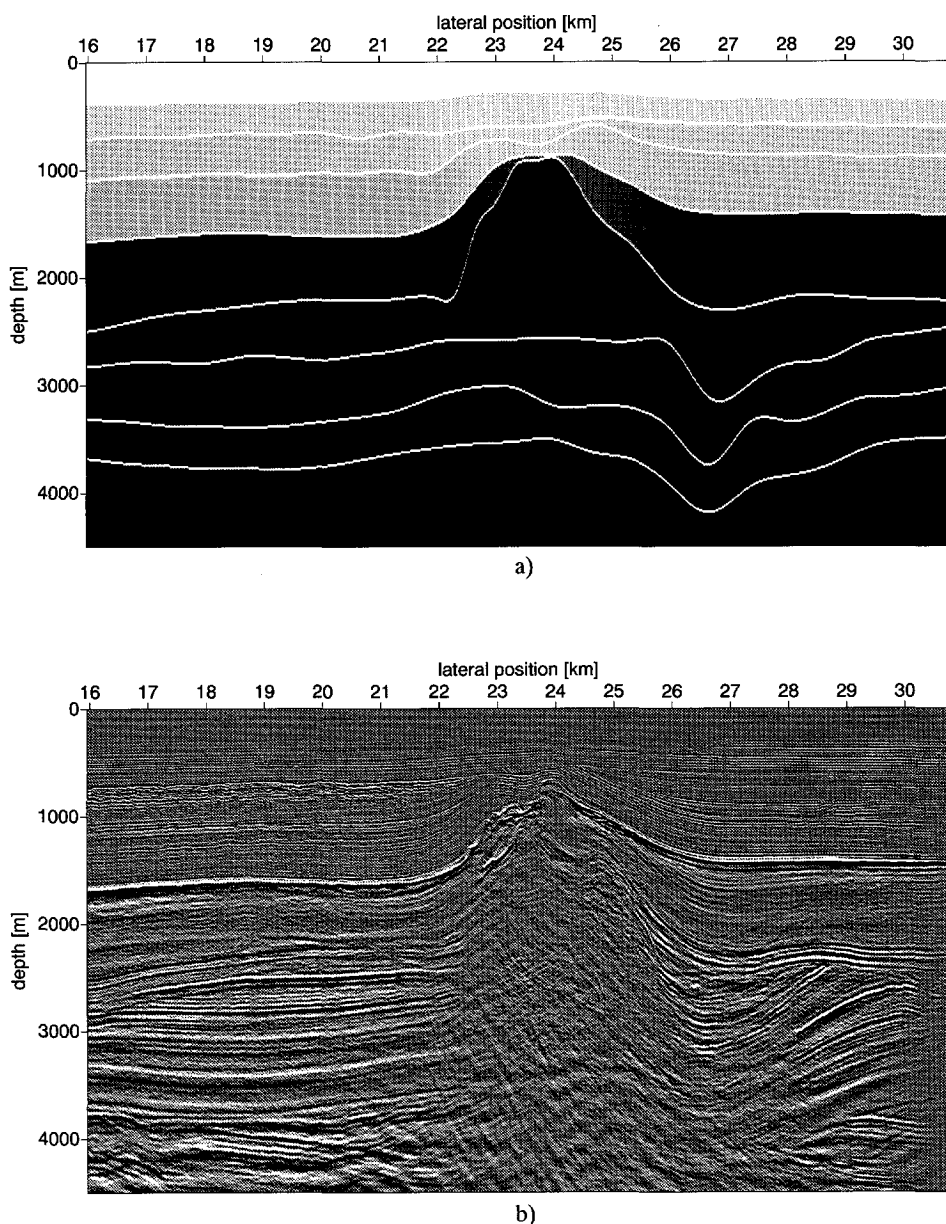


Figure 6.20 a) Estimated macro model for the field data example (courtesy ELF) and b) depth image after full prestack depth migration.
The data was recorded in the North Sea.

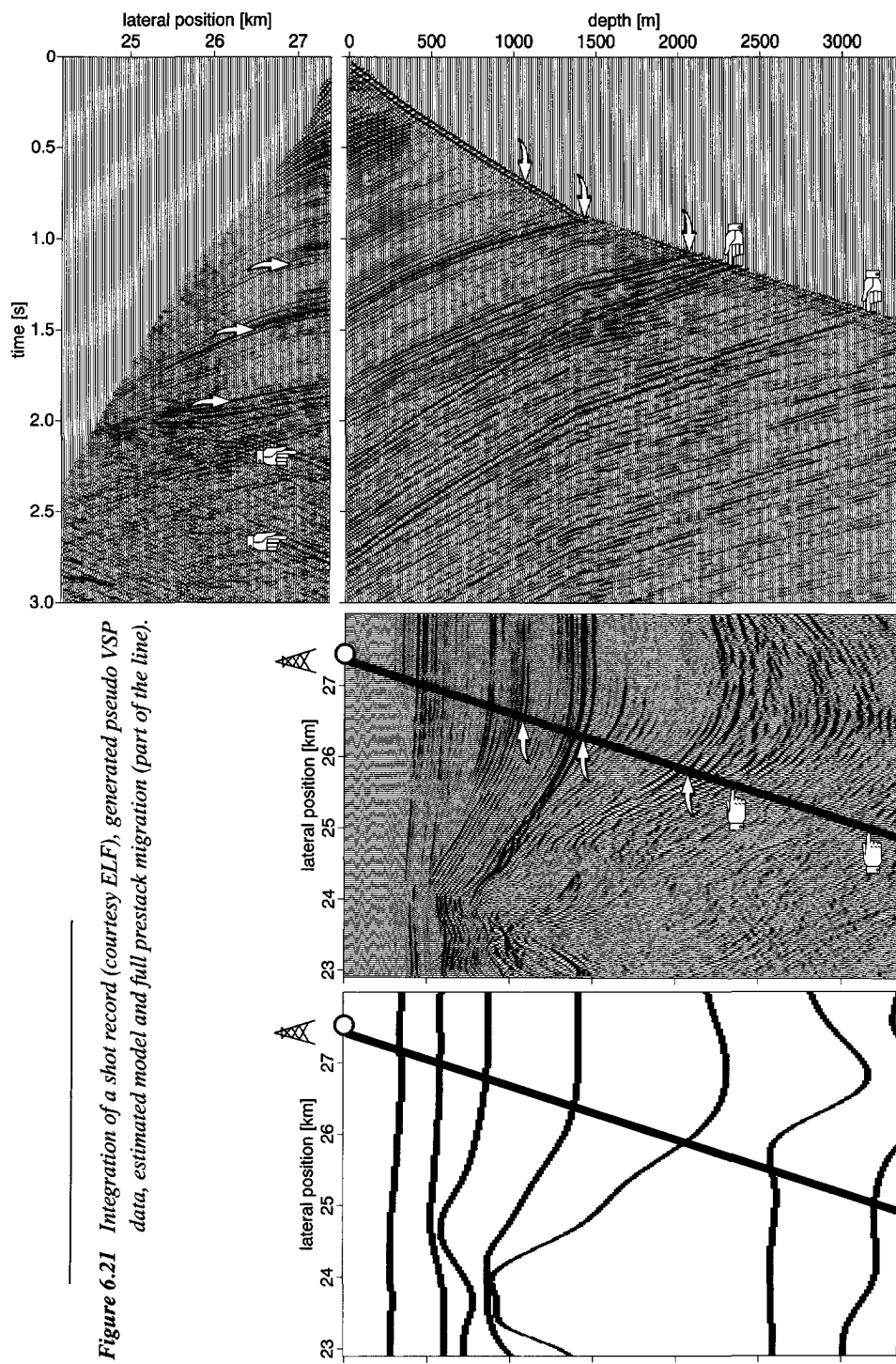


Figure 6.21 Integration of a shot record (courtesy ELF), generated pseudo VSP data, estimated model and full prestack migration (part of the line).

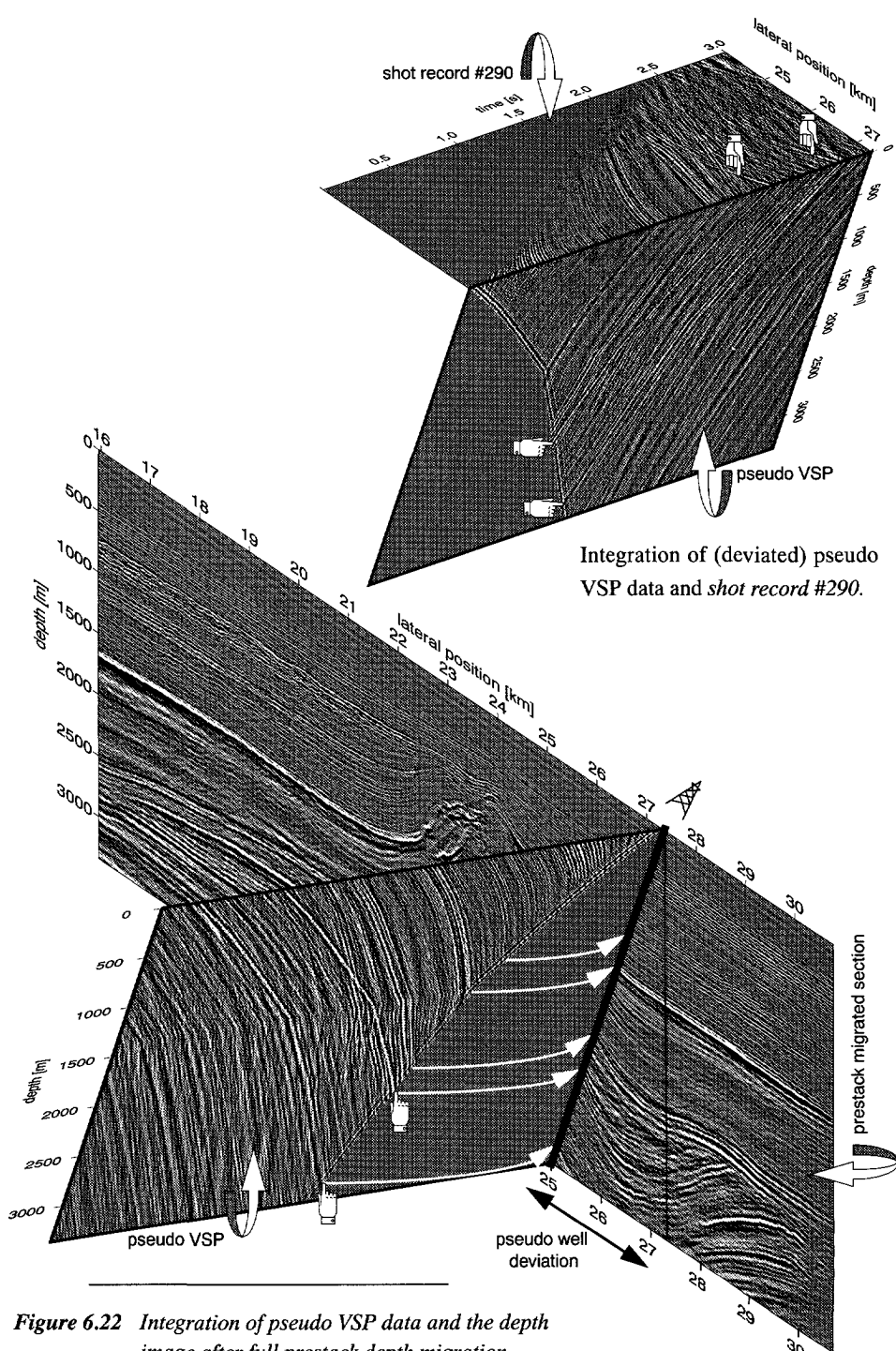


Figure 6.22 Integration of pseudo VSP data and the depth image after full prestack depth migration.

The one-way time common-offset sections constructed along the whole seismic line are shown in Figure 6.23a (for deviated wells) and in Figure 6.23b (for vertical wells). It is interesting to notice the imaging of the different structures in both sections: in Figure 6.23a the right flank is imaged because of the deviation of the well. On the other hand by using vertical wells, the horizontal structures are illuminated. Note that one trace from the one-way common-offset sections (Figure 6.23a and b) represents the result of one single shot record. Each trace is the result of generating pseudo VSP data from the shots and mapping the VSP image points to the one-way time axis.

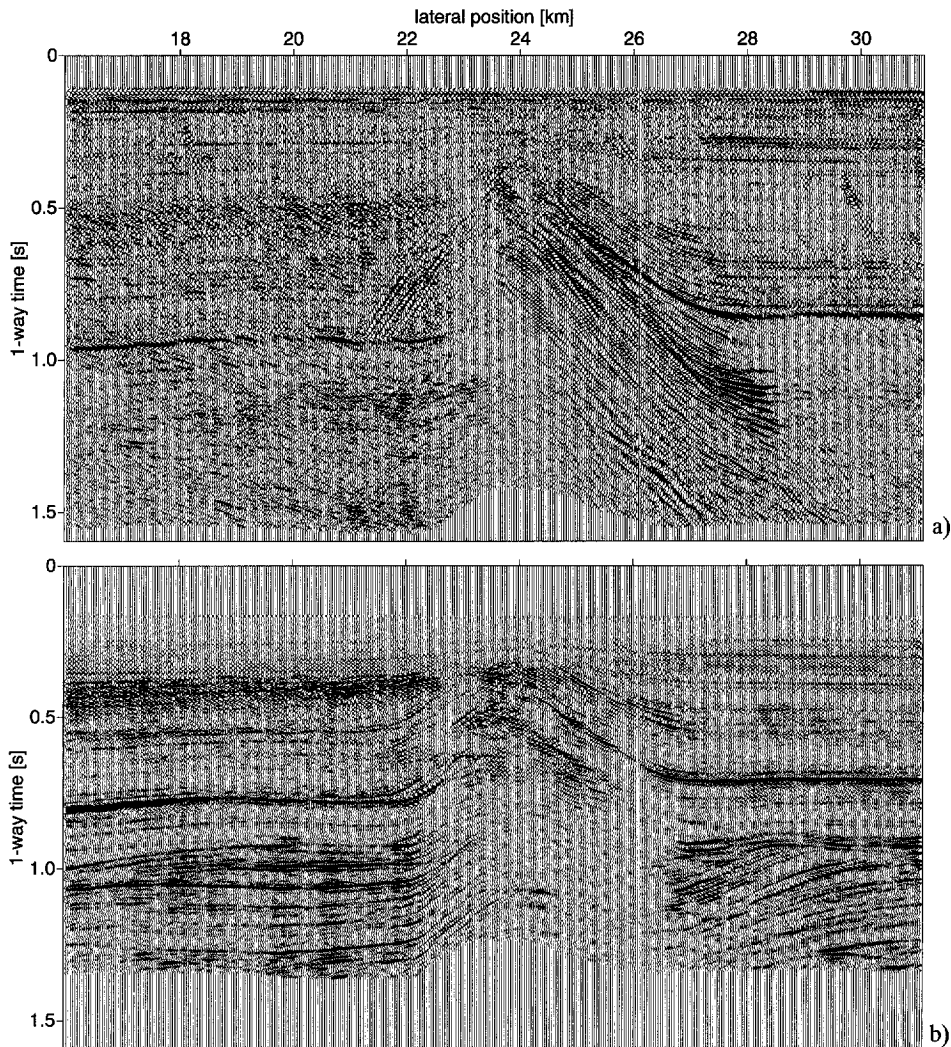


Figure 6.23 One-way time common-offset sections : a) deviated wells and b) vertical wells.

The construction of *two-way time* and *one-way time* common-offset sections is illustrated in Figure 6.24 (Figure 6.24a : two-way time common-offset section with source-receiver offset: 800m. Figure 6.24b shows the one-way time common-offset section (single-fold migrated data). The image points from 400m offset (source-well offset) pseudo VSP data have been mapped to the one-way time axis. To obtain a one-way time image, the one-way time common-offset section of Figure 6.24b need to be corrected to the one-way times such that the main boundaries will appear at their correct one-way image time.

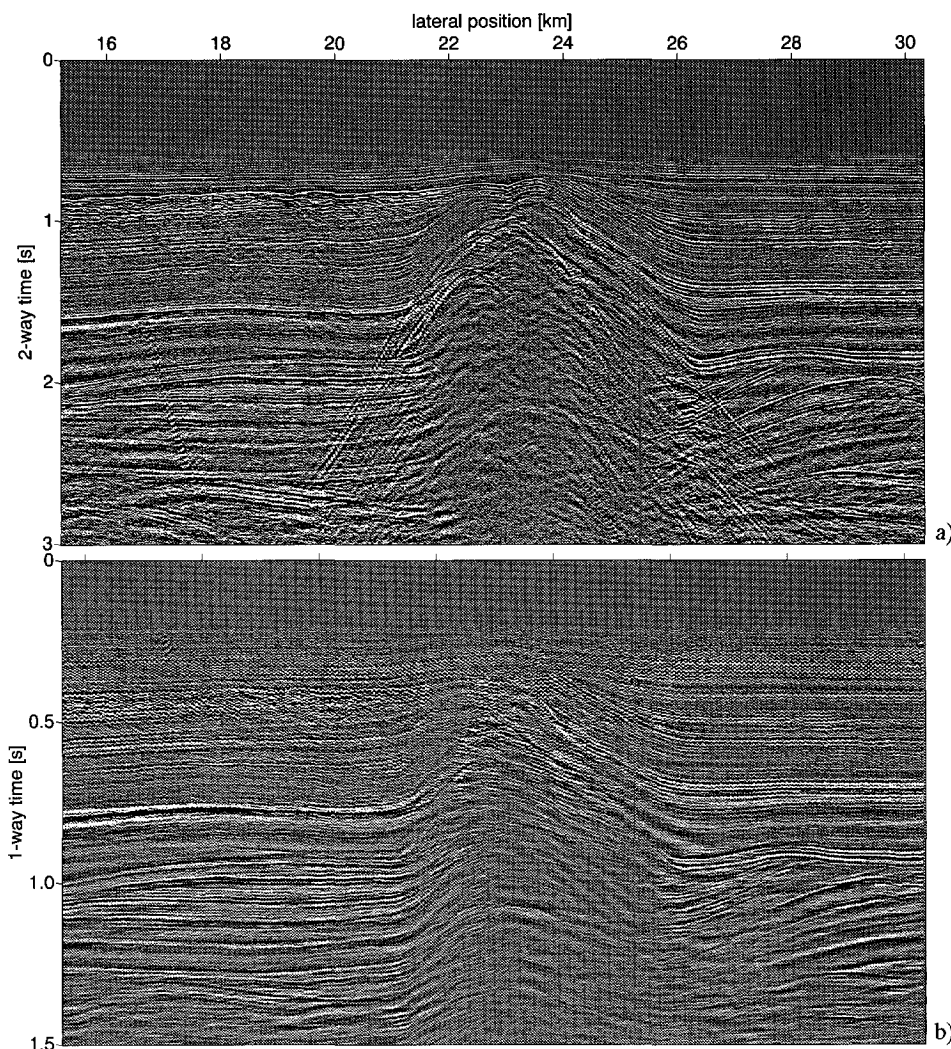


Figure 6.24 Common-offset sections : a)two-way time and b)one-way time.

6.4.2 NAM model and dataset

The field dataset used in the following example was provided by the Nederlandse Aardolie Maatschappij (N.A.M.), Assen. The data was recorded on land along a line of about 10km length. The data has been preprocessed to remove ground-roll. The acquisition geometry parameters are as follows : split spread geometry, number of shots :301, shot spacing :30m, number of detectors per shot :120, detector spacing :30m, near offset :115m, far offset :1935m, registration time :4s and time sampling interval :4 ms. The missing near offsets were interpolated using a CMP interpolation technique. Figure 6.25 illustrates the full prestack depth migration of the NAM data. The prestack migration is based on recursive wave field extrapolation and is performed in the space frequency domain.

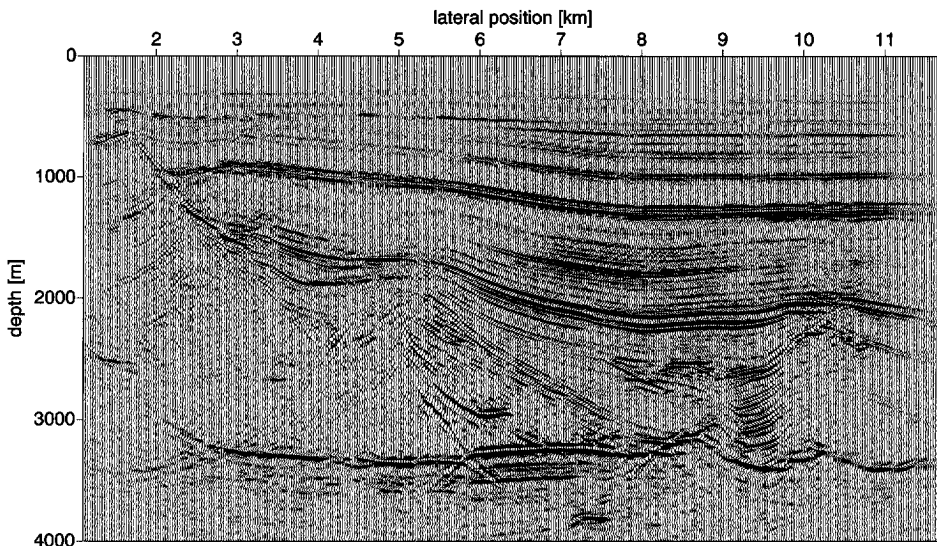


Figure 6.25 Depth section after full prestack depth migration.

Figure 6.26 shows an Integrated Seismic Display (ISD) of shot record, pseudo VSP, velocity log at pseudo well and part of the full prestack migrated section (Figure 6.25). Two-way wave field extrapolation operators have been used in the generation of the pseudo VSP data. The arrows in Figure 6.26 show the integration of the various events in the different planes. It is important to notice that the event (indicated with the pointer in the prestack migrated section) is difficult to identify in the pseudo VSP data. The major contribution to that image comes from the larger offsets. The construction of a vertical well for imaging that particular image will be quite difficult. A deviated well would indeed show a better correspondence with the prestack migrated depth section.

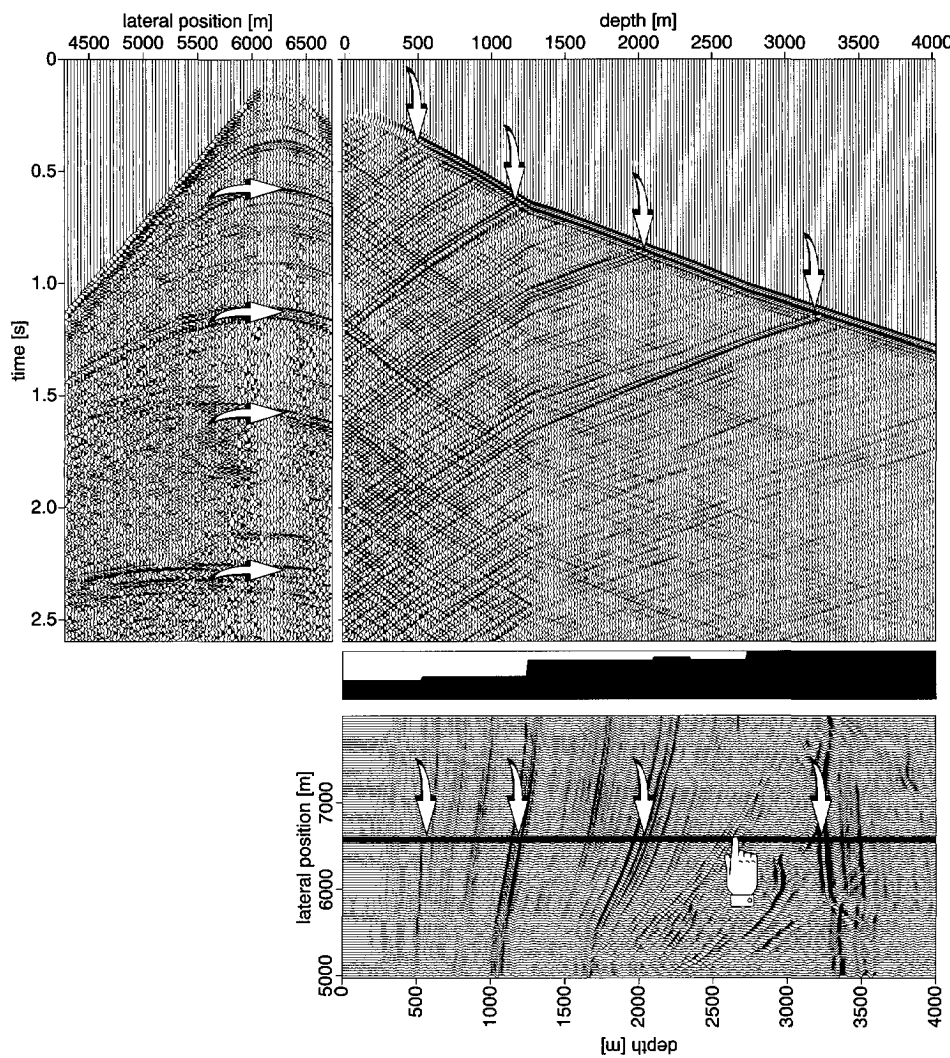


Figure 6.26 Integrated Seismic Display (ISD) of shot record (courtesy NAM), pseudo VSP, velocity log at pseudo well and part of the full prestack migrated depth section.

The used macro model in this experiment was estimated using a traveltime inversion method.

Figure 6.27 shows the constructed two-way time (source-receiver offset 930m) and one-way time (source-well offset 465m) common-offset sections. Note that the data in Figure 6.27b is half-migrated.

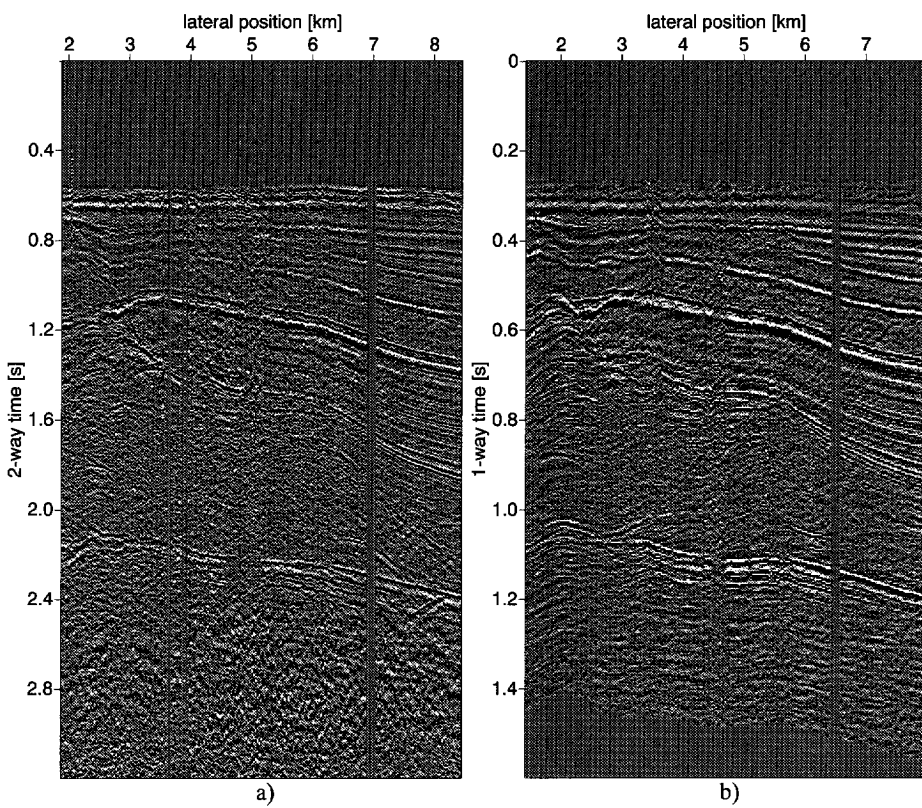


Figure 6.27 Common-offset sections: a) two-way time (two-way offset : 930m); b) one-way time (one-way offset : 465m).

In this chapter the single-fold imaging of data has been shown using multi-well, common-offset pseudo VSP data. The availability of virtual multi-wells along a seismic line enables the lateral imaging with the aid of common-offset pseudo VSP data. The advantage to illustrate the imaging of structures with the aid of pseudo VSP data is that particular structures can be illuminated from various angles defined by the borehole/detector configuration. The result of the imaging with the aid of multi-well, common-offset pseudo VSP data leads to a composite section, the common-offset (source-well offset) section showing single-fold migrated results. The common-offset sections in *one-way time* or *depth* show single-fold migrated results (along predefined pseudo wells) and clearly reveal possible acquisition deficiencies for the coverage of data given a source and receiver configuration. The construction of so-called *sector scans* in one-way time or depth showed migrated results due to illumination from one specific surface point to many different directions. Two-way time common-offset sections (unmigrated data) have been shown in comparison with one-way time common-offset sections (half-migrated data) on several field datasets.

Chapter 7

2-D case studies

7.1 Introduction

In this chapter some 2-D case studies will be discussed on various data examples. The transformation of the surface measurements into depth or one-way time profiles has shown its value in the understanding and interpretation of seismic events. Since the VSP type of display is a valuable tool in the mapping of events from the surface data to the migrated data, single shot record migration displays can be used to decide where to define a pseudo well configuration. From single shot record migrations, it can be easily seen where the energy is mapped to for various angles of illumination. The energy distribution in the migrated data can be selected for a specific borehole/detector configuration and be used as a tool to integrate the unmigrated data (surface data) with the migrated data. In this chapter some examples will be shown on this integration of the data. However it is very important that the surface data, which is the input to the algorithm, is preprocessed. That means that e.g. surface-related multiples have to be removed from the surface data to improve the interpretation of the primary reflections.

In Chapter 4, 5 and 6 the generation of pseudo VSP data was shown in relation with focusing techniques yielding pseudo profiles as function of the one-way time. In using focusing techniques, surface data was rearranged such that responses from different depth points could be studied. The focusing in detection (described in Chapter 4) can be seen as an alternative view for the walkaway VSP configuration where a receiver is held at a specific depth and the source is moved along the surface. In a similar way, the focusing in emission can be seen as the response at the surface from downhole seismic sources : e.g recording of a reverse VSP (RVSP) survey or Seismic While Drilling (SWD) data.

Here a series of receivers along the surface, measure the response of a source which is located in the well. In this way, the use of the CFP gather is very attractive in the comparison with real VSP data at various depth levels. The common assumption is that the principle of reciprocity can be applied to RVSP and conventional VSP data since the travel paths for both configurations are equivalent. This allows to integrate VSP measurements, recorded at a particular depth, with CFP gathers at the well location. Examples will be shown on the integration of the CFP gathers with VSP measurements and also on comparisons of pseudo VSP data with real VSP data.

In Sections 7.2 to 7.4 some examples on marine datasets are discussed to show how surface data ties to pseudo VSP data and illustrating its integration with migrated sections via the pseudo VSP data. Since the marine datasets are affected with strong surface-related multiples, these multiples have been removed from the data prior to pseudo VSP generation. Some illustrations on different land datasets will be given in Sections 7.5, 7.6 and 7.7. Finally Section 7.8 discusses a study on physically modeled data.

7.2 Marine dataset (I)

To provide a realistic test, a real dataset was obtained from Mobil Exploration and Producing Technical Center Dallas, U.S.A., containing marine seismic data and well log measurements. The well log data came from two wells that intersect the seismic line. The dataset comes from the North Viking Graben in the North Sea. The seismic line consists of 1001 shot records, oriented in a structural dip direction (each shot record was recorded on 120 channels for six seconds). The sampling time of the data is four milliseconds. The shot point interval and receiver group interval are 25 meters. An airgun array (depth is 6 meters) provided the seismic source. The dataset (acquired in approximately 350 meters of water) is strongly contaminated with surface-related multiples. Two wells intersect the seismic line: well *A* and *B* respectively.

The Mobil data also contained vertical seismic profiles recorded in wells *A* and *B*. The VSP data for well *B* has been used to investigate how it ties to the surface data. The objective of this example is to generate pseudo VSP data from a shot record along the seismic line at well *B* and making comparisons with the real VSP data recorded in well *B*. The data will be generated from preprocessed surface data with all multiples included and also from data after surface-related multiple elimination methods have been applied to it (Verschuur et al., 1992). Finally the comparison between the pseudo VSP and the preprocessed real VSP data will be discussed.

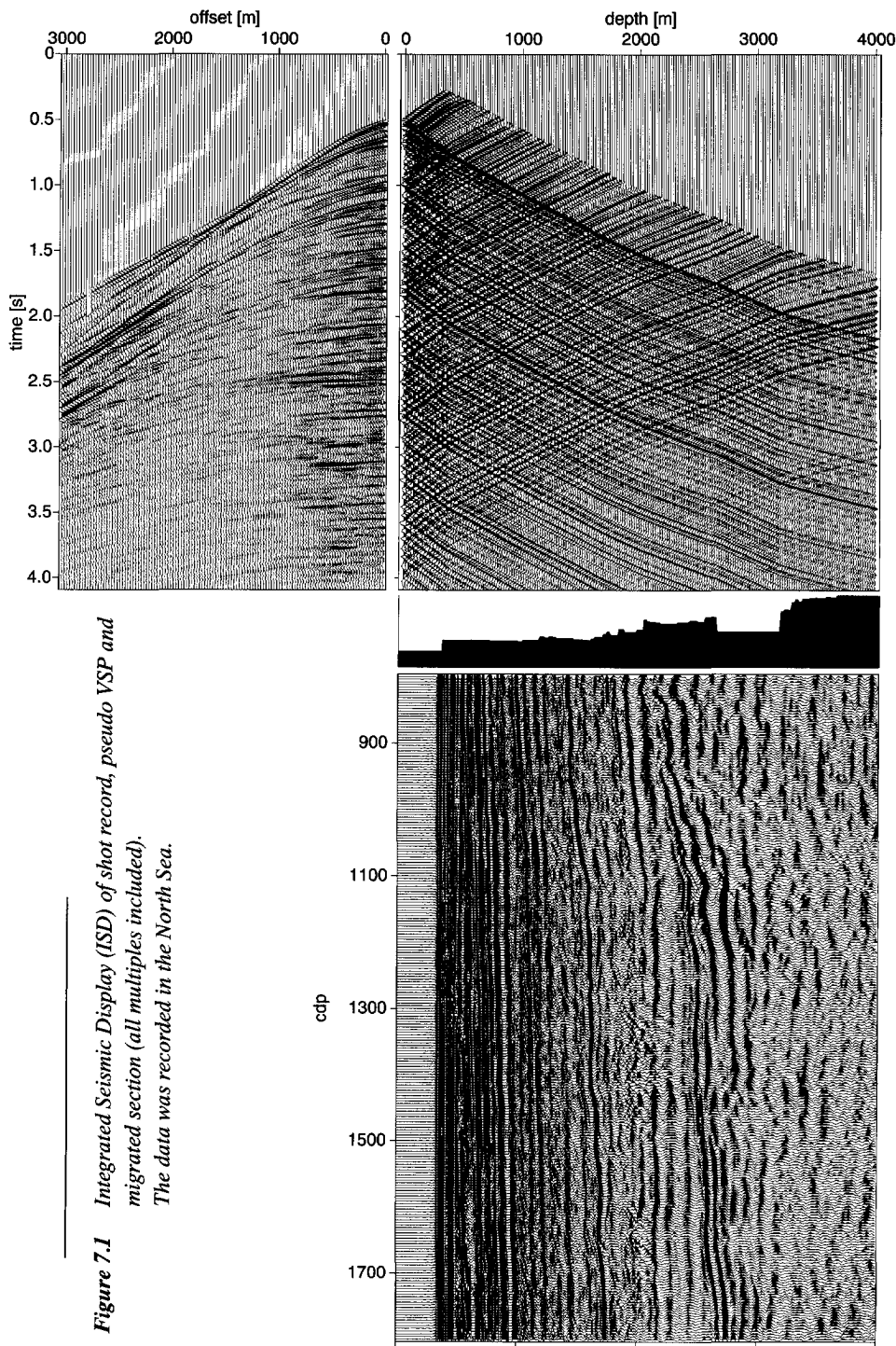
7.2.1 Integration of pseudo VSP and real VSP data

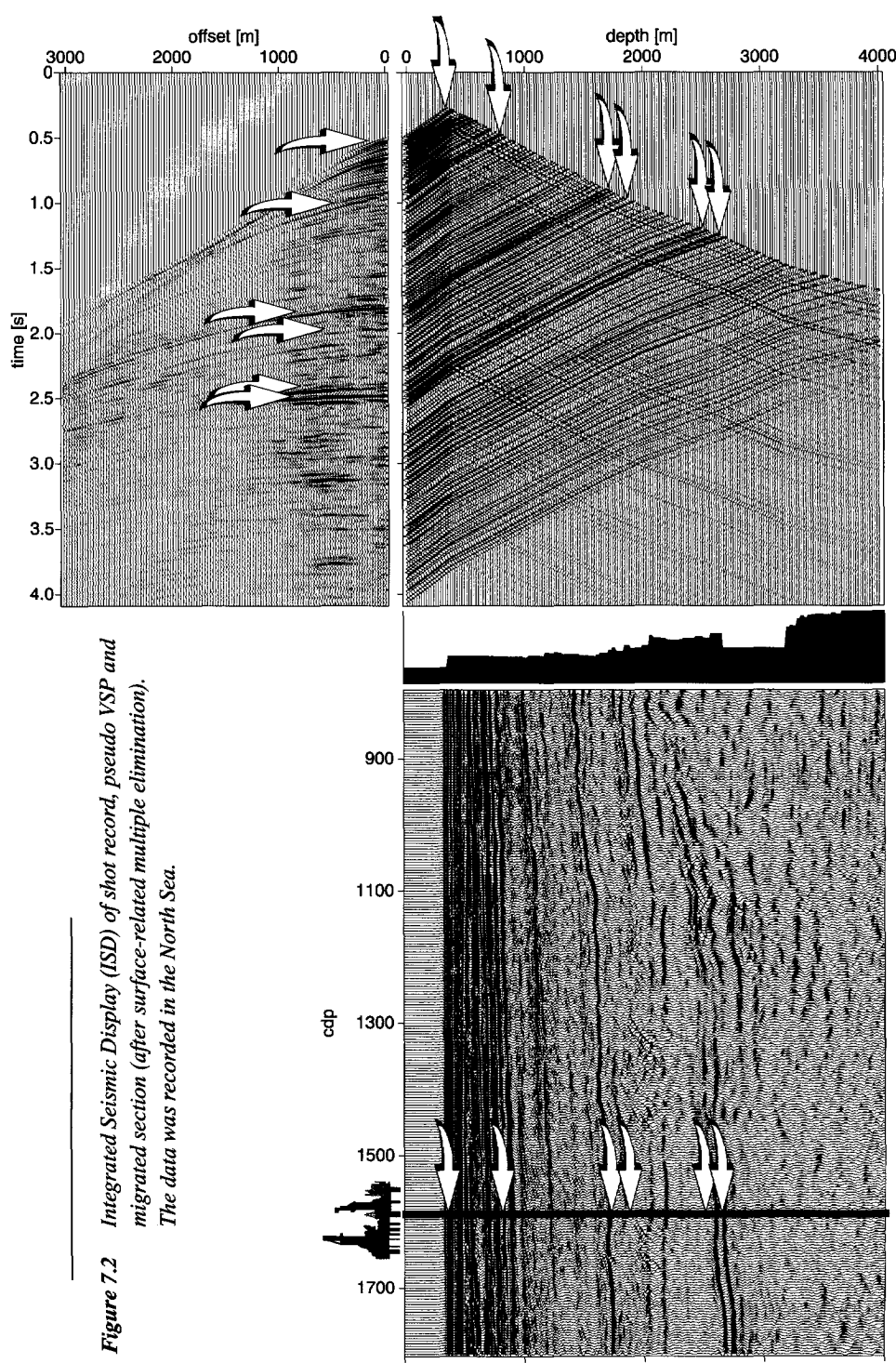
In the following, the generation of pseudo VSP data is shown for the real shot record (shot point 822; CDP no. 1572) at well *B*. The pseudo VSP data have been generated at 200m offset to avoid the influence of near offset interpolation in the surface data; the events become better identifiable in the pseudo VSP data. In this way, an *optimal* offset can be chosen from the surface data (offset with good data quality) to have a better interpretation of the events mapped to depth.

First the result of the pseudo VSP is shown generated from the shot record with all multiples included (Figure 7.1). Acoustic two-way wave field extrapolation operators are used in this pseudo VSP generation. Notice that only reflected wave fields in the shot record are used as input. The direct source wave field is not taken into account. The non-causal events appearing prior to the direct wave have been zeroed. The seismic dataset is affected by very strong multiples and the primaries are not clearly visible because of these strong multiples. Therefore the pseudo VSP is also generated from the same shot record after adaptive surface multiple elimination has been applied to it. A blocked version of the true velocity log used for the generation of the pseudo VSP is displayed next to the pseudo VSP to show its relation in depth with the migrated section.

Figure 7.2 shows the generation of pseudo VSP data from the shot record (at shot point 822, i.e. at well *B*) after surface-related multiple elimination. The primaries become more identifiable in comparison with the pseudo VSP in Figure 7.1. Note the downgoing multiple reflections from the seabottom (at approximately 375m depth). The transformation of the surface data into the pseudo VSP data gives a better understanding of the complex events (e.g. internal multiples). Some reference arrows are displayed showing the relation of the different datasets in the different planes (*x-t*, *t-z*, *x-z*) : this facilitates following an event from the shot record to the VSP data and trace it back to the intersection with the direct source wave field at the original reflector depth. In fact the pseudo VSP data can be used as a tool to map an event in the shot record (time event) into depth (depth event): the generation of the pseudo VSP data provides us with an unambiguous tie between seismic events on a time section and their geological interface in depth.

Having generated the pseudo VSP data from the surface data, a comparison will be made with the real VSP data that was recorded in well *B*. Because the *acquisition* in a real VSP is completely *different* from the one at the surface, the recordings have in general a different frequency content : the pseudo VSP data may have a lower frequency band (and therefore a lower resolution) than the real VSP data.





On the other hand, after proper preprocessing¹, the pseudo VSP may have a better SNR. Also the sources and detectors used in both recordings are different. Hence in practical situations both VSP data may enhance each other significantly. Now the fundamental importance in the pseudo VSP generation method is that one can walk away from the well with the optimally determined matching parameters at the well and extend the geological knowledge in all lateral directions. In general the acquisition for real VSP data is quite difficult and expensive. The real VSP data is generally contaminated with different types of noise; obtaining noise-free recordings at each depth level is quite difficult in practical situations (e.g. bad coupling of VSP geophone to the borehole wall). The pseudo VSP which can be generated from the surface seismic data, can be used to interpolate the missing recordings in real VSP data at various depth levels. This would be very helpful to integrate the real surface data (shot record) with the VSP data. An example of using pseudo VSP data to link surface data with real VSP data is depicted in Figure 7.3. The traces that represent pseudo VSP traces, indicate a depth interval where no receivers were positioned or bad traces which are removed.

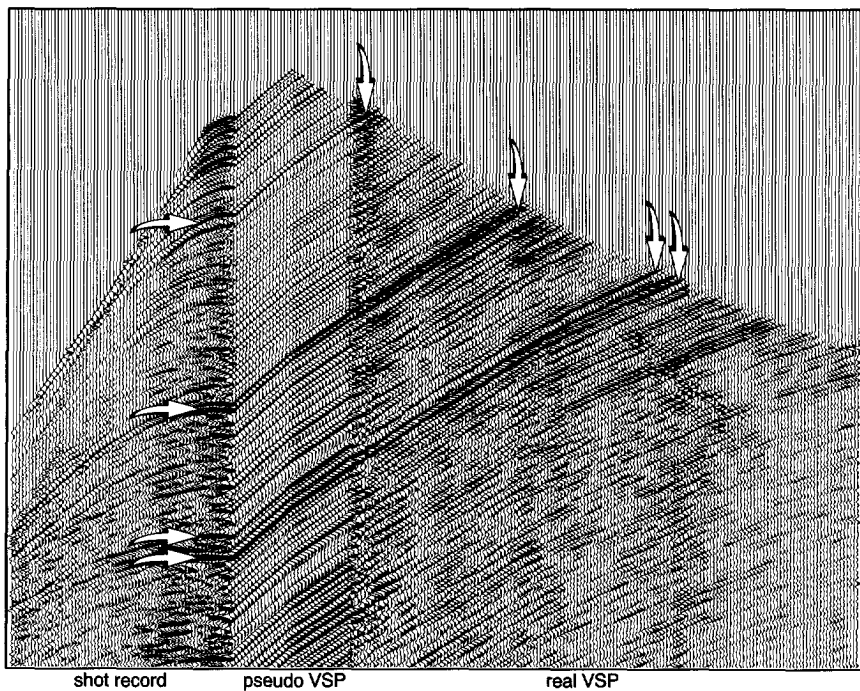


Figure 7.3 *Integration of real VSP and surface data with the aid of pseudo VSP data : pseudo VSP data is inserted in the missing gap between the real VSP and shot record.*

1. This may include a thorough study of the sources and detectors that are used in both situations.

Only the upgoing waves of the pseudo VSP and the real VSP have been integrated here. The strong downgoing wave modes have been subtracted from the real VSP to obtain an easier identification of the weaker upgoing waves (see Appendix C). Some arrows indicate the corresponding reflections which can be identified in both the pseudo and real VSP data. In a similar way, pseudo VSP data can be integrated with real VSP data below the total depth of the well for the prediction ahead of the drill bit. The combination of horizontal and vertical profiling acquires a special meaning for the study of the origin of waves recorded on the surface. The waves observed on the surface may be tracked on the vertical profile down to the boundaries with which they are associated (see e.g. arrows in Figure 7.3 linking the surface data with the VSP data with the aid of pseudo VSP data). Vertical and horizontal traveltimes curves are linked by time values corresponding to the borehole location at depth zero, since this is the point that is common to both profiles. Although there was not sufficient information available on the shot location of the VSP data, comparable results (of upgoing waves) have been shown for integrating surface seismic data with real VSP data. In other words, the pseudo VSP data appears to be useful in bridging gaps in real VSP data (missing data: bad traces or depth intervals where no receivers were positioned) and in tying surface data with VSP data. For optimal integration, the surface and VSP data should be at the same “level”.

7.2.2 Integration of the corridor stack with surface data

In this part, the corridor stack of real VSP data is integrated with surface data. For the pre-processing steps applied on the VSP data, the reader is referred to Appendix C. Figure 7.4a illustrates the VSP corridor stack of the upcoming wave profile inserted in the processed surface seismic section for comparison. The section represents a time-stack of the surface seismic data (stack after NMO) after surface-related multiple elimination. Comparison of the surface section with the VSP corridor stack at the well location indicates a good correlation of the events. The difference in frequency content is partly attributed to differences in processing these two sections and is partly attributed to less high-frequency attenuation effects due to the shorter traveltimes associated with the VSP recordings. The VSP configuration allows to distinguish between primary reflections and multiples. The VSP corridor stack can be seen as the best surface seismic trace within a given bandwidth. The VSP traveltimes have been related to surface seismic travel times with the aid of the VSP corridor stack with primary reflections enhanced and multiples excluded. Depending on how well thin-layer multiple events are rejected that extend into the narrow corridor around the first arrivals, the events on the surface seismic data that correlate with events on the corridor stack should be primaries, and other may represent remaining internal multiple energy. Figure 7.4b shows a comparison between the VSP migrated trace (repeated 5 times) and a poststack depth migration of the surface seismic line (after surface-related multiple elimination) crossing the well.

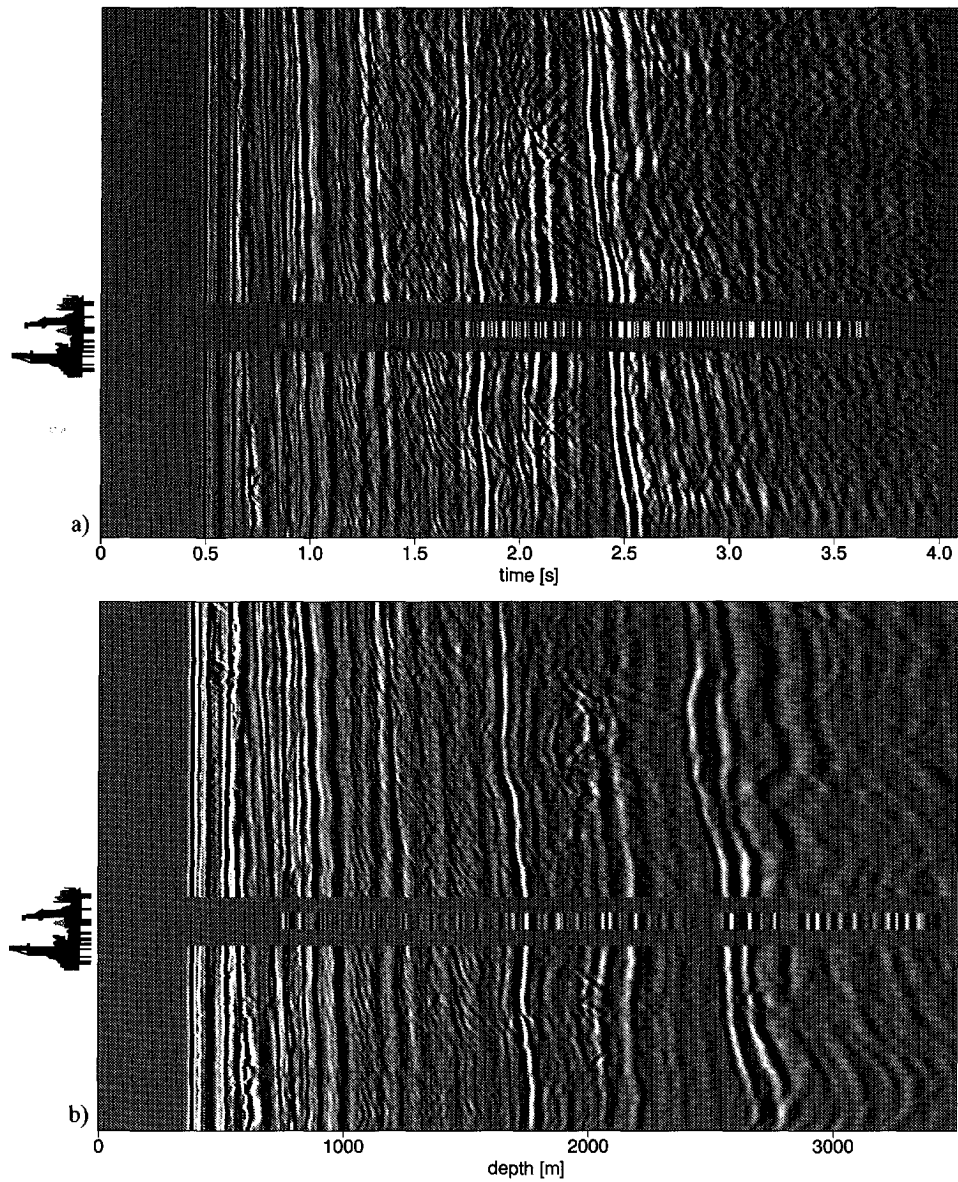


Figure 7.4 a)Corridor stack of the VSP data spliced into the surface seismic data (after surface-related multiple elimination) at the borehole location. The corridor-stacked trace, which has been reproduced 5 times contains events which should correspond to primary reflections and b)migration of the VSP data spliced into the depth migration of the surface seismic data (after surface-related multiple elimination) at the borehole location. The migrated result (1 trace) has been reproduced 5 times. The data was recorded in the North Sea.

A good match is observed between the various events. The difference in frequency content is partly attributed to differences in processing these two sections and is partly attributed to less high-frequency attenuation effects due to the shorter traveltimes associated with VSP recordings.

7.2.3 Source wavelet estimation using two-way operators

As shown in Chapter 2, two-way wave field extrapolation operators are very sensitive to errors in the parameters of the model. If a wrong macro model is used in the generation of pseudo VSP data, non-causal events will appear at the reflecting boundaries. This sensitivity of the two-way wave field extrapolation operators can also be used (see also Figure 3.16) to estimate the source wavelet from a marine shot record with all multiples included (from the same marine line as in the previous example, courtesy Mobil). Figure 7.5a shows a part of the shot record (surface-related multiples included). The preprocessing applied on the data consists of direct wave removal and missing near offset interpolation. As a first stage, a pseudo VSP (Figure 7.5b) is generated from the shot record at 213m offset using a homogeneous macro model with the parameters of the sea water layer (compressional velocity $c_{p1}=1490\text{m/s}$ and density $\rho=1000\text{ kg/m}^3$). Note that the downgoing source wave field is missing. The small offset has been chosen to validate the use of the acoustic scheme and avoid the influence of shear waves. The events of the second multiple reflection (indicated with white arrow and number 2) can be followed through the pseudo VSP till its intersection with the downgoing multiple reflection (indicated with number 1) to determine the depth of the seabottom ($z=355\text{m}$). Next, a model is defined with the water layer and a layer below $z=355\text{m}$ for a fixed density value $\rho=1500\text{ kg/m}^3$ but in which the velocity c_{p2} of the second layer has been ‘scanned’ from 1500m/s to 3000m/s . By generating a series of pseudo VSP data for the varying velocities, and studying the behaviour of the non-causal event (indicated with black arrow in Figure 7.5b) in the different generated pseudo VSP data, an optimal result is obtained for $c_{p2}=1700\text{m/s}$. The result is shown in Figure 7.5c, from which it can be clearly seen that the non-causal event (indicated in Figure 7.5d) has completely disappeared. For this particular model, the multiple reflection has been handled correctly at the boundary, but there is still a non-causal event appearing at the seabottom (indicated with the white arrow in Figure 7.5c). The final step is to estimate the source wavelet (by changing the amplitude and delay of the wavelet) such that this non-causal event will disappear. Figure 7.5d shows a result in which the estimated source wavelet is still not correct in amplitude. Therefore the non-causal event at the first break is still quite strong (white arrow). Figure 7.5g shows the final iteration in which the non-causal event has completely disappeared. Figure 7.5h shows the final estimation of the source wavelet. Figure 7.5e and f show the integration with the original shot record and the identified multiple reflection paths.

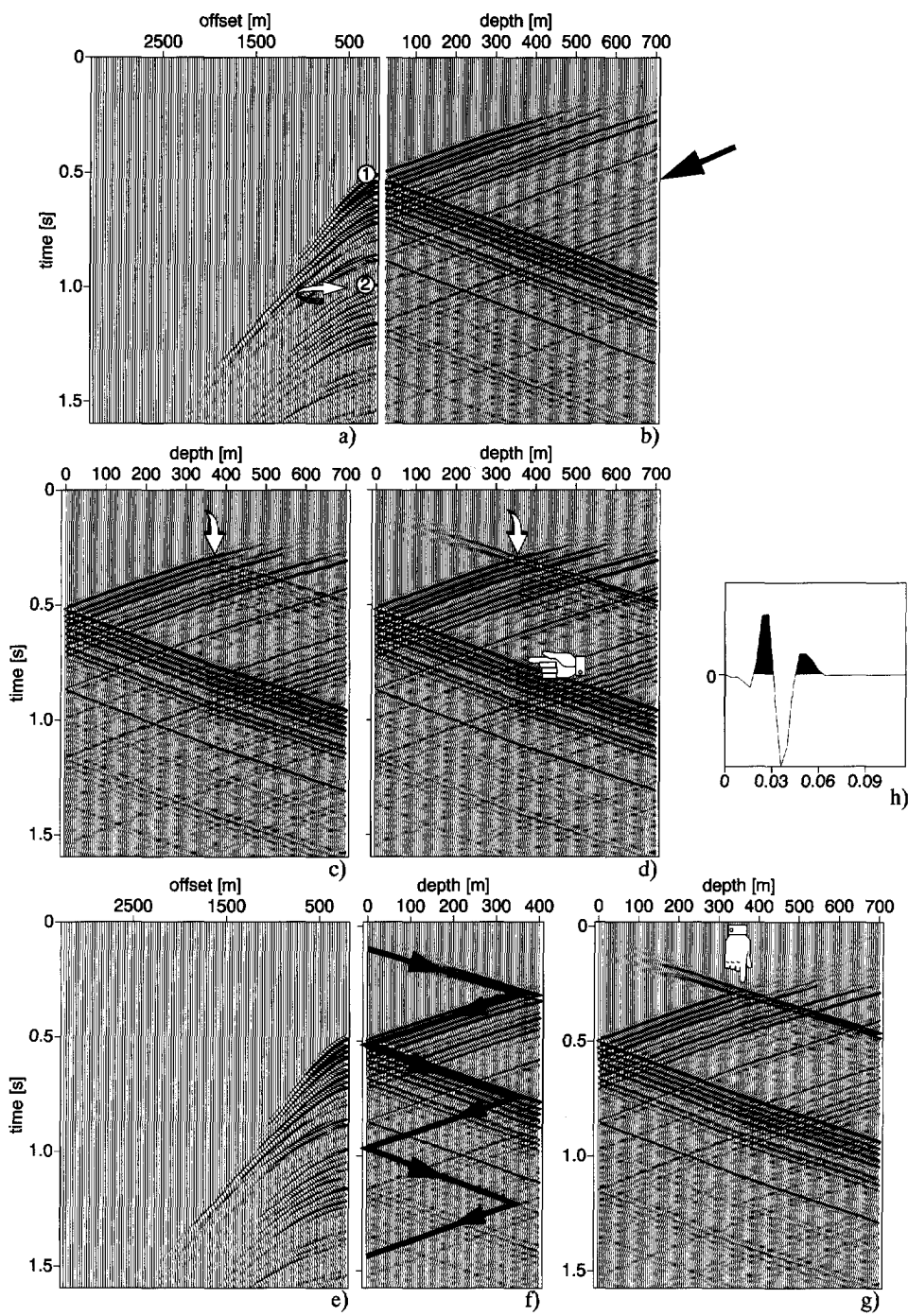


Figure 7.5 Source wavelet estimation from marine data (surface-related multiples included).

7.3 Marine dataset (II)

In this section the pseudo VSP generation method is demonstrated on another field dataset which was acquired also in the North Sea and provided by SAGA Petroleum A.S.. The data is from the Haltenbanken offshore area Norway with a sea bottom depth of almost 300m. From a seismic line 301 shot records have been processed, each shot record consisting of 120 traces with 25m shot and receiver spacing. The missing near-offset gap is 150m which corresponds to 6 missing traces. Some faults occur in the target area, which ranges from 2400m to 2600m. The following preprocessing steps have been applied to the data (see Verschuur,1991) : 1)muting of the direct wave in the x - t domain, 2)amplitude correction by a \sqrt{t} gain (3-D to 2-D amplitude correction), 3)near offset interpolation by applying a NMO correction followed by a lateral interpolation algorithm and 4)the adaptive surface-related multiple elimination procedure has been applied for all shot records together with a source signature estimation. In Figure 7.6, the prestack migrated depth section is shown. The prestack migration has been performed with a recursive algorithm in the space frequency domain. From the SAGA dataset, a VSP data was available which was recorded in a well along the seismic line (approximate lateral location: 13.13km). The available VSP data for this dataset was ranging from depth level $z=1739m$ to $3204m$ at 87 levels. Similar to the example in the previous section, a combined display is shown in Figure 7.7 between the surface section and the VSP corridor stack. The VSP preprocessing steps for real VSP data are illustrated in Appendix C.

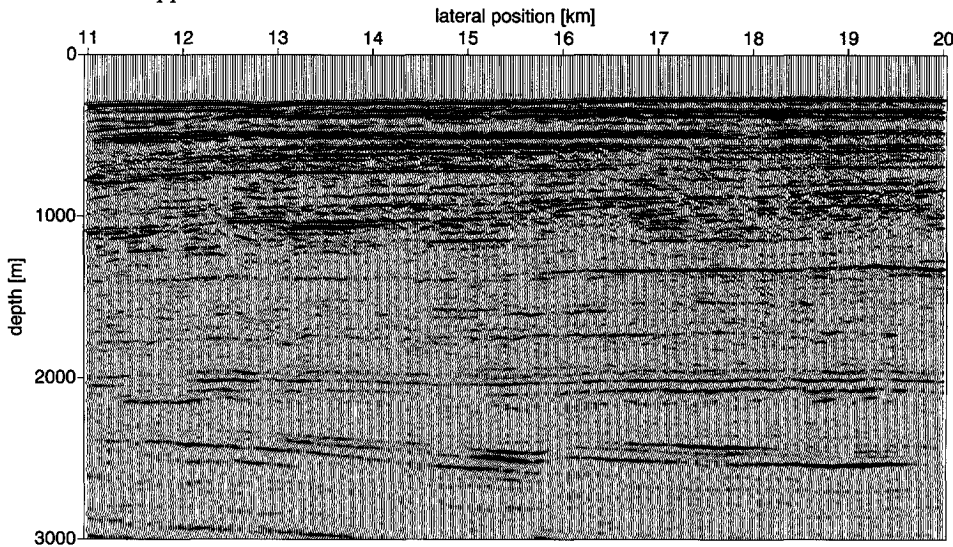


Figure 7.6 Depth image after full prestack depth migration.
The data was recorded in the North Sea.

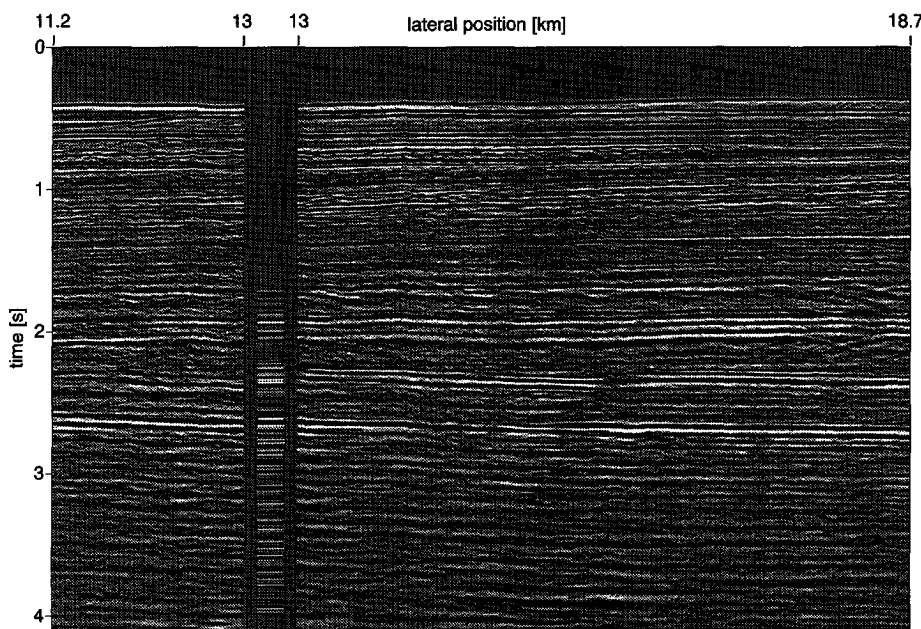


Figure 7.7 VSP corridor stack spliced into the surface data (after surface-related multiple elimination) at the well. The corridor-stacked trace has been reproduced 10 times.

Figure 7.8 shows an Integrated Seismic Display (ISD) of a shot record (after surface-related multiple elimination), pseudo VSP, velocity profile at the well and the migrated section. The pseudo VSP has been generated using two-way wave field extrapolation operators.

For the generation of the pseudo VSP data using two-way wave field extrapolation operators, a density model was necessary. The density model was determined from the macro velocity model using Gardner's equation :

$$\rho = 1741 \left(\frac{c_p}{1000} \right)^{0.25} . \quad (7.1)$$

As noticed from Figure 7.8, a "transparent surface" boundary condition has been applied prior to generating pseudo VSP data, since the surface-related multiples were removed from the surface data. The downgoing seabottom multiple reflections are visible in the pseudo VSP data. Figure 7.9 shows the integration of the shot record, pseudo VSP and real VSP data (upgoing waves). The downgoing waves have been removed from both VSP data and both datasets have been shifted to two-way time (two-way time correction) for a better integration with the preprocessed surface data. Here again, the pseudo VSP data has been used to integrate the surface data with the real VSP data. The integration of both VSP data has been made at depth 1740m.

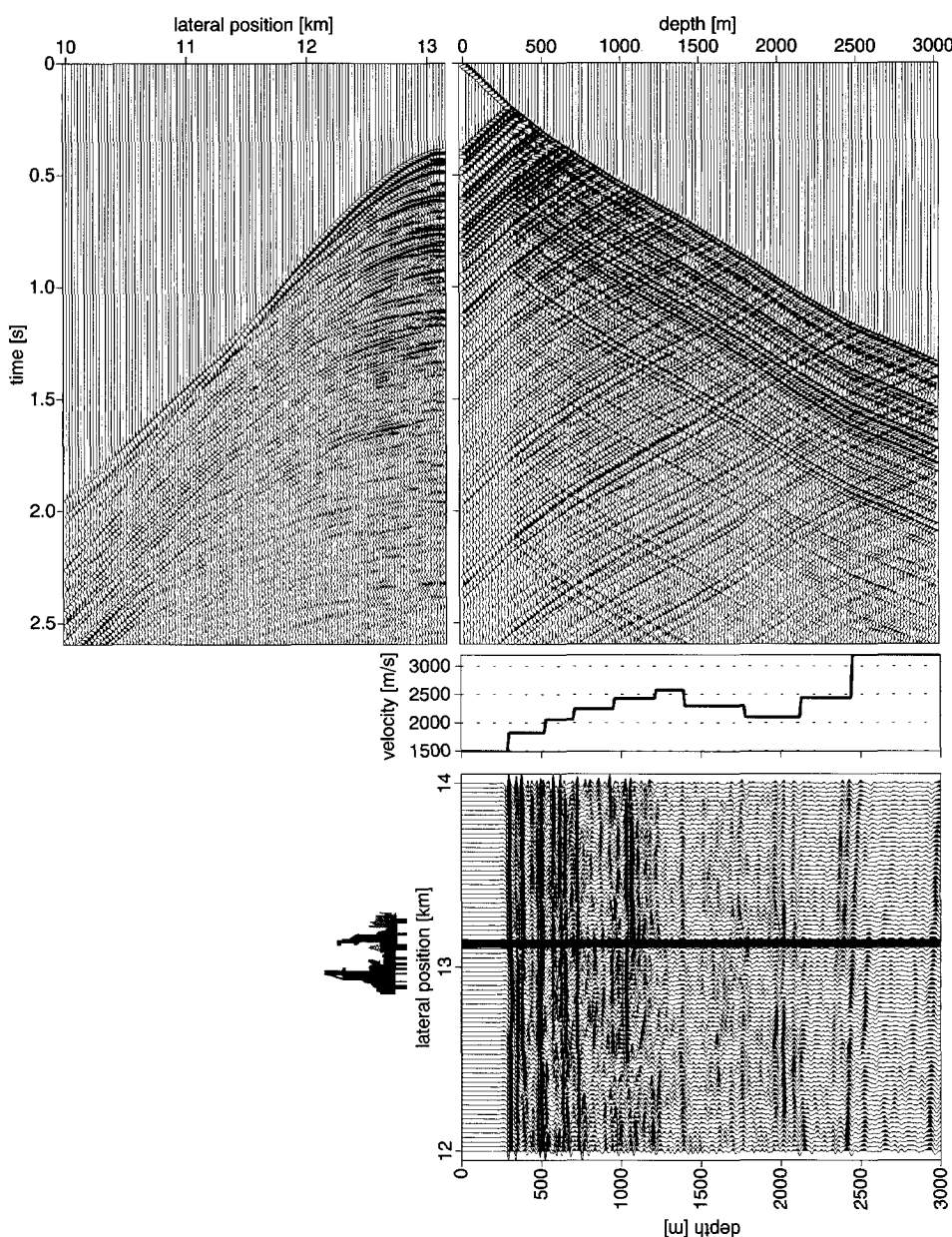


Figure 7.8 Integrated Seismic Display (ISD) of shot record (after surface-related multiple elimination), pseudo VSP, velocity profile at the well, and part of the image after full prestack depth migration.

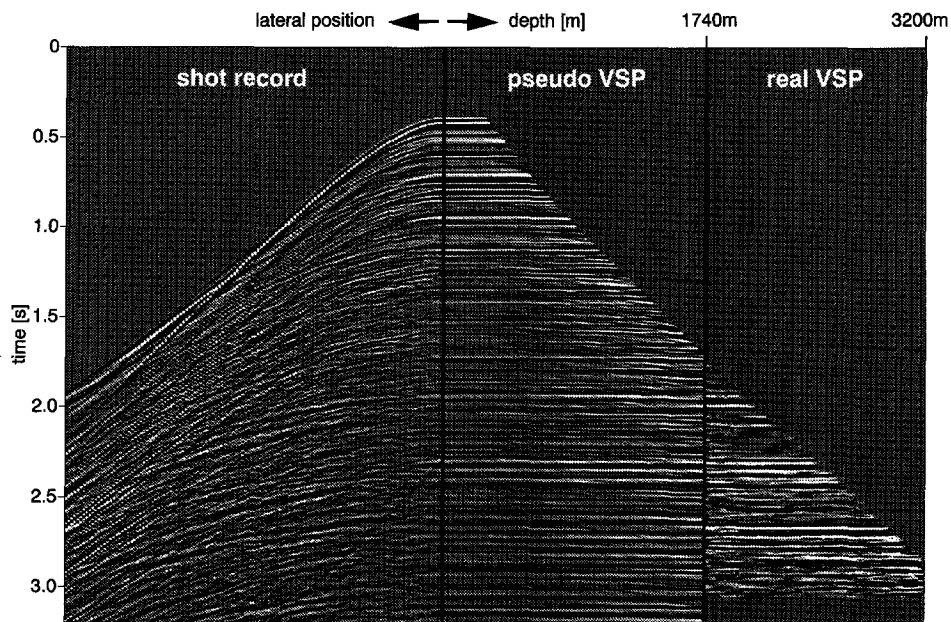


Figure 7.9 Integrated display of shot gather, pseudo VSP data (upgoing wave modes; two-way time corrected) and real VSP data (two-way time corrected).
The integration of the pseudo VSP data is made at a depth of $z=1740\text{m}$.

The integration of the different events in the different datasets is clear in spite of the poor definition of the events in the record below the times $t=1.75\text{s}$. The comparison of the pseudo and real VSP data can also be made using their relation with the CFP technology as described in Chapter 4. Similar to the data volumes as constructed in Chapter 4, a data volume is constructed at the well location by generating offset pseudo VSP data from various shot records with varying shot locations. One depth slice of this volume represents a CFP gather for that particular depth location allowing to integrate a real VSP trace recorded at that particular depth location. Figure 7.10 shows the integration of the CFP gathers with traces from a VSP data recorded at 2 particular depth levels. Two different depth levels are considered here : the integration has been made at depth levels $z=1800\text{m}$ and $z=2500\text{m}$ (Figure 7.10a respectively Figure 7.10c). The offset of the source from the well is ranging from -1175m to 1175m with increments of 25m . The trace with zero-offset (from the CFP gather) has been replaced by a trace of the VSP data recorded respectively at $z=1800\text{m}$ and $z=2500\text{m}$. This trace has been reproduced 9 times for a better interpretation. The integrations have been blown up for a better view and are illustrated in Figure 7.10b respectively Figure 7.10d. From these figures which show some part in more detail, a clear match can be observed between the events from the CFP gather (constructed from pseudo VSP data) and the real VSP. At some particular one-way times t' the match is not good.

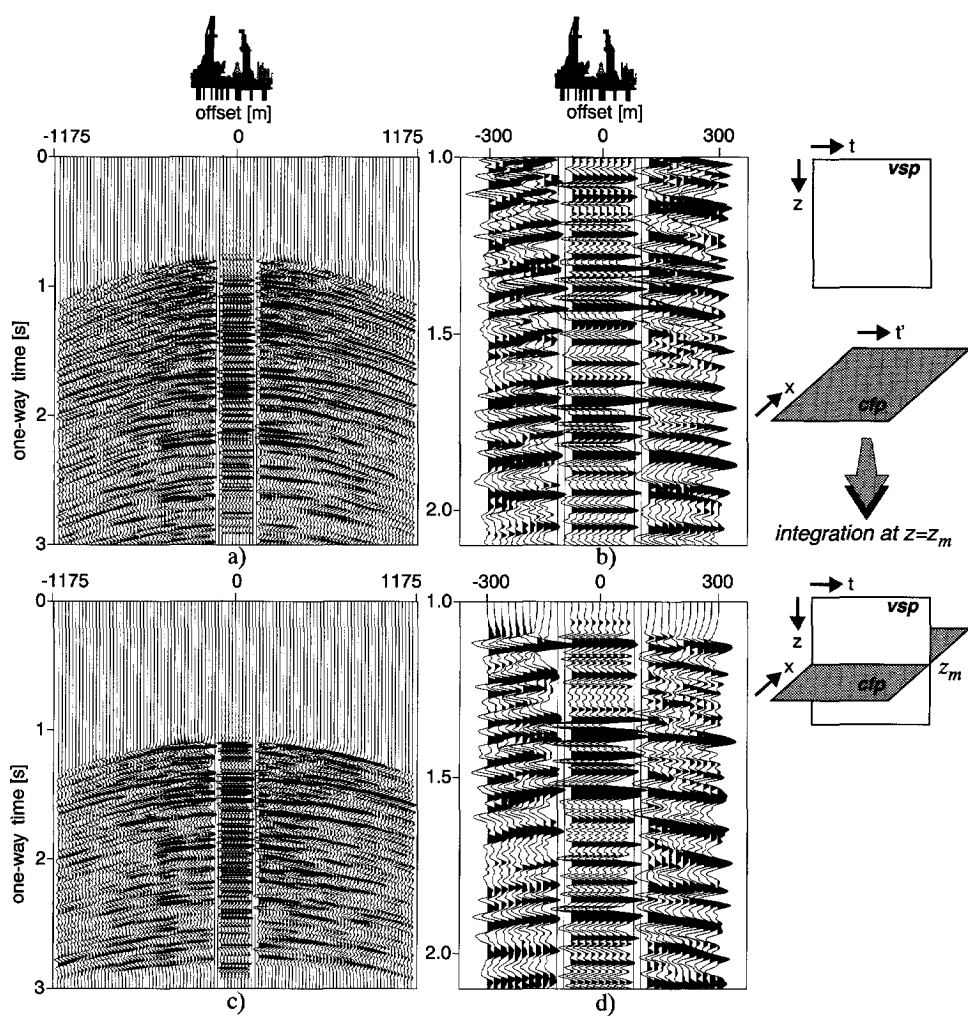


Figure 7.10 a) Integration of a CFP gather with focus point at depth $z = z_m = 1800$ m and a real VSP trace at depth $z = z_m = 1800$ m and b) blow up showing the area in detail between time $t' = 1$ s and $t' = 2$ s. c) and d) same but for a depth ($z_m = 2500$ m).

The VSP trace at z_m for zero offset has been reproduced 9 times for display purposes.

Here it should be noticed that in the CFP gather only upgoing waves have been taken into account. This in comparison with the real VSP in which the recorded traces contain both upgoing and downgoing waves. From the constructed pictures, the Amplitude Versus Angle (AVA) behaviour of the reflected wave field can be studied. This is a very important aspect which can be viewed by this type of integrated displays. The construction of the integrated displays is schematically shown at the right of Figure 7.10 : one trace of a CFP gather (constructed for a focus point at depth z_m) is equal to a trace from a VSP data (at depth z_m).

7.4 Marine dataset (III)

In this section an example will be illustrated on a marine dataset that was recorded in the Persian Gulf. The waterbottom is rather shallow (depth about 70m). From the marine seismic line consisting of 201 shot records, one shot record was selected (shot #100) to be used as input to the pseudo VSP data generation.

The acquisition parameters for the marine data are shown in Table 4.

Table 4 Acquisition geometry for the marine data
(recorded in the Persian Gulf).

geometry	end of spread
number of shots	201
shot and receiver spacing	25m
number of receivers per shot	96
nearest offset is (3 missing traces including zero-offset trace)	80m
number of receivers per shot	96

Due to the relatively strong sea bottom and several strong sub-bottom reflectors, a lot of surface-related multiple energy is present in the data which obscures the weaker primary reflections. Figure 7.11a shows the stacked section after surface-related multiple elimination (srme), Verschuur (1991). Figure 7.11b illustrates that a large amount of multiples have been removed from the data, resulting in the restoration of the continuous events as indicated with the arrows in Figure 7.11a. The stacking velocities of primaries and multiples are apparently very close. This means that stacking would not result in a considerable reduction of multiples. The following preprocessing have been applied on the data : first, an NMO correction has been applied on the data followed by a spline interpolation to estimate the missing near offsets. The intermediate missing offsets have been interpolated linearly between two nearest traces. Secondly, the direct wave has been muted in x - t domain.

Prior to pseudo VSP generation, a split spread shot record (shot #100) has been constructed using the principle of reciprocity on the end of spread data. Note that the created shot gather is not anymore the response of a single shot experiment; it approximates a split spread shot record if the source function is relatively invariant for all shot records that contribute to the constructed split spread shot gather. The split spread shot record which has been used as input to the pseudo VSP generation is displayed in Figure 7.11c. The location of the well is indicated in this figure. In this example, the pseudo VSP data is generated using the one-way wave field extrapolation operators. The reflected wave field is inversely extrapolated and the source wave field is forward extrapolated. The result of the zero-offset pseudo VSP data is depicted in Figure 7.11d (Note that the events prior to the direct wave have been zeroed).

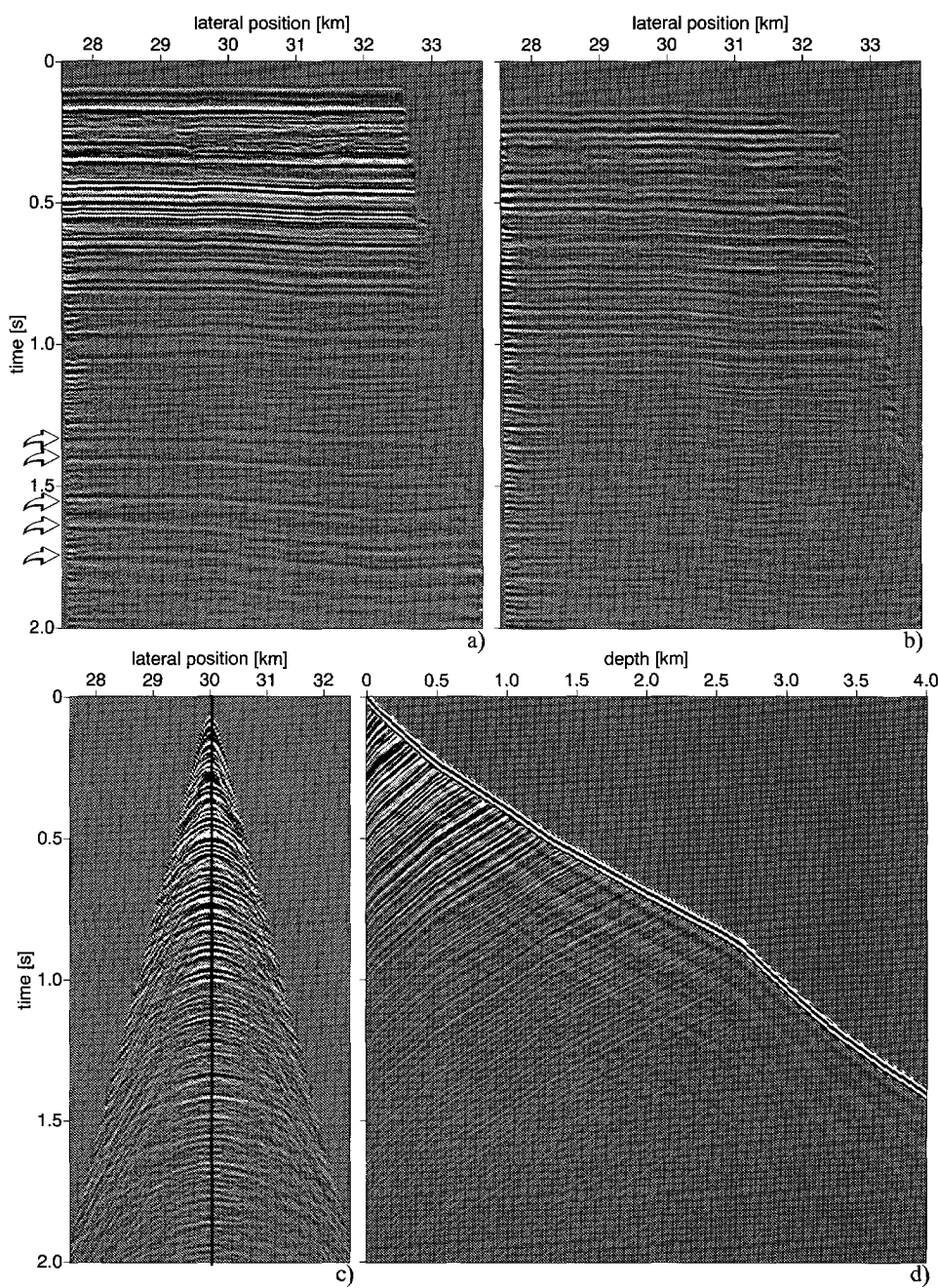


Figure 7.11 a)Stacked section after adaptive srme, b)the eliminated multiples, c)shot #100 after srme and split spread data construction by reciprocity and d)pseudo VSP data. The data was recorded in the Persian Gulf.

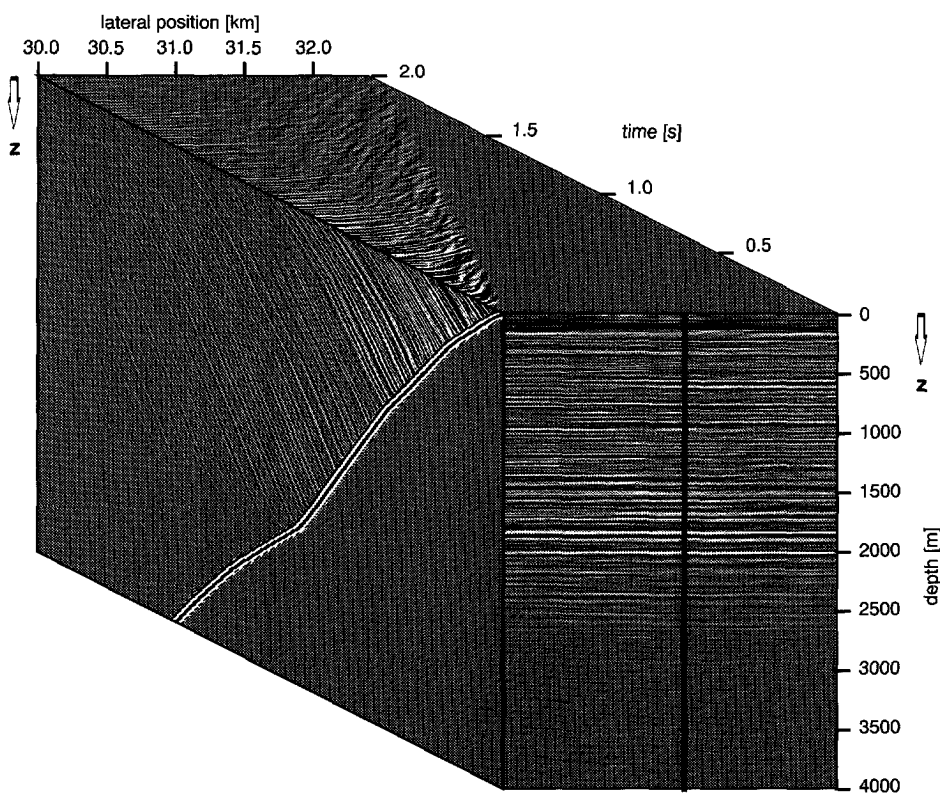


Figure 7.12 Display of 3 combined datasets : shot record (after surface-related multiple elimination), generated pseudo VSP data and part of the image after full prestack depth migration (the seismic marine data was recorded in the Persian Gulf).

Figure 7.12 shows a combined display of the shot record, the generated pseudo VSP data and the full prestack migrated depth section. The data at the front of the cube represents the full prestack migrated depth section for the Persian Gulf data. The location of the well is indicated with the black line.

7.5 Land dataset (I)

In this section, the generation of pseudo VSP data will be demonstrated on a land dataset which was recorded in the Middle East. The field dataset was measured on land (three-components recordings) using a seismic vibrator. Figure 7.13a shows a raw shot gather at station #1540. The data is heavily contaminated with groundroll. Despite the strong groundroll, the reflection response of some of the main boundaries is visible in the shot gather.

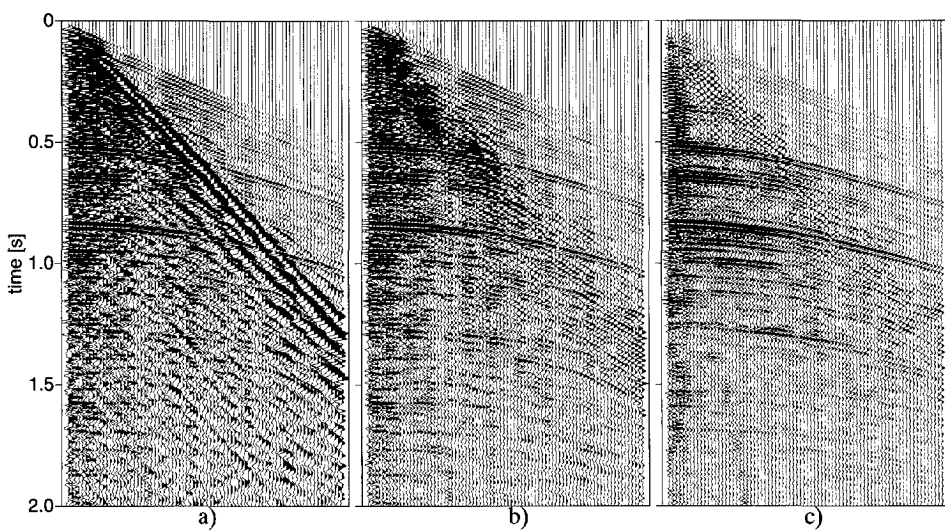


Figure 7.13 a)Raw (initial) shot record (station nr. #1540), b)estimated signal (after suppressing the groundroll by using the linear Radon transform) and c)supergather (summation of 10 shot gathers) used for the generation of the pseudo VSP data. The data was recorded in the Middle East.

The commonly used methods for removing or reducing groundroll from surface seismic data are 1)filtering in the f - k domain or 2)the use of linear Radon methods. Fyfe and Kelamis (1992) have shown that f - k filtering may leave strong linear artifacts in the data and may not be a powerful tool to suppress the groundroll. The application of the linear Radon transform to the data improves the quality of the data. The shot gather after applying the linear Radon transform is shown in Figure 7.13b. Some of the reflections are better visible in the shot gather. Most of the groundroll energy has been removed from the data. The result for the pseudo VSP generation on a single shot gather will not give good results since the events in the shot gathers are not coherent enough. The results for the pseudo VSP data will be much better if the reflectors of interest are clearly identifiable in the shot gather. Since there was a little lateral variation in the data (almost 1-D subsurface), 10 shot gathers (after groundroll suppression) have been summed together to produce an adequate gather to be used for the generation of the pseudo VSP data. This so-called “supergather” is displayed in Figure 7.13c. A well was drilled with the well head located on the seismic line, at station #1524.5. An offset VSP data was also available for this dataset. The offset VSP data has been shown already in Chapter 4. The source location for this offset VSP is 914 meters from the well head, about 803m north of station #1540. Although this is a substantial distance from the wellhead, the geology changes very little and is almost flat. A 1-D interval velocity model has been derived from the recorded offset VSP data and is compared and incorporated with the interval velocities derived from the shot gathers to build up a 1-D model that was used

for the pseudo VSP generation. The pseudo VSP data is generated at approximately $914m$ offset and is used to bridge the gap between the supergather at the real VSP data which contains data below depth $z=518m$ (1700ft). Figure 7.14 shows an integrated display of the supergather, $914m$ offset pseudo VSP and the $914m$ offset real VSP.

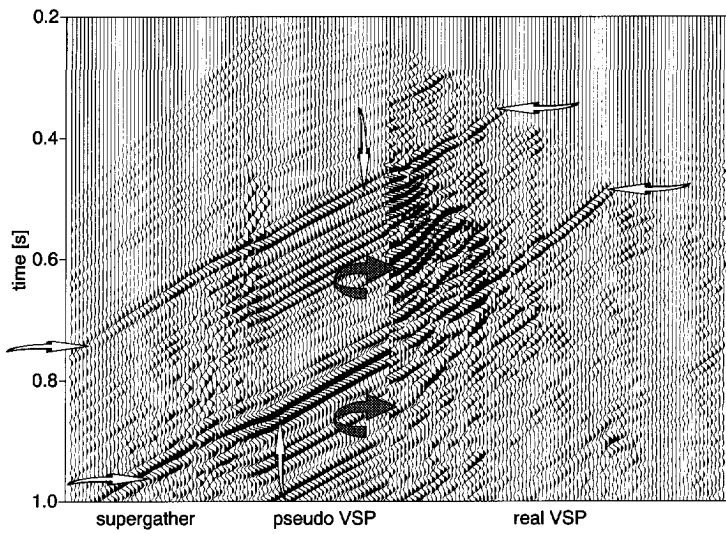


Figure 7.14 Integrated display of supergather, pseudo VSP data and real VSP recording. The data was recorded in the Middle East.

Note the corresponding events (compressional velocity) in all data-displays for the two main boundaries (indicated with white arrows). The strong downgoing waves have been removed from the offset VSP data. Note that there is some upgoing S-wave energy visible in the real VSP data (indicated with gray arrows). For the identification of P- and S-waves on this VSP data see Chapter 4.

In the neighbourhood of this line another seismic line was recorded. The multi-component line consists of 80 traces per record (with record length: 5000ms). The spacing between the detectors is 30m. The shot gathers were also heavily infested with very strong groundroll. The groundroll was visible due to its low frequency, high amplitude and its low group velocity. The estimated macro subsurface velocity model is depicted at the top of Figure 7.15. To understand to which depth the time-events in the shot record are mapped, the pseudo VSP data (at zero offset) is depicted along the stack of the dataset (CDP stack with a conventional processing sequence including linear removal, spiking deconvolution, residual statics, AGC, NMO and CDP stack), see Figure 7.15. This facilitates following an event at the well through the stacked section to the pseudo VSP data and trace it back down to the intersection with the direct source wave field at the original reflector depth.

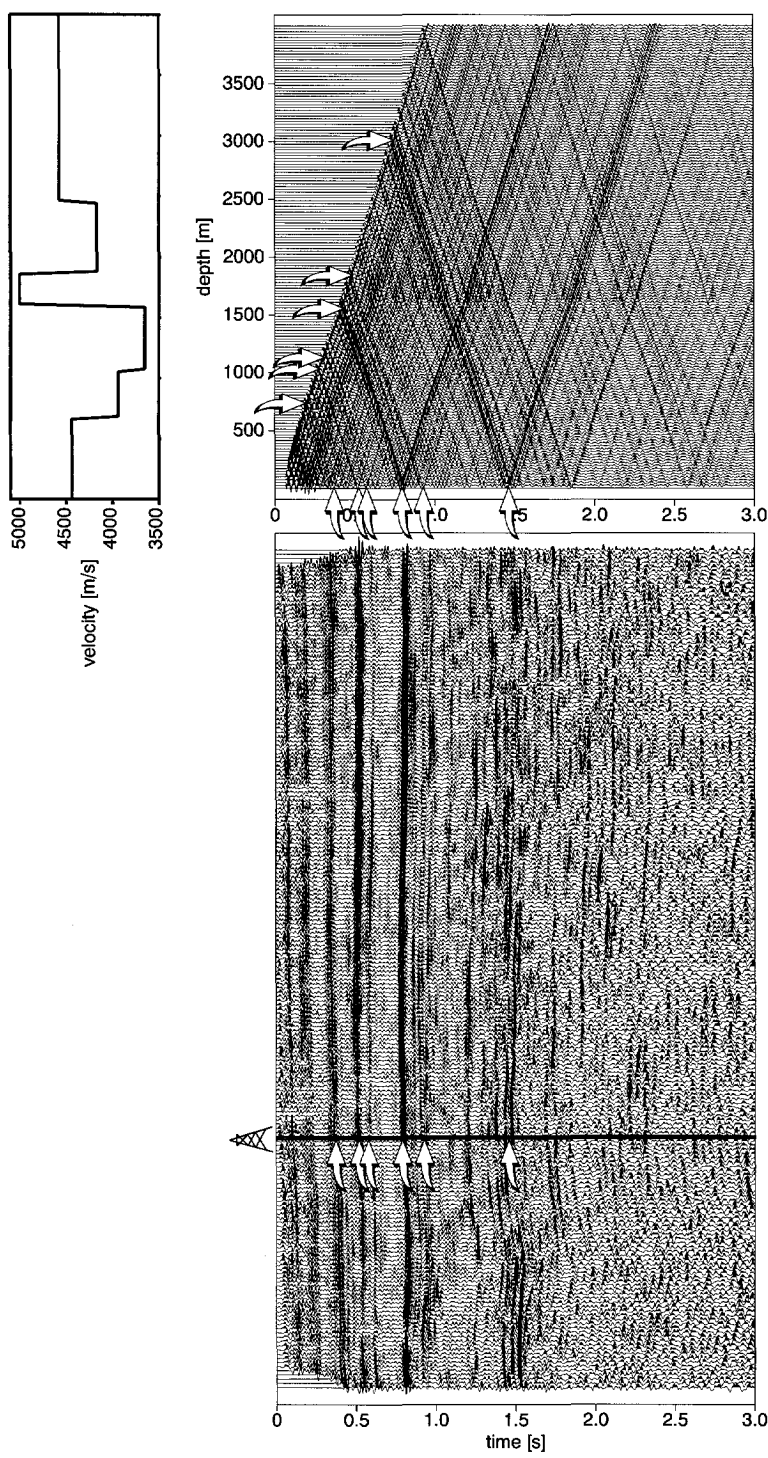


Figure 7.15 Stack of the dataset showing its relation with the pseudo VSP data generation at zero offset. The data was recorded in the Middle East.

7.6 Land dataset (II)

This land dataset was recorded in North Africa and was provided by the Atlantic Richfield Company (ARCO) Plano, U.S.A.. In this example some results will be shown on the dataset from North Africa. The pseudo VSP process works best if there is a coherency in the reflectors of interest and if the events in the shot record are clearly identifiable. Since the single preprocessed shot gathers did not show enough coherency and the variation of the data was little, 11 shot records around the well location were summed together to form a supergather. The missing near offset traces were filled in using NMO and spline interpolation. This process produced an adequate gather which can be used as input to the pseudo VSP process. The supergather is depicted in Figure 7.16a.

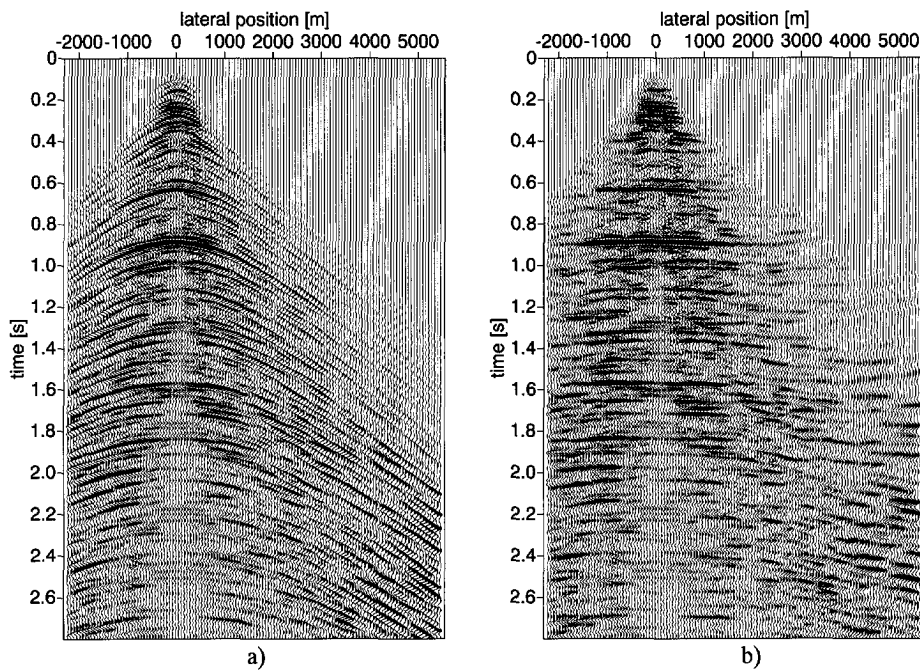


Figure 7.16 a)Supergather (summation of 11 shot records) and b)supergather after NMO. The data was recorded in North Africa (and provided by ARCO).

The flattened events are the primaries and also some of the multiples. The slightly dipping events at the larger offsets in Figure 7.16b may be some multiple energy and also some mode converted waves. These will not be of problem in the generation of the pseudo VSP data since pseudo VSP data will be generated for small offsets.

Figure 7.17 shows the c_p , c_s and ρ values at the well location. The tops of some of the major lithologic boundaries have been indicated on the c_p curve and are listed in Table 5.

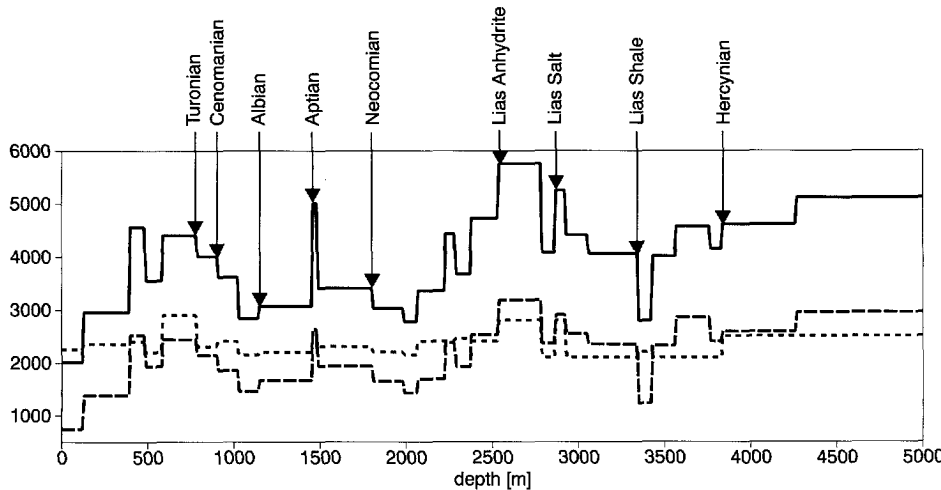


Figure 7.17 The values for the velocities (c_p and c_s) and density (ρ) at the well. Some of the major formations are indicated on the c_p curve. The units for c_p and c_s are [m/s]. The unit for ρ is [kg/m^3].

Table 5 Well tops.

sur- face	sea level	turo- nian	ceno- manian	albian	aptian	neoco- mian	lias anhy- drite	lias salt	lias shale	S4	tri- assic top t2	top serie infe- rieure	hercy- nian	
z [m]	0	190	780	900	1150	1450	1810	2540	2790	3350	3420	3570	3760	3830
t [s]	0.000	0.123	0.440	0.501	0.645	0.842	1.051	1.469	1.554	1.818	1.868	1.942	2.022	2.055

The objective of this example is to generate pseudo VSP data from the supergather (shown in Figure 7.16a, Figure 7.18a) using the model (given in Figure 7.17, Figure 7.18b), and tie the geological interpretation via the events in the pseudo VSP (Figure 7.18c) to the events in the shot record. A pseudo VSP data has been generated at 120m offset using the one-way wave field extrapolation operators since the objective was to tie the information from the surface into the depth and using the pseudo VSP as a (time-to-depth conversion) tool. The first break arrival times for the VSP have been determined using ray-tracing and the upgoing waves in the generated pseudo VSP data have been cut at the first break arrival times to obtain the pseudo VSP image points.

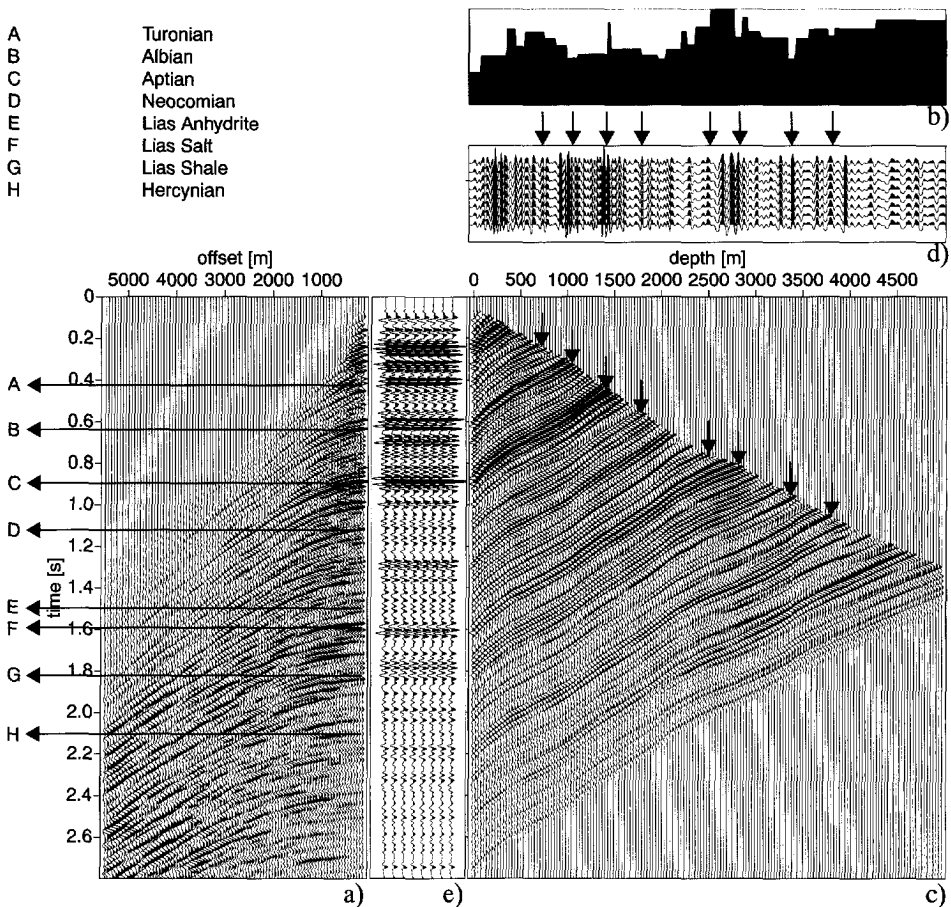


Figure 7.18 Geological integration from well log to surface seismic data via the pseudo VSP.

These image points have been mapped towards the depth axis and the resulting trace is reproduced 8 times for a better distinction of the different events (Figure 7.18d). The trace from the shot records at the well location has also been reproduced 8 times for a better coherency of the events and for an easier interpretation and integration with the pseudo VSP. Here the pseudo VSP has been spliced onto the supergather at the lateral location of the well and is tied to the c_p model with the geological interpretations. In this way, some of the main geological formations can be integrated with the surface seismic data : the formations indicated on the depth model can be tied to the events on the shot gather via the pseudo VSP data.

7.7 Land dataset (III)

This dataset was recorded at a survey in West Texas, U.S.A., as part of the corporate research project between UNOCAL and JNOC. The data was provided by the Japan National Oil Corporation (JNOC). The acquired data quality was quite good despite most of the sediments in this field are high velocity carbonates. These carbonates generate strong ground roll noise. For a description of the dataset the reader is referred to Kozawa et al. (1996). Figure 7.19a illustrates a 2-D slice from the 3-D shot record which was recorded at the surface. Some offset VSP data have been acquired in the neighbourhood of the seismic line. The offset VSP data have been mapped to depth with the aid of the VSP-CDP transform (see Appendix C for a brief description on VSP-CDP transforms). The objective of this example is to use a 2-D slice from the 3-D shot record, generate a pseudo VSP data, and integrate the events from the pseudo VSP to the VSP-CDP depth profile obtained by the acquired offset VSP data. Figure 7.19a shows a 2-D slice from the *raw* 3-D shot surface shot record. The shot record has to be preprocessed to be used as input to the pseudo VSP generation. Figure 7.19b shows the same shot record after preprocessing. The preprocessing steps were frequency filtering, NMO correction and lateral median filtering, and inverse NMO.

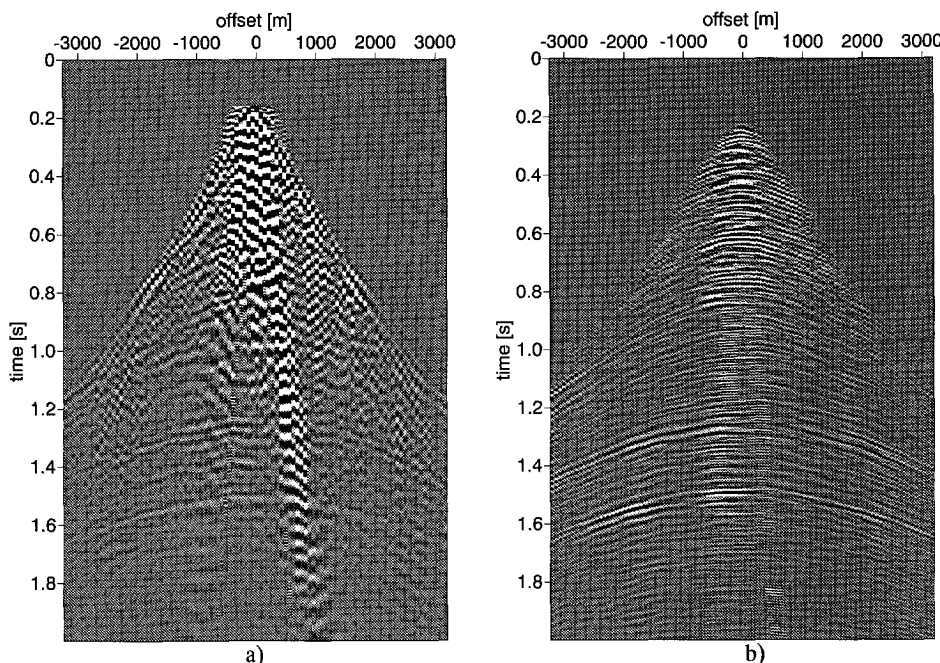


Figure 7.19 a) 2-D slice from the raw 3-D shot record and b) same shot record after preprocessing. The data was recorded at a survey in West Texas, U.S.A. and was provided by the Japan National Oil Corporation (JNOC).

Figure 7.20 shows respectively the offset VSP-CDP mapping (Figure 7.20a) and drillbit reverse VSP-CDP mapping (Figure 7.20b) inserted into the surface seismic section (Kozawa et al., 1996). As can be noticed the data quality of the offset VSP data and drillbit data are quite good and show a very good match with the seismic surface data. The target reflections are indicated in Figure 7.20a and b.

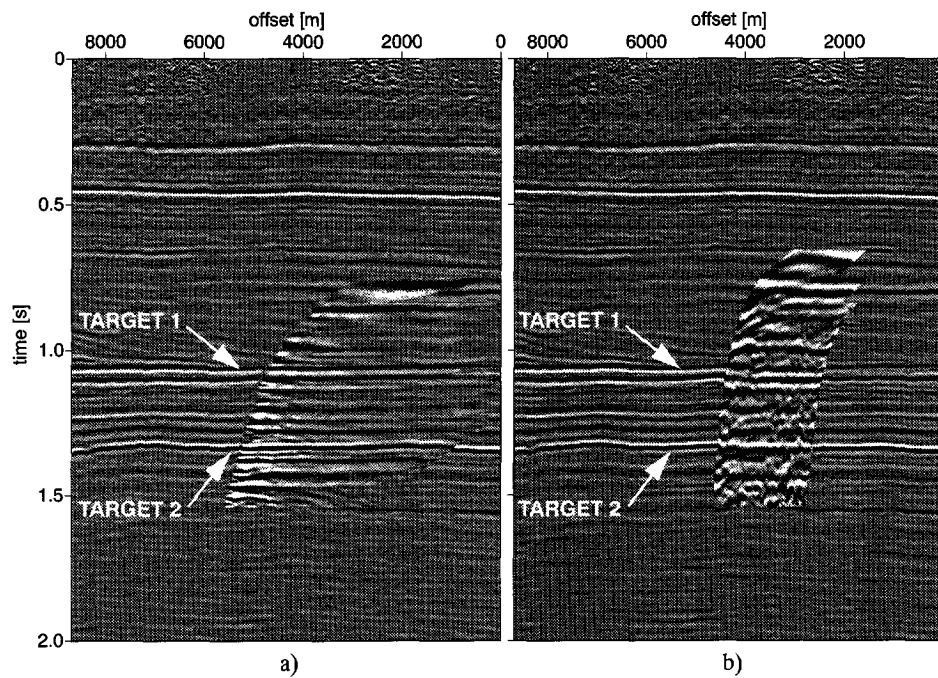


Figure 7.20 a)Offset VSP-CDP mapping inserted into the surface seismic section,
b)Drillbit reverse VSP-CDP mapping inserted into the surface seismic section.
The data was recorded at a survey in West Texas, U.S.A. and was provided by the
Japan National Oil Corporation (JNOC).

Figure 7.21 illustrates an Integrated Seismic Display (ISD) of the preprocessed shot record, pseudo VSP and the comparison with the VSP-CDP depth image obtained from the acquired offset VSP data. The two target reflections are indicated in the VSP-CDP profile.

The pseudo VSP has been generated from the shot record and the upgoing waves have been cut at the first break times. The pseudo VSP image points have been integrated with the events in the VSP-CDP depth image (black arrows). This integration of data with the aid of the pseudo VSP shows the correlation of the target reflections in the different displays.

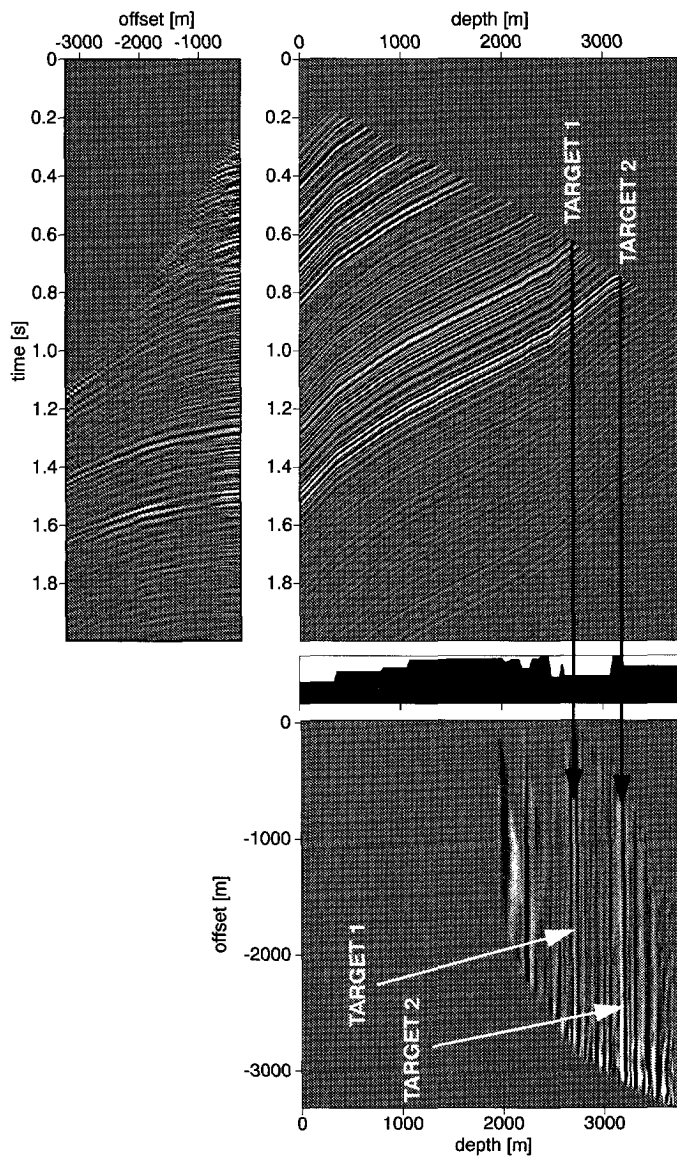


Figure 7.21 Integrated Seismic Display (ISD) of preprocessed shot record, pseudo VSP data and VSP-CDP depth image, obtained from the acquired offset VSP data. The velocity profile that was used for the generation of the pseudo VSP data is also integrated. The two target reflections can be observed in the data. The data was recorded at a survey in West Texas, U.S.A. and was provided by the Japan National Oil Corporation (JNOC).

7.8 Physically modeled dataset

An experiment has been carried out with two different acquisition geometries for respectively recording a standard shot record and a VSP recording (without surface-related multiples). The geometry for the acquisition of both datasets is depicted in Figure 7.22 (the experimental facility scale to seismic scale is 1:20.000). The values in this section refer all to the seismic scale. The total number of receivers along the surface is 401 with a spatial sampling of 8m. An object ($c_p=5000\text{m/s}$ and $\rho=9000\text{kg/m}^3$) with the shape of a salt dome (Figure 7.22) has been placed on a horizontal plate ($c_p=5800\text{m/s}$ and $\rho=7890\text{kg/m}^3$) with a thickness of 40m (seismic scale). The dimensions of the object are shown in Figure 7.22. The source has a 100m offset from the VSP and from the nearest hydrophone at the surface.

The objective of this experiment is to illustrate the propagation and reflection of waves for this configuration with the aid of the VSP data. For a better understanding of the events appearing in the surface shot record, the display has been integrated with the VSP recording. Figure 7.23a and b show respectively the recording of the surface shot record and the VSP recording (the hydrophone spacing in the VSP is 8m). Such integrated displays of vertical and horizontal receiver datasets in the use of seismic interpretation has been regularly shown in this thesis.

Due to the structure of the object, a lot of diffraction energy is generated. The appearance of the diffraction energy is clearly visible in the VSP recording (see e.g. arrows in Figure 7.23b numbered as 1 and 2). The arrow numbered 1 shows clearly the origin and depth of the diffraction point (being the top of the object). Some energy is propagating upwards reaching the surface and some part is propagating downwards. The arrow indicated with number 2 shows clearly that some energy is propagating downwards, reflects at the plate at 1100m depth and is recorded in the surface data. Note that the direct wave is present in both datasets. For larger angles, the higher frequencies are attenuated more than the lower frequencies due to the directivity of the receivers. The arrow numbered 3 shows the reflection from the source transducer. Arrow 4 shows an internal multiple reflection between the plate and the receiver transducer and in this way shows an apparent velocity propagating up with 1/3 of the direct wave velocity.

Different views of the Delft experimental facility during recording are depicted in Figure 7.24. The arrows in the different pictures indicate the “well” near the object. A near offset (100m) section has been extracted from all the shot records (shot distance of 8m) and the result is illustrated in Figure 7.25. The lateral position indicated with “0” represents the location of the VSP (indicated with the black line). It should be noticed that the trace along the black line is corresponding to the common trace in Figure 7.23.

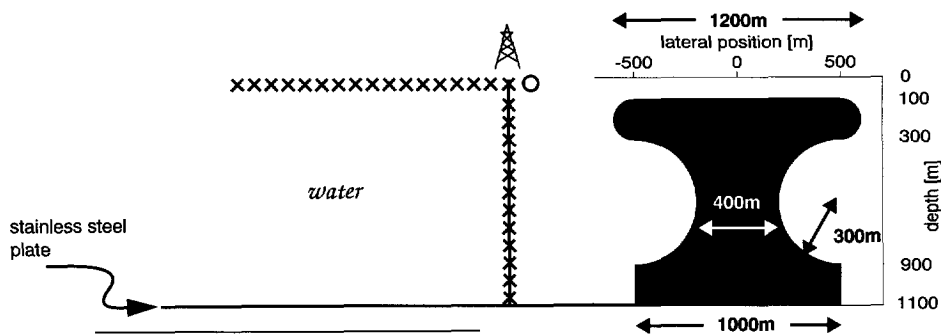


Figure 7.22 Geometry for the acquisition and recording of a shot record and a VSP in the Delft experimental facility.

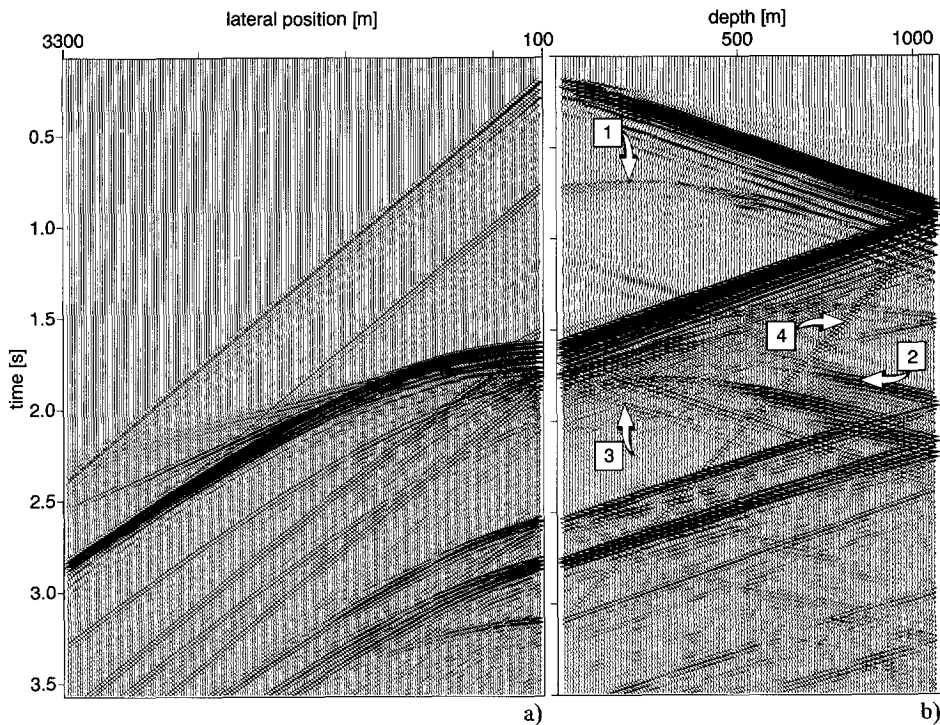


Figure 7.23 a) Shot record and b) VSP recording.

The shot record which is depicted in Figure 7.23a has been used to generate pseudo VSP data and make comparisons with the recorded VSP data. Here the one-way wave field extrapolation operators have been used to generate a pseudo VSP data until the depth of the stainless steel plate at 1100 m (Figure 7.26). From the recorded VSP data it is very clear that some diffraction energy is propagating downwards and reflects at the stainless steel plate.

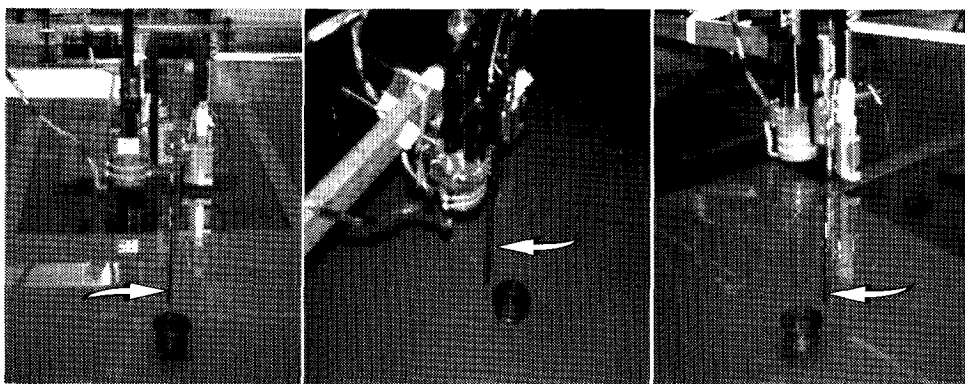


Figure 7.24 The acquisition and VSP recording in the Delft experimental facility.

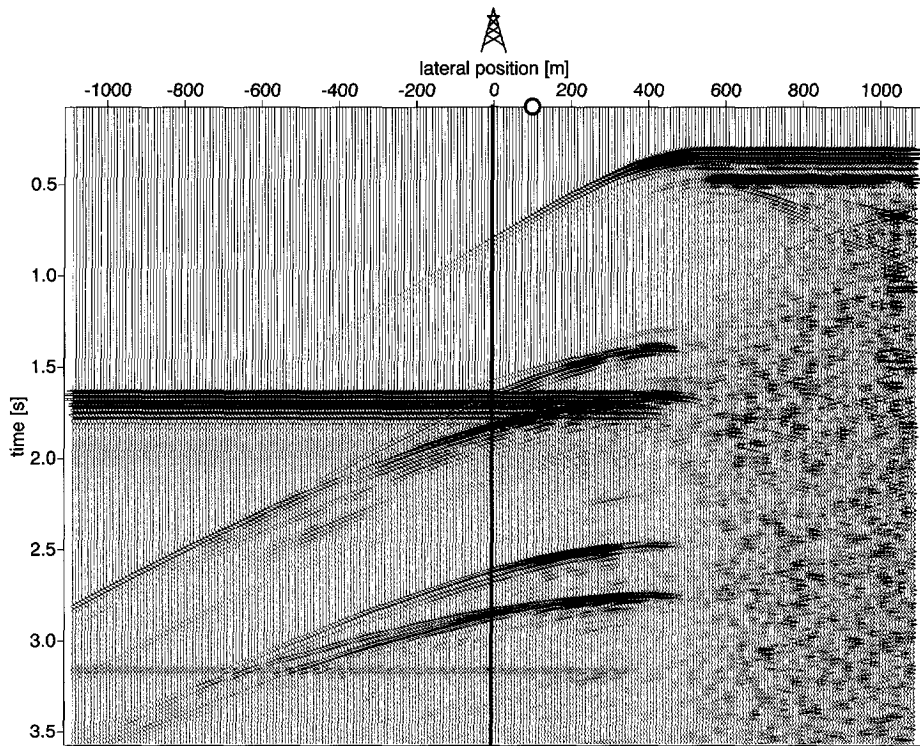


Figure 7.25 Near offset section extracted from the surface shot records. The near offset is 100m. The lateral position indicated with "0" represents the location of the VSP.

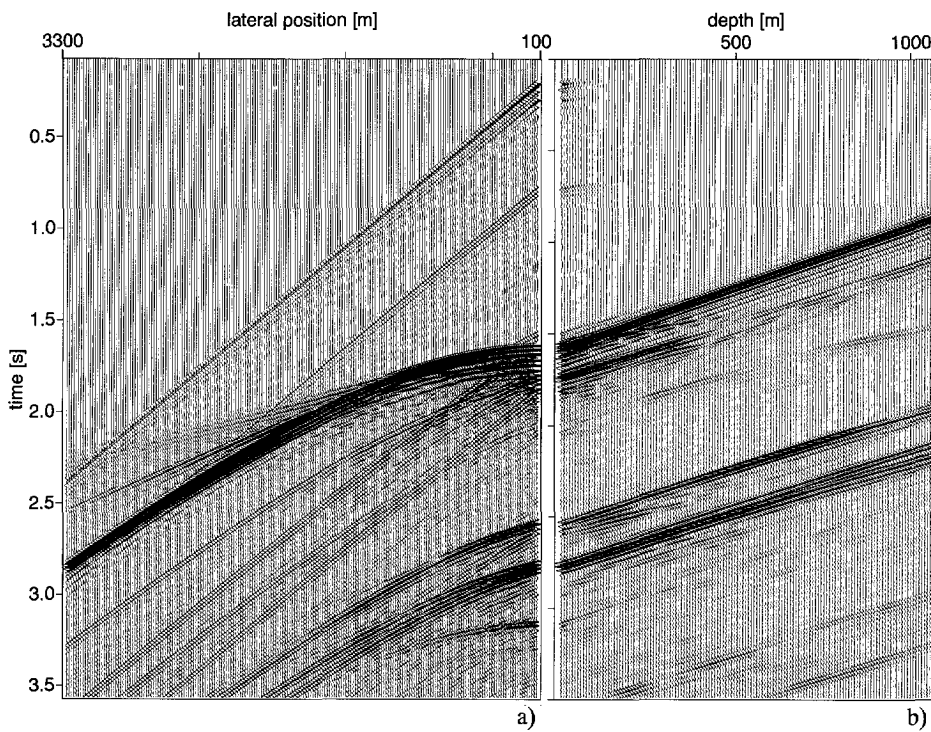


Figure 7.26 a)Shot record and b)generated pseudo VSP data.

For taking the stainless steel plate into account, the pseudo VSP is also generated to a depth of 2200m. The information below the stainless steel plate (larger depths than 1100m) contains information to define later on the downgoing waves in the generated pseudo VSP data above 1100m. The result of this idea is demonstrated in Figure 7.27.

The pseudo VSP data in Figure 7.27a has been divided into two parts : one part above 1100m and the other below 1100m. Using the impedance of the stainless steel plate (equal to $45 \cdot 10^6$ kg/(m²s) and the impedance of water = $1.49 \cdot 10^6$ kg/(m²s)),
the reflection coefficient for a fluid-fluid boundary can be determined according to :

$$R = \frac{Z_2 - Z_1}{Z_2 + Z_1} = \frac{45 - 1.490}{45 + 1.490} = 0.94 , \quad (7.2)$$

which has to be divided to the data part below 1100m before mirroring and adding it to the part above 1100m. The symbols Z_1 and Z_2 represent respectively the impedances for the medium above and below the stainless steel plate.

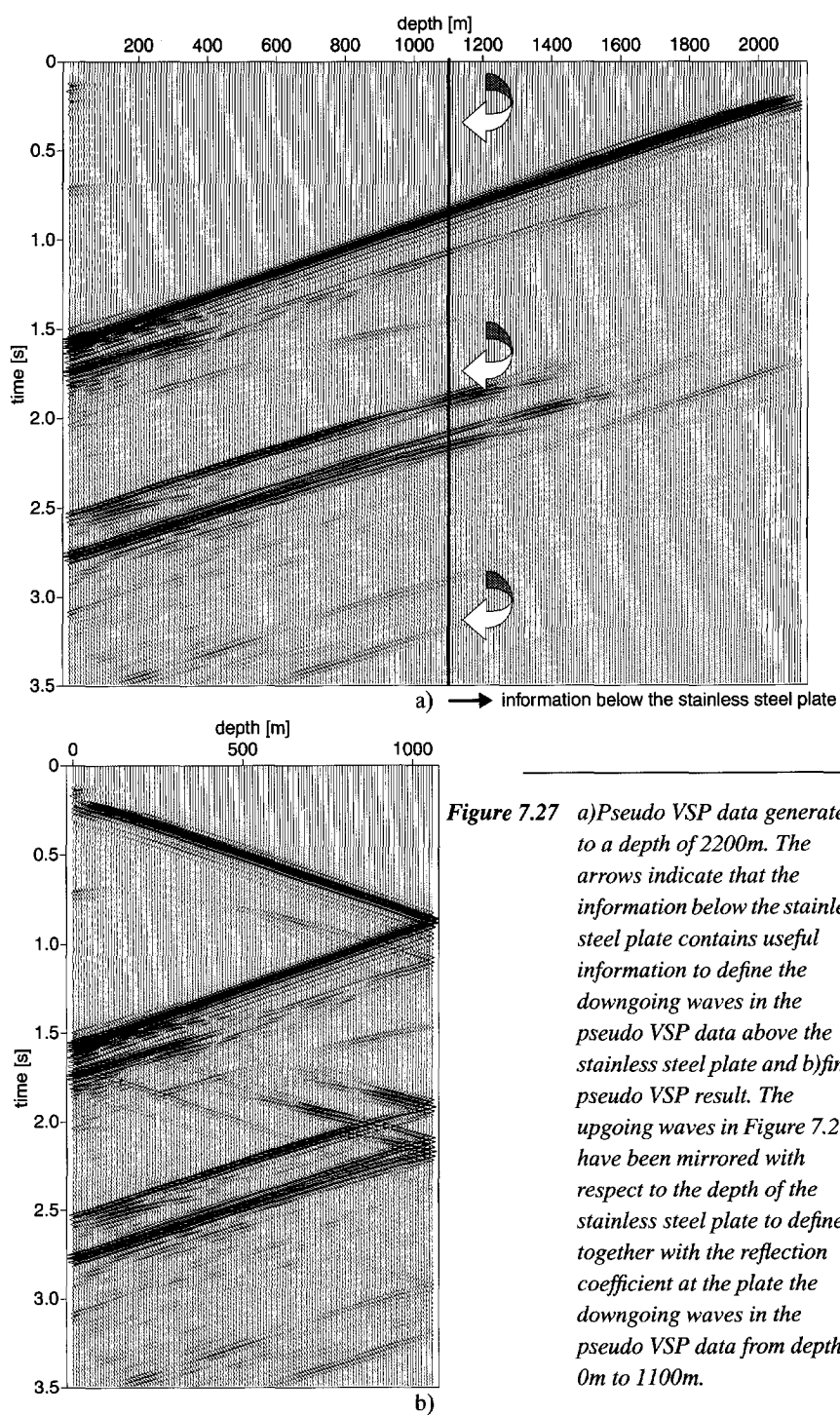


Figure 7.27 a)Pseudo VSP data generated to a depth of 2200m. The arrows indicate that the information below the stainless steel plate contains useful information to define the downgoing waves in the pseudo VSP data above the stainless steel plate and b)final pseudo VSP result. The upgoing waves in Figure 7.27a have been mirrored with respect to the depth of the stainless steel plate to define together with the reflection coefficient at the plate the downgoing waves in the pseudo VSP data from depth 0m to 1100m.

The final result of the pseudo VSP generation which is depicted in Figure 7.27b shows a very good match with the VSP data which was recorded in the Delft experimental facility. The generated pseudo VSP below $1100m$ has been used to determine the reflection at the stainless steel plate and define in this way the downgoing waves in the pseudo VSP data above the stainless steel plate.

This example showed the successful recording of VSP data in the Delft experimental facility. The measurements of a traditional shot record and VSP registration have been integrated to each other for a better understanding of the waves which have propagated through the watertank.

In this chapter some 2-D case studies were presented on field data and physically modeled data. It was illustrated that by showing Integrated Seismic Displays (ISD) with the pseudo VSP data, different data types can be integrated to each other for a better data interpretation and integration. Furthermore some real VSP data were compared with single source and multi source pseudo VSP data. The pseudo VSP data appeared to be a very useful tool in bridging gaps in real VSP data and in tying surface data with real VSP data. Real VSP corridor stack traces have been inserted into unmigrated and migrated surface seismic sections. Taking all boundary conditions at the seabottom into account, using two-way techniques, source wavelets can be estimated interactively by generating pseudo VSP data from marine surface data with all surface-related multiples included. An experiment was performed for the recording of a combined shot record/VSP configuration in the Delft experimental facility. The recorded VSP showed a good comparison with the generated pseudo VSP data from the surface recorded data.

Chapter 8

3-D case studies

8.1 Introduction

In 2-D seismic exploration, the sources and receivers are positioned along a line at the surface. Here it is assumed that the earth can be considered to be two-dimensional (invariant in the lateral direction perpendicular to the line of the measurement). Actually the earth's subsurface is three-dimensional and the amount of 3-D seismic measurements have increased enormously the last years.

In this chapter, the generation of 3-D pseudo VSP data is discussed and illustrated on different datasets. 3-D shot records (x, y, z_0, t) will be used for the generation of the 3-D pseudo VSP data. The 3-D shot records will be transformed to pseudo VSP datasets (x_0, y_0, z, t) . Examples will be shown on the SEG/EAGE 3-D Overthrust model, physically modeled datasets and a 3 layered model. The results of the pseudo VSP data generations are compared with modeled VSP and integrated in combination with the slices from the 3-D migrated volumes (x, y, z) of data. In combination, the integration of different datasets yields a better insight and understanding of the wave propagation and the various events originating from the complex subsurface model. Some 3-D snapshots are shown at the end of the chapter to improve the data interpretation, further showing the wave propagation at different times.

The method of 3-D pseudo VSP generation is based on the recursive acoustic one-way wave field extrapolation schemes that are aimed at removing propagation effects and thus improving the interpretability of seismic data (Alá'i et al., 1995).

In other words, the methods that are used in this thesis, result in seismic data as if they were measured in the subsurface instead of measurements recorded at the earth's surface.

The total wave field at the surface (3-D shot record (x, y, z_0, t)) is decomposed into down- and upgoing wave fields. These wave fields are extrapolated separately and at each depth level, the wave field is extracted for a predefined borehole/detector configuration (x_0, y_0, z) , where x_0 and y_0 may be functions of z in case of deviated boreholes. The 3-D wave field extrapolation can be formulated in terms of forward extrapolation of the downgoing (*source*) wave field and inverse extrapolation of the upgoing (*reflected*) wave field. In the wavenumber frequency domain, the monochromatic wave field extrapolation from depth level z_{m-1} to z_m is given by the following expression :

$$\begin{pmatrix} \tilde{P}^+ \\ \tilde{P}^- \end{pmatrix}_{z_m} = \begin{pmatrix} \tilde{W}(z_m, z_{m-1}) & 0 \\ 0 & [\tilde{W}(z_m, z_{m-1})]^* \end{pmatrix} \begin{pmatrix} \tilde{P}^+ \\ \tilde{P}^- \end{pmatrix}_{z_{m-1}}, \quad (8.1)$$

where the asterisk * denotes the complex conjugate. \tilde{W} is called the forward wave field extrapolation operator :

$$\tilde{W}(k_x, k_y, \omega, \Delta z) = \exp\left(-j\sqrt{\frac{\omega^2}{c^2} - (k_x^2 + k_y^2)} \Delta z\right), \quad (8.2)$$

with $\Delta z = z_m - z_{m-1}$. These operators have been transformed to the space-frequency domain in an optimized way (Thorbecke and Berkhouw, 1994) such that spatial 2-D convolutions can be performed along the x - and y -coordinate, which can be easily generalized to accommodate lateral velocity variations. At each depth level the downgoing and upgoing wave fields are selected at x_0, y_0 , thus building up the pseudo VSP step by step.

In this chapter, three-dimensional (3-D) wave field extrapolation operators are used for the generation of 3-D pseudo VSP data from 3-D surface data. The generation of 3-D pseudo VSP data deals with the focusing of all the information registered on a plane into the different depth locations for a predefined well.

Figure 8.1 illustrates the generation of 3-D pseudo VSP data from 3-D surface data. The 3-D wave field extrapolation is done by a recursive x, y, ω algorithm.

Section 8.2 shows an example on a 3-D shot record from the SEG/EAGE Overthrust model. In Section 8.3 the 3-D pseudo VSP is generated from a 3-D shot record respectively a 3-D areal shot record and finally Section 8.4, illustrates the wave propagation through a 3 layered model where the uppermost layer is a water layer on top of an irregular layer and a dipping plane.

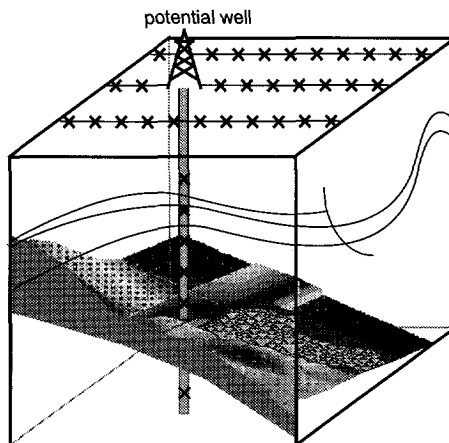


Figure 8.1 3-D pseudo VSP generation from 3-D seismic surface measurements.

8.2 SEG/EAGE 3-D Overthrust model and dataset

In this section a short description is given on the *SEG/EAGE 3-D Overthrust model* and some results are illustrated. In the next section an example is illustrated on 3-D watertank data. The 3-D wave field extrapolation operators used to extrapolate the wave field from the surface into the subsurface are based on the one-way wave equation.

The synthetic data used in this section, are issued from the joint SEG/EAGE 3-D Modeling Project (SEM). The aim of the SEG/EAGE 3-D Modeling Project is to provide worldwide the Oil & Gas industry and academia with 3-D synthetic seismic datasets (simulation of realistic 3-D surveys through numerical calculations). The modeling of the seismic data has been computed by Institute Français du Pétrole (IFP- 20%) and the Department of Energy (DOE U.S.A. - 80%). The *3-D Overthrust model* has been designed and built in 1994 by IFP (with the help of TNO using the GOCAD software, from Nancy Geological School (France). For a thorough description and discussion the reader is referred to the three reports on the SEM in the Leading Edge: 1) Aminzadeh et al. (1994), 2) Aminzadeh et al. (1995) and 3) Aminzadeh et al (1996).

The Overthrust model includes a thrusted sedimentary sequence constructed on top of a structurally decoupled extensional basement block. Some features such as the convergence of the faults, the presence of channels and lenses, will allow to test the ability of the seismic tools to resolve details in the structure in presence of strong velocity contrasts.

The energetic and flat seismic marker at the base of the salt unconformity level will provide a reference level for the processing.

Figure 8.2 illustrates some different views on the 3-D gridded Overthrust model with dimensions $20 \times 20 \times 4 \text{ km}$ and 17 layers in all. The model comprises a regular grid with a spacing of 25 m . Figure 8.2a shows a general view of the model where the 2 converging faults and the upper channel are visible (the dimensions are indicated along the axes). The surface layer of the model is eroded (Figure 8.2b). Figures 8.2c, d and e show the complexity of the model by some depth slices. The model consists of upper and deeper channels. The upper channels can be seen in Figure 8.2c. The deep channels with meandriform structures can be clearly identified at the slice with depth $z=2625 \text{ m}$ (see Figure 8.2e).

A 3-D VSP data has been modeled in the Overthrust model. Figure 8.3 shows two orthogonal vertical sections of the velocity cube : 2-D dip-section ($y=455$) respectively 2-D strike section ($x=540$). In the area where the well is located (indicated with black line in Figure 8.3), the structure is rather flat although lateral velocity variations are present. Notice that the well intersects the deep channel with meandriform structure (at 2625 m depth).

An Overthrust model shot gather (1 shot) provided by IFP, has been used in this section to test the idea on generating 3-D pseudo VSP data and making comparisons with the 3-D modeled VSP data. The pseudo VSP has proven to be a useful tool in understanding the nature (multiple or primary) and the origination point of different events on a seismic trace.

Figure 8.2f illustrates a top view of the Overthrust model at depth $z=1125 \text{ m}$. Note that the intersection of the black lines represent the well location. The black lines represent the 2-D dip and strike section as depicted in Figure 8.3. Furthermore the surface receiver area and the shot location are marked in Figure 8.2f. The 3-D VSP is modeled at an offset of 100 m with respect to the source location. Figure 8.4a illustrates the geometry of the modeled 3-D shot record and the 3-D VSP (submodel). Two vertical sections at the well are displayed in Figure 8.4b showing the area of receivers in the (x, y) plane used in the 3-D pseudo VSP generation and the 3-D shot record migration.

In the modeling of the data, a Ricker wavelet was used with a central frequency of 15 Hz and max frequency content of 37.5 Hz .

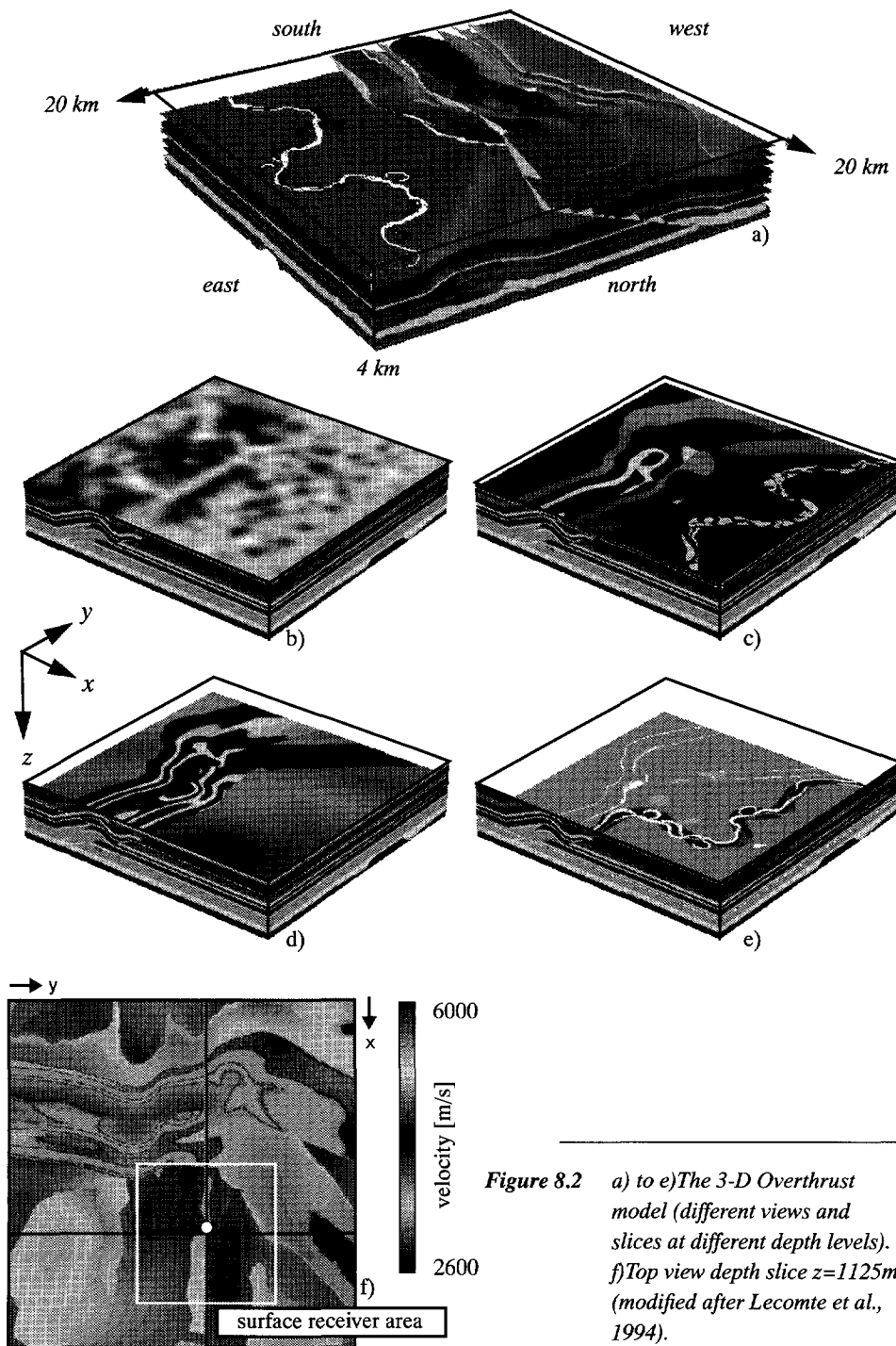


Figure 8.2 a) to e) The 3-D Overthrust model (different views and slices at different depth levels). f) Top view depth slice $z=1125\text{m}$ (modified after Lecomte et al., 1994).

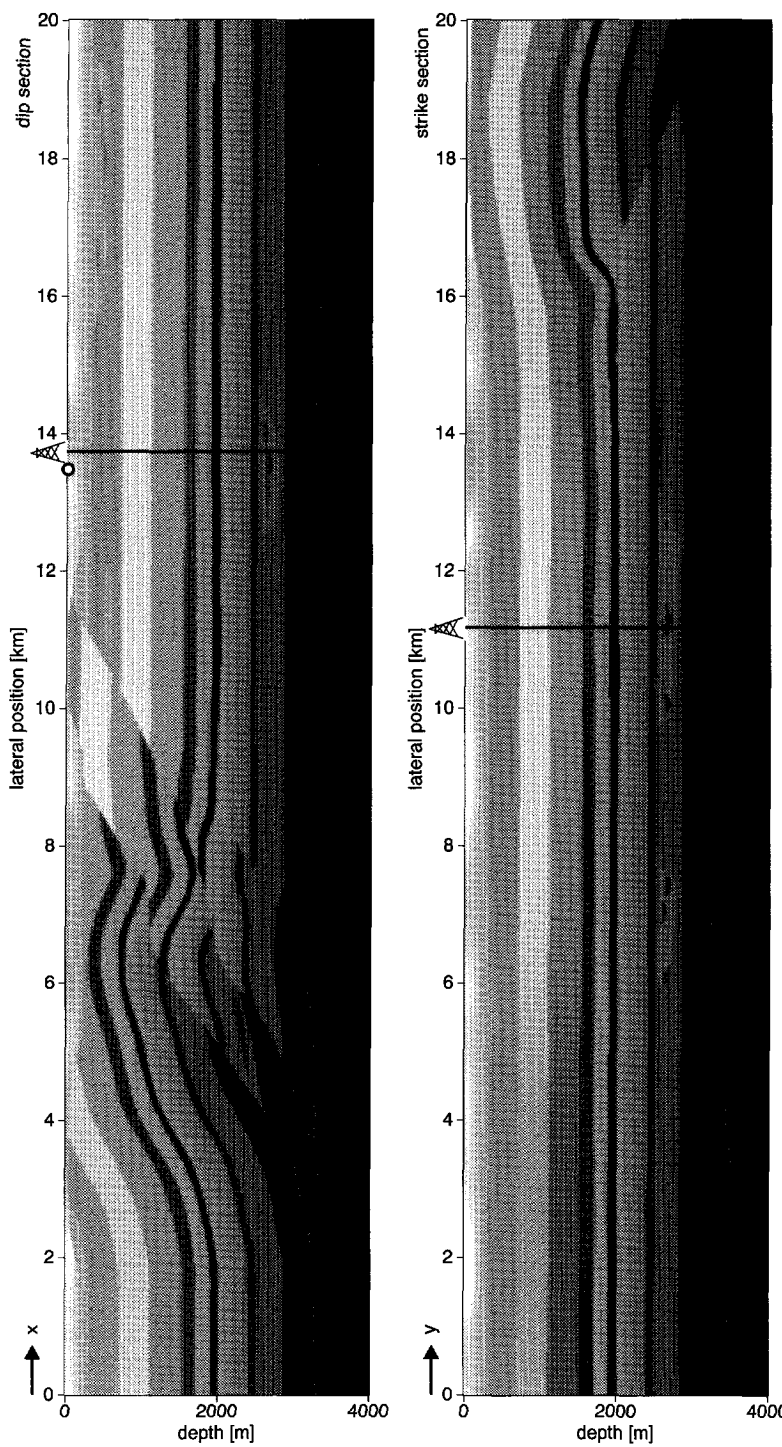


Figure 8.3 Two vertical sections (2-D dip section • slice $y=455$; $y=11350$ m and 2-D strike section • slice $x=540$; $x=13475$ m) along the coordinate axes of the velocity volume of the 3-D Overthrust model. The black line lines indicate the location of the dip and strike directions.

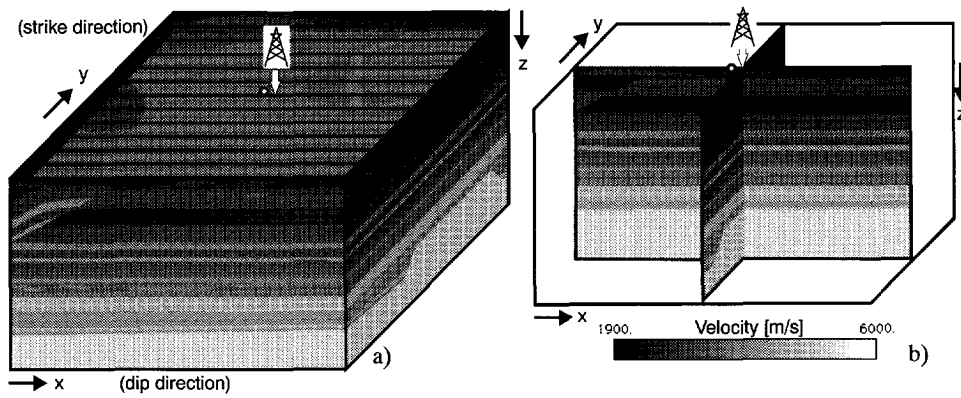


Figure 8.4 a) Submodel and b) two sections at the well (x,y area is used to generate 3-D VSP data).

Figure 8.5a illustrates a 3-D snapshot at time $t=1s$ showing the complex 3-D wave propagation of a shot point. A 3-D shot record is displayed in Figure 8.5b.

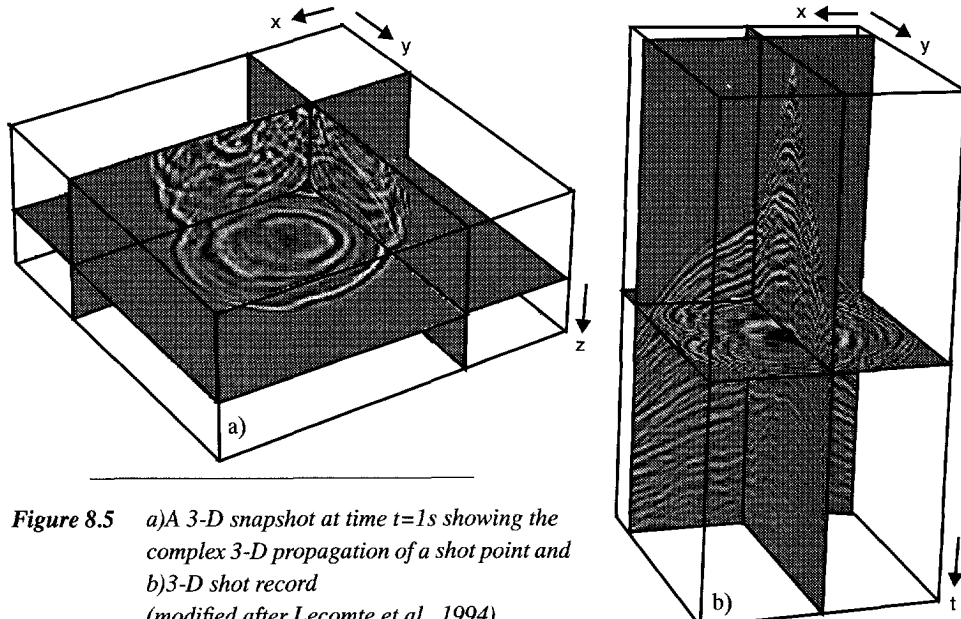


Figure 8.5 a) A 3-D snapshot at time $t=1s$ showing the complex 3-D propagation of a shot point and b) 3-D shot record (modified after Lecomte et al., 1994).

Figure 8.6 shows another view of a 3-D snapshot integrated with some layers of the Overthrust model.

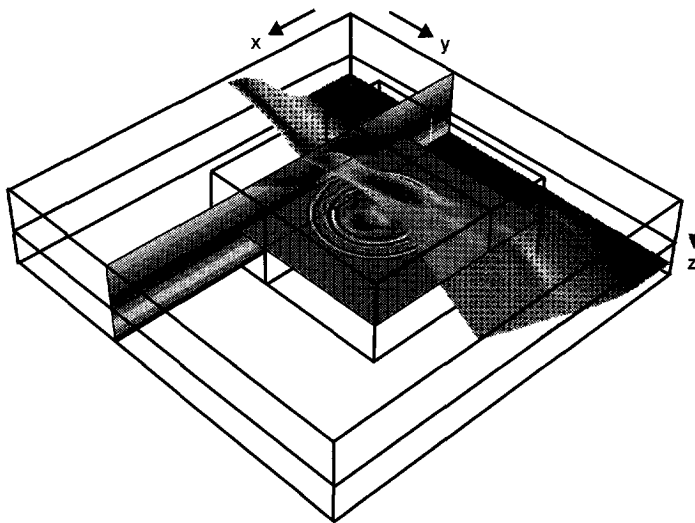


Figure 8.6 Overthrust model designed and built by IFP using GOCAD software in collaboration with TNO Institute of Applied Geoscience february 1994 (modified after Lecomte et al., 1994).

Figure 8.7 shows some time and vertical slices from the 3-D shot record modeled in the Overthrust model. Note that the (x,y) plane represents the area of surface receivers which is used in the generation of the 3-D pseudo VSP data. The vertical cross sections are taken at the well location. Note that the vertical resolution in the data looks quite high-frequent (apparent velocity of the wave fronts is visible). On the other hand, in the horizontal slices, the apparent high frequent shape of the wave front disappears (consequently the resolution is less) and becomes worse as time progresses (see deeper slice in Figure 8.7b). Some 2-D slices from the 3-D shot record modeled in the Overthrust submodel are displayed in Figure 8.8 (see Figure 8.4a for the geometry). Note that the slice ($y=161$) represent the 2-D slice from the 3-D shot record through the well location (receivers along the dip direction).

Figure 8.9 (left) illustrates an integrated display of a)slice of velocity subvolume 2-D strike section, b)slice of velocity subvolume 2-D dip section, c)velocity profile at well, d)combined slice of modeled 3-D shot record $y=161$ and 3-D modeled VSP data. From the modeled 3-D shot record, a 3-D pseudo VSP is generated using 3-D wave field extrapolation operators (based on a recursive x,y,ω extrapolation algorithm). The 3-D shot record has been also migrated. Figure 8.9e and f show respectively slices from the migrated volume where it can be seen that the sand channel as in the velocity model (Figure 8.9a and b) is clearly imaged.

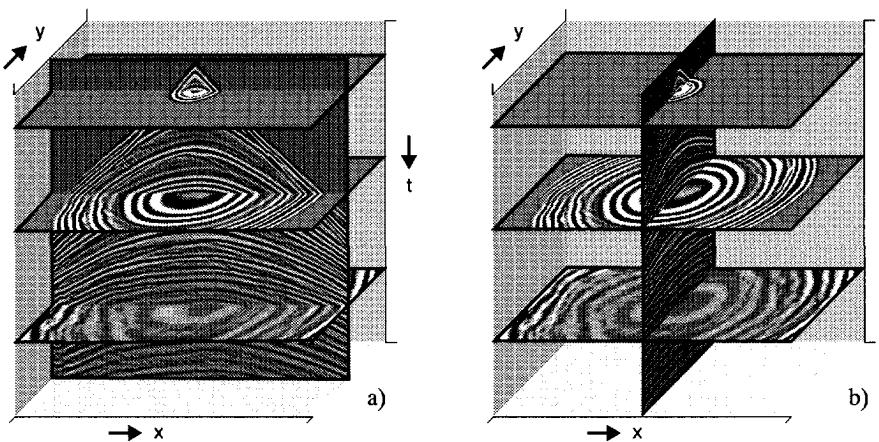


Figure 8.7 Time and vertical slices (at well location) through the 3-D shot record modeled in the SEG/EAGE 3-D Overthrust model.

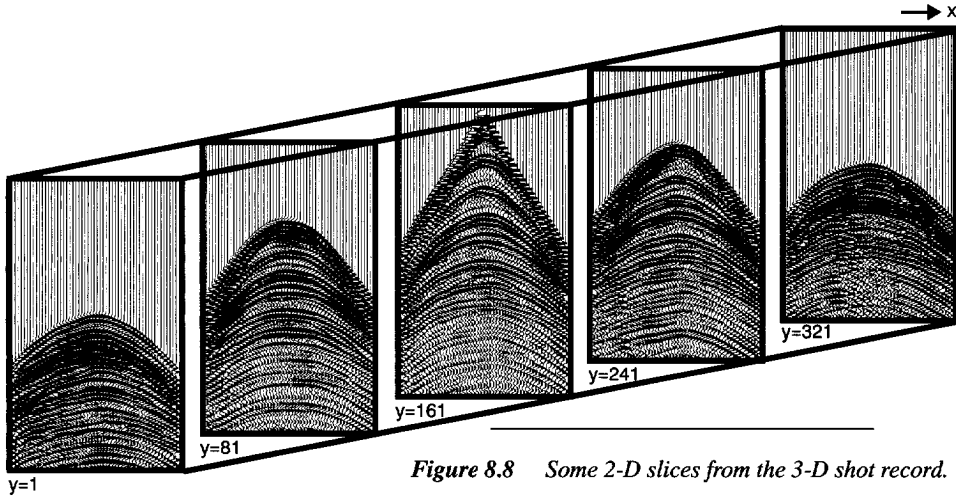


Figure 8.8 Some 2-D slices from the 3-D shot record.

Figure 8.9 (right) illustrates an integrated display of e)slice of 3-D migrated volume -strike section, f)slice of 3-D migrated volume - dip section, g)velocity profile at well and h)slice of modeled 3-D shot record $y=161$ and a generated 3-D pseudo VSP data. The 3-D pseudo VSP data display helps to establish the relationship between events in the original gather and the 3-D shot record migrated section. The match between the modeled VSP (in Figure 8.9d) and the pseudo VSP data (Figure 8.9h) is remarkable. Comparison of both VSP data shows that internal multiples are handled incorrect in the pseudo VSP data. In the one-way wave field extrapolation scheme, the boundary conditions are not fulfilled at the reflector. Therefore these events are extrapolated below the reflecting interface and cause an intersection with the downgoing source wave field.

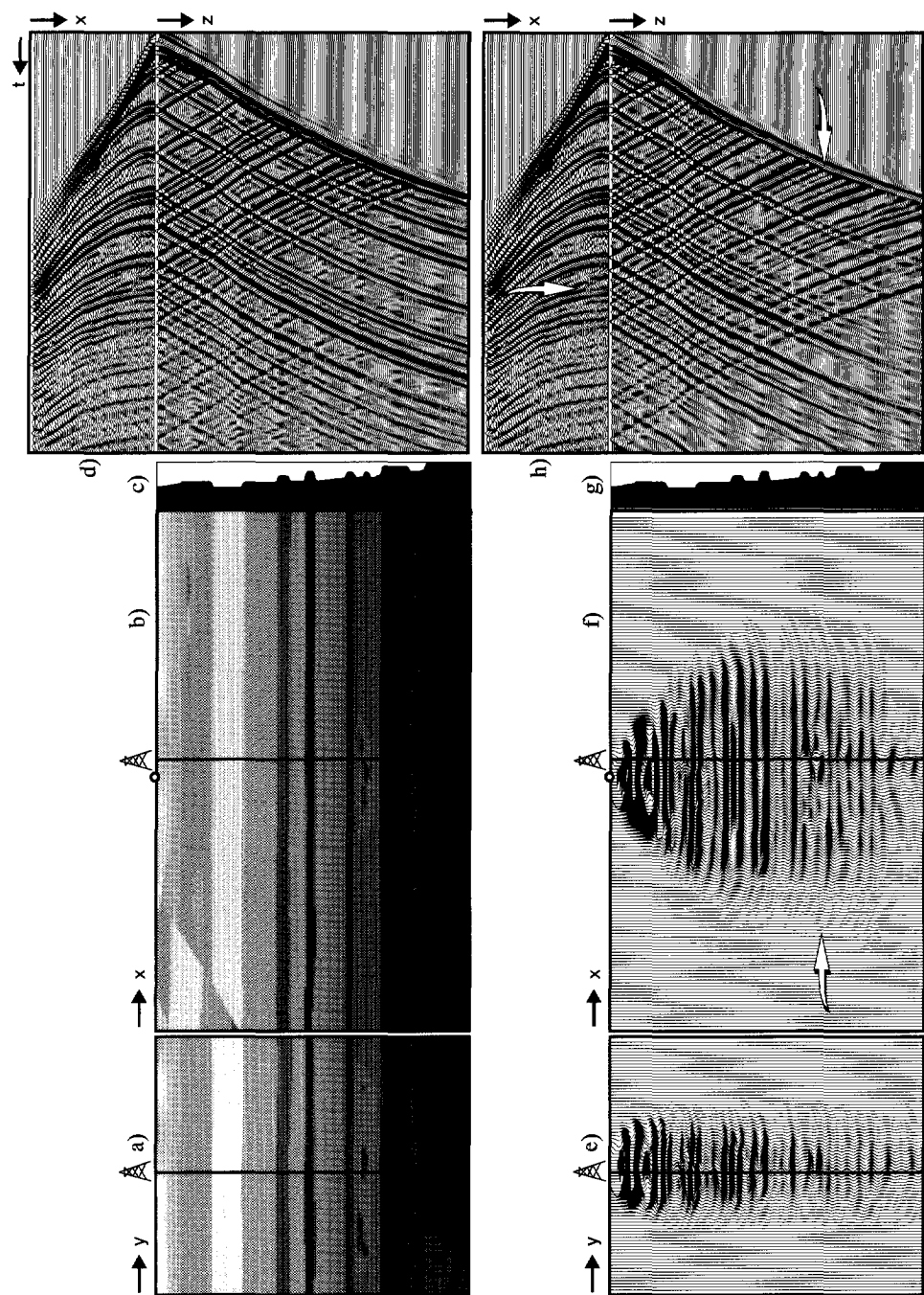


Figure 8.9 Integrated display of slice of 3-D shot record ($y=161$), 3-D modeled VSP, slices of 3-D migrated volume, velocity profile at well and 3-D pseudo VSP data.

Pseudo VSP data are particularly useful for detailed structural interpretation : a specific event in the surface data is connected to an event in the 3-D pseudo VSP which can be tied to its image in depth (see arrows in Figure 8.9f and h). Hence, the relation between events in the original data and in the migrated section becomes immediately clear. Note that multiple 2-D cross sections of the migrated 3-D volume can be used to integrate with the 3-D pseudo VSP for interpreting the data.

Figure 8.10a illustrates two slices from the 3-D shot record migrated volume (1 shot) at the well. These two vertical slices are at the same location as shown in Figure 8.4b. From the 3-D migrated volume, 4 depth slices are depicted in Figure 8.10b, in which the shot location and the area of illumination for that particular shot can be clearly seen (note that only amplitudes above certain threshold values have been depicted). Furthermore it can be seen that the sand channel at depth $z=2625m$ is clearly imaged. The imaged sand channels are indicated in Figure 8.10b by *I* and *II*. Figure 8.10c shows the depth slice of the submodel at depth $z=2625m$ for comparison with the migrated depth section. The channels at depth $z=2625m$ are indicated in Figure 8.10c by *I* and *II*. Note that channel (*I* in Figure 8.10b, white) corresponds to channel (*I* in Figure 8.10c, gray) and channel (*II* in Figure 8.10b, black) corresponds to channel (*II* in Figure 8.10b, black). From this comparison the area of illumination from one 3-D shot record can be observed.

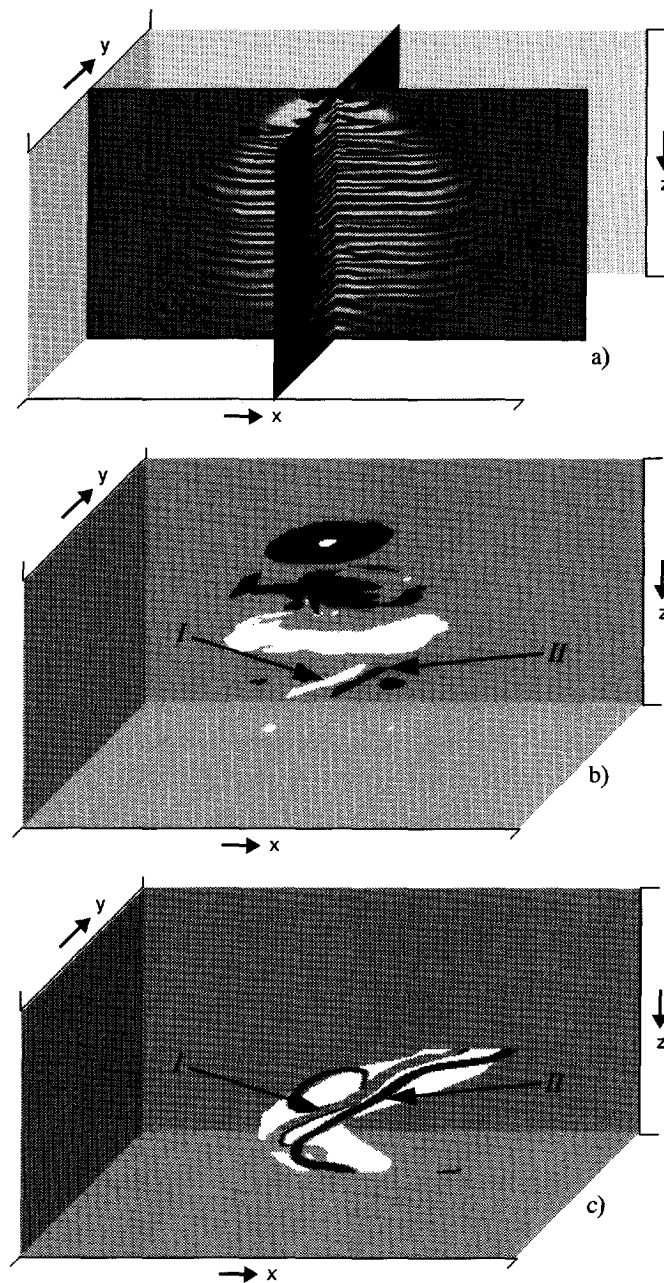


Figure 8.10 a) 3-D shot record migrated volume (1 shot), b) 4 depth slices of the migrated volume and c) depth slice of the Overthrust velocity submodel (depth 2625m).

Figure 8.11 shows for comparison the difference in 2-D and 3-D shot record migration applied on 2-D and 3-D data. Note the correctly imaged sand channels in Figure 8.11 b (3-D->3-D) and d (2-D->2-D) at depth $z=2625m$ (see arrows). This in contrast with Figure 8.11c (3-D->2-D) where the channels are not clearly imaged and some artifacts are visible.

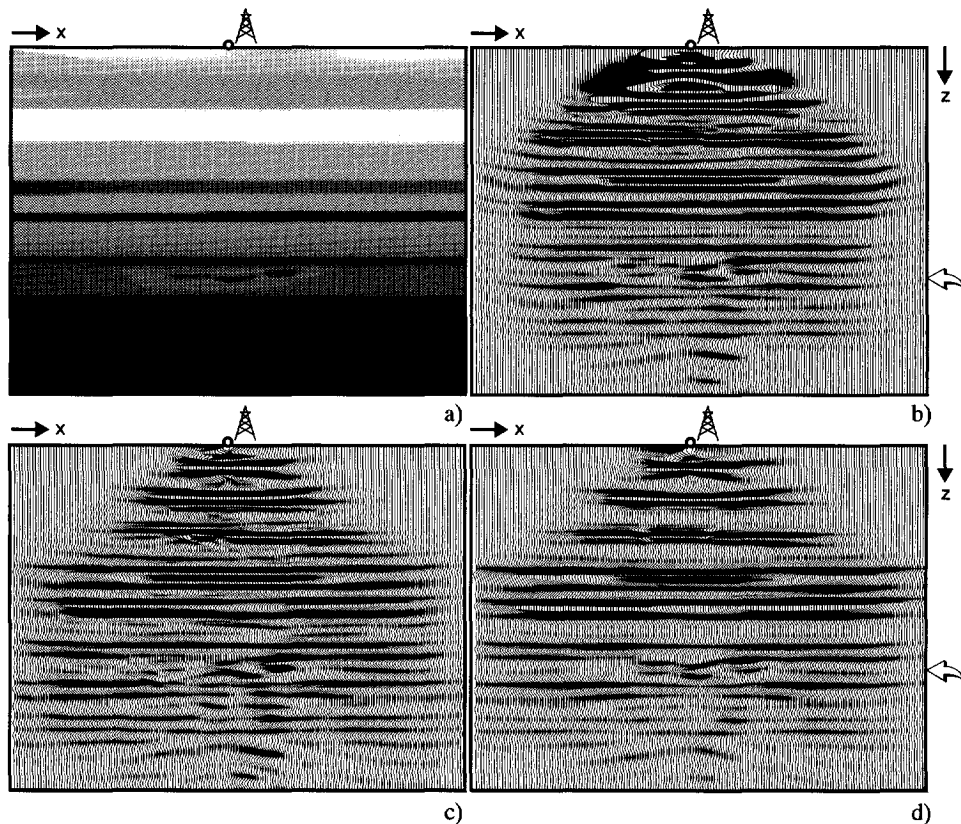


Figure 8.11 Part of dip section, slice of : a)velocity submodel ($y=161$), b)3-D shot record migration from full 3-D shot record, c)2-D shot record migration from 2-D slice $y=161$ of 3-D shot record and d)2-D shot record migration from 2-D shot record modeled along $y=161$.

8.3 Watertank model and dataset

In this section the pseudo VSP generation algorithm is applied to data measured in a watertank over a physical scale model (seismic scale 1:20000). All the values mentioned in this section are based on the seismic scale. The level of the marine acquisition is $z=0m$. Figure 8.12a shows the watertank 3-D model that is used for the 3-D data acquisition.

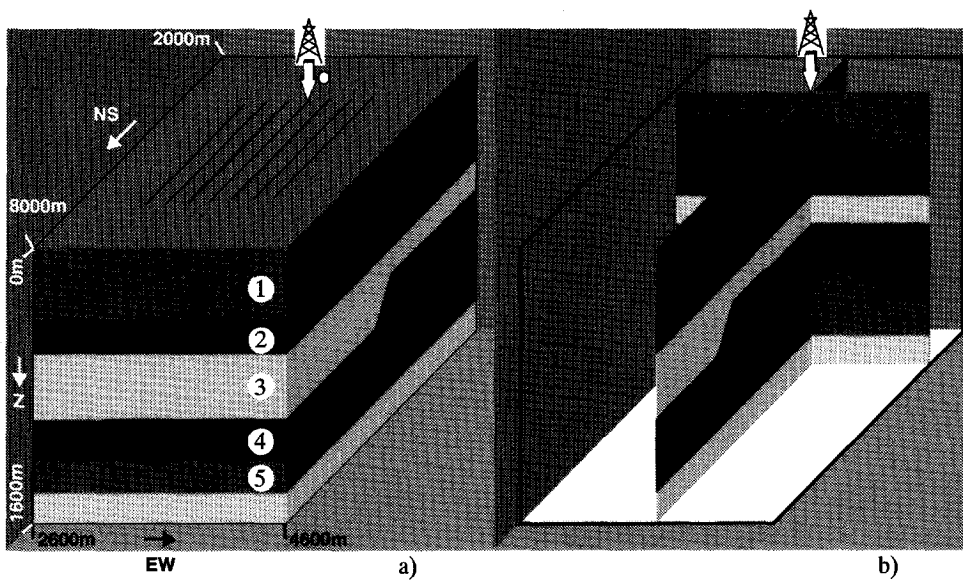


Figure 8.12 The watertank 3-D subsurface model.

The materials chosen in the scale model are mainly rubber like materials and do hardly support any shear waves. The dataset is acquired without water surface-related multiples. The data was recorded, using parallel shot lines with an in-line sampling (North-South direction) of 20m and a cross-line sampling (East-West direction) of 60m. The positioning will be referenced via their East-West (EW) and North-South (NS) on the model. The configuration for the data acquisition in the watertank is summarized in Table 6. The materials used for the model are listed in Table 7. Hydrophones were used with 7 parallel streamers (with in-line sampling of 20m and cross-line sampling of 60m), centered behind the source position (see Figure 8.12a). Figure 8.12 shows some vertical cross sections, to get a better view on the faults and domes of the 3-D model. One shot record is used to generate pseudo VSP data, the well being located at nearest offset of the middle streamer. The well position for the pseudo VSP generation is illustrated in Figure 8.12a and Figure 8.12b (NS3160, EW3680). Furthermore in Figure 8.12b two slices are shown to get an idea about the model around the well. Figure 8.13a shows the 4th streamer registration on line EW3680 of the total shot record measured in the watertank and the pseudo VSP generation from the total 7 streamer shot record. For the generation of the pseudo VSP data, 3-D wave field extrapolation operators have been used which are based on the one-way wave equation. For a discussion on 3-D extrapolation operators and their application (in 3-D migration) the reader is to Thorbecke and Rietveld (1994). Note that in this case, all the 2-D cross sections of the 3-D model through the well can be used for the interpretation of the data.

Table 6 The shooting geometry of the watertank data.

geometry	7 streamer marine data acquisition		
scale	1 : 20000		
nearest offset	100m		
far offset	2560m		
number of shots	250		
shot spacing	20m		
number of detectors per streamer	120 detectors	in-line detector spacing :	20m
		cross-line detector spacing :	60m
registration time	2460ms		
time sampling interval	4ms		
number of time samples	616		

Figure 8.13 illustrates the relation between the shot record, near offset section, 2-D zero-offset migration and pseudo VSP generation (Figure 8.13a, b, c and d respectively). A 2-D slice from the model is depicted in Figure 8.13e (the pseudo well location is indicated). As noticed the pseudo VSP data is not directly integrated to the shot record, but via the near offset section and the zero-offset migration. Following events through these paths gives a clear view on the propagation of the events through the 3-D watertank model. The events, indicated by I and II should not intersect the downgoing source wave field, because both events are internal multiples (see raypaths in Figure 8.13d). In the one-way wave field extrapolation scheme, the boundary conditions are not fulfilled at the reflector. Therefore these events are extrapolated further to the intersection with the downgoing source wave field.

In this way, 3-D areal shot record migration is integrated with the pseudo VSP generation, by generating VSP data at several lateral positions during the depth migration. By this integration a significantly better interpretation of the events visible in the areal shot record and their positioning in the 3-D depth image can be obtained.

Table 7 The materials used in the watertank model.

Layer	Material	Velocity [m/s]	Density [kg/m ³]
1	water	1487	1000
2	silgel	1018	959
3	beewax	2190	1035
4	silgel	1018	959
5	devcon	1510	1070

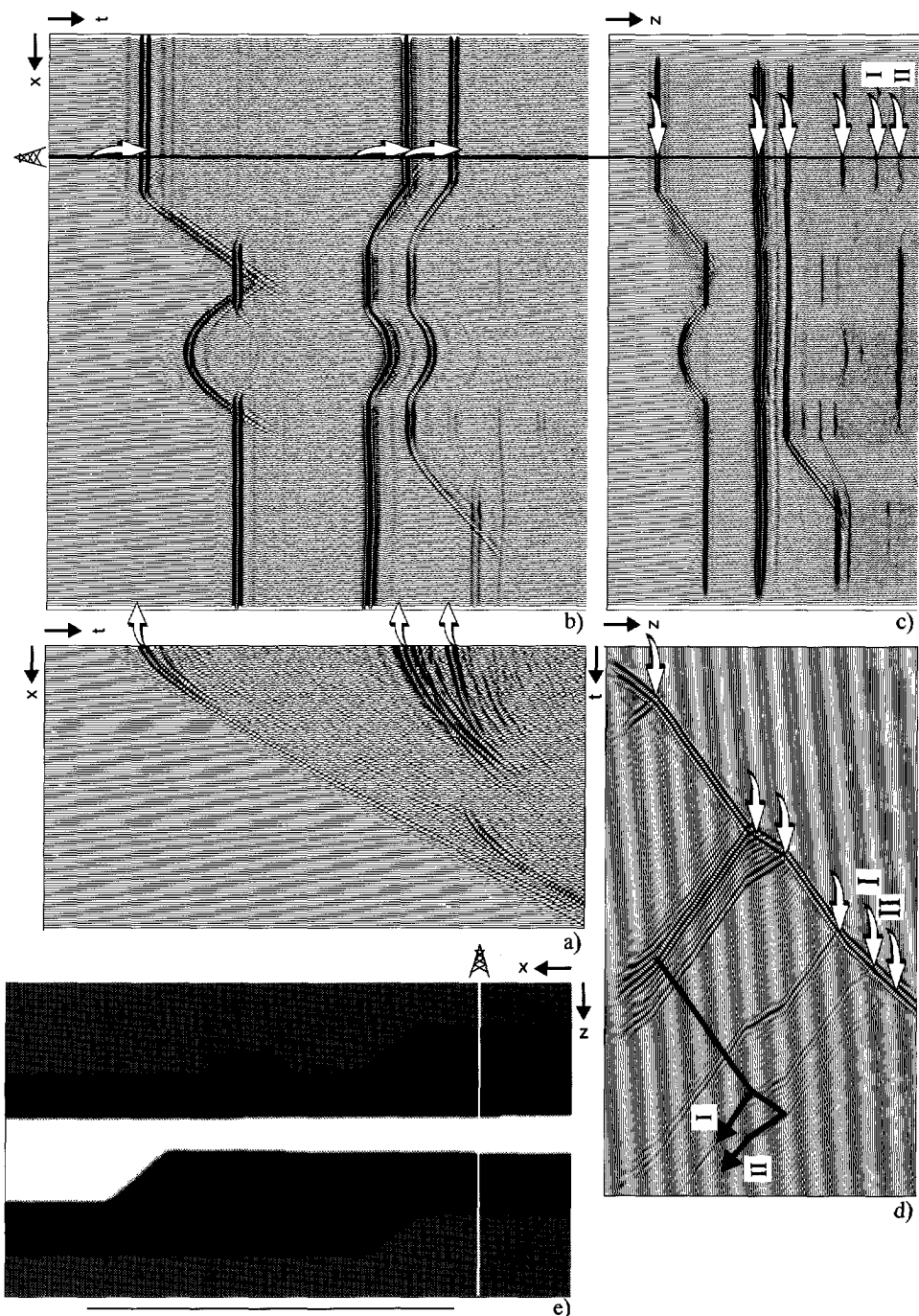


Figure 8.13 The relation between the a)shot record, b)near offset section, c)2-D zero-offset migration and d)3-D pseudo VSP generation and e)2-D slice from the macro model.

So far results have been shown on the generation of 3-D pseudo VSP data from surface data for one shot (point source response).

However, in this part some results are presented in which *a line source* response is constructed from the prestack data (a so-called *areal* shot record). The physical model is depicted in Figure 8.14a. The faults in the structure are crossed under an azimuth angle of 45 degrees. This has been designed to include some 3-D effects. The shooting geometry for the data acquisition in the watertank is as follows: *geometry*- 7 streamer marine data acquisition, *scale*- 1:20000, *nearest offset*- 100m, *far offset*- 2560m, *number of shots*- 250, *shot spacing*- 20m, *number of detectors per streamer*- 120 detectors, *inline detector spacing*- 20m, *crossline detector spacing*- 60m, *registration time*- 2460ms, *time sampling interval*- 4ms and *number of time samples*- 616. The seismic data was recorded without surface-related multiples.

Due to the 3-D structure of the model it can occur that the major contribution of the reflections are out of plane reflections. In this experiment the pseudo VSP is generated on *two* different lateral positions to show its value in 3-D interpretation and showing the propagation paths of the waves in time and depth (see Figure 8.14a for the locations of the well).

Figure 8.14b shows the registration of the 4th of 7 streamers of the constructed areal shot record, the 3-D pseudo VSP and the 2-D zero-offset migrated section. The integrated display allows a better interpretation of the data in different dimensions. Note that multiple 2-D cross sections of the 3-D model through the well can be used for interpretation of the data. The registration time for the data is larger than shown here. It can be clearly seen in the 3-D pseudo VSP that the amplitude of the first event decreases in arriving at the first reflector depth. This is because the main contribution of this reflection comes from a position away from the well (an out-of-plane reflection; see also Figure 8.14a).

Secondly the 3-D pseudo VSP is generated on a lateral position crossing the top of the dome. The result is displayed in Figure 8.14c. Note that the first primary does not show any amplitude decrease because at this location there are no 3-D effects. The intersections are mapped correctly except for the internal multiples. The propagation path for the waves propagating through the model are displayed in the pseudo VSP (black arrows). The internal multiples are not handled correctly and cause an incorrect intersection with the downgoing source wave field. These intersections for the internal multiples appear also in the migrated section (see arrows for 2 particular internal multiple reflections). In the one-way wave field extrapolation scheme, the boundary conditions are not fulfilled at the reflector : events are extrapolated below the reflecting interface. An important thing to note in the 3-D pseudo VSP data display is that all event appearing or disappearing at certain depth levels are 3-D effects.

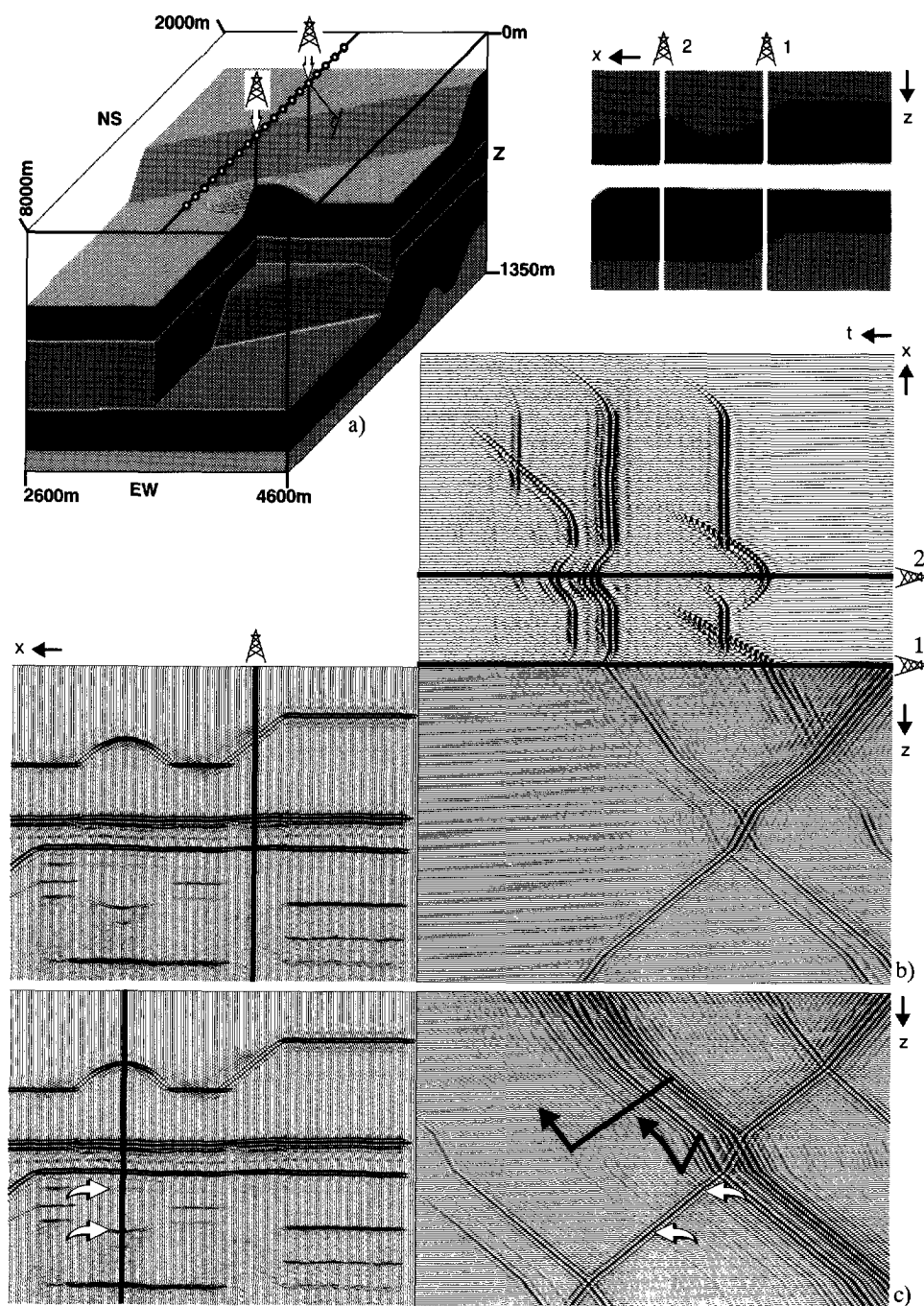


Figure 8.14 3-D pseudo VSP generated at well no.1 and 2 from an areal shot record. The areal shot record is displayed only up to the well position.

8.4 3-layered model and dataset

In this section the pseudo VSP method is illustrated by applying it to a 3-D dataset generated using a 3-D visco-elastic finite-difference algorithm (Robertsson et al., 1994).

The model contains three layers where the uppermost layer is a water layer on top of an irregular layer and a dipping plane. Absorbing boundaries have been applied around the entire model. In Figure 8.15a the volume of the 3-D model is depicted (3 axes x , y and z are indicated). The dimensions of the model are $x_{max}=1000m$, $y_{max}=500m$ and $z_{max}=800m$ including a 50m wide absorbing frame around the cube (see Figure 8.15b; note that the absorbing frame around the model is not shown). The distance between the gridpoints is 5m in all directions. Notice that the model as depicted in Figure 8.15 is displayed with a coarser grid than 5m. Figure 8.15c shows the model with the uppermost water layer removed. From this figure the irregular structure of the water bottom can be seen. The model after the removal of the waterlayer and the second layer is displayed in Figure 8.15d. Figure 8.15e illustrates two vertical sections (x - and y -direction) through the model at the well location. From the slice along the y -axis it can be easily seen that some energy will be diffracted due to the structure.

A monopole source is located at the center of the model : $x=500m$, $y=250m$ and $z=55m$. A Ricker wavelet has been used with a central frequency of 25Hz. The receivers of the 3-D shot record were placed over the whole (x,y) plane at depth level $z=55m$ (see Figure 8.15a for the geometry of the receivers and the source location). The sampling rate in the data is 2.5ms.

The elastic material properties of the model are given in Table 8.

Table 8 Material properties of the model.

layer	c_p [m/s]	c_s [m/s]	ρ [kg/m ³]
1	1500	0	1000
2	2000	0	1300
3	3000	1200	1500

The third layer of the model contains a compressional and a shear wave velocity whereas the layers above are acoustic. Q values of 10,000 for both P - and S - waves were used in the viscoelastic finite-difference simulations to obtain a perfectly acoustic/elastic response.

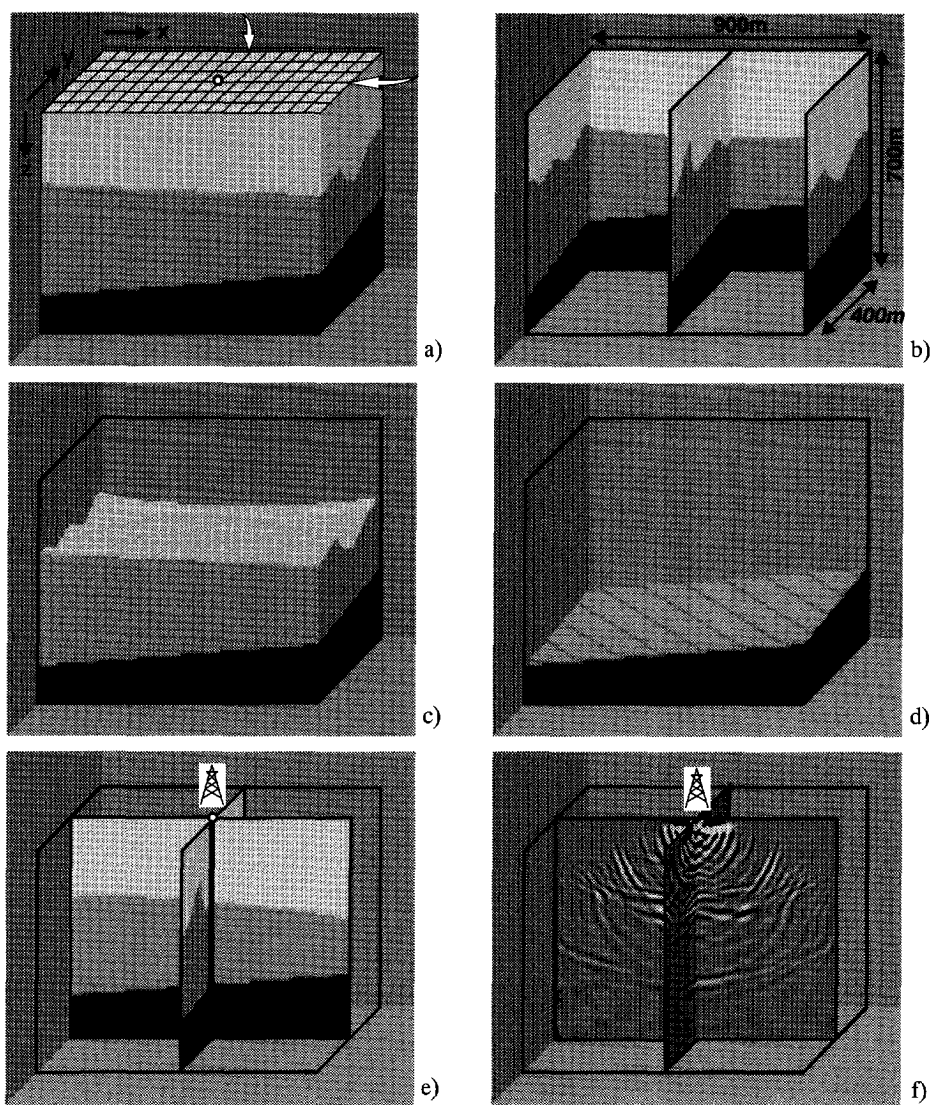


Figure 8.15 a)Geometry of 3-D model (irregular surface above a dipping plane), b)some slices through model (and dimensions of the model), c)model after removal of the uppermost water layer, d)model after removing the first and second layer, e)vertical slices at the well location (source on top of well) and f)vertical slices of the 3-D migrated volume at the well location.

Figure 8.16a gives a 3-D view of the interfaces of the model. The black line represents the well location. Some depth slices at increasing depth levels are depicted in Figure 8.16b.

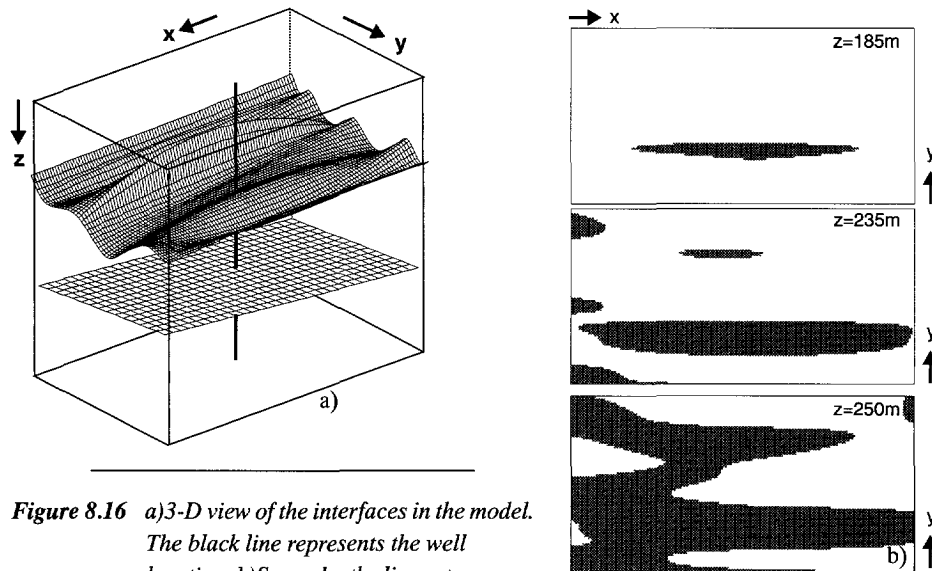


Figure 8.16 a) 3-D view of the interfaces in the model. The black line represents the well location. b) Some depth slices at increasing depth levels $z=185m$, $z=235m$ and $z=250m$.

At the well location the 2 slices along respectively the x -coordinate and the y -coordinate are shown in Figure 8.17a and b. The corresponding 2-D slices from the 3-D shot record are illustrated in Figure 8.17c and d. The black line in the figures represents the well location.

The numbers **1** and **2** refer respectively to layer boundaries **1** and **2**. The events corresponding to these layers have been labeled in the shot record. As can be noticed in Figure 8.17b, the structure indicated with number **3** acts as a diffraction point and its corresponding event is indicated with number **3** in the shot record along the x and y -coordinate (Figure 8.17c and d).

Event **3** arrives earlier at the surface than the reflections from layer boundary **1**. The energy emitted by the diffraction point (along the y -coordinate) is also visible in the shot record (along x ; 3-D out of plane effect). At first glance, it is not obvious to identify the origins of the events indicated with **A** and **B** in Figure 8.17c. However, a more careful study of the shot record in Figure 8.17d shows that both these events are responses from other diffractions which occur in the model. The diffraction points are located one at the left and the other at the right of the model (along the y -coordinate).

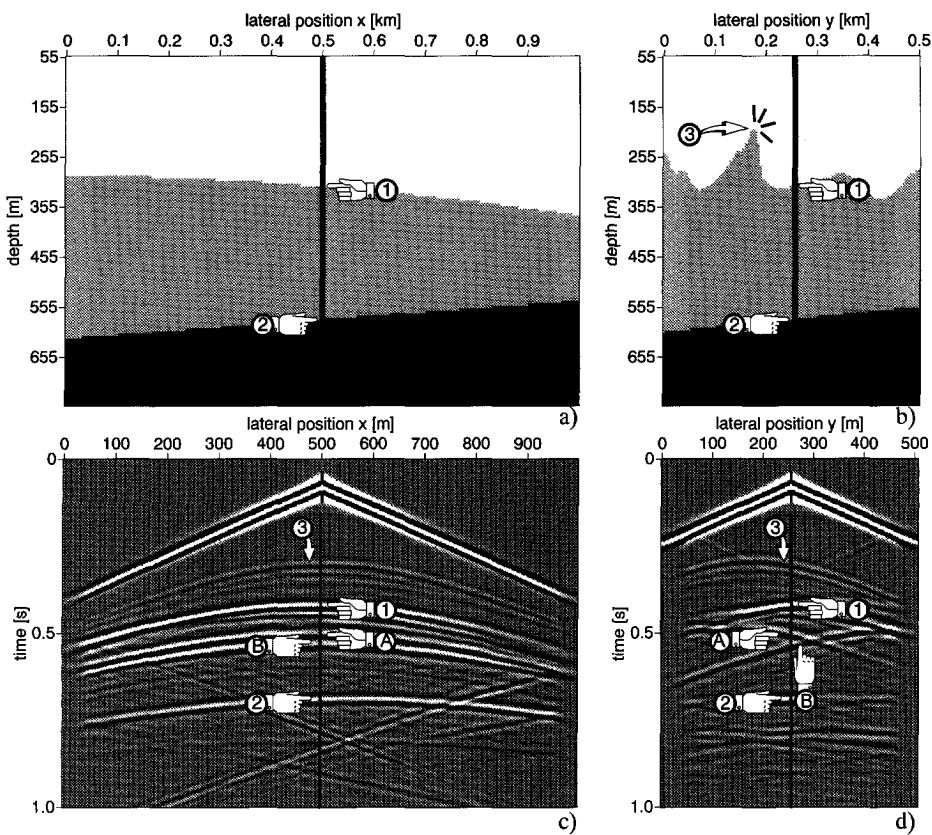


Figure 8.17 Vertical slices at the well location a) 2-D slice of the subsurface model along the x -coordinate and b) along the y -coordinate. c) 2-D slice from the 3-D shot record at the well, along x and d) 2-D slice along y (see also white arrows in Figure 8.15a).

The objective of this example was to generate a 3-D pseudo VSP dataset from the 3-D shot record and making comparisons with a modeled VSP.

To get a better understanding of the events visible in the shot record, a 3-D VSP has been modeled in the 3-D model with the source location chosen to be the same as that for the 3-D shot record. The 3-D VSP data is a zero-offset VSP (source at wellhead). The well is vertical and is located at the center of the model (location $x=500m$, $y=250m$, $z=55m$ to $z=750m$, see also Figure 8.16a). Figure 8.18a and b illustrate an integrated display of the 2-D slice from the 3-D shot record along the y -coordinate and the 3-D modeled VSP data for a better understanding of the various events. The origin of event 3 is revealed in the 3-D modeled VSP data. The diffractor starts emitting energy upward and downward at a depth above the first reflector (see indication in Figure 8.18b).

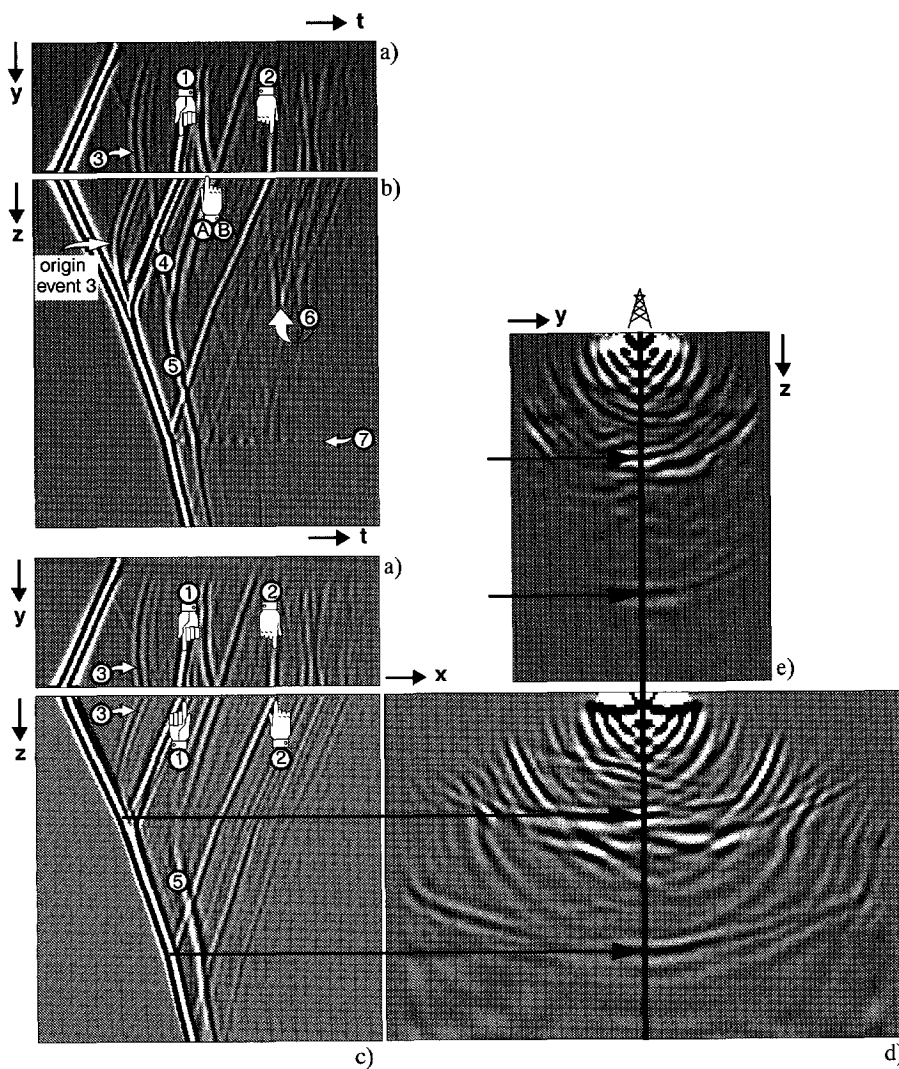


Figure 8.18 a) 2-D slice from 3-D shot record (along y), b) 3-D modeled VSP, c) 3-D pseudo VSP, d) 2-D slice from 3-D migrated volume at well (along x-coordinate) and e) 2-D slice from 3-D migrated volume at well (along y-coordinate); the black line indicates the location of the well.

A 3-D pseudo VSP dataset has been generated from the 3-D shot record using one-way wave field extrapolation operators. In the use of one-way operators the upgoing and downgoing waves are separately handled and boundary conditions are thus not taken into account at layer boundaries. The generated 3-D pseudo VSP is displayed in Figure 8.18c for making a comparison with the modeled VSP. The events prior to the direct wave have been zeroed.

An event that is fully absent in the pseudo VSP is the event that is indicated with number **4**. This event is a reflection from the boundary of the model (along the *y* direction).

Figure 8.15f shows the same slices as in Figure 8.15e (at the well location) but through the *3-D* migrated volume (1 shot). The *2-D* slices of the *3-D* shot record migration along the *x* and *y*-coordinate are also depicted in Figure 8.18. (respectively Figure 8.18d and e). Notice the integration of the generated *3-D* pseudo VSP data with the *2-D* slices of the *3-D* migrated volume (see black arrows). The *3-D* migration is done by a recursive *x,y,ω* algorithm (performed in the space frequency domain). The *3-D* wave field extrapolation operators used to extrapolate the wave field from the surface into the subsurface are based on the one-way wave equation. To get a better understanding of the event numbered **4**, some *3-D* snapshots have been generated which are depicted in Figure 8.19. Figure 8.19a and b are different views of the snapshot at time $t=300ms$ and Figure 8.19c shows the snapshot for time $t=600ms$. The event number **4** has been indicated in the snapshot of Figure 8.19a. It is now clear that this originates from the boundary on the side of the model. The boundary reflections (*y*-direction) could have been made significantly weaker by a better choice of grid parameters in the finite-difference simulation. However, this was not the purpose of this investigation.

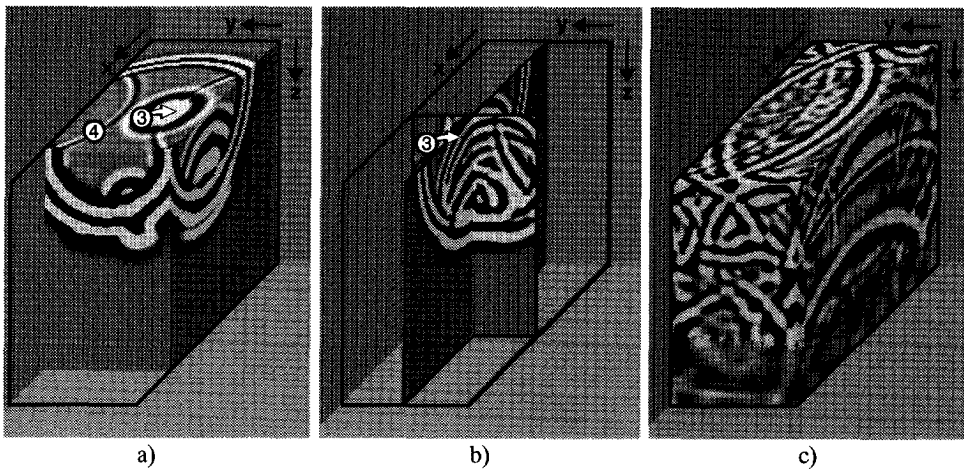


Figure 8.19 Various views and slices of *3-D* snapshots : a) and b)snapshots at $t=300ms$ and c)snapshot at $t=600ms$.

Furthermore the primary reflection from the diffractor as discussed earlier is indicated in this snapshot with the number **3** (see also its correspondence with the event numbered **3** in Figure 8.19b).

The origin of the events labeled **A** and **B** in Figure 8.18b, are diffractors starting emitting energy upward and downward. It is very interesting to see its correspondence with the pseudo VSP data in Figure 8.18c. The event number **5** represents the downward propagation of the diffraction energy. Comparison of the modeled VSP and the pseudo VSP shows that the internal multiple events indicated in Figure 8.18 with number **6** is absent in the pseudo VSP (Figure 8.18c). This is because for the generation of the pseudo VSP data, one-way operators have been used which do not take any boundary conditions into account. Finally, event number **7** in the modeled VSP shows a dispersive interface wave between the acoustic and the elastic layers. This is generated at the roughness caused by the discretization of the "flat" dipping plane (Figure 8.16a). This event is absent in the pseudo VSP since the interface wave is not recorded in the surface data.

Figure 8.20 illustrates some slices of the 3-D shot record at the same times as displayed for the 3-D snapshots. The horizontal slices represent the time slices at respectively time $t=300\text{ms}$ and time $t=600\text{ms}$ (Figure 8.20a). Note the correspondence with the snapshots at $z=55\text{m}$ (i.e. depth of the source) of Figure 8.19a and c. The vertical slice in Figure 8.20b represents the 2-D slice from the 3-D shot record along the y -coordinate (same as Figure 8.17d).

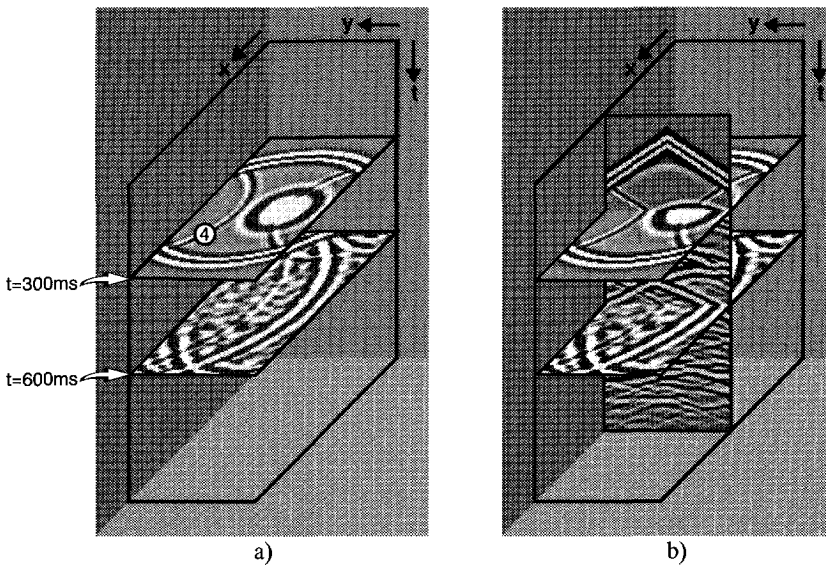


Figure 8.20 Slices through the 3-D shot record.

In this section the generation of 3-D pseudo VSP data from surface measurements was demonstrated. The data has been generated from a 3-D shot record that was modeled in a 3-D subsurface consisting of an irregular interface above a dipping layer.

Different datasets have been integrated for a better understanding and interpretability of the seismic data. The pseudo VSP data has been compared with the VSP data that was modeled at zero offset (with respect to the shot location at the surface). The generation of the pseudo VSP showed the clear appearance of diffraction energy which was emitted in the model. The appearance of the diffraction energy was visible in the shot record and the VSP data. Finally, some 3-D snapshots were shown as well, to illustrate the wave propagation through the model at various increasing times.

In this chapter some 3-D case studies have been presented on the generation of 3-D pseudo VSP data from numerical modeled data and physically modeled data. Figure 8.21 shows as a general conclusion, the value of the pseudo VSP data as an integration tool in relation with other data types. The axes of the different data types are indicated with the arrows around the boxes. Here it is shown that pseudo VSP data, (t, z) as well as (t, t') , can be integrated with other data types to improve the interpretation of data (integrating of various data sets with their axes in common). For example the comparison of well log measurements and real VSP on one hand and real VSP data and pseudo VSP data on the other, offers a promising two-step process in integrating shot records and well log measurements. Also the generation of pseudo VSP data from surface data gives excellent insight into the properties of the CFP gather and the migrated sections.

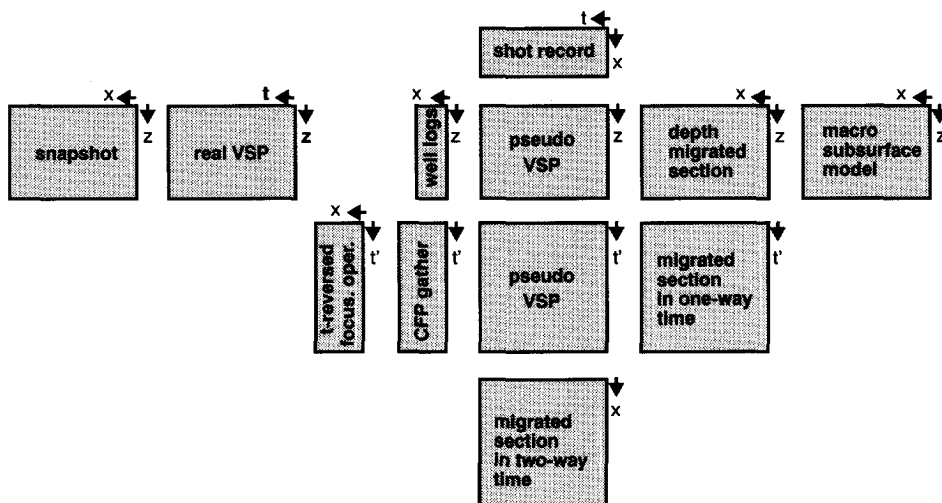


Figure 8.21 Diagram showing the capabilities of pseudo VSP data as an integration tool.

Appendix A

Data matrix notation

This appendix discusses in more detail, the notation of the data matrices which are used in this thesis. The matrix notation was introduced by Berkhouit (1982) and relates the seismic data with its propagation and reflection through a medium as a network of various wave field processes. For the description of seismic wave fields the matrix notation is very useful because of its simplicity. In this section the matrix operators are discussed based on the acoustic approximation. One of the advantages of the matrix notation is that all formulations derived for the acoustic 2-D case will be the same, even for multi-component elastic data and 3-D situations; only the interpretation of the matrices changes.

The origin of the matrix notation comes from the fact that seismic measurements are *discrete* in both space and time. As illustrated in Chapter 2, wave theory based operations on seismic data are practically applied as discrete summations instead of continuous integral operators. Moreover, the physical processes involved with seismic wave propagation (emission, downward propagation, reflection, upward propagation and detection) are fixed by the order in which they appear in the matrix equations.

Consider a two-dimensional wave field $p(x, z_0; t)$, which is measured at a constant depth level (acquisition surface z_0). The 2-D wave field p is a function of the lateral position x and time t . The earth is considered as a time-invariant medium and therefore the seismic problem can be described by independent frequency components.

After a Fourier transformation from time to frequency, the 2-D wave field p is described by the Fourier transformed wave field $P(x, z_0; \omega)$. The symbol ω denotes the angular frequency ($\omega=2\pi f$).

As the measured seismic wave field is a real signal, the wave field can be completely described by the positive components of the Fourier transformation. Consider a seismic experiment consisting of M shot records with M single-component detectors (e.g. the measured pressure field). Suppose a fixed spread equally for the sources and receivers. The two-dimensional dataset can then be described by $p_{ijk}(i\Delta x_r, j\Delta x_s, z_0; k\Delta t)$, where i, j, k are integers and Δx_r , Δx_s and $k\Delta t$ denote respectively the sample intervals of respectively receiver coordinate, source coordinate and the time axis. p_{ijk} is a broad band wave field in terms of acoustic pressure. After a Fourier transformation from time to frequency the data can be stored (for one *positive* frequency component ω_k) in the data matrix as :

$$P(z_0) = \begin{bmatrix} P(\Delta x_r, \Delta x_s) & P(\Delta x_r, 2\Delta x_s) & \cdots & P(\Delta x_r, j\Delta x_s) & \cdots & P(\Delta x_r, M\Delta x_s) \\ P(2\Delta x_r, \Delta x_s) & \ddots & & P(2\Delta x_r, j\Delta x_s) & \cdots & \vdots \\ \vdots & \vdots & \ddots & \vdots & \ddots & \vdots \\ P(i\Delta x_r, \Delta x_s) & P(i\Delta x_r, 2\Delta x_s) & \cdots & P(i\Delta x_r, j\Delta x_s) & \cdots & P(i\Delta x_r, M\Delta x_s) \\ \vdots & \vdots & \ddots & \vdots & \ddots & \vdots \\ P(M\Delta x_r, \Delta x_s) & \cdots & \cdots & P(M\Delta x_r, j\Delta x_s) & \cdots & P(M\Delta x_r, M\Delta x_s) \end{bmatrix} \quad (A.1)$$

Note that each element of the matrix is denoted in a simplified form for notation convenience from $P(i\Delta x_r, j\Delta x_s, z_0; \omega_k)$ to $P(i\Delta x_r, j\Delta x_s)$. z_0 indicates the depth level $z=z_0$ to which the matrix $P(z_0)$ is related. The matrix $P(z_0)$ contains prestack data for *one* frequency component (in this case ω_k). The different gathers which can be identified from the data matrix $P(z_0)$ are shown in Figure A.1.

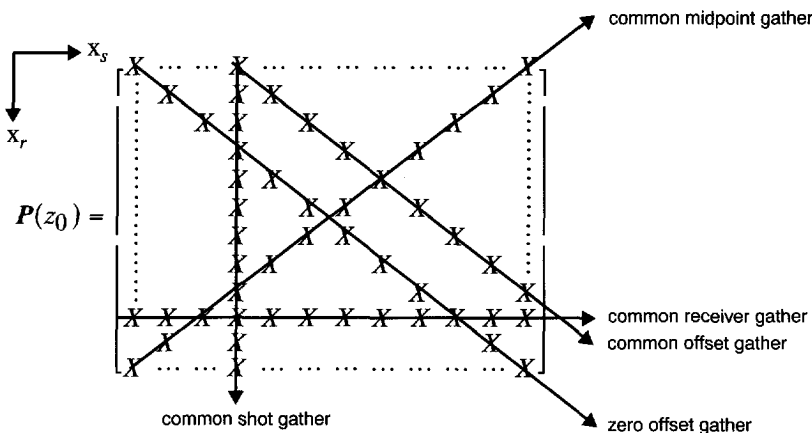


Figure A.1 The different cross sections in the monochromatic data matrix $P(z_0)$ correspond to different seismic data gathers.

Each column j of the matrix $\mathbf{P}(z_0)$ corresponds to one monochromatic data vector in a common shot gather (CSG) with the shot positioned at $x_s=j\Delta x_s$; each element P_{ij} corresponds to a fixed lateral receiver coordinate $x_{r,i}$ and a fixed lateral source coordinate $x_{s,j}$. Each row corresponds to one monochromatic common receiver gather (CRG). The diagonal ($x_s=x_r$) represents the zero offset gather and the anti-diagonal ($x_s=-x_r$) represents a common mid-point (CMP) gather. Figure A.2 shows the procedure of constructing the data matrix $\mathbf{P}(z_0)$ from seismic shot records.

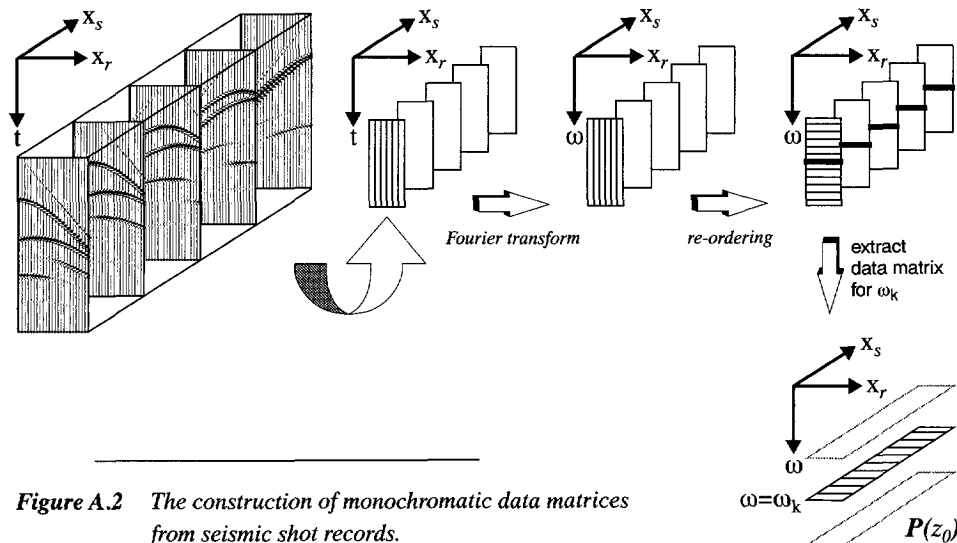


Figure A.2 The construction of monochromatic data matrices from seismic shot records.

For 2-D marine data acquisition (moving end of spread) the matrix is partly filled like illustrated in Figure A.3a (after Verschuur, 1991). The other half of the matrix is can be filled using the reciprocity theorem. Acquisition of land data may be done split spread. The data matrix will then have a structure as depicted in Figure A.3c. Note that the near-offset data is not measured in most applications, as they suffer from noise or distorted input signals (being close to the source). Note that reciprocity may only be applied if the source and receivers have equal characteristics. The reciprocity may be used after removal of the directivity effects. The reader is referred to (de Hoop, 1988; Fokkema and Van den Berg, 1993) for applications of acoustic reciprocity theorems which are fundamental in seismic wave theory. In a similar way, the matrix representation can be formulated for the integration of surface data and borehole data (Figure A.4).

For 3-D situations the monochromatic wave field can be formulated as $\mathbf{P}(x_r, y_r, y_s, y_s, z_0; \omega_k)$. Figure A.5 shows the organization of the 3-D seismic data (Kinneging et al., 1989). All the receiver data in the x - y plane due to one shot record can be stored in one column of the data matrix.

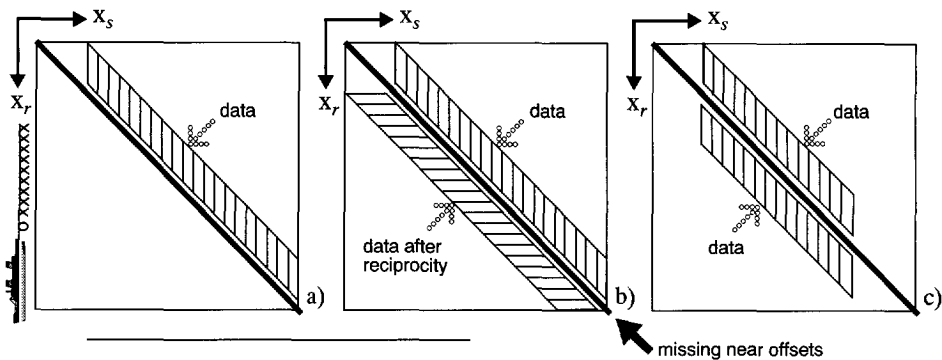


Figure A.3 a) Data matrix for end of spread data acquisition (typical 2-D marine data), b) other half of data is acquired using reciprocity, c) moving split spread data (often in land data acquisition). Note the direction of the boat in a).

$$\begin{array}{c}
 \text{sources} \\
 \text{at the surface} \\
 \Rightarrow
 \end{array}
 \quad
 \begin{array}{c}
 \text{receivers} \\
 \text{at the surface} \\
 \Downarrow
 \end{array}
 \quad
 \begin{array}{c}
 \text{sources} \\
 \text{at the surface} \\
 \Rightarrow
 \end{array}
 \quad
 \begin{array}{c}
 \text{receivers} \\
 \text{in well A} \\
 \Downarrow
 \end{array}
 \quad
 \begin{array}{c}
 \text{sources} \\
 \text{in well A} \\
 \Rightarrow
 \end{array}
 \quad
 \begin{array}{c}
 \text{receivers} \\
 \text{in well B} \\
 \Downarrow
 \end{array}$$

$P_{\text{surface}} = \left(\begin{array}{|c|c|c|c|} \hline & & & \\ \hline & \dots & & \\ \hline & & & \\ \hline & & & \\ \hline & & & \\ \hline \end{array} \right)$ a) \Downarrow
 $P_{\text{vsp}} = \left(\begin{array}{|c|c|c|c|} \hline & & & \\ \hline & \dots & & \\ \hline & & & \\ \hline & & & \\ \hline & & & \\ \hline \end{array} \right)$ b) \Downarrow
 $P_{\text{crosswell}} = \left(\begin{array}{|c|c|c|c|} \hline & & & \\ \hline & \dots & & \\ \hline & & & \\ \hline & & & \\ \hline & & & \\ \hline \end{array} \right)$ c) \Downarrow

Figure A.4 Matrix data representation of a) surface data, b) VSP data and c) crosswell data.

Repeating this for all shot records results into submatrices containing a 2-D matrix for fixed *source positions* y_s and *receiver positions* y_r . Each 2-D matrix contains a 2-D experiment for all receivers of one line in x (for fixed y) and the source varying along another line in x with a fixed y -coordinate. One column of the matrix $P(z_0)$ describes a 3-D shot record, one row describes a 3-D common receiver gather. This guarantees that matrix multiplications now describe two-dimensional spatial convolutions in the x - and y -direction. However, the diagonal elements do not contain common offset information anymore, except for the main diagonal.

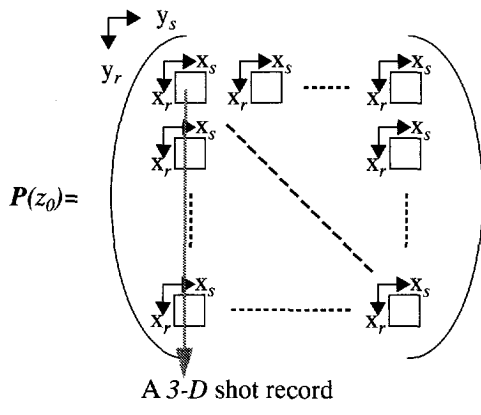


Figure A.5 Organization of the data matrix for 3-D experiments. This matrix consists of submatrices for 2-D acquisition for each pair of cross-line source and cross-line receiver coordinates y_s and y_r .

Appendix B

Optimized wave field extrapolation operators

In this appendix a method is considered for the calculation of optimized short spatial operators after transforming the expression of the operators (derived in the wavenumber frequency domain) back to the space frequency domain in a non standard way. For an extensive discussion and design of these optimized short spatial operators the reader is referred to (Thorbecke, 1997). It is known from wave theory analysis that many wave field operators are difficult to be used directly in the space frequency domain. This in contradiction with many wave field operators which have an exact expression in the wavenumber frequency domain for laterally homogeneous isotropic media. Wave field extrapolation in the wavenumber frequency domain is performed by multiplications of the data with the operators. Generalized convolution operators in the space frequency domain have to be used to allow laterally varying medium parameters.

One of the aims is to design a *short* space frequency operator, with a wavenumber frequency spectrum which is, over a desired wavenumber band, equal or close to the exact formulation in the wavenumber frequency domain. This can be written as the following integral equation (one-way wave field extrapolation operator):

$$\tilde{Y}(k_x) = \int_{x_1}^{x_2} e^{(jk_x x)} Y(x) dx \quad \text{for } k_1 \leq k_x \leq k_2 , \quad (\text{B.1})$$

where $Y(x)$ denotes the wave field extrapolation operator to be designed in the space frequency domain and $\tilde{Y}(k_x)$ denotes the analytical expression of the to be designed operator in the wavenumber frequency domain.

A simple way to obtain the space frequency operators is to transform the discrete operators, which are derived in the wavenumber frequency domain (one-way and two-way wave field extrapolation operators), back to the space frequency domain in a numerical way.

This inverse transformation is not very efficient, because the spatial convolution operators obtained in this way become very long operators. From a computational point of view, long spatial operators are not desired because multiplications in the wavenumber frequency domain are replaced by convolutions in the space frequency domain.

In the integral equation (B.1) an integration is performed over a limited spatial domain (*short operator*) and the wavenumber frequency spectrum of the operator is bandlimited.

A discrete formulation of the integral Equation (B.1) reads :

$$\tilde{Y}(n\Delta k_x) = \Delta x \sum_{m=M_1}^{M_2} e^{(jn\Delta k_x m\Delta x)} Y(m\Delta x) \quad \text{for } N_1 \leq n \leq N_2. \quad (\text{B.2})$$

or in matrix notation ($\tilde{Y} = \mathbf{\Gamma} \tilde{Y}$)

$$\begin{pmatrix} \tilde{Y}(N_1\Delta k_x) \\ \vdots \\ \tilde{Y}(0) \\ \vdots \\ \tilde{Y}(N_2\Delta k_x) \end{pmatrix} = \Delta x \begin{pmatrix} e^{(jN_1\Delta k_x M_1\Delta x)} & \dots & 1 & \dots & e^{(jN_1\Delta k_x M_2\Delta x)} \\ \vdots & & \vdots & & \vdots \\ 1 & & \dots & 1 & \dots & 1 \\ \vdots & & & \vdots & & \vdots \\ e^{(jN_2\Delta k_x M_1\Delta x)} & \dots & 1 & \dots & e^{(jN_2\Delta k_x M_2\Delta x)} \end{pmatrix} \begin{pmatrix} Y(M_1\Delta x) \\ \vdots \\ Y(0) \\ \vdots \\ Y(M_2\Delta x) \end{pmatrix} \quad (\text{B.3})$$

with M_1+M_2+1 the length of the desired short operator and N_1+N_2+1 the length of the Fourier transformation.

Δk_x represents the wavenumber sampling $\Delta k_x = 2\pi/[(N_1 + N_2 + 1)\Delta x]$. \tilde{Y} is the vector that contains the coefficients of the discrete version of the desired short operator Y , \tilde{Y} represents the operator in the wavenumber frequency domain. The matrix $\mathbf{\Gamma}$ represents the discrete Fourier transform with the desired properties.

The number of samples in the wavenumber frequency domain must be chosen such that the short spatial operator is zero outside its working length (number of samples in the wavenumber frequency domain must be greater or equal to the number of traces to be extrapolated). The number of equations in Matrix Equation (B.3) is larger than the number of unknowns. Therefore it is impossible to find a unique solution satisfying all equations.

An error function $\tilde{\epsilon}$ can be defined such that the solution approximately satisfies all the equations in a Weighted Least Square (WLSQ) approach : minimization of the error function

$$\tilde{\epsilon} = \tilde{\tilde{E}}^h \tilde{\Lambda} \tilde{\tilde{E}} \quad , \quad (B.4)$$

with $\tilde{\mathbf{E}} = \mathbf{\Gamma} \langle \tilde{\mathbf{Y}} \rangle - \tilde{\mathbf{Y}}^h$. The superscript h denotes complex-conjugate transpose. The weight-ing matrix $\tilde{\mathbf{\Lambda}}$ is a diagonal matrix containing a weighting function on its diagonal. The weight-ing function is defined such that the wavenumbers of interest are given a larger weight than others with less of interest (low weight factor). The introduction of the weight-ing function forms a good control for the desired function of the space frequency operators. The error function $\tilde{\epsilon}$ can be minimized by (least squares solution):

$$\frac{\partial \tilde{\epsilon}}{\partial \langle \langle \bar{Y}^h \rangle \rangle_i} = 0 \quad \forall \langle \langle \bar{Y}^h \rangle \rangle_i. \quad (\text{B.5})$$

with $\tilde{\varepsilon} = \left(\langle \tilde{Y}^h \rangle \mathbf{F}^h - \tilde{Y}^h \right) \tilde{\mathbf{A}} \left(\mathbf{F} \langle \tilde{Y} \rangle - \tilde{Y} \right)$

The solution is given by (slightly modified after Claerbout, 1976):

$$\mathbf{\Gamma}^h \tilde{\mathbf{\Lambda}} \left(\mathbf{\Gamma} \langle \tilde{Y} \rangle - \tilde{Y} \right) = \mathbf{0} \quad or \quad \langle \tilde{Y} \rangle = \left[\mathbf{\Gamma}^h \tilde{\mathbf{\Lambda}} \mathbf{\Gamma} \right]^{-1} \mathbf{\Gamma}^h \tilde{\mathbf{\Lambda}} \tilde{Y} \mathbf{\Gamma} \quad (B.6)$$

Figure B.1 illustrates the weighted least squares solution in a matrix representation.

$$\begin{array}{ccccc}
 \text{[diagonal lines]} & \text{[square with diagonal]} & \text{[vertical lines]} & \text{[empty]} & \text{[empty]} \\
 \Gamma^h & \tilde{\Lambda} & \Gamma & \langle \tilde{Y} \rangle & = \\
 \end{array}$$

Figure B.1 Weighted least squares solution in a matrix representation.

The weight function (diagonal matrix) is given by :

$$\tilde{\Lambda}_{mn} = w(n\Delta k_x)\delta_{nm} \quad (B.7)$$

The components of the Fourier transformation and the inverse Fourier transformation matrices are given by :

$$(\mathbf{\Gamma})_{nm} = e^{(jn\Delta k_x m\Delta x)} \quad \text{and} \quad \left(\mathbf{I}^h\right)_{mn} = e^{(-jn\Delta k_x m\Delta x)} \quad . \quad (\text{B.8})$$

Matrix $\mathbf{\Gamma}^h \tilde{\mathbf{\Lambda}} \mathbf{\Gamma}$ is a square $M \times M$ matrix with a Toeplitz structure (for a 1-D optimization problem). The matrix can be inverted relatively fast using the Levinson scheme.

If the weight matrix $\tilde{\mathbf{A}}$ is taken to be the unity matrix \mathbf{I} ; $\tilde{\mathbf{A}} = \mathbf{I}$ and if \mathbf{F} is a square matrix then no optimization is carried out and $\langle \tilde{Y} \rangle \approx \mathbf{F}^h \tilde{Y}$. It can be easily verified that $\langle \tilde{Y} \rangle$ is the truncated inverse Fourier transform of \tilde{Y} .

The right-hand side of the second equation in Equation (B.6) is an inverse Fourier transform (N -points) which is reduced (by truncating) to M -points in the spatial domain. Figure B.2 shows different domains in the wavenumber frequency domain. The following bandlimitations should be considered : 1)limited temporal frequency range, 2)maximum angle of propagation and 3)Nyquist wavenumber $\pm\pi/\Delta x$. These three bandlimitations determine together the domain of interest for the different operators. The gray shaded area in Figure B.2 shows the location of the computations (area of propagating P -waves). Recordings are discrete so there is a Nyquist wavenumber which limits the maximum operator angle for a given frequency. This angle declines for higher frequencies because of the aliasing of the wavenumber frequency spectrum. According to these considerations a strategy is developed to calculate operators only for their specific band of interest.

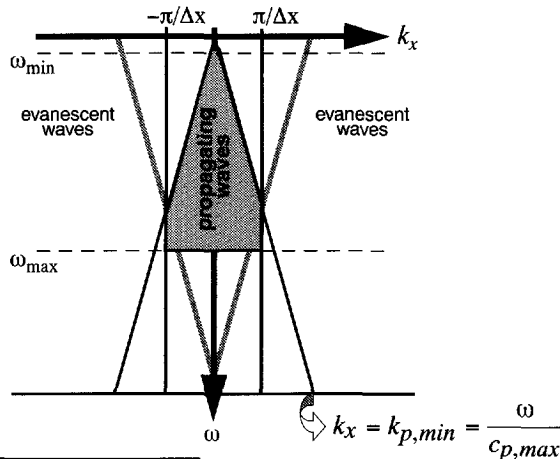


Figure B.2 Different domains of interest subdivided in the wavenumber frequency domain.

For the recursive wave field extrapolation, the operator behaviour of the wavenumber should be stable (*amplitude < 1*) in the evanescent region. The weighting function can be a simple block with a weight of “one” inside the range of angles of interest (see the area of propagating waves in Figure B.2) and a small value (1.10^{-5}) outside this band. The amplitude behaviour in the wavenumber frequency domain of the optimized one-way and two-way wave field extrapolation operators is depicted respectively in Figure B.3 and Figure B.4. The phase spectra show the same accurate behaviour. Note that the wavenumber spectra are accurate for all wavenumbers within the band of interest. The spatial operators are accurate within the band of interest.

Within each extrapolation step the assumption is made that the medium is assumed homogeneous in the vertical direction. The same applies to the lateral extent of the operator, i.e. the medium is assumed homogeneous within the length of the operator.

Figure B.3 shows the amplitude k_x spectra for the acoustic one-way extrapolation operator, see Equation (2.24).

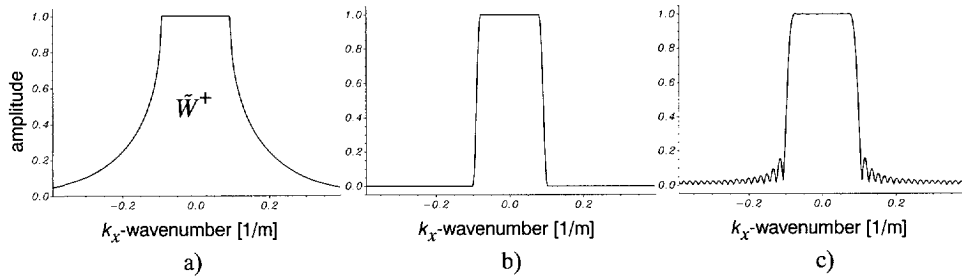


Figure B.3 Amplitude k_x spectra of the acoustic one-way forward wave field extrapolation operator: a) exact k_x -operator, b) filtered k_x -operator and c) WLSQ optimized k_x -operator.

Figure B.3b and c illustrate the k_x amplitude spectra for respectively the filtered one-way k_x -operator and optimized one-way x -operator. In this example, the optimized operators have been calculated for the following parameters at frequency 30Hz : the number of k_x samples: 256, sampling in spatial direction: 8m, the length of the spatial operator: 51, minimum and maximum k_x -filtering windows -60 and 60 degrees respectively, the weighting windows boundaries are chosen similar to the minimum respectively maximum k_x -filtering windows, compressional wave velocity: $c_p=2000m/s$ and density: $\rho=1000kg/m^3$.

Figure B.4a shows the amplitude k_x spectra for the acoustic two-way wave field extrapolation operators (see also Equation (2.16) of chapter 2). Figure B.4b and c illustrate the amplitude k_x spectra for respectively the filtered two-way k_x -operators and optimized two-way x -suboperators.

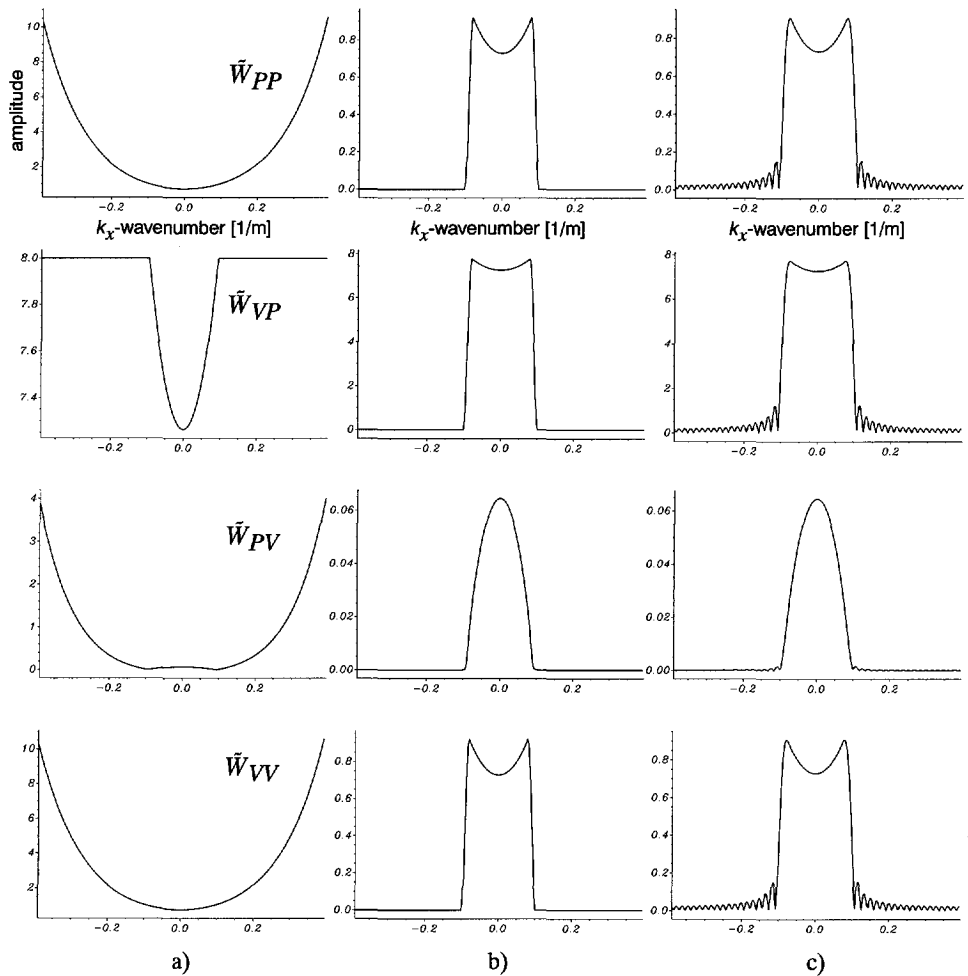


Figure B.4 Amplitude k_x spectra of the acoustic two-way wave field extrapolating suboperators:
 a) exact k_x -suboperators, b) filtered k_x -suboperators and c) WLSQ optimized k_x -suboperators.

Appendix C

Processing of VSP data

In the past a lot of effort has been put in linking VSP data to surface seismics. The classic way to integrate surface data and VSP data is the VSP *corridor stack*. Starting from a VSP seismogram it is possible to separate down- and upgoing wavetrains, deconvolve the upgoing reflections using the downgoing waves, and eventually define a zone, or *corridor*, where the *SNR* is the best and multiples are absent. The result of the corridor stack is a trace without multiples which corresponds to the convolution of a simple zero or minimum phase wavelet with the series of reflection coefficients. The corridor stack can be seen as the *best seismic trace* within a given bandwidth. The VSP corridor stack trace may be used as a check of the surface trace deconvolution in the surroundings of the well.

The fact remains that, at least near the well, a more rigorous quality control can be applied to the CDP traces than the usual criteria of continuity, sharpness of events, and agreement with the synthetic seismogram. Aspects regarding the corridor stack processing technique are well known and can be found in Hardage (1983) and Toksöz and Stewart (1984).

Throughout the years many papers have been written on methods of extracting different kind of information from VSP data. Omnes (1978) used the VSP data for the correlation of well log and seismic data. Kennett et al. (1980) used the VSP data for the identification of multiple reflections, Hauge (1981) for the investigation on the effects of attenuation, and Wyatt (1981) for analyzing the source signature effects. A description of how to image reflecting horizons with offset VSP data has been given by Wyatt and Wyatt (1981). Li (1990) described an inversion method of *P* and *S*-waves using VSP and surface data together.

Another important technique to integrate surface data with VSP data is *deconvolution*. VSP makes it possible to deconvolve surface seismic traces very effectively through the use of the wavelet derived from the VSP traces.

The concept of designing deconvolution operators from the downgoing VSP wave field is described by Anstey (1980) and Fitch and Dillon (1983).

For a general overview on different VSP processing techniques the reader is referred to Hardage (1983). Wong and Noponen (1986) deconvolved surface-recorded seismic data with operators jointly derived from VSP and surface data.

The separation of up- and downgoing wave modes is the first step in 1)studying the generation of multiples and primaries in VSP data, Kennett et al. (1980), 2)calculating the transfer function between the two wavetrains for stratigraphic studies, Balch et al. (1984), 3)designing deconvolution operators for the upcoming waves and for surface data from the downgoing waves Hubbard (1979) and Omnes (1984), 4)predicting impedances below the well (“prediction ahead of the drillbit”) Grivelet (1985) and Tal-virsky and Tabakov (1983).

In the following some basic VSP processing steps will be illustrated on the marine dataset provided by Mobil Exploration and Producing Technical Center Dallas, U.S.A.. For a description of this dataset the reader is referred to Chapter 7 of this thesis. For a general overview on VSP processing techniques see Hardage (1983) and Yilmaz (1988).

VSP data processing necessarily varies according to the dataset, because each set is unique and has its own characteristics (the recording and shooting conditions are different from well to well). In order to create a high quality composite trace per depth level, it is advised to record several seismic shots at each recording depth and sum these records into one single trace. Note that with this shooting procedure, a much weaker energy source can be used in VSP acquisition (advantage in environmental constraints in highly populated areas). Furthermore it allows an effective way to cancel random noise by summing the data into a high quality composite trace (after editing of noisy spikes).

In general, the upgoing primary reflections are considerably weaker in amplitudes than the dominant downgoing wave fields and thus often difficult to interpret. A fundamental processing procedure to emphasize the upgoing primary reflections is the separation of the upgoing VSP events from the downward traveling waves. The analysis of upgoing wave modes is particularly important since these are the only events recorded by surface seismic measurements.

The following processing steps should be applied in general to real VSP data:

Preprocessing :

- A) trace editing : manually removal of bad traces
- B) common depth sorting
- C) near source sensor picking (only for airgun sources)
- D) t_{zero} correction (only for airgun sources)
- E) signature deconvolution (optional)
- F) editing
- G) common level stacking

(a successful method for this type of noise is the application of alpha-trim median stacking)

Processing :

- A) first arrival picking
- B) bandpass filtering
- C) amplitude correction
- D) separation of up- and downgoing waves
- E) deconvolutions
- F) imaging : corridor stacking, VSP-CDP mapping or migration

For VSP data there are some basic preprocessing steps. After the removal of the surface waves (groundroll), tube noise and trace editing the processing of VSP data starts with the stacking.

For an extensive discussion and applications of alpha-trim median filtering the reader is referred to Schieck and Stewart (1991) and Frinking (1994). Schieck and Stewart (1991) discussed the performance of a median $f\text{-}k$ filter on prestack gathers with a number of different noise types (bad or dead traces, noise bursts or glitches, aliased and unaliased groundroll). Figure C.2b to d illustrate the alpha-trim stack procedure of sorting and stacking at a certain depth level : for each time sample the data is sorted in ascending order of amplitude. This is repeated for all time samples. Next a window will be selected within which the data is stacked. The width of the window depends on the value of alpha which varies between $\alpha=0$ and $\alpha=1$. $\alpha=0$ corresponds to selecting all traces per depth level before stack (i.e. a plain stack of all traces per depth with a weight) and $\alpha=1$ corresponds to selecting only 1 trace (the so-called median filtering technique: the samples are sorted by amplitude at a particular time from all seismic traces in an input ensemble in order to find the median value. For an odd number of traces, the median sample is the output sample; if the number of live traces is even, the output sample is the average of the two median samples. If all traces in an ensemble are dead, a dead trace is output in sequence).

The alpha-trim stack can be used in this case to exclude the coherent noise or outliers from the stacking process in an automatic way. Increasing the parameter α means reducing the number of traces (datapoints) taken into account for stacking. The value of α must be chosen such that the stacked result contains only one *clean* trace per depth level.

An exhaustive comparison of separation methods is discussed in (Kommedal and Tjostheim, 1989). A separation technique to separate the downgoing waves from the upcoming (reflections) is the *f-k* filtering technique. Because the downgoing and upcoming waves in VSP data have different dips, they will map in the *f-k* domain into different half planes. The downgoing energy is arbitrarily defined as having a positive propagation velocity. From this follows that the Fourier transform expresses downgoing wave modes in terms of positive wavenumbers and upgoing wave modes in negative wavenumbers. This method of *f-k* filtering has some minor problems. A prerequisite for *f-k* filtering is the uniform receiver sampling in depth. Because sometimes a VSP dataset may not have the uniform receiver sampling in depth this will focus on some problems. The *f-k* filtering technique faces also with often observable amplitude smearing and edge effects.

An alternative technique to separate the upcoming waves from the downgoing waves is the so-called approach of median filtering. Hardage (1983) showed how median filters could be used to considerable advantage to enhance events of interest. This method is based on smoothing data in which the signal that needs to be preserved contains abrupt discontinuities. The use of median filtering in smoothing data is very robust; the noise spikes, glitches or bad traces are not included in the estimate (Claerbout and Muir, 1973). The use of median filtering methods was first introduced by Tukey (1977). In the following the total procedure is discussed for the application of median filters in the separation of up- and downgoing events in VSP data. The method is based on the application of a *long* median filter along the depth axis to VSP data. After first break picking, a time shift with the *picked* function is applied for flattening the downgoing waves (vertical alignment of downgoing events). It should be emphasized that the first break times must be measured with extreme care. Next a long median filter is applied to yield the downgoing waves. The data is then shifted back to original position in time and after subtraction from the original VSP dataset only the upgoing wave modes will remain. The upgoing waves are shifted to two-way time and again a median filtering is applied to enhance the upgoing waves. The ability of retrieving the complete downgoing wave field allows the advantageous calculation of robust deconvolution filters (much stronger signal strength than data recordings at the surface).

Some results will be shown on the preprocessing of the raw three-component Mobil VSP data (well B - starting at the seabottom at 375m depth). Here a fast and efficient method is used to suppress the noisy and spiky parts in the VSP data registrations.

The method will be applied to the zero offset vertical seismic profile for well *B*. The used registration tool for the recordings of well *B* consisted of four detectors (each measuring three-component data). Figure C.1 illustrates the raw VSP data registrations for the four detectors (only the vertical component is shown). Figure C.2a shows a blow up of a selected part of the registrations for detector 1. The blow up of the data registrations is shown here to have a better view on the noise in the VSP dataset : multiple recordings have been made at each depth level. As can be seen from the raw VSP data registrations there are many bad traces in this dataset.

Figure C.3 shows the result of the application of the alpha-trim stacking to the raw VSP data for different α values being respectively 0, 0.7. $\alpha=0.7$ has been chosen as the optimal result for the removal of noisy datapoints and preserving the amplitudes of the useful data. This choice appears to be the best trade off between good noise reduction and little distortion of the desired events. Furthermore we have balanced this VSP data in energy. Note the conversion from the direct *P* to a *S*-wave (see arrow in Figure C.3b). Due to the strong downgoing wave modes the weaker upgoing reflections are quite difficult to identify.

In general, the downgoing wave field in a VSP dataset is so dominant that upgoing primary reflections are difficult to identify and any interpretation is often impossible to make. In addition, the shape of the source wavelet may vary from trace to trace and often the data is contaminated with numerous surface and intrabed multiples.

Figure C.4 shows some processing steps on the VSP data of Figure C.3b. Figure C.4a shows the Mobil VSP data after alpha-trim stacking and energy balancing starting at 720m depth. In Figure C.4b a negative time shift is applied to the VSP data (Figure C.3b) to align the downgoing wave modes. By using the median filtering scheme along the depth axis, the downgoing *P*-waves are extracted (after shift with first break time) from the original VSP data (Figure C.4a). The result of the separation of the upgoing waves from the downgoing is depicted in Figure C.4c. Note that the upgoing waves are better identifiable after the attenuation of the strong downgoing *P*-wave modes. Figure C.4d shows the data after deconvolution with the wavelet determined from the downgoing waves (because downgoing waves are much stronger than the upgoing waves; operators are based on a stronger signal). Observations show that the seismic wavelet is in most cases more complicated and longer than frequently expected. Downgoing waves in VSP data are easily separable from upgoing wave modes since the direction of the VSP geophone deployment creates opposite time-depth steepouts for downward and upward traveling wavelets. The retrieval of the complete downgoing seismic wave field from VSP data allows the calculation of robust deconvolution operators which will separate upgoing multiples from upgoing primary reflections.

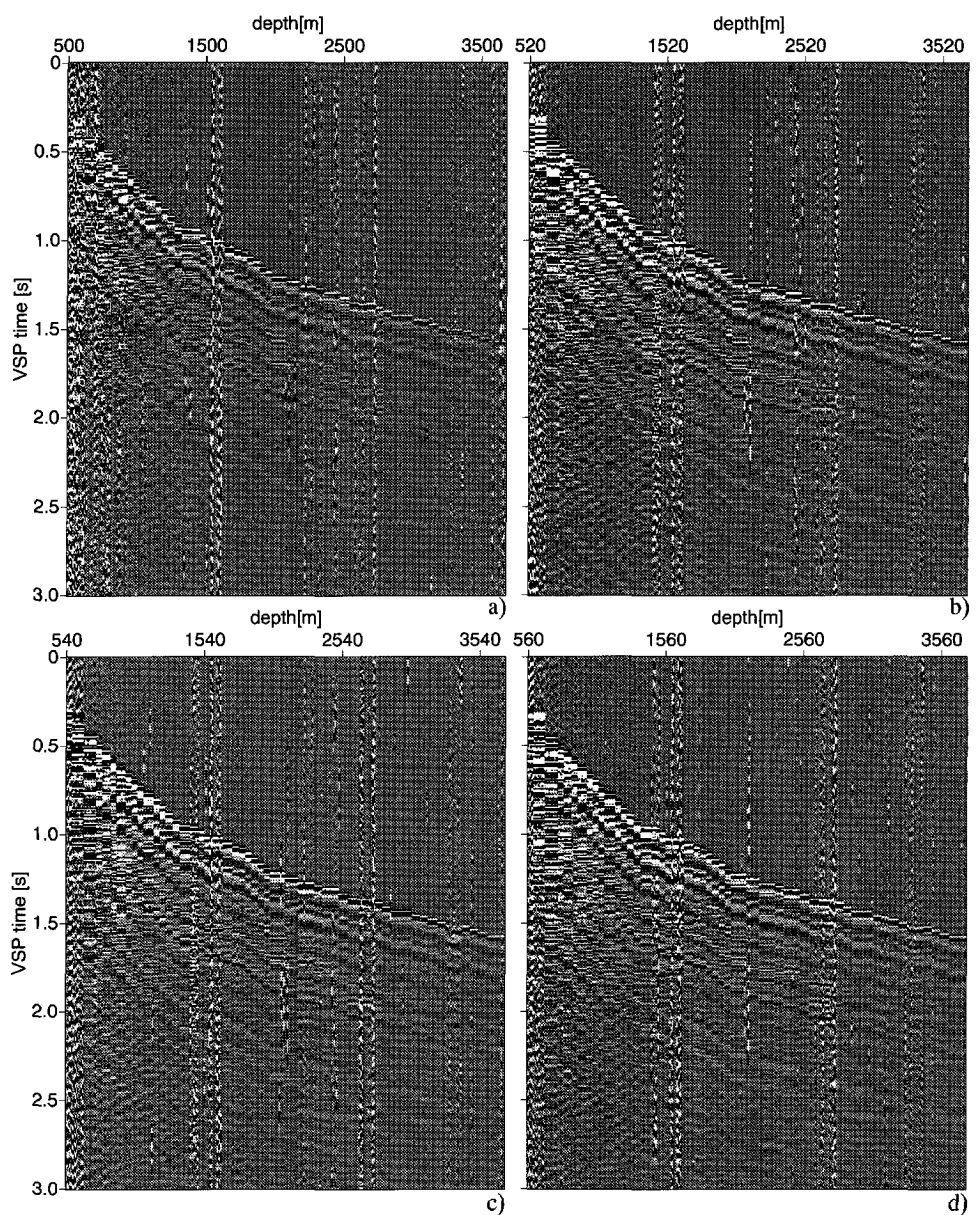


Figure C.1 Raw VSP data registrations (well B - vertical component; detector 1 to 4). The data was provided by Mobil Exploration and Producing Technical Center Dallas U.S.A..

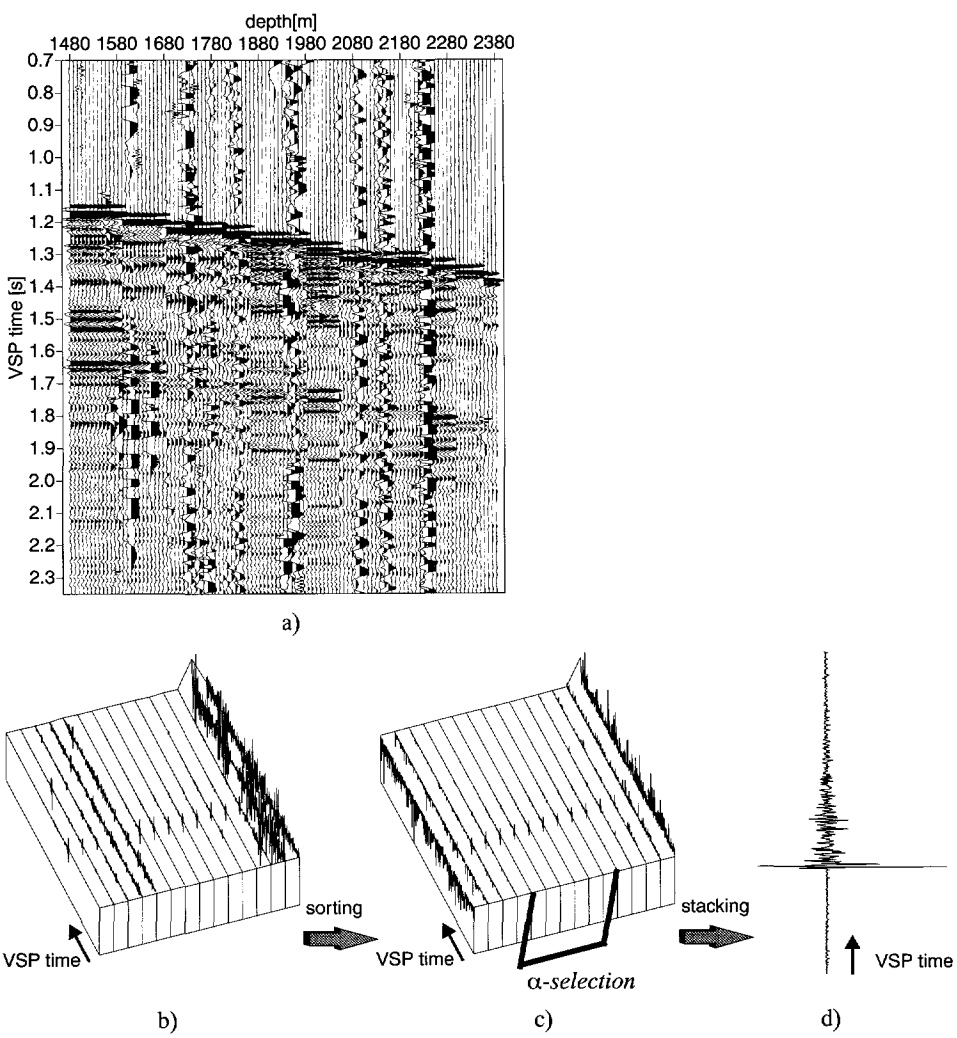


Figure C.2 a)Partial blow up of the data registrations for detector 1 (several registrations at one certain depth level). b) to d) : Alpha-trim sorting and stacking procedure applied on VSP data.

In order to position the upgoing waves to their correct two-way time every trace is shifted by the first break time. The next VSP processing step involves datuming all receivers to the well head. A corridor is defined (see Figure C.4e) after two-way time correction of the upgoing wave modes. The reference of the data is set to the Mean Sea Level (MSL). Finally, the last step involves stacking the traces in Figure C.4e.

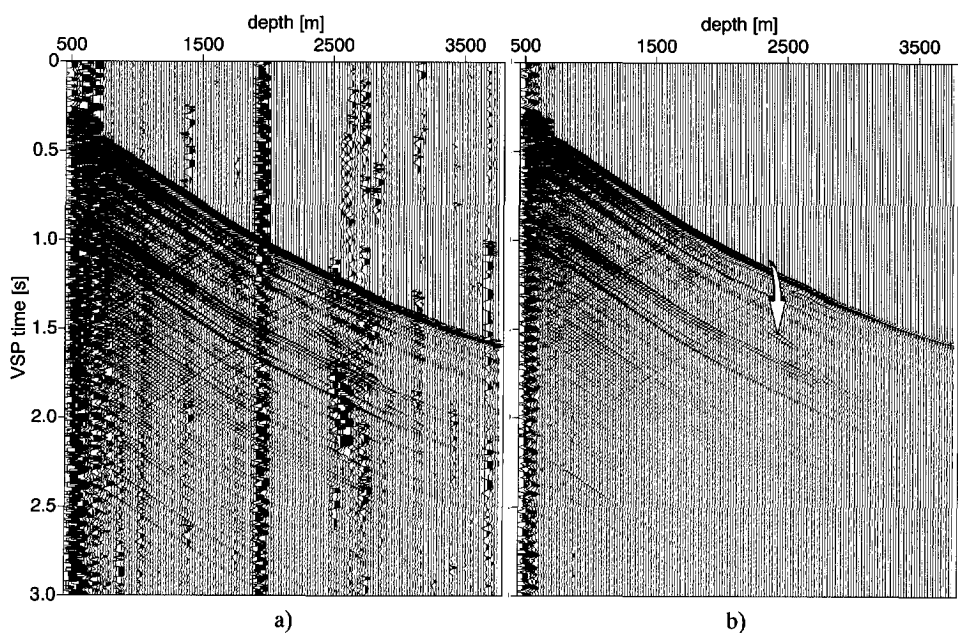


Figure C.3 VSP data after alpha-trim stacking for different α values : $\alpha=0$ and $\alpha=0.7$.

The stacking includes a narrow corridor along the region in which up- and downgoing waves coincide. Figure C.4f illustrates the result of VSP corridor stacking. The VSP corridor stack is repeated 10 times. The *corridor stack* corresponds to a trace without multiples which is the convolution of a wavelet with the series of reflection coefficients. In other words, the trace in Figure C.4f can be considered an alternative to a zero-offset synthetic seismogram derived from the sonic log : it can be compared to the stack of the seismic section at the well location.

Investigation of Figure C.4d in more detail shows a rather remarkable change in the nature of the reflection from right to left. The events at the slope correspond with the first arrival times contain the first upwave arrivals and no multiples (corresponds in other words to the migrated deconvolved section). On the other hand the left hand side which is closely to the seismic surface trace contains multiples and is not migrated. Following the events from the left hand side to the slope (right hand side), the data changes from a non migrated multiples included data into migrated deconvolved data. Further to Figure C.4e a zone or *corridor* can be defined where the signal-to-noise ratio is the best and multiples are absent.

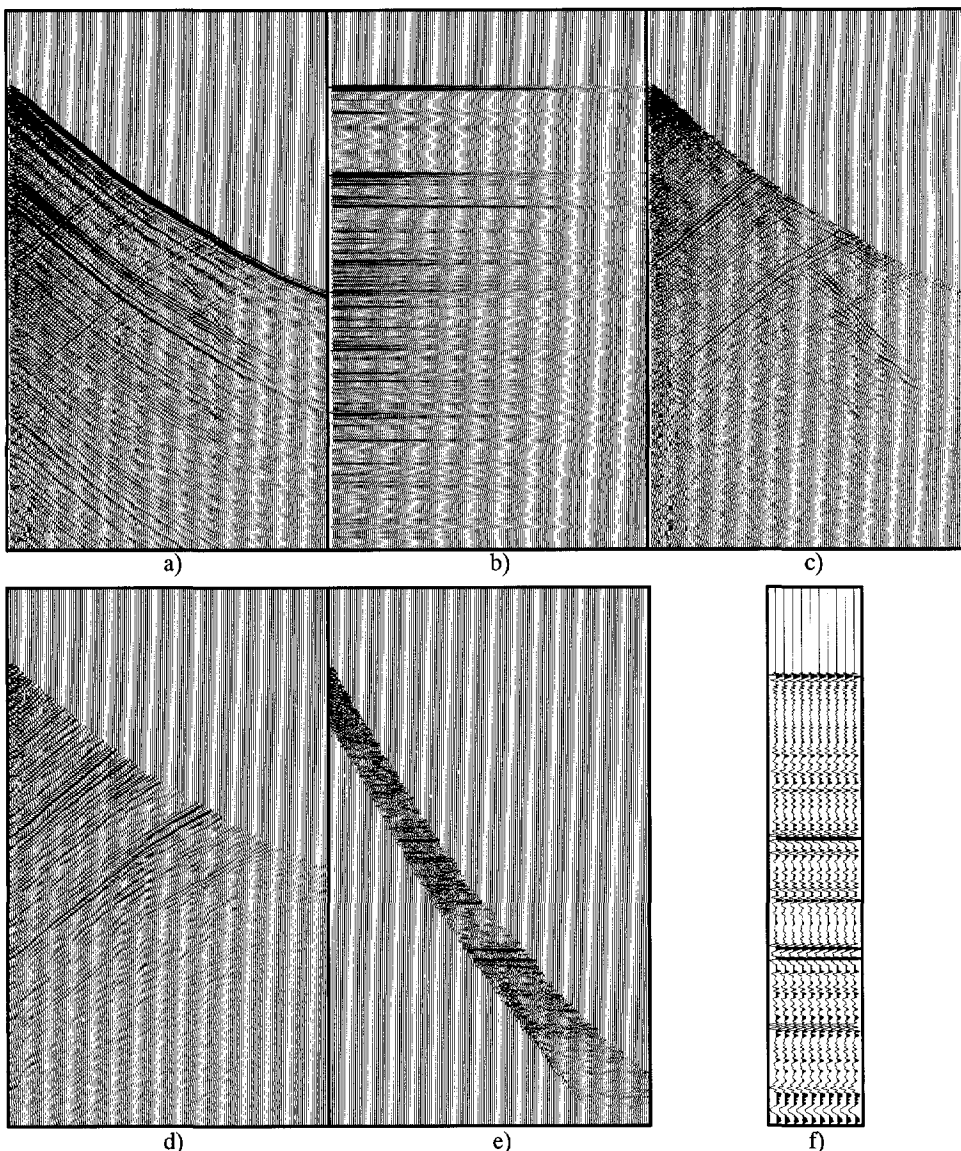


Figure C.4 Processing of Mobil VSP data : a) data after alpha-trim stacking and energy balancing, b) vertically aligned downgoing waves, c) upgoing waves, d) upgoing waves after deconvolution, e) two-way time correction and corridor mute and f) corridor stack (reproduced 10 times).

One of the last VSP processing step is the so-called VSP-CDP transform. The VSP-CDP transform images the data into a CDP-time domain, equivalent to a CDP stacked section, Wyatt and Wyatt (1981). In Figure C.5 the algorithm of the VSP-CDP transform is illustrated. The left panel shows two primary reflection raypaths for a single detector at depth. In the centre, the VSP is displayed with the two reflected events.

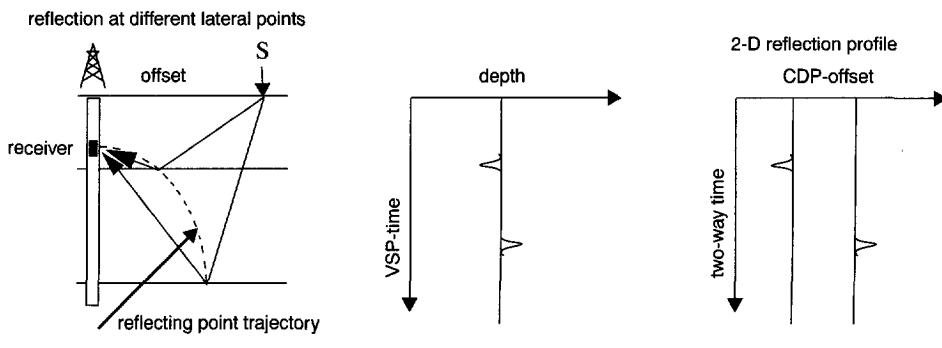


Figure C.5 VSP-CDP transformation of an offset VSP. All reflection points lie along the reflection point trajectory (dashed line). CDP traces are created by moving each event on its correct reflecting point offset and two-way time (from Cassell 1984).

The VSP-CDP transform splits up the trace and positions each event at its correct offset location to yield a 2-D reflection profile. In this transformation, the amplitudes on a single VSP trace are mapped onto several traces on the (x, t) plane, where x is the lateral distance of reflection-points from the borehole. The method used by Wyatt and Wyatt (1981) is the so-called VSP-CDP transform. For each recorded VSP trace, the distance from the reflection point to the borehole is estimated as function of time and the trace is divided into segments which are corrected to two-way travel time to obtain a two-dimensional reflection profile. This transform is closely related to the migration of VSP data. The relationship of the VSP-CDP transform and VSP migration is analogous to the relationship of ray-theoretical and wave-theoretical depth migration when applied to surface seismic data Wiggins et al. (1986). The VSP-CDP transform is not exactly a migration process. It handles neither diffractions nor curved interfaces. To handle these features, VSP data must be migrated, Dillon and Thomson (1983). The VSP geometry is like the geometry of a common shot gather, except the shot axis is perpendicular to the receiver axis. Migration of VSP data can be viewed as mapping amplitudes along semi-elliptical trajectories with their focal points being the source and receiver locations. Superposition of all these trajectories yields the migrated section. As VSP data are known to be highly consistent, one might tune the surface seismic processing scheme in order to get a better match between the two data types, Inoublie et al. (1990). The most common used VSP migration scheme nowadays, is the application of the VSP Kirchhoff migration as discussed by Dillon (1988).

References

Alá'i, R., and Wapenaar, C.P.A., 1994, *Pseudo VSP generation from surface measurements: A new tool for seismic interpretation*, Journal of Seismic Exploration, Vol. 3, No. 1, 79-94.

Alá'i, Riaz, Rietveld, W.E.A., Wapenaar, C.P.A., and Berkhouit, A.J., 1995, *From seismic surface measurements to pseudo VSP data: a new tool in 3-D seismic interpretation* 4th International Congress of the Brazilian Geophysical Society, 1st Latin American Geophysical Conference, Rio de Janeiro, Brazil.

Al-Yahya, K.M., 1989, *Velocity analysis by iterative profile migration*, Geophysics Vol. 54, No. 6, 718-729.

Aminzadeh, F., and Mendel, J.M., 1985, *Synthetic vertical seismic profiles for nonnormal incidence plane waves*, Geophysics Vol. 50, No. 1, 127-141.

Aminzadeh, F., Burkhard, N., Nicoletis, L., Rocca, F., and Wyatt, K., 1994, *SEG/EAGE 3-D modeling project : 2nd update*, The Leading Edge, Vol. 13, No. 9, 949-952.

Aminzadeh, F., Burkhard, N., Kunz, T., Nicoletis, L., and Rocca, F., 1995, *3-D Modeling Project : 3rd report*, The Leading Edge, Vol. 14, No. 2, 125-128.

Aminzadeh, F., Burkhard, N., Long, J., Kunz, T., Duclos, P., 1996, *Three dimensional SEG/-EAGE models - an update*, The Leading Edge, Vol. 15, No. 2, 131-134.

Anstey, N.A., 1980, *Seismic delineation of oil and gas reservoirs using borehole geophones*, Seismograph Services Ltd.

Balch, A.H., Lee, M.W., Miller, J.J., and Ryder, R.T., 1982, *The use of vertical seismic profiles in seismic investigations of the earth*, Geophysics Vol. 47, No. 6, 906-918.

Balch, A.H., and Lee, M.W., Eds., 1984, *Vertical Seismic Profiling : Technique, applications, and case histories*, International Human Resources Dev. Corp. (IHRDC), Boston.

Berkhout, A.J., 1982, *Seismic Migration : Imaging of acoustic energy by wave field extrapolation, Volume 14A, Theoretical Aspects*, 2nd edition, Elsevier, Amsterdam.

Berkhout, A.J., 1984, *Seismic Migration : Imaging of acoustic energy by wave field extrapolation, Volume 14B, Practical Aspects*, Elsevier, Amsterdam.

Berkhout, A.J., 1985, *Seismic migration: Imaging of Acoustics energy by wavefield extrapolation, 14A, Theoretical Aspects*, 3rd edition, Elsevier, Amsterdam.

Berkhout, A.J., 1987, *Applied seismic wave theory*, Elsevier, Amsterdam.

Berkhout, A.J., 1992, *Areal shot record technology*, J. Seis. Expl., Vol. 1, No. 3, 251-264.

Berkhout, A.J., 1993, *A unified approach to acoustical reflection imaging. I: The forward model*, J. Acoust. Soc. Am., **93**, No. 4, 2005-2016.

Berkhout, A.J., and Rietveld, W.E.A., 1994, *Determination of macro models for prestack migration: Part I, Estimation of macro velocities*, 64th Annual SEG Conference and Exhibition, Expanded Abstracts, 1330-1333.

Berkhout, A.J., 1997a, *Pushing the limits of seismic imaging, Part I : Prestack migration in terms of double dynamic focusing*, Geophysics Vol. **62**, No. 3, 937-953.

Berkhout, A.J., 1997b, *Pushing the limits of seismic imaging, Part II: Integration of prestack migration, velocity estimation, and AVO analysis*, Geophysics Vol. **62**, No. 3, 954-969.

Blacquière, G., 1989, *3D wave field extrapolation in seismic depth migration*, Ph.D. thesis, Delft University of Technology, Delft.

Cassell, B., 1984, *Vertical seismic profiles - an introduction*, First Break 2, No. 11, 9-19.

Claerbout, J.F., 1971, *Toward a unified theory of reflector mapping*, Geophysics Vol. **36**, No. 3, 467-481.

Claerbout, J.F., and Muir, F., 1973, *Robust modelling with erratic data*, Geophysics Vol. **38**, No. 5, 826-844.

Claerbout, J.F., 1976, *Fundamentals of geophysical data processing*. McGraw-Hill.

Cox, H.L.H., 1991, *Estimation of macro velocity models by wave field extrapolation*, Ph.D. thesis, Delft University of Technology, Delft.

De Hoop, A.T., 1988, *Time-domain reciprocity theorems for acoustic wave fields in fluids with relaxation*, Journal of the Acoustical Society of America, **84**, 1877-1882.

Dillon, P.B., and Thomson, R.C., 1983, *Image reconstruction for offset source VSP surveys*, 45th Annual EAEG Conference and Exhibition, Extended Abstracts.

Dillon, P.B., and Thomson, R.C., 1984, *Offset source VSP surveys and their image reconstruction*, Geophysical Prospecting, **32**, 790-811.

Dillon, P. B., 1988, *Vertical seismic profile migration using the Kirchhoff integral*, Geophysics Vol. **53**, No. 6, 786-799.

Dougherty, M. E., and Stephen, R. A., 1988, *Seismic energy partitioning and scattering in laterally heterogeneous ocean crust*, J. Pure Appl. Geophys., Vol. **128**, 195-229.

Dupal, L., Ekmann, G., Hansen, R., and Opedal, A., 1993, *Triaxial offset VSP in a horizontal well in the Gullfaks field*, 55th Annual EAEG Conference and Exhibition, Extended Abstracts, C038.

Ehinger, A., 1994, *Picrocol model and data set*, Internal Publication, Institut Français du Pétrole.

Faye, J.P., and Jeannot, J.P., 1986, *Prestack migration velocities from focusing depth analysis*, 56th Annual SEG Conference and Exhibition, Expanded Abstracts, S7.6.

Fessenden, R.A., 1917, *Method and apparatus for locating ore bodies*, U.S. Patent No. 1,240,328.

Fitch, A.A., and Dillon, P.B., 1983, *Removal of the reverberant tails from the reflections recorded in the vertical seismic profile*, Seismograph Services Ltd.

Fitch, A.A., 1984, *Interpretation of Vertical Seismic Profiles*, First Break 2, No. 6, 19-23.

Fokkema, J.T., and Van den Berg, P.M., 1993, *Seismic applications of acoustic reciprocity*, Elsevier, Amsterdam.

Frinking, P.J.A., 1994, *Integration of L_1 and L_2 filtering with application to seismic data processing*, M.Sc. Thesis, Delft University of Technology, Delft.

Fyfe, D.J., and Kelamis, P.G., 1992, *Removing coherent noise using linear Radon transformation*, 54th Annual EAEG Conference and Exhibition, Extended Abstracts, 550-551.

Gal'perin, E.I., 1974, *Vertical seismic profiling*, Society of Exploration Geophysicists Special Publication No. 12, Tulsa, 270 pages.

Grimbergen, J.L.T., Wapenaar, C.P.A., and Dessim, F.J., 1995, *One-Way Operators in Laterally Varying Media*, 57th Annual EAGE Conference and Exhibition, Extended Abstracts, C032.

Grivelet, P., 1985, *Inversion of vertical seismic profiling by iterative modeling*, Geophysics Vol. **50**, No. 6, 924-930.

Hardage, B.A., 1983, *Vertical Seismic Profiling*, Geophysical Press, London - Amsterdam.

Hauge, P.S., 1981, *Measurements of attenuation from vertical seismic profiles*, Geophysics Vol. **46**, No. 11, 1548-1558.

Hinds, R.C., Anderson, N.L., and Kuzmiski, R.D., 1996, *VSP interpretive Processing : Theory and Practice*, Open File Publications No. 3, Soc. Expl. Geophys., Tulsa, Oklahoma.

Holberg, O., 1988, *Towards optimum one-way wave propagation*, Geophysical Prospecting, **36**, 99-114.

Hubbard, T.P., 1979, *Deconvolution of surface recorded data using vertical seismic profiles*, 49th Annual SEG Conference and Exhibition, Expanded Abstracts.

Inoubli, M.H., Richard, Vincent and Ricarte, P., 1990, *Seismic processing by integrated analysis of borehole and surface seismic data*, 60th Annual SEG Conference and Exhibition, Expanded Abstracts, 281-284.

Kabir, M.M.N., 1997, *Velocity estimation of the complex subsurface using the common focus point technology*, Ph.D. thesis, Delft University of Technology, Delft.

Kennett, P., Ireson, R.L., and Conn, P.J., 1980, *Vertical Seismic Profiling - Their applications in exploration geophysics*, Geophysical Prospecting, **28**, 676-699.

Kinneging, N. A., Budejicky, V., Wapenaar, C. P. A. and Berkhouit, A. J., 1989, *Efficient 2D and 3D shot record redatuming*, Geophysical Prospecting, **37**, No. 5, 493-530.

Kommedal, J. H., and Tjostheim, B.A., 1989, *Tutorial: A study of different methods of wave-field separation for application to VSP data*, Geophysical Prospecting, **37**, No. 2, 117-142.

Kozawa, T., Tsuru, T., and Walden, S., 1996, *Reverse VSP with Drill Bit source in Carbonates*, 58th Annual EAGE Conference and Exhibition, P174.

Lafond, C.F., and Levander, A.R., 1993, *Migration moveout analysis and depth focusing*, Geophysics Vol. **58**, No. 1, 91-100.

Lecomte, J.C. et al., 1994, *SEG/EAGE 3D overthrust model*, CD-ROM IFP Publications, Annual SEG Conference and Exhibition, Los Angeles, U.S.A.

Li, Z., 1990, *Structure and velocity inversions of P and S-waves of VSP and surface seismic data*, 60th Annual SEG Conference and Exhibition, Expanded Abstracts, 94-97.

O'Brien, M.J., and Gray, S.H., 1996, *Can we image beneath salt?*, The Leading Edge, **15**, 17-22.

Omnes, G., 1978, *Vertical seismic profiling: a bridge between velocity logs and surface seismicograms*, 53rd Annual SPE Fall Conference, SPE paper No. 7436, Houston Texas.

Omnes, G., 1984, *Deconvolution of surface seismic traces using VSP data*, in Toksöz, M.N., Stewart, R.R., Eds., *Vertical seismic profiling, Part B: Advanced concepts*, Geophysical Press, 113-121.

Oristaglio, M.L., 1985, *A guide to the current uses of vertical-seismic-profiles*, Geophysics Vol. **50**, No. 12, 2473-2479.

Rayleigh, J.W., 1896, *Theory of sound*, Volume II, second edition; reprint 1945 : Dover Publications, Inc., New York.

Rietveld, W.E.A., 1995, *Controlled Illumination in Prestack Seismic Migration*, Ph.D. thesis, Delft University of Technology, Delft.

Robertsson, J.O.A., Blanch, J.O., and Symes, W.W., 1994, *Viscoelastic finite-difference modeling*, Geophysics Vol. **59**, No. 9, 1444-1456.

Schieck, D.G., and Stewart, R.R., 1991, *Prestack Median f-k Filtering*, 61st Annual SEG Conference and Exhibition, Expanded Abstracts, 1480-1483.

Stewart, R.R., and DiSiena, J.P., 1989, *The values of VSP in interpretation*, The Leading Edge, **8**, 16-23.

Thorbecke, J.W., and Berkhout, A.J., 1994, *3-D recursive extrapolation operators: An overview*, 64th Annual SEG Conference and Exhibition, Expanded Abstracts, 1262-1265.

Thorbecke, J. W., and Rietveld, W. E. A., 1994, *Optimum extrapolation operators - A comparison*, 56th Annual EAEG Conference and Exhibition, Extended Abstracts, P105.

Thorbecke, J.W., 1997, *Common Focus Point Technology*, Ph.D. thesis, Delft University of Technology, Delft.

Tal-virsky, B.B., and Tabakov, A.A., 1983, *High resolution prediction of acoustic impedances below bottom-of-hole*, Geophysical Prospecting, **31**, 225-236.

Toksöz, N.M., and Stewart, R.R., 1984, *Vertical Seismic Profiling, part B : advanced concepts*, Volume 14B, Geophysical Press, London - Amsterdam.

Tukey, J.W., 1977, *Exploratory Data Analysis*, Addison -Wesley, Reading Massachusetts.

Ursin, B., 1983, *Review of elastic and electromagnetic wave propagation in horizontally media*, Geophysics Vol. **48**, No. 8, 1063-1081.

Verrier, G., and Branco, F.C., 1972, *La fosse tertiaire et le gisement de Quenguela-Nord*, Revue de l'Institut Français du Pétrole, 27(1), 51-72.

Verschuur, D.J., 1991, *Surface-related multiple elimination: an inversion approach*, Ph.D. thesis, Delft University of Technology, Delft.

Verschuur, D.J., Berkhouit, A.J., and Wapenaar, C.P.A., 1992, *Adaptive surface-related multiple elimination*, Geophysics Vol. **57**, No. 9, 1166-1177.

Versteeg, R., and Grau, G., 1991, *The Marmousi Experience* : Proceedings of the 1990 EAEG workshop on Practical Aspects of Seismic Data inversion, EAEG.

Wapenaar, C.P.A., and Berkhouit, A.J., 1989, *Elastic wave field extrapolation : Redatuming of single- and multi-component seismic data*, Elsevier, Amsterdam.

Wapenaar, C.P.A., 1993, *Representation of seismic reflection data; Part : II New developments*, Journal of Seismic Exploration., Vol. **2**, No. 3, 247-256.

Wapenaar, C.P.A., 1996, *Reciprocity theorems for two-way and one-way wave vectors: a comparison*, J. Acoust. Soc. Am., **100**, (6), p 3508-3518.

Wiggins, W., Ng, P., and Manzur, A., 1986, *The relation between the VSP-CDP transformation and VSP migration*, 56th Annual SEG Conference and Exhibition, Expanded Abstracts, S14.2.

Wong, W. and Noponen, I., 1986, *Deconvolution of surface-recorded seismic data with a wavelet jointly derived from VSP and surface seismic observations*, 56th Annual SEG Conference and Exhibition, Expanded Abstracts, S11.2, 507-509.

Wyatt, K.D., and Wyatt, S.B., 1981, *The determination of subsurface structural information using the vertical seismic profile*, 51st Annual SEG Conference and Exhibition, Expanded Abstracts, S5.2.

Wyatt, K.D., 1981, *Synthetic vertical seismic profile*, Geophysics Vol. **46**, No. 6, 880-891.

Yilmaz, O., and Chambers, R.E., 1984, *Migration velocity analysis by wave-field extrapolation*, Geophysics Vol. **49**, No. 10, 1664-1674.

Yilmaz, Özdogan, 1988, *Seismic Data Processing*, Society of Exploration Geophysicists.

Summary

Seismic methods employ elastodynamic waves to obtain information of the earth's subsurface. Usually seismic data are recorded at the surface as a response of the earth's subsurface generated due to impulsive sources at the surface. However, the existence of a borehole allows the seismic method to be applied with sources and/or detectors in the borehole as well. With this special type of survey high resolution information can be obtained in the neighbourhood of the borehole, particularly for accurately mapping oil and gas reservoirs in the target zone. Data acquisition with sources at the surface and receivers in a borehole is generally referred to as Vertical Seismic Profiling (VSP). The VSP method has the extra advantage that it yields excellent insight into the complex elastic wave propagation process in the subsurface.

In this thesis a new approach is presented to seismic imaging and interpretation by the transformation of surface seismic data into pseudo VSP data for various prespecified (deviated) borehole / detector configurations. This transformation is performed numerically; the result simulates the seismic recording in a borehole.

Chapter 1 discusses the motivation and objectives of the research : improved insight and possibilities in processing and interpretation due to data reorganization. In the standard 'shot record' organization the type of wave fields (up, down; compressional, shear) are difficult to discriminate. However, in the VSP organization the different wave types are well visible due to the large difference in moveout. This underlines the importance of data reorganization.

Chapter 2 deals with the formulation of the propagation and reflection of waves through the subsurface. Starting from the acoustic wave equation, the two-way and one-way wave field extrapolation operators are determined in the wavenumber frequency domain and are used in designing short optimized space frequency operators that are valid in complex structural subsurface models.

In Chapter 3, the principle of the proposed transformation (from surface measurements to pseudo VSP data) is formulated. *Wave field extrapolation* lies at the basis of the transformation. Using a macro model of the subsurface, wave fields are reconstructed at various depths and information is extracted at particular depth levels for predefined deviated borehole/detector configurations. The importance of data organization is illustrated with the aid of Integrated Seismic Displays (ISD); here the pseudo VSP demonstrates the possibility of integration between unmigrated and migrated data and thus improves the data interpretation of structural images.

Chapter 4 discusses the pseudo VSP data generation in relation with the Common Focus Point (CFP) Technology. In the CFP technology, virtual sources and/or detectors are simulated in the subsurface from surface seismic data by a focusing process in order to analyse 'half-migration results'. The CFP approach prompts a new display for VSP data (in one-way time t'), which offers extra advantages in data processing and interpretation.

Chapter 5 discusses the single-fold imaging using so-called multi-offset, common-well pseudo VSP data. The construction of pseudo VSP image points in depth and/or one-way time is illustrated. The contribution of the individual shot records to the image points at a common-well is stored in a composite image gather, which can be used to verify the used macro model.

In Chapter 6, the single-fold imaging is illustrated using so-called multi-well, common-offset pseudo VSP data. The construction of two-way and one-way common-offset sections is presented on numerical and field datasets. The usual two-way common (source-receiver) offset sections refer to unmigrated sections. The proposed one-way common (source-well) offset sections refer to half-migrated sections showing the illumination of structures for various angles defined by the pseudo wells. They clearly reveal which shot records contribute to images at specific subsurface gridpoints.

Chapter 7 is devoted to illustrate the pseudo VSP method on 2-D field data examples and physically modeled data.

Finally in Chapter 8, 3-D case studies are presented on various 3-D numerically and physically modeled data.

As a general conclusion, it may be stated that the generation of pseudo borehole data may be seen as a tool to generate from seismic surface measurements wave fields along pseudo boreholes to allow a better analysis of complex wave fields and to facilitate new data processing and data integration techniques.

Samenvatting

Seismische methoden maken gebruik van elastodynamische golven om informatie te verkrijgen van de ondergrond. Gewoonlijk worden seismische data geregistreerd aan het aardoppervlak als een responsie van de ondergrond door gebruik te maken van impulsieve bronnen aan het aardoppervlak. Echter, de aanwezigheid van een boorgat maakt het ook mogelijk om de seismische methode toe te passen met bronnen en/of detectoren in het boorgat. Met dit speciale type configuratie kan men hoge resolutie informatie verkrijgen in de nabijheid van het boorgat, voornamelijk voor het nauwkeurig afbeelden van olie en gas reservoirs in het doelgebied. Data registratie waarin bronnen geplaatst worden aan het aardoppervlak en ontvangers in een boorgat wordt een Vertikale Seismische Profiel (VSP) genoemd. De VSP methode heeft het extra voordeel dat het uitstekend inzicht biedt in het complex elastische golfpropagatie proces in de ondergrond.

In dit proefschrift wordt een nieuwe aanpak gepresenteerd voor het afbeelden en interpreteren van seismische data door seismische oppervlakte data naar pseudo VSP data te transformeren voor verschillende boorgat/detector configuraties. Deze transformatie wordt numeriek uitgevoerd; het resultaat simuleert de seismische registratie in een boorgat.

Hoofdstuk 1 bespreekt de motivatie en het doel van het onderzoek : verbeterd inzicht en mogelijkheden in processing and interpretatie door data reorganisatie. In de standaard ‘shot record’ organisatie is het moeilijk om de type golfvelden (opgaand, neergaand; longitudinaal, transversaal) te onderscheiden. Echter, in de VSP organisatie, zijn de verschillende golftypes goed zichtbaar door het grote verschil in ‘moveout’. Dit benadrukt het belang van data reorganisatie.

Hoofdstuk 2 behandelt de formulering van de propagatie en reflectie van golven in de ondergrond. Vanuit de akoestische golfvergelijking, worden de zogenaamde twee-weg en éénweg golfveldextrapolatie operatoren bepaald in het golftal domein; deze worden gebruikt

in het ontwerpen van korte geoptimaliseerde plaats-frequentie operatoren welke geldig zijn in complexe structurele ondergrond modellen.

In Hoofdstuk 3 wordt het principe van de voorgestelde transformatie (van oppervlakte metingen naar pseudo VSP data) geformuleerd. Golfveldextrapolatie vormt de basis van de transformatie. Door gebruik te maken van een macro model, worden golfvelden gereconstrueerd op verschillende diepten op posities volgens vooraf beschreven boorgat/detector configuraties. Het belang van de data transformatie wordt geïllustreerd met behulp van geïntegreerde seismische displays (ISD); de pseudo VSP toont hiermee de mogelijkheden van integratie aan tussen ongemigreerde en gemigreerde data en verbetert dus de data interpretatie van structurele afbeeldingen.

Hoofdstuk 4 bespreekt het genereren van pseudo VSP data in relatie met de "Common Focus Point" (CFP) techniek. In de CFP techniek worden virtuele bronnen en/of detectoren gesimuleerd in de ondergrond vanuit seismische oppervlakte data met een focusseringen methode om 'half gemigreerde resultaten' te analyseren. De CFP benadering geeft een aanzet voor een nieuwe display voor VSP data (in één-weg looptijd 't'), welke extra voordelen biedt in data processing en interpretatie.

Hoofdstuk 5 bespreekt het gebruik van zogeheten multi-offset, common-well pseudo VSP data. De constructie van pseudo VSP afbeeldingspunten in diepte en/of één-weg looptijd wordt geïllustreerd. De bijdrage van de individuele shot records tot de afbeeldingspunten langs een common-well wordt verzameld in een samengestelde afbeeldingsdataset, welke gebruikt kan worden om het macro model te verifiëren.

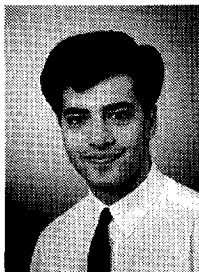
In Hoofdstuk 6 wordt gebruik gemaakt van zogeheten multi-well, common-offset pseudo VSP data. De constructie van twee-weg en één-weg common-offset secties wordt gepresenteerd aan de hand van numerieke data en velddata. De gebruikelijke twee-weg common (bron-ontvanger) offset secties verwijzen naar ongemigreerde secties. De voorgestelde één-weg common (bron-well) offset secties verwijzen naar half-gemigreerde secties welke de belichting van structuren laten zien onder verschillende hoeken, die gedefinieerd worden met behulp van pseudo wells. Deze laten duidelijk zien welke shot records bijdragen tot de afbeeldingen aan specifieke gridpunten in de ondergrond.

Hoofdstuk 7 is gewijd aan het illustreren van de pseudo VSP methode aan de hand van 2-dimensionale velddata en fysisch gemodelleerde data.

Ten slotte worden in Hoofdstuk 8, 3-dimensionale analyses gepresenteerd aan de hand van enkele 3-dimensionale numerieke en fysisch gemodelleerde datasets.

Algemeen concluderend kan worden gesteld dat de generatie van pseudo boorgat data kan worden gezien als een gereedschap om van seismische oppervlakte metingen, golfvelden te genereren langs pseudo boorgaten, om een betere analyse van complexe golfvelden te maken en om nieuwe data processing en data integratie technieken mogelijk te maken.

Curriculum Vitae



Riaz Alá'i was born in Teheran, Iran, on November 5, 1968. He received his primary school education from 1974 to 1980 and his secondary and high school education from 1980 to 1986 (at the Lorentz Lyceum; Atheneum B) both in Eindhoven, The Netherlands. In the same year, he started his study at the Delft University of Technology, Department of Electrical Engineering specializing in Control Engineering. He obtained his Master of Science degree at the Control Laboratory in June 1991. For his Master's thesis, he joined the Royal Dutch/Shell Exploration and Production Laboratory (KSEPL), Rijswijk, The Netherlands. The research was reported in the Master's thesis entitled "*Modelling and Control of a Spinning Weight Shear Wave Source*". In 1991, he started his own company and since then he is the President of Graz Company. In 1992 he started his Ph.D. research at the Delft University of Technology, Centre for Technical Geoscience, Department of Applied Physics, where he was a staff member of the Internationally sponsored DELPHI (DELft PHIlosophy on Inversion) Consortium at the Laboratory of Seismics and Acoustics. During his Ph.D. thesis work, he has written numerous reports and articles and gave presentations in many International Geophysical Conferences (and Seminars) and in several Oil Companies in The Netherlands, Brazil, Switzerland, Bahrain, Qatar, Saudi Arabia, United Arab Emirates, U.S.A., Great Britain and Italy. He attended the course "*Applications of 2-D and 3-D filtering*", given by Professor Claerbout (Stanford University) in Manama, Bahrain, 1994. He received the Best paper Award at the 4th International Congress of the Brazilian Geophysical Society, Rio de Janeiro, Brazil. He is affiliated with the Society of Exploration Geophysicists (SEG) and the European Association of Geoscientists & Engineers (EAGE). Towards the end of 1997 he joined the Atlantic Richfield Company (ARCO) in Plano, Texas, U.S.A.

LIST OF PUBLICATIONS

Riaz Alá'i, 1989, *Control of a hoisting-crane*, Report, Delft University of Technology, Department of Electrical Engineering, Control Laboratory, Delft, The Netherlands.

Riaz Alá'i, 1990, *Identification of a first order plant controlled by a PID regulator*, Report nr. T.90.010, Delft University of Technology, Department of Electrical Engineering, Control Laboratory, Delft, The Netherlands.

Riaz Alá'i, 1991, *Modelling and Control of a Spinning Weight Shear Wave Source*, M.Sc. thesis, A.90.072 (548), Delft University of Technology, Delft, The Netherlands.

Riaz Alá'i, 1991, *Modelling and Control of a Spinning Weight Shear Wave Source*, M.Sc. thesis, Report nr. 91.128, Royal Dutch/SHELL Exploration and Production Laboratory, Rijswijk, The Netherlands.

Riaz Alá'i, 1993, *From Surface to VSP data*, DELPHI Volume IV : From seismic measurements to rock and pore parameters, Ch. 15, 349-386.

Riaz Alá'i, 1993, *The full elastic two-way wave-field extrapolation*, DELPHI Volume IV : From seismic measurements to rock and pore parameters, App. 15A, 387-392.

Riaz Alá'i and C.P.A. Wapenaar, 1993, *Transformation of Surface Data into VSP Data*, 63rd Annual SEG Conference and Exhibition, September 26-30, Washington, District of Columbia, U.S.A., Expanded Abstracts, BG5.7, 143-146.

Riaz Alá'i, 1994, *Pseudo VSP generation from Surface data*, DELPHI Volume V : From seismic measurements to rock and pore parameters, Ch. 14, 355-414.

Riaz Alá'i and C.P.A. Wapenaar, 1994, *Pseudo VSP generation from surface measurements : A new tool for seismic interpretation*, Journal of Seismic Exploration, Vol. 3, No. 1, 79-94.

Riaz Alá'i and C.P.A. Wapenaar, 1994, *Pseudo VSP Generation from Surface Measurements: A New Tool for Seismic Interpretation*, The Middle East Conference on Geosciences GEO'94, April 25-27, Manama, Bahrain.

Riaz Alá'i and C.P.A. Wapenaar, 1994, *From seismic surface measurements to pseudo VSP data*, 56th Annual EAEG Conference and Exhibition, June 6-10, Vienna, Austria, Extended Abstracts, G025.

Riaz Alá'i and C.P.A. Wapenaar, 1994, *The Generation of Pseudo VSP data : Field data example*, 64th Annual SEG Conference and Exhibition, October 23-28, Los Angeles, California, U.S.A., Expanded Abstracts, Im1.2, 463-466

Eric Verschuur, Aart-Jan van Wijngaarden and Riaz Alá'i, 1994, *Comparison of Seismic Inversion Methods to a Single Real Data Set : DELPHI stepwise approach to AVO processing*, 64th Post convention SEG workshop, Los Angeles, California, U.S.A.

Riaz Alá'i, 1995, *Use of Pseudo VSP data in lateral prediction*, DELPHI Volume VI : From seismic measurements to rock and pore parameters, Ch. 14, 14.1-14.42.

Riaz Alá'i and D. 't Hart, 1995, *Performance of two-way wave field extrapolation methods*, DELPHI Volume VI : From seismic measurements to rock and pore parameters, App. 14A, 14.43-14.50.

Aart-Jan van Wijngaarden, Eric Verschuur and Riaz Alá'i, 1995, *The Mobil Project, preliminary results of the DELPHI scheme*, DELPHI Volume VI : From seismic measurements to rock and pore parameters, Ch. 15, 15.1-15.24.

Riaz Alá'i and C.P.A. Wapenaar, 1995, *The generation of pseudo VSP data from land data*, 57th Annual EAEG Conference and Exhibition, May 29 - June 2, Glasgow, Scotland, Extended Abstracts, P075.

Riaz Alá'i and C.P.A. Wapenaar, 1995, *Integration of Seismic Data with Well Logs via the pseudo VSP generation technique*, SEG Summer Research Workshop : Integration of Seismic Data with Well Logs, August 13-17, Vail, Colorado, U.S.A.

Riaz Alá'i, W.E.A. Rietveld, C.P.A. Wapenaar and A.J. Berkhouit, 1995, *From seismic surface measurements to pseudo VSP data: a new tool in 3-D seismic interpretation*, 4th International Congress of the Brazilian Geophysical Society, 1st Latin American Geophysical Conference, August 20-24, Rio de Janeiro, Brazil, Expanded Abstracts, Volume I, 451-455.

A.J. Berkhouit and Riaz Alá'i, 1995, *Improving predrilling views at reservoirs*, Organization of Arab Petroleum Exporting Countries (OAPEC)/John Brown Workshop : "New Technologies Applied to Hydrocarbon Production", September 12-15, Delft, The Netherlands, Proceedings, 1-10.

Riaz Alá'i, W.E.A. Rietveld, C.P.A. Wapenaar and A.J. Berkhouit, 1995, *From seismic surface measurements to pseudo VSP data: a new tool in 3-D seismic interpretation*, Selected papers : Best of RIO'95 and St. Petersburg Meetings, 65th Annual SEG Conference and Exhibition, October 8-13, Houston, Texas, U.S.A.

A.J. van Wijngaarden, D.J. Verschuur and Riaz Alá'i, 1995, *AVO/Inversion - Applications in Risk Reduction*, 65th Post convention SEG workshop, Houston, Texas, U.S.A.

Riaz Alá'i and Kees Wapenaar, 1996, *Use of pseudo VSP in 3-D interpretation*, DELPHI Volume VII : From seismic measurements to rock and pore parameters, Ch. 15, 15.1-15.16.

Riaz Alá'i and Frank Weissbach, 1996, *Pseudo VSP generation : comparison with actual VSP recordings*, DELPHI Volume VII : From seismic measurements to rock and pore parameters, App. 15A, 15A.1-15A.18.

Riaz Alá'i and A.J. Berkhouit, 1996, *Lateral prediction with the aid of pseudo VSP data*, DELPHI Volume VII : From seismic measurements to rock and pore parameters, Ch. 16, 16.1-16.26.

A.J. Berkhouit and Riaz Alá'i, 1996, *Bifocal imaging for pseudo seismic borehole data*, DELPHI Volume VII : From seismic measurements to rock and pore parameters, Ch. 17, 17.1-17.8.

Riaz Alá'i and A.J. Berkhouit, 1996, *From multi-streamer seismic measurements to 3-D pseudo VSP data*, THE DOLPHIN PROJECT Volume I : Optimum Data Acquisition Technology for Maximum Image Quality, Ch. 7, 7.1-7.10.

Riaz Alá'i and C.P.A. Wapenaar, 1996, *Pseudo VSP Data Generation : Field Data Example from the Middle East*, The Middle East Conference on Geosciences GEO'96, April 15-17, Manama, Bahrain.

Riaz Alá'i and C.P.A. Wapenaar, 1996, *Pseudo VSP Data Generation : Field Data Example from the Middle East*, The Middle East Conference on Geosciences GEO'96, April 15-17, Manama, Bahrain, in GeoArabia Middle East Petroleum Geosciences Volume 1, Number 1, March 1996, page 110.

Riaz Alá'i and A.J. Berkhouit, 1996, *Generation of Pseudo VSP data from Common Focus Point gathers*, 58th Annual EAGE Conference and Exhibition, June 3-7, Amsterdam, The Netherlands, Extended Abstracts, P135.

Riaz Alá'i and C.P.A. Wapenaar, 1996, *From surface to pseudo borehole data interpretation*, AAPG International Conference and Exhibition, CARACAS'96, September 8-11, Caracas, Venezuela.

Riaz Alá'i and C.P.A. Wapenaar, 1996, *From surface to pseudo borehole data interpretation*, AAPG International Conference and Exhibition, CARACAS'96, September 8-11, Caracas, Venezuela, in AAPG Bulletin, An international Geological Organization, Volume 80, Number 8, August 1996, Abstracts, p. 1328.

Riaz Alá'i and A.J. Berkhouit, 1996, *Transformation of 3-D surface data into pseudo VSP data for the SEG/EAGE Overthrust model*, 66th Annual SEG Conference and Exhibition, November 10-15, Denver, Colorado, U.S.A., Expanded Abstracts, PP 3.2, 1029-1032.

Riaz Alá'i and A.J. Berkhouit, 1997, *Pseudo VSPs and their application in seismic migration*, DELPHI The Imaging and Characterization Programme Volume VIII : From seismic measurements to rock and pore parameters, Ch. 16, 16.1-16.60.

A.J. Berkhouit, Riaz Alá'i and Alexander Koek, 1997, *Acquisition with vertical marine cables, a CFP view*, DELPHI The Acquisition and Preprocessing Programme Volume I : Optimum data acquisition for maximum image quality, Ch. 12, 12.1-12.10.

Riaz Alá'i, 1997, *Towards an indicator for the Poisson's ratio using VSP data*, 59th Annual EAGE Conference and Exhibition, May 26-30, Geneva, Switzerland, Extended Abstracts, P072.

Riaz Alá'i, A.J. Berkhouit, C.P.A. Wapenaar and J.O.A. Robertsson, 1997, *Pseudo VSP's : A 3-D case study*, submitted for presentation at the 67th Annual SEG Conference and Exhibition, November 2-7, Dallas, Texas, U.S.A.

